



HAL
open science

Study of Ultra Wide Band Modulated Backscattering Based RFID Systems

Francesco Guidi

► **To cite this version:**

Francesco Guidi. Study of Ultra Wide Band Modulated Backscattering Based RFID Systems. Electromagnetism. EDX, 2013. English. NNT: . pastel-00848627

HAL Id: pastel-00848627

<https://pastel.hal.science/pastel-00848627>

Submitted on 26 Jul 2013

HAL is a multi-disciplinary open access archive for the deposit and dissemination of scientific research documents, whether they are published or not. The documents may come from teaching and research institutions in France or abroad, or from public or private research centers.

L'archive ouverte pluridisciplinaire **HAL**, est destinée au dépôt et à la diffusion de documents scientifiques de niveau recherche, publiés ou non, émanant des établissements d'enseignement et de recherche français ou étrangers, des laboratoires publics ou privés.

In fulfillment of the requirements for the joint Ph.D. degrees of

ÉCOLE POLYTECHNIQUE PARISTECH

Ecole Doctorale de l'X - Spécialité Informatique

and

UNIVERSITÀ DEGLI STUDI DI BOLOGNA

Dipartimento di Ingegneria dell'Energia Elettrica e dell'Informazione

"Guglielmo Marconi"

STUDY OF ULTRA WIDE BAND MODULATED BACKSCATTERING BASED RFID SYSTEMS

Ph.D. Candidate

FRANCESCO GUIDI

Jury Members

Ghàis El Zein

Klaus Witrissal

Martine Liénard

Davide Dardari

Alain Sibille

Marco Chiani

Raffaele D'Errico

Reviewer

Reviewer

Examiner

(Co-Supervisor) Examiner

Supervisor

Supervisor

Invited Member

15 May 2013

To my mother

INDEX TERMS

UWB

RFID

Backscatter

Tag

Detection

Acknowledgment

I would like to express my deepest gratitude to all those who provided me the possibility to complete this report, which includes three years and a half of efforts, work and cooperation with many brilliant researchers.

Among all, a special thank goes to my advisors, Prof. Alain Sibille, Prof. Davide Dardari and Prof. Marco Chiani, whose contribution in stimulating suggestions and encouragement, helped me to coordinate my activity. Their valuable competences, knowledge and willingness have transmitted me passion for research. I would like also to thank Prof. Christophe Roblin, who acted like an advisor during these years, and his suggestions and experience were very precious to overcome many difficulties encountered during the work. I will never forget his help. I would like to express my gratitude to the reviewers, Prof. Klaus Witrissal and Prof. Ghais El Zein, for their very fruitful comments and for having accepted to review my manuscript, and to Prof. Martine Liénard, for taking part to the jury and her comments on my work. A particular thank goes to Raffaele D’Errico for his help and suggestions at the beginning of my thesis, and for his presence in the jury at my defense.

I would like to thank the RFM group at Telecom ParisTech and all the group at ENSTA-UEI for having hosted part of my activity. When I arrived the first time in Paris, the help of Amir Yousuf was fundamental for my integration with the staff members. I will be always grateful for his patience with me. I would like also to express my gratitude to Gilles Poncelet for his technical support for the measurements equipment, and to Moussa, Yunfei, Zeinab, Taghrid, Luca, Reda, Lila, Fabrice, Francesco and David, who shared with me great moments.

For what my Italian activity was concerned, a particular thank goes to the Telecommunication group at University of Bologna, Cesena Campus, which hosted me. I would like to mention Nico for all the efforts and the moments shared in the European project SELECT, or for the great ”work experience” in USA. Unforgettable. In Cesena, I found also a great friends as Simone, with whom I shared many coffee breaks and a real friendship. I would like

also to thank the other group members Andrea, Enrico, Matteo, Stefano, Vincenzo, Anna and Bità. Last, but not least, Mario. During the pursuing of our PhDs and studies, we shared a friendship that has become stronger and stronger during years!

Un ringraziamento particolare va alla mia famiglia, ai miei genitori che mi hanno sempre sostenuto in ogni scelta e in ogni momento, e a mio fratello e a mia sorella che sono sempre stati presenti. Senza di loro la mia vita sarebbe molto più monotona. Ringrazio anche Luca B. e Caterina, che mi ha reso orgoglioso di essere zio.

Vorrei ringraziare Nico T. per la sua amicizia che dura ormai da quando abbiamo 8 anni, Andre, che è sempre stato presente nonostante la lontananza e si è sempre dimostrato un vero amico, e Segale e Jack, con cui ho condiviso delle vacanze indimenticabili. Nonostante gli anni trascorsi la nostra amicizia non è mai mutata! Ricordo anche il supporto di Fiorella, Paola, Giulia, Luca C., Viola, Flavia, Fede R., Fede G., Tore, Marco, Cristina e Fra. che han condiviso con me diversi momenti a Cesena. Ringrazio anche i ragazzi dello Stock 84 per i calcetti e per il supporto, e Filo, che è tornato a Parigi per sentire la mia discussione.

Un ringraziamento speciale a Anna, Luna, Mary, Vania e Yole, che mi son sempre state vicine in ogni difficoltà, e mi hanno cucinato piatti eccezionali nel corso del mio soggiorno a Parigi (a base di pasta). Ringrazio Macu e Fede per le nostre cene parigine-vegetariane, e Carla, Valentina e Alessia per le serate trascorse insieme ogni tanto lungo la Senna. Last, but not least, Denis ("il migliore amico di Parigi"). La prima persona che ho conosciuto per sbaglio in Francia, è diventata nel tempo un vero amico e un supporto nelle difficoltà. Senza contare l'aiuto per il "pot" e la pizza speciale preparata!

I would like to thank all the people I have met during my great stay at MEASE, where I had the possibility to discover the world of CIUP. I will never forget this period of my life.

Un ringraziamento finale a Anna per il supporto via skype durante il mio soggiorno parigino, e soprattutto la pazienza che ha avuto nei momenti finali di stress..."Ma è che se guardo giù c'ho le vertigini"

Abstract (English)

In the recent years, the idea of the Internet of Things, that is to say a pervasive presence of electronics devices embedded in every-day objects, is facing a rapid adoption and will create a new era in the Internet scenario. Among all the technologies, radio frequency identification (RFID) seems one of the most promising. In addition, when tag cost, size and power consumption become stringent requirements, passive or semi-passive solutions based on the modulation of the backscatter signal represent a good choice. Thus, this work was developed with the intent to study UWB RFID systems based on the modulation of the backscattered signal considering different related issues. The European Project SELECT gave the motivation and the opportunity to investigate the combination of UWB and RFID technologies, which are expected together to overcome many limitations of current narrowband RFID devices. The consciousness that, before the design of proper system architectures for backscatter communication, it was fundamental to understand the basic electromagnetic mechanisms underlying the interaction between readers and tags, was reflected in a wide investigation ranging from EM characterization of backscatter links to the definition and design of signal structures and transmission schemes. This dual need motivated a joint french-italian agreement between two laboratories for the supervision of the thesis. In particular, in the course of the work carried out in France, the analysis of the tag backscattering has been analyzed in several ways, both in ideal and real conditions. The results and competences were then exploited in Italy, in order to study an architecture able to ensure a reliable communication between reader and tag. The thesis and the work are organized as follows.

Chapter 1 is a general overview about current UWB RFID technologies, discussing their main limitation when adopted in industrial environments.

In Chapter 2 the tag backscattering properties are analyzed in several ways, both in ideal and real conditions. Simple approaches for the tag antenna backscattering component reconstruction are shown and validated, with the final conclusion that the same results can be obtained by perform-

ing direct simulations/measurements or by means of the superposition and reciprocity principles.

Chapter 3 addresses the interaction between passive UWB RFID antennas with close disturbers, the study being based on measurements in an anechoic chamber. In particular, it is shown how the tag radiation characteristics are greatly affected by the presence of an object and the measured data are further exploited to compute detection and localization coverage maps using the system set-up described in Chapter 4 and the SNR threshold derived in Chapter 5. The interaction between a tag and a close metallic reflector is also investigated.

Chapter 4 concentrates on an UWB RFID system based on the modulation of the backscattered signals, highlighting potential implementation issues. Corresponding solutions are proposed in order to counteract the main difficulties. The joint adoption of code acquisition schemes with codes properly designed to combat all the system non-idealities is subsequently investigated in order to guarantee reliable performance.

Chapter 5 shows, in particular, that the joint use of orthogonal Gold codes with proper low-complexity detection and synchronization schemes involving bin-dependent thresholding is a promising solution to overcome implementation impairments, such as tag clock drift and near-far effects.

Chapter 6 describes an UWB RFID reader and tag architecture for data communication based on backscatter modulation, which is able to work in the presence of strong clutter and interference. The achievable range and performance are investigated, showing that clutter is the main limiting factor and that it can be mitigated or suppressed through the architecture proposed and the adoption of zero mean spreading codes.

The manuscript contains a final conclusions and perspectives, where it is stressed that a UWB RFID system based on the modulation of the backscatter signal is a promising candidate for the next RFID generation, in terms of cost-performance trade-off.

Résumé (Français)

Depuis quelques années le nouveau paradigme “d’internet des objets”, qui se traduit par la connection des objets de la vie quotidienne à internet grâce à des dispositifs électroniques intégrés, est devenu plus qu’un simple concept et a commencé à entrer dans la réalité. Il en est ainsi des systèmes d’identification par radiofréquence (RFID), qui font partie des technologies disponibles. Lorsque le coût et la taille des “tags” deviennent des exigences prépondérantes, l’adoption de tags (semi-)passifs fondés sur la modulation d’un signal rétro diffusé représente une solution attractive. En outre, l’utilisation de techniques ultra large bande (ULB) apporte des avantages propres à favoriser le remplacement d’une partie des systèmes RFID actuels, fonctionnant en UHF et qui souffrent de certains défauts tels qu’une trop forte consommation ou une faible robustesse en présence d’interférences ou de canaux multi-trajets. La thèse de doctorat se place dans ce contexte: elle a pour objectif l’étude des systèmes ULB RFID semi-passifs et se situe dans le cadre du projet européen SELECT, qui vise à développer et à évaluer un tel système. La prise de conscience qu’il était fondamental de comprendre les mécanismes électromagnétiques intrinsèques à la communication lecteur-tag, préalablement à la conception du système, s’est traduite par la mise en œuvre d’une collaboration étroite franco-italienne dans le cadre d’une cotutelle de thèse et du projet SELECT. C’est donc au départ autour d’une analyse fine et d’une modélisation des aspects antennaires et du canal radio entre le lecteur et le tag que la 1re partie du travail s’est construite (partie française). La 2nde partie a exploité ces travaux pour l’élaboration des schémas de modulation et de codage du lecteur et du tag pour les systèmes semi-passifs (partie italienne). L’ensemble de ces travaux est décrit dans le manuscrit.

Le chapitre 1 montre un aperçu général des technologies RFID actuelles et des techniques ULB et en discute les principales limitations dans le cas des environnements industriels.

Le chapitre 2 traite de plusieurs façons de l’analyse des signaux de rétro-diffusion des tags, au départ dans une situation idéale puis dans des cas

plus réalistes. Des approches simples pour la reconstruction de signal de rétrodiffusion sont présentées et validées, d'où il en ressort que les mêmes résultats peuvent être obtenus par des simulations/mesures directes ou alternativement par l'exploitation des principes de superposition et de réciprocité. Les méthodes proposées permettent ainsi d'accroître la maîtrise des phénomènes qui apparaissent dans la rétrodiffusion et de limiter la complexité ou la lourdeur des simulations et des mesures.

Le chapitre 3 aborde l'étude de l'interaction compliquée entre les antennes des tags ULB et divers perturbateurs représentant les objets sur lesquels ils seraient placés dans des cas d'usage. L'étude s'appuie sur des mesures en chambre anéchoïque et on montre en particulier comment les caractéristiques de rayonnement du tag sont grandement affectées par la présence de l'objet. Les données de mesure sont ensuite exploitées pour évaluer sous forme de cartes de couverture les performances potentielles du système RFID en termes de détection et de localisation, pour des paramètres représentant la configuration décrite dans le chapitre 4 et le rapport signal-bruit obtenu dans le chapitre 5. L'interaction entre un tag et un réflecteur métallique proche est également étudiée.

Le chapitre 4 est consacré à l'étude globale du système ULB RFID. Diverses problématiques importantes sont exposées et des solutions proposées. L'adoption conjointe de schémas robustes d'acquisition de la phase des codes grâce à des codes bien conçus pour combattre toutes les non idéalités du système est ainsi étudiée, afin de garantir des performances fiables.

Le chapitre 5 se concentre sur l'utilisation de codes de Gold orthogonaux avec une stratégie de détection de tag mettant en jeu un seuillage fonction de la case temporelle, qui apparaît être une solution prometteuse pour combattre les effets d'interférence "near-far" et pour traiter les problématiques soulevées dans le chapitre précédent.

Le chapitre 6 développe une architecture lecteur-tag pour la communication reposant sur la démodulation des données contenues dans la mémoire du tag, capable d'opérer en fort fouillis d'environnement et en présence d'interférences.

Enfin le manuscrit se termine par une conclusion et des perspectives. Les résultats obtenus montrent ainsi que les solutions ULB proposées ont la capacité de répondre à certains besoins de systèmes RFID, alliant performance et faible coût.

Sommario (Italiano)

Recentemente il concetto de “l’internet degli oggetti” è diventato più che una semplice idea. L’espressione, coniata dall’AutoID labs (MIT, USA), viene riferita alla presenza pervasiva di dispositivi elettronici sugli oggetti della vita quotidiana, permettendo di mappare il mondo reale in quello di Internet. Fra le tecnologie a disposizione, i sistemi d’identificazione a radio-frequenza (RFID) rappresentano una delle soluzioni più appetibili.

Quando il costo e le dimensioni dei tag RFID diventano requisiti importanti da soddisfare, l’adozione di tag (semi-)passivi rappresenta la scelta migliore, non essendo dotati di una batteria che alimenti il trasmettitore. Una delle tecniche più diffuse per la comunicazione tra reader e tag semi-passivi consiste nella modulazione del segnale riflesso tramite opportune variazioni del carico connesso all’antenna del tag. Inoltre l’utilizzo congiunto delle tecnologie a banda ultralarga (UWB) e RFID, costituisce un valido candidato per sostituire gli attuali sistemi RFID che operano nelle bande UHF e sono affetti da limitazioni ben note quali un più elevato consumo di potenza o una scarsa robustezza alla presenza di forte interferenza o di canali multi-percorso. Per queste ragioni, nate dall’urgenza di trovare una nuova tecnologia che possa sostituire quella attuale, la tesi di dottorato ha come scopo primario lo studio dei sistemi UWB RFID semi-passivi attraverso una collaborazione universitaria italo-francese. Da un lato, sfruttando le competenze del laboratorio francese, si sono caratterizzati i fenomeni che sono alla base del meccanismo di riflessione, sia per antenne isolate che in presenza di perturbatori in prossimità del tag. Le competenze acquisite sono state poi integrate con il background italiano per studiare un’architettura reader-tag che permetta di discriminare la presenza di utenti nello scenario anche in mezzo a una forte interferenza, riflessioni dell’ambiente circostante, e tutte le non-idealità che emergono quando un sistema reale deve essere implementato.

La collaborazione si è inserita nell’ambito del progetto europeo SELECT, che fra i vari obiettivi si pone quello della realizzazione di un sistema UWB RFID semi-passivo. La tesi è stata organizzata come segue.

Il capitolo 1 introduce i concetti di base delle tecnologie UWB e RFID,

con particolare enfasi sul contesto e sulle motivazioni alla base di questo lavoro.

Il capitolo 2 è dedicato allo studio del meccanismo di riflessione dell'antenna tag, utilizzando i principi di reciprocità e di sovrapposizione degli effetti. Si propone anche una metodologia alternativa per legare il segnale riflesso alla funzione di trasferimento del tag.

L'interazione tra il tag e oggetti posti nelle vicinanze viene analizzato nel capitolo 3. Attraverso una campagna di misure, si è valutato come le caratteristiche elettromagnetiche delle antenne variano in presenza di un perturbatore. Le misure sono state poi rielaborate (sfruttando le relazioni del capitolo 2) per valutare le prestazioni di detection e di localizzazione del sistema UWB RFID sotto forma di mappe di copertura in uno scenario controllato. Nell'ultima parte del capitolo si analizza l'interazione tag-oggetto metallico, e si mostrano gli effetti sulle caratteristiche elettromagnetiche dell'antenna.

Nel capitolo 4 si propone un'architettura reader-tag dove vengono descritti alcuni dei problemi che emergono durante la realizzazione del sistema proposto. Differenti famiglie di codici sono inoltre studiate per valutare quale garantisce le prestazioni migliori negli scenari considerati.

Il capitolo 5 mostra che l'utilizzo congiunto di codici di Gold ortogonali e di schemi di acquisizione della fase dei codici garantisce buone prestazioni anche in presenza di forte interferenza e di non-idealità. Viene inoltre proposto uno schema che permetta di rilevare correttamente la presenza di un tag limitando gli effetti di interferenza near-far dovuti alla natura passiva della comunicazione.

Una volta che il tag è stato rilevato, si deve valutare la qualità della comunicazione RFID. A tale scopo, nel capitolo 6 si propone un'architettura reader-tag in cui il payload contenuto nella memoria del tag viene modulato in modo opportuno mitigando gli effetti del clutter e dell'interferenza.

La tesi si chiude con le conclusioni e le prospettive future. I risultati ottenuti hanno mostrato che il sistema UWB RFID proposto rappresenta un serio candidato per la nuova generazione di sistemi RFID, garantendo un buon trade-off in termini di prestazioni e costo.

Contents

List of Figures	xxiii
List of Tables	xxv
List of Acronyms	xxx
Introduction	xxxi
Author Contributions	xxxv
List of publications	xxxvii
1 State of the art of RFID and UWB Technologies	1
1.1 Introduction	1
1.2 The RFID Concept	1
1.3 Main Characteristics of RFID Systems and Technologies . . .	3
1.3.1 Active Tags	5
1.3.2 Passive and Semi-Passive Tags	5
1.3.3 SAW Tags	8
1.4 Summary of the Main radio-frequency identification (RFID) Tag Characteristics	9
1.5 Basic Features of UWB Technologies	10
1.5.1 UWB History	10
1.5.2 Characteristics of UWB Signals	11
1.5.3 Impulse Radio UWB	14
1.6 Passive and Semi-Passive UWB-RFID	15
1.6.1 UWB Antenna Backscattering	16
1.7 UWB RFID Backscattering: The State of The Art	17
1.8 General Motivations of the thesis work	19

2	Electromagnetic Analysis of UWB RFID Tag Backscattering	23
2.1	Introduction	23
2.2	Application of Superposition and Reciprocity Principles in Ideal Scenarios	23
2.3	Proposed Procedures for Tag Backscattering Reconstruction .	26
2.4	Application of Superposition and Reciprocity Principles in Presence of Scatterers	33
2.5	Proposed Methodologies in Presence of Scatterers	37
2.5.1	General Representation	37
2.6	A Different Approach for Tag Backscattering Characterization	43
2.7	Conclusions	46
3	Tag Backscattering Characterization in Presence of Nearby Objects	47
3.1	Introduction	47
3.2	Tag Interaction with Objects	48
3.2.1	Measurement Set-Up	48
3.2.2	Results	51
3.3	Impact of Tag Backscattering Characteristics on the Detection Coverage	58
3.3.1	Case Study Scenario	58
3.3.2	Simulation Results	59
3.4	A Case Study: Tag Interaction with a Perfect Electric Conductor	61
3.4.1	Antenna Backscattering Measurements in Presence of Metal	62
3.4.2	Simulation of the Antenna Backscattering	64
3.5	Total Backscattered Energy in Presence of Metal	70
3.6	Conclusions	71
4	UWB RFID System Architecture and Implementation Is- sues	75
4.1	Introduction	75
4.2	System Design	76
4.3	Reader Transmitted Signal Format	77
4.4	Tag Backscatter Modulation	78
4.5	Design Issues	80
4.5.1	Synchronization Procedure	81
4.5.2	ADC design analysis	82
4.5.3	Tag Clock Drift Model	87
4.6	Tag-to-Reader Communication	87
4.7	Signal De-Spreading	89

4.8	Tags Code Assignment Strategies	91
4.9	Inter-Reader Interference	96
4.10	Conclusions	99
5	Robust Tag Detection Scheme to the Presence of Interference and Drift	101
5.1	Introduction	101
5.2	Signal De-Spreading	102
5.3	Tag Detection	103
5.3.1	Threshold Evaluation Criteria	105
5.4	Numerical Results	111
5.4.1	Simulation Parameters	111
5.4.2	System Design	112
5.4.3	Results	114
5.4.4	Considerations on Threshold SNR for Detection Coverage in Sec. 3.3	117
5.5	Conclusions	118
6	Processing Scheme for Data Demodulation	121
6.1	Introduction	121
6.2	System Model	121
6.3	Laboratory Measurements	127
6.4	Numerical Results	131
6.4.1	System Performance in a Single-Tag Scenario	131
6.5	System performance in a Multi-Tags Scenario	134
6.5.1	BER-SIR in Multi-Tags Anechoic Chamber Scenario with Artificial Clutter	134
6.5.2	BER- N_s in Multi-Tag Laboratory Scenario	135
6.5.3	BER- N_s in Multi-Tags Multipath Scenario with Artificial Clutter	136
6.6	Conclusions	137
A	Theoretical Analysis on the SQNR Before and After De-spreading	143
A.1	Analysis at Low SNR	145
A.2	Analysis at High SNR	145
B	General Solutions for Readers Medium Access Control	149
B.1	Codewords Assignment	149
B.1.1	Same Codewords Assigned to all the Readers	149
B.1.2	Adoption of Performing Codes	150

B.1.3	Alternative Solutions	152
-------	---------------------------------	-----

List of Figures

1.1	Example of a scenario with some reference nodes and tagged and untagged objects.	3
1.2	Classic RFID scenario with a reader interrogating several tags employed in the scenario.	4
1.3	Magnetic field in a coil [28].	6
1.4	FCC and EU spectral masks, respectively, for indoor commercial systems in the absence of appropriate mitigation techniques. An example of 6th derivative of the Gaussian pulse spectrum is also reported [12].	12
1.5	Example of a root raised cosine (RRC) power spectral density (PSD).	15
1.6	Multi-reader scenario with tags and scatterers placed in the environment.	17
1.7	Structural and antenna modes measured in an anechoic chamber.	18
1.8	Antenna mode scattering contribution.	19
1.9	The internal logistics of a manufacturing plant [15].	20
2.1	Ideal reader (left) and tag (right) antennas in LOS.	24
2.2	Left: Ideal reader antenna (transmitting) and tag antenna (receiving) in LOS. Right: Ideal reader antenna (receiving) and tag antenna (transmitting) in LOS.	24
2.3	Tag electric scheme.	28
2.4	Summary scheme of the methodologies proposed.	29
2.5	Dipole in proximity to a metal plate.	30
2.6	Average backscattered power flux vs. tag/metal plate distance. DS refers to the reference simulation.	31
2.7	Simulated dipole in front of a metal plate.	33
2.8	Total Backscattered power over the sphere vs tag/metal plate distance. DS refers to the reference simulation.	34
2.9	Ideal reader antenna (receiving) and tag antenna (transmitting) in LOS.	35

2.10	Left: Ideal reader antenna (transmitting) and tag antenna (receiving) in LOS and in presence of scatterers. Right: Ideal reader antenna (receiving) and tag antenna (transmitting) in LOS and in presence of scatterers.	35
2.11	Left: Reader side for configuration of Fig. 2.10 on the right. Right: Tag side for configuration of Fig. 2.10 on the left.	36
2.12	Sketch of the 2-ports system.	38
2.13	Simulated scenario.	41
2.14	Left: complete received signal (b_{1Open}). Right: Comparison between direct simulations and use of the superposition principle adopting method 1.	42
2.15	Measurement set-up inside the anechoic chamber.	42
2.16	Measurement results. Method 1 is adopted for the superposition principle.	43
2.17	Reader tag configuration.	44
3.1	Measurement scenario	48
3.2	Left: Antenna connection and support configuration. Right: Measurement system rotations.	49
3.3	Left: 22 mm plywood block. Middle: 64 mm composite wood block. Right: plastic bottle full of tap water.	51
3.4	Paper block composition	51
3.5	Wood panel in proximity of the tag antenna for $\varphi = 0$	52
3.6	a) $\varphi = 0^\circ$. b) $\varphi = 90^\circ$ c) $\varphi = 270^\circ$	53
3.7	Linear normalized antenna mode tag backscattering gain for different antennas in the azimuth plane. The maximum measured isolated Antenna Mode tag backscattering values are in dB: Dual Feed Monopole Monostrip (DFMM)=-0.94. monopole dual feed stripline antenna (DFMS)=2.31. SLOT=7.99. Planar balance dipole (PBD)=5.32.	54
3.8	$ S_{11} $ for the DFMM antenna.	55
3.9	$ S_{11} $ for the DFMS antenna.	55
3.10	$ S_{11} $ for the SLOT antenna.	56
3.11	$ S_{11} $ for the PBD antenna.	56
3.12	Left: Average tag backscattering gain cumulative distribution function (CDF)s concerning the antenna mode scattering. Right: Average tag backscattering gain CDFs concerning the structural mode scattering.	57
3.13	Ideal reader antenna (receiving) and tag antenna (transmitting) in LOS.	59

3.14	Top: Service coverage analysis for $N_r = 1$ (left), $N_r = 2$ (middle) and $N_r \geq 3$ (right). Bottom: same conditions of the top, with a boost of 10 dB in the transmitted power.	60
3.15	Service coverage analysis $N_r = 1$ and $\text{SNR}_{\text{th}} = -25$ dB. Top: DFMS with wood of thickness 22 mm (left) and wood of thickness 64 mm (right). Bottom: DFMS with paper and with bottle of water (right).	61
3.16	Service coverage analysis $N_r = 2$ and $\text{SNR}_{\text{th}} = -25$ dB. Top: DFMS with wood of thickness 22 mm (left) and wood of thickness 64 mm (right). Bottom: DFMS with paper and with bottle of water (right).	62
3.17	Service coverage analysis for $N_r = 2$ (middle) and power boost of 10 dB. Top: Isolated antennas. Middle: Antennas with wood of thickness 22 mm. Bottom: antennas with bottle. DFMM (left), SLOT (middle) and PBD (right).	63
3.18	Measured antennas in presence of a metallic reflector.	64
3.19	ultrawide-band (UWB) thick dipole in the presence of a metal plate with dimensions (5×5) cm ²	65
3.20	Top: Measured Antenna mode scattering with 10x10 cm ² metal placed 1 cm behind the DFMS. Bottom: isolated antenna case.	66
3.21	Left: simulated DFMM. Right: simulated thick broadband dipole.	66
3.22	Metal can placed behind the planar UWB dipole.	67
3.23	Simulated antenna mode scattering for the planar dipole.	67
3.24	Average backscattered energy over the azimuth plane (measured DFMS).	68
3.25	Top: Simulated average energy over the azimuth plane for the DFMM. Bottom: Measured average energy over the azimuth plane for the DFMM.	68
3.26	Top: Simulated average energy over the azimuth plane for the dipole. Bottom: Measured Average energy over the azimuth plane for the dipole.	69
3.27	Top: 3-D mean realized gain for isolated dipole (left) and with a plate (10×10) cm ² behind (right). Bottom: mean realized gain over the azimuth plane for isolated dipole and in presence of metals.	71
3.28	Left: total backscattered power over the sphere vs tag/metal plate distance. Right: Average 3D power flux.	73
4.1	Multi-reader scenario with N_{tag} tags.	76

4.2	Reader ultra-high frequency (UHF) and UWB transmitted signals.	77
4.3	The UWB interrogation signal structure.	78
4.4	Example of reader internal structure.	79
4.5	Tag internal structure.	80
4.6	Wake-up synchronization procedure.	82
4.7	Received signal amplitude $[V]$. Concerning interference from other readers, different cell sizes are considered.	84
4.8	Received signal amplitude $[V]$, where quantization steps amplitudes are associated to different m . Interfering reader amplitude and quantization levels related to a $(10 \times 10) \text{ m}^2$ square cell.	85
4.9	SQNR_{in} at the de-spreader input for a $10 \times 10 \text{ m}^2$ square cell, as a function of useful tag distance, reported for different m	86
4.10	The considered clock skew model.	88
4.11	Clock drift effects on passive and active communication.	90
4.12	Parallel de-spreading blocks.	91
4.13	Interference scenario.	97
5.1	Reader internal structure.	102
5.2	Tag detection scheme.	104
5.3	Example of energy matrix \mathbf{E} in presence of wake-up offset, clock drift and near-far interference effect.	106
5.4	Minimum number of pulses per symbol as function of the reader-tag distance.	113
5.5	receiver operating characteristic (ROC) for tag detection in UWB backscatter system. Continuous lines (–) refer to the perfectly synchronous scenario, dashed lines (– –) refer to the asynchronous scenario, with ideal code phase retrieving.	115
5.6	ROC for tag detection in UWB backscatter system, when orthogonal Gold codes are adopted in presence of tag clock drift and code acquisition schemes in a quasi-synchronous scenario. Continuous lines (–) refer to $N_c = 128$, dashed lines (– –) refer to $N_c = 1024$	116
5.7	ROC for tag detection in presence of synchronization offset, clock drift and near-far interference effects. Continuous lines (–) refer to the bin-dependent threshold, dashed lines (– –) refer to the constant threshold.	118
6.1	The behavior of the signals described in Sec. 6.2.	123
6.2	Clutter removal after signal de-spreading.	125

6.3	Grid considered for the measurement campaign at ENSTA-ParisTech. The distances between each point and the antennas connected to the vector network analyzer are also reported.	128
6.4	Indoor scenario considered for the measurement campaign at ENSTA-ParisTech.	129
6.5	Example of backscatter responses collected inside in the anechoic chamber (plot a) at distance $d_{\text{ref}} = 1.46$ m, in the laboratory (plot b) grid location H at distance of 3.10 m, and of the only antenna mode contribution after clutter removal (plot c) in the same location H.	130
6.6	BEP as a function of the bit rate R_b in different tag locations (Laboratory scenario). The SPMF receiver is considered.	132
6.7	BEP as a function of the bit rate R_b in different tag locations (Laboratory scenario). The IMF receiver is considered.	133
6.8	BER as a function of the SIR in the anechoic chamber scenario where clutter is summed up artificially. DFMS antenna considered.	134
6.9	BER vs N_s in multi-tag laboratory environment and asynchronous scenario.	135
6.10	BER vs N_s in multipath 802.15.4a CM1 channel.	137
A.1	The considered scheme for the ADC and despreader.	144
A.2	signal-to-quantization-noise ratio (SQNR) at the output of the de-spreader-accumulator, for low signal-to-noise ratio (SNR).	146
A.3	SQNR_{out} as a function of N_s , for high SNR.	147
A.4	Relation between SQNR_{out} and SQNR_{in} , for high SNR.	148
B.1	Double/triple cross-correlations when orthogonal Gold Codes ($N_c = 128$) are assigned to the readers and to the tags.	151

List of Tables

1.1	Comparison among the different operative RFID frequencies. . .	9
2.1	Average % error on the backscattered power for each method with respect to direct simulations.	32
3.1	Antennas and descriptions	50
4.1	Clutter rejection and process gain properties of odd codes. . .	92
4.2	Interference mitigation properties of PN codes.	94

List of Acronyms

ACF	autocorrelation function
ADC	analog-to-digital converter
ASK	amplitude shift keying
AUT	antenna under test
Auto-ID	automatic identification
AWGN	additive white Gaussian noise
BEP	bit error probability
BER	bit error rate
BPSK	binary phase shift keying
CCF	cross correlation function
CDF	cumulative distribution function
CDMA	code division multiple access
CIR	channel impulse response
CR	channel response
CS	clock skew
CW	continuous wave
DFMM	Dual Feed Monopole Monostrip
DFMS	monopole dual feed stripline antenna
ED	energy detector

EEPROM Electrically Erasable Programmable Read-Only-Memory

EIRP effective radiated isotropic power

ELP equivalent low-pass

EM electromagnetic

EU European Union

PFA probability of false alarm

FCC Federal Communications Commission

FSK frequency shift keying

HF high frequencies

HW hardware

IDT interdigital transducer

IMF ideal matched filter

INR interference-to-noise ratio

IR-UWB impulse radio UWB

IR impulse radio

ISNR interference-plus-signal-to-noise-ratio

LF low frequencies

LNA low-noise amplifier

LOS line-of-sight

MAC medium access control

MUI multi-user interference

NPF normalized power flux

OC open circuit

OFDM orthogonal frequency division multiplexing

p.d.f. probability distribution function

PBD Planar balance dipole
PD probability of detection
PN pseudo-noise
PPM pulse position modulation
PRP pulse repetition period
PSD power spectral density
PSK phase shift keying
QAM quadrature amplitude modulation
r.v. random variable
RCS radar cross section
RF radio-frequency
RFID radio-frequency identification
ROC receiver operating characteristic
RRC root raised cosine
RTLS real time locating systems
SAW surface acoustic wave
SC short circuit
SCM supply chain management
SCR signal-to-clutter ratio
SIR signal-to-interference ratio
SNR signal-to-noise ratio
SPMF single-path matched filter
SQNR signal-to-quantization-noise ratio
SRAM static random access memory
SS spread spectrum

TDMA time division multiple access

TH time-hopping

TOA time-of-arrival

UHF ultra-high frequency

UWB ultrawide-band

VNA vector network analyzer

WSN wireless sensor network

Introduction

The recent idea of the “Internet of Things”, a pervasive presence of electronics devices embedded in every-day objects, is facing a rapid adoption and will create a new era in the Internet scenario. Ideally, it is expected that every object in our every-day life will be assigned to an IP address and will be sensitive and responsive to the presence of people [1–4].

Considering working and domestic fields, a few possible application scenarios will be domotics, assisted living, e-health and enhanced learning. Similarly, from the perspective of business users, the most apparent consequences will be equally visible in fields such as automation and industrial manufacturing, logistics, business/process management, intelligent transportation of people and goods [5].

Nowadays, a significant number of industrial realities have moved towards the so-called supply chain management (SCM) approach [6], relying on the administration of the various logistics activities of the companies. One of the main requirements of this approach is the knowledge of what a given object is and where it can be found at a given temporal instant. The adoption of automatic identification (Auto-ID) systems for the identification of the goods is widely diffuse, usually exploiting barcode reading or standard RFID tags. These approaches excel in answering the question regarding an item identity, but fail at providing its position to the users. On the contrary, real time locating systems (RTLS) offer an expensive high-precision localization solution, but are not usually integrated with Auto-ID standards. These novel systems are composed of a certain number of readers or anchor nodes interrogating tags deployed in a given area, in order to obtain data stored on them as well as localize the objects they are attached to. Existing RFID systems in SCM employ active tags that periodically send signals to anchor nodes placed in strategic points of the warehouse. Despite ensuring a greater precision, the adoption of active tags, which are equipped with active transmitters, leads to an increased price of the network and to a reduced battery life, causing an increased cost of the overall system and its maintenance. These drawbacks represent significant limitations to the adoption of

active tags in RFID and RTLS, and passive or semi-passive solutions become a good alternative to overcome such a limitation, as the energy necessary for tag-reader communication is harvested from the reader's signal or the surrounding environment [7]. Communication with passive tags usually relies on backscatter modulation, where the antenna reflection properties are changed according to information data, avoiding the need of a transmitter.

In order to achieve a sub-meter level precision, the majority of current RTLS solutions rely on UWB signals [8,9]. The adoption of UWB pulses in conjunction with ranging techniques [10,11], allows sub-nanosecond time resolution, which significantly enhances the localization precision with respect to other radio technologies. Recently it has been shown that impulse radio (IR)-UWB is a very promising technique, which could meet the stringent requirements of passive tag localization in terms of accuracy [12]. The advantage of such a technology is to provide the typical accuracy of UWB-RTLS by employing a very simple tag, based on a backscattering modulation instead of using a complete UWB active transmitter. However one of the most important issues in these systems is the energy supply as no sufficient energy can be transferred through UWB signals due to severe regulating limitations in the emission mask. Combining UWB (semi-)passive RFID with already existing UHF technologies is a possible approach, either through energy harvesting [13] or through the implementation of a wake-up technique in order to increase the battery lifetime. Moreover the UHF module can be employed to ensure compatibility with already existing RFID systems. These technologies are also proposed and studied in the European project SELECT, which is briefly described in Sec. 1.8.

In this context, from a real and urgent necessity to overcome the main limitations of actual RFID technology adopted in industrial environments, the present thesis aims to study from different perspectives a UWB semi-passive RFID system, based on backscatter modulation. The design of robust backscatter communication scheme requires the comprehension of the electromagnetic (EM) aspects involved in the backscattering mechanism. In addition, simulated and measured UWB RFID backscattering data can be exploited for the validation of the proposed system design, in order to evaluate system performance in terms of detection and communication range. For this reason, the need to combine these different aspects has motivated a joint work between two laboratories associated with Ecole Polytechnique and University of Bologna, having a strong background in the complementary competences necessary for a deep investigation on the thesis subject.

The manuscript is organized as follows.

Chapter 1 introduces the basic concept of the UWB and RFID technologies and provides an up-to-date bibliography on the topic. The main

motivations of the work are explained.

Chapter 2 is dedicated to the study of the antenna backscattering physics, using the superposition and the reciprocity principles. An alternative methodology to link the tag transfer function with the backscattered response is also described, this relation being exploited in the following chapters.

Chapter 3 concerns the characterization of the interaction between an UWB RFID antenna and a close disturber modifying the antenna radiation characteristics. Measurements are post-processed in order to assess the detection coverage of tags and see how the presence of an object behind a tag affects the probability that the tag itself is seen by the reader, considering all possible tag positions and orientations. Finally, the interaction of an UWB antenna with a metallic reflector, whose presence greatly affects the antenna radiation characteristics, is addressed.

Chapter 4 provides a reader-tag signaling structure, where the clock drift problem and the quantization issue are modeled. A system architecture for mitigating the presence of multi-tag interference and strong clock drifts is also presented, jointly with the investigation of different spreading code design strategies.

In Chapter 5, the design of a system architecture capable of tag detection even in presence of multi-tag interference and strong clock drift is investigated, starting from the general system analysis conducted in Chapter 4. A low complexity non-coherent detection scheme is proposed and analyzed, by investigating the impact of different spreading codes on system performance. Specifically, the near-far interference problem, which derives from the semi-passive nature of the system, is addressed, and a solution to counteract this issue and guarantee robust tag detection is proposed.

Once the presence of a tag has been correctly revealed, reader-tag communication performance has to be assessed. Chapter 6 discusses the architecture of a system of tags and readers together with related signal processing schemes with the purpose to demodulate the payload contained in the tag memory even in the presence of multiple tags, starting from the considerations reported in Chapter 4. The system performance is simulated in terms of range/data rate trade-off, clutter suppression and multiple access capability, using experimental data collected both in ideal and real environments.

Finally, general conclusions assess the contributions carried out within this thesis and which are described in each chapter.

Author Contributions

The thesis activity has been conducted for about three years and a half, with interleaved periods spent in France and in Italy, in the context of the European project SELECT, whose aims and perspectives are briefly described in Sec. 1.8

In particular, during the collaboration at Ecole Polytechnique, the analysis of the tag backscattering has been analyzed in several ways, both in ideal and real conditions, starting from the previous works carried out in the laboratory (A. Sibille, C. Roblin and R. D’Errico). After the study and the proposal of some approaches to reconstruct the antenna backscattering by means of the superposition principle, simulations and measurements have been performed to assess the methodologies.

Further measurements and simulations campaigns have then been done to investigate the interaction of the tag antenna with a disturber placed in its proximity. While for current RFID technology many studies have been conducted on this topic, for UWB RFID the research was in its infancy. Apart from the case where a metallic object is considered, which has been studied specifically, the detection and localization coverage with other types of objects have been evaluated adopting measurement results.

During his work at University of Bologna, the author participated with other participants of the SELECT consortium in finding reliable solutions for the design of ad hoc and robust UWB RFID system architecture. This part of the thesis has mainly been carried out in collaboration with Davide Dardari and Nicolò Decarli and has focused on signal processing techniques and practical solutions to overcome hardware (HW) limitations and implementations issues. Part of the analyses carried out within the project is detailed in Chapter 4 and has been reported in the technical reports listed below.

During the periods spent at University of Bologna, A proper reader and tag architecture based on UWB backscatter modulation has been analyzed, starting from the model proposed by Dardari and D’Errico in [14]. A low-complexity detection and synchronization scheme involving bin-dependent thresholding has also been proposed in order to overcome implementation

impairments and near-far effects, as in the literature no studies were available to cope with these problems, at the best of the authors knowledge. The system performance has been evaluated considering different scenarios in terms of detection and false alarm rate, involving the analysis of the robustness of different code families in different scenarios, and when code acquisition schemes are adopted to counteract the presence of strong tag clock drift. The performance of the proposed architecture has been also assessed in terms of range/data rate trade-off, clutter suppression and multiple access capability.

The obtained results have been published in journal papers and in the proceedings of international conferences, which are listed below.

List of publications

Journal papers

- D. Dardari, F. Guidi, C. Roblin, and A. Sibille, "Ultra-wide bandwidth backscatter modulation: Processing schemes and performance," *EURASIP Journal on Wireless Communications and Networking*, no. 1, 2011.
- N. Decarli, F. Guidi, D. Dardari, "A novel joint RFID and radar sensor network for passive localization: design and performance bounds," *submitted to IEEE Journal on Selected Topics in Signal Processing*.
- F. Guidi, A. Sibille, D. Dardari, C. Roblin, "Impact of Tag Backscattering Characteristics on the Detection Coverage," *submitted to IEEE Trans. On Antennas and Propagations*.
- F. Guidi, N. Decarli, S. Bartoletti, A. Conti, D. Dardari, "Robust detection of UWB backscatter signals in multi-tag environment," *submitted to IEEE Trans. On Wireless Communications*.

Conference papers

- F. Guidi, D. Dardari, C. Roblin, and A. Sibille, "Backscatter communication using ultrawide bandwidth signals for RFID applications," *in D. Giusto et al. (eds.), The Internet of Things: 20th Tyrrhenian Workshop on Digital Communications SpringerScience+BusinessMedia*, Pula, Sardinia, ITALY, Sep. 2009, pp. 251262
- F. Guidi, M. Sacko, A. Sibille, and C. Roblin, "Electromagnetic analysis of RFID tag backscattering," in JNCW, 2011, Paris, France, 2011
- F. Guidi, A. Sibille, D. Dardari, and C. Roblin, "UWB RFID backscattered energy in the presence of nearby metallic reflectors," in Antennas

and Propagation (EUCAP), Proceedings of the 5th European Conference on, april 2011, pp. 1425 1429

- F. Guidi, M. Sacko, A. Sibille, and C. Roblin, "Analysis of UWB RFID tag backscattering in the presence of scatterers," in General Assembly and Scientific Symposium, 2011 XXXth URSI, aug. 2011, pp. 1 4
- F. Guidi N. Decarli, D. Dardari, C. Roblin, A. Sibille, "Performance of UWB backscatter modulation in multi-tag RFID scenario using experimental data," in *Proc. of the 2011 IEEE International Conference on Ultra-Wideband (ICUWB 2011)* , Bologna, Italy, Sep. 2011.
- A. Sibille, M. Sacko, Z. Mhanna, F. Guidi, and C. Roblin: "Joint antenna-channel statistical modelling of UWB backscattering RFID," in *Proc. of the 2011 IEEE International Conference on Ultra-Wideband (ICUWB 2011)*, Bologna, Italy, Sep. 2011.
- N. Decarli, F. Guidi, A. Conti, D. Dardari, "Interference and clock drift effects in UWB RFID systems using backscatter modulation," in *Proc. of the IEEE International Conference on Ultra Wideband, (ICUWB 2012)*, Syracuse, New York, USA, Sep. 2012.
- R. D'Errico, M. Bottazzi, F. Natali, E. Savioli, S. Bartoletti, A. Conti, D. Dardari, N. Decarli, F. Guidi, F. Dehmas, L. Ouvry, U. Alvarado, N. Hadaschik, C. Frankek, A. Zhangk., Mhanna, M. Sacko, Y. Wei, A. Sibille, "An UWB-UHF semi-passive RFID system for localization and tracking applications," in *Proc. of the IEEE International Conference on RFID-Technology and Applications (RFID-TA 2012)*, Nice, France, Nov. 2012.
- E. Savioli, M. Bottazzi, F. Natali, N. Decarli, F. Guidi, N. Hadaschik, R. D'Errico, L. Ouvry, "Semi-passive UHF-UWB RFID: architecture and localization performance," in *Proc. of the IEEE International Conference on Communications (ICC 2013)* .

Technical reports

- F. Guidi, N. Decarli, A. Guerra, V. Casadei, S. Bartoletti, M. Guerra, C. La Palombara, A. Conti, D. Dardari, N. Hadaschik, R. D'Errico, L. Ouvry, F. Dehmas, A. Sibille, C. Roblin: SELECT Deliverable D2.3.2, "Multi-functional network design: final system specification," Jun. 2012.

- D. Dardari, A. Conti, N. Decarli, S. Bartoletti, V. Casadei, M. Guerra, A. Mariani, A. Giorgetti, A. Sibille, F. Guidi, F. Dehmas, R. D’Errico: SELECT Deliverable D2.2.2, ”Signal Processing techniques: final report,” Apr. 2012.
- A. Sibille, C. Roblin, D. Dardari, A. Conti, N. Decarli, F. Guidi, N. Hadaschik, T. Nowak, F. Natali, E. Savioli, M. Bottazzi: SELECT Deliverable D2.3.1, ”Multi-functional network design: intermediate system specification,” Sep. 2011.
- D. Dardari, A. Conti, N. Decarli, S. Bartoletti, V. Casadei, M. Guerra, A. Mariani, A. Sibille, F. Guidi, F. Dehmas, V. Heiries, R. D’Errico: SELECT Deliverable D2.2.1, ”Signal Processing techniques: interim report,” Jul. 2011.
- C. Roblin, A. Sibille, F. Guidi, M. Sacko, Z. Mhanna, R. D’Errico, V. Heiries, J. Keignart, D. Dardari, N. Decarli: SELECT Deliverable D2.1.1, ”Backscatter propagation modeling: interim report,” Jul. 2011.

Chapter 1

State of the art of RFID and UWB Technologies

1.1 Introduction

This chapter briefly describes the RFID and the UWB technologies, with a particular perspective on the main limitations of the current adopted technologies, and on the advantages carried out by the joint use of UWB with RFID. Some of the latest works on this topic are here referenced, with an emphasis on the subjects where the thesis aims to bring a novel contribution. Within this context, the European project SELECT [15] is shortly reported. It has enriched the inter-disciplinarity of the work and also has led to face some of the practical issues that arise in industrial scenarios.

1.2 The RFID Concept

The concept of the “Internet of Things”, defined by the MIT Auto-ID Labs, is expected to introduce a new era where the physical world will be mapped into the internet space, thus enabling a potentially huge number of novel applications [1–4]. Ideally, it is expected that every object in our every-day life will be assigned to an IP address and will be sensitive and responsive to the presence of people. From the technological point of view, a key enabling technology is represented by RFID [16–26]. In recent years, the RFID technology has become a common occurrence in every day life. It is mainly used for real time identification of objects, and the development of RFID systems is due to the fact they do not need line of sight visibility, as happens in other communication systems such as bar codes, or physical contact which is also need by several other technologies. In fact, a RFID system consists of

readers and tags located on objects, where the readers interrogate the tags via a wireless link in order to obtain the data stored on these tags [27]. The maximum distance between the data carrier and the reader can be a few meters, the communication being based on radio-frequency signals [28].

The RFID technology was first introduced in the second World War to identify aircraft and it was called *Identity-friend or foe*; later in the decade, Vinding developed (January 1967) a simple and inexpensive interrogator-transponder system based on inductive coupling, [7]. As soon as the prices of RFID dropped, the industry started using them in many applications. For instance since 1979 it has been in use to identify and track animals. In 1994 all rail cars in the United States used RFID for identification [29] and today this promising technology has been applied to a huge variety of fields such as [28]:

- managing vehicle fleets;
- increasing highway throughput;
- speeding up transactions at the point of sale;
- gaining entrance to buildings;
- shipping containers;
- identifying livestock and pets;
- and many other fields.

Nowadays, there is a growing interest in the convergence of RFID and high accuracy RTLS technologies to enhance the functionalities offered to the end user and enable new potential wide market applications [12, 30, 31]. Figure 4.1 shows an example of RFID-RTLS network where some interrogators, placed in a controlled environment, monitor a certain area to detect and localize tagged people and objects present in the scenario. In fact, future advanced RFID systems are expected to provide both reliable identification and high accuracy localization of tags at submeter level. Thus, new important requirements, such as accurate real-time localization, high security, large numbers of tag management, in addition to extremely low power consumption, small size, and low cost, will be mandatory [17]. Unfortunately, most of these requirements cannot be fulfilled completely by the current first and second generation RFID or wireless sensor network (WSN) technologies, such as those based on ZigBee standard [24, 32].

In fact, RFID systems using standard continuous wave (CW)-oriented communication in the UHF band have an insufficient range resolution to

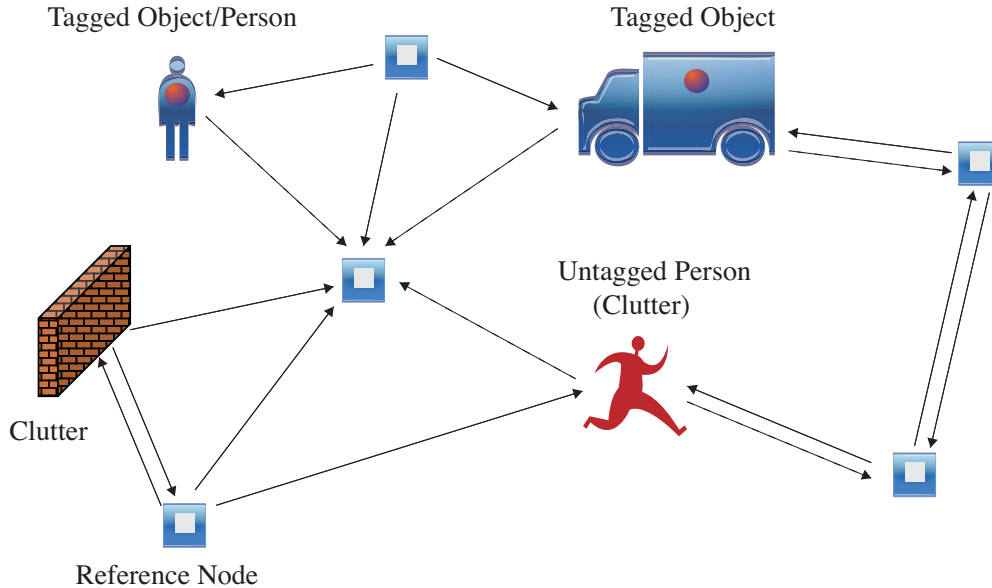


Figure 1.1: Example of a scenario with some reference nodes and tagged and untagged objects.

achieve accurate localization, are affected by multipath signal cancellation (due to the extreme narrow bandwidth signal), are very sensitive to narrowband interference and multi-user interference, and have an intrinsic low security [18, 20, 22, 28, 33, 34]. Although some of these limitations, such as security and signal cancellation due to multipath, are going to be reduced or overcome in future versions of UHF RFID systems [23, 35], a technology change is required to fully satisfy new applications requirements, especially those related to high-definition localization at the submeter level [36, 37].

In the following, the RFID technology is described and possible solutions to overcome current system limitations are detailed. Particular emphasis is put on the motivations of the present thesis, which arise in the described context of interest.

1.3 Main Characteristics of RFID Systems and Technologies

The RFID system is composed of respectively one or more readers and tags according to the specific purpose. Figure 1.2 shows an example of a scenario composed of a reader, which interrogates tags located in the same area. There

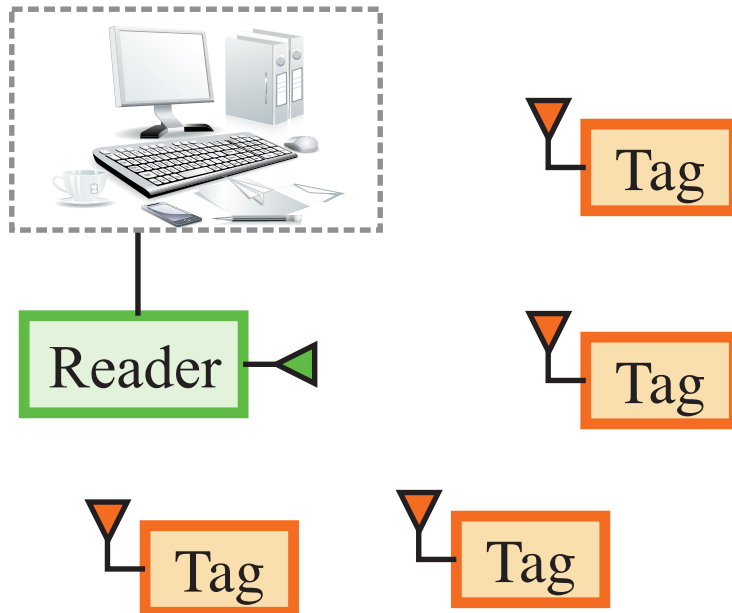


Figure 1.2: Classic RFID scenario with a reader interrogating several tags employed in the scenario.

are numerous methods of extracting the information stored in the tag, like the modulation of the backscattered signal or the generation of another signal by the tag itself, depending on whether it is passive (semi-passive) or active.

The reader, or interrogator, is usually constituted of a control unit, a memory, a radio frequency module (transmitter and receiver) and a coupling element (like an antenna) as it should guarantee three main functions: energizing, demodulating and decoding. The control unit commonly contains one or more processors and "controls" the operations of the reader; it executes the software instructions stored in the memory. The transmitter has the function to generate the signal that is sent through the coupling element to the tag. Then the receiver probes the environment to collect the received signal from the interrogated devices; its design often includes a low-noise amplifier (LNA) and in some cases also two separate antennas, dedicated for signal transmission and reception. In addition, the coexistence of the transmitter and the receiver is managed by a circulator, allowing to separate the transmitted and received signals. The reader also has an additional interface enabling the communication with an external controller, such as a PC [28].

For what tags are concerned, they actually represent the data-carrying device of the RFID system and they basically consist of a coupling element,

interacting with the reader, and a microchip. There are different ways for the tag to transmit back the information to the reader, according to the fact it is active, semi-passive or passive, which are strictly related to the internal structure of the transponder. In the following, the tag categories are distinguished and their main features are analyzed.

1.3.1 Active Tags

Active tags are usually fed by their own battery and their internal structure is similar to the reader, being full-fledged radios equipped with a battery, receiver, transmitter, a memory and a control circuitry. The tag generates a carrier signal using a local oscillator and a crystal reference, so that it can apply different kind of modulations, like amplitude shift keying (ASK), phase shift keying (PSK) or frequency shift keying (FSK), quadrature amplitude modulation (QAM), etc.

Since active tags have a significant amount of energy provided by the battery, large operating ranges are achievable and big memories like static random access memory (SRAM), suited for both reading and writing, are often integrated. In active tags there is also the possibility to integrate sensors in order to monitor the surrounding environment. Current studies are directed towards decreasing the power consumption, since the device operation lifetime is strictly related to the duration of the battery. A promising perspective is to harvests energy from the environment (i.e. photovoltaic cells) in order to guarantee a continuous power supply and a recharging of the battery [38, 39].

1.3.2 Passive and Semi-Passive Tags

When the cost, size, and power consumption requirements of RFID tags become particularly stringent, passive or semi-passive ones have the largest commercial potential, the energy necessary for tag-reader communication being harvested from the reader's signal or the surrounding environment [7]. Since the feeding system is usually off, passive tags are generally equipped with a nonvolatile memory like Electrically Erasable Programmable Read-Only-Memory (EEPROM), which have smaller dimensions than active tag memories [38, 39]. The downside of the coin is that the lack of a battery to feed the tag signal prevents operating at the same high distances as active tags.

Communication with passive tags usually relies on backscatter modulation, where the antenna reflection properties are changed according to information data, avoiding the need of a transmitter. In fact, specific variations

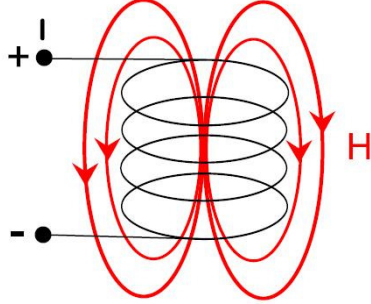


Figure 1.3: Magnetic field in a coil [28].

of the load create a code sequence that identifies the object where the tag is attached. In particular, the antenna interacts with the incident electromagnetic fields, producing a high-frequency voltage. Then the voltage is rectified by a diode and the final signal is smoothed using a storage capacitor. The intent is to obtain a constant voltage to feed the tag's logic circuitry and memory access. Two different ways of interaction between the reader and the tag are used: near field coupling and far-field coupling [7].

Near-field coupling The EM field in the near-field region is reactive in nature, and the electric and magnetic fields are orthogonal and quasi-static. A field dominates the other one according to the kind of the antenna adopted in the application: if a coil is considered, the magnetic is prevalent on the electric field, whereas the contrary happens if a generic dipole is considered. Most near-field tags rely on the magnetic field through inductive coupling in the tag coil and this principle is based upon Faraday's principle law [7]. In the general form, this principle can be stated as follows: "the contour integral of magnetic field strength H along a closed curve is equal to the sum of the current strengths I of the currents within it" [28, 40]

$$\sum I = \oint \vec{H} \cdot \vec{d}s. \quad (1.1)$$

Then, (1.1) can be used to evaluate H for different conductors. Consider a straight conductor: the field strength H along a circular *flux line* at distance equal to r is constant and it is expressed in the following way [28]:

$$H = \frac{1}{2\pi r} . \quad (1.2)$$

A rectilinear conductor is not suited to induce a current in the components of a RFID system; once the distance r is fixed, the field is constant. For this reason cylindrical coil antennas are used in the RFID applications where magnetic coupling is the basic principle exploited to communicate. The path of field strength along the axis of the radius of the coil is given by

$$H = \frac{I \cdot N \cdot R^2}{2\sqrt{(R^2 + x^2)^3}} \quad (1.3)$$

where N is the number of windings, R is the circle radius and x is the distance from the centre of the coil in the x direction [28]. At distance 0, that is, in the center of the antenna, (1.3) becomes:

$$H = \frac{I \cdot N}{2R} . \quad (1.4)$$

In passive and semi-passive tags, the communication is usually based upon load modulation: each load variation causes a change of the current in the tag, which generates itself a small current variation at the reader side due to the mutual inductance. Tag information data can thus be extrapolated by the reader through a proper "reading" of these current fluctuations at its side.

For this kind of interaction, low carrier frequencies are adopted: for example, the two most common ones are 128 kHz in the low frequencies (LF) and 13.56 MHz on the high frequencies (HF) side, with a boundary distance of respectively 372 m and 3.5 m. In these conditions, there is the necessity to adopt large antenna coils, and the use of a magnetic dipole is not convenient because its magnetic field in the near-field region drops as $1/d^6$ where d is the reader-tag distance. There is also a boundary between near-field and far-field regions, which is about $2D^2/\lambda$, where c is the light speed [7].

Far-field coupling Due to the mutual dependence of the time varying fields, there is a chain effect of electric field and magnetic fields in space [28] which propagates with the light speed ($\approx 3 \cdot 10^8$ m/s). This concept is explained by the Faraday's law, given by

$$\nabla \times \vec{E} = -\frac{\partial \vec{H}}{\partial t} . \quad (1.5)$$

As the magnetic field strength rapidly decays when the electromagnetic wave travels in the space away from the antenna, the EM field in the condition of far-field is radiative in nature. The EM waves propagate until they encounter the tag, and if its dimensions are equal to or bigger than a half wavelength of the EM wave, the incident signal gets reflected. The amount of the reflected signal partially depends on the impedance mismatch between the antenna and the load circuit: variations of the load affect backscattered signal, hence they can be used to carry information data.

For far-field coupling there is no boundary (as a difference for near field) and this technique is usually adopted for long range (5 – 20 m). Another advantage is related to the attenuation during the trip of the wave, as for near field it is in the order of $1/d^6$, while in this case the attenuation is proportional to d^2 . Usually far-field tags operate in the band 860 – 960 MHz (UHF) and in the 2.45 GHz Microwave band [7] and they adopt different sizes and shapes according to the application requirements. Unfortunately, one of the problems in operating at frequencies greater than 100 MHz is the interaction between the EM waves and the surrounding environment. Mitigating it is one important parts of the present thesis work.

1.3.3 SAW Tags

There is another completely different interaction in RFID communication that exploits the conversion of EM wave in a nanoscale surface acoustic wave (SAW). In fact, in the presence of SAW tags, the reader transmits a radio wave pulse that is directly converted into a nanoscale SAW by an interdigital transducer (IDT) put on a surface chip. Then this signal travels on the surface of the SAW chip and it encounters a set of wave reflectors that create a precise sequence of acoustic wave pulses, which subsequently travels back to the IDT. These pulses are converted into an encoded radio wave reply signal that is backscattered to the reader. A great advantage of this technique is the absence of the DC power, as a piezoelectric effect is exploited. In the beginning, the interest for SAW was very low due to the higher costs than traditional technologies like silicon-based RFID tags. Recent improvements, such as more precision with the phase weighting of the reflectors and more accurate control in the parasitic effects, led to an increase of the global interest for SAW tags [41, 42]. It must also be taken into account that there is a longer read range in the presence of water and metallic objects, guaranteeing a more reliable performance [7].

Table 1.1: Comparison among the different operative RFID frequencies.

Type frequency	Freq. range	Read range	Memory
Microwave	2.45 GHz	2m at best	less than 1kbit
UHF	865 to 960 MHz or 915 MHz (US)	6m or more	more than 1kbit
HF	3 to 30MHz (usually 13.56MHz)	1.5m at best	256 bit to 8×32 bit blocks, 4 kByte additional data memory available
LF	30KHz to 300KHz	1m at best	64 bits to 1360bits

1.4 Summary of the Main RFID Tag Characteristics

RFID systems usually operate at microwave, UHF, HF and LF frequencies. In the case of microwaves (i.e, 2.45 GHz), the read range is smaller than 2 meters, due to power link budget constraints. Usually the memories integrated in the structure of the tag are less than 1 kbit [7, 43, 44].

For UHF instead, RFID devices typically operate at the frequencies of 865 MHz and 960 MHz, apart from U.S. deployments in which it is 915 MHz. The read range is greater than 6 meters, according to the regulatory requirements (4 Watt in U.S. and only 2 in Europe for the emitted power). In particular, the european UHF band between 865 MHz and 868 MHz is composed of 15 channels of 200 kHz each. Integrated memories can be equal to or greater than 1 kbit, the communication is faster (higher *bit-rate*) than for lower frequencies, and larger distances can be achieved. A limitation of UHF is the lack of global compatibility, since the spectrum allocation varies in the different countries.

For LF and HF there is no restriction for the emitted power and their spectrum is allocated in the same way all over the world. Considering HF, the frequency ranges from 3 MHz to 30 MHz (usually 13.56 MHz) and the

maximum distance between reader and tag is 1.5 m. Near-field coupling is usually exploited between transmitter and receiver, and memories of 256 bit to 8×32 bit blocks or data memory of 4 kB are used at these frequencies.

LF devices operate from 30 kHz to 300 kHz and most of the tags operate at 125 kHz with full duplex connection and 134 kHz with half duplex connection. The typical read range is 1 m (best performance), memories are very small (64 bits to 1360 bits) and the communication is very slow and without any anti-collision system. On the other side, it is the only technology that allows reading tags through water [7, 43].

1.5 Basic Features of UWB Technologies

As previously stated, a promising wireless technique for next generation RFID is the UWB technology. It is based, in its impulse radio UWB (IR-UWB) implementation, on the transmission of sub-nanosecond duration pulses [12]. Thanks to their low power consumption, IR-UWB transmitters can be adopted successfully for both active and passive tags. UWB has been proposed to implement low consumption and low complexity active radio-frequency (RF) tags for precision asset location systems [45].

The potential advantages of UWB include, but are not limited to, low power consumption at the transmitter side, extremely accurate ranging and positioning capability at the submeter level, robustness to multipath (better area coverage), low detection probability (higher security), and a large number of devices operating and co-existing in small areas (efficient multiple channel access and interference mitigation) [11, 22, 46–49]. Thus it is considered a very promising technology with uniquely attractive features inviting major advances in wireless communication, networking, radar, imaging and positioning systems [49].

In the following, after a short history of UWB technology, the main features of this appealing technology are described.

1.5.1 UWB History

The first emissions of UWB signals are more than 100 years old and can be seen as a major milestone of modern radio, when Guglielmo Marconi sent the first UWB wireless pulses in 1901. Other contributors for developing this new concept came much later, starting from 1960 [50], when the specific advantages of such signals were recognized. In 1960 the Lawrence Livermore National Laboratory (LLNL) and Los Alamos National Laboratory (LANL) conducted various researches on UWB transmitters and receivers. Cook and

Bernfeld, with their first book published in 1967 summarized all the developments of UWB studies, which started since 1952 at Sperry Gyroscope Company. In 1970, the LLNL widened its research field in instrumentation from diagnostic based on laser to diagnostic based on sub-nanosecond pulses and so, since 1975, an UWB system (for radar or communication) could be built with Tektronix components. After 1970 there were only developments of the already known subsystems but not in general of overall systems. From 1969 to 1984 Harmuth published books and articles as [51] that turned out to be fundamental to the creation of the first project about UWB receiver and transmitter. From 1972 then 1987, Ross and Robbins were instead the first scientists who applied the UWB signals to several applications, such as voice and data communications, and they were granted a few patents for transmitter and receiver systems operating with sub-nanosecond duration pulses [52, 53].

In 1978 Bennet and Ross merged their knowledge about methods for pulse generation and, around that period, many conferences were held to discuss the different pulses generation techniques. From 1977 to 1989, the United States Air Force (USAF) presented a program for the organization of a laboratory intended to develop UWB systems, where the project was directed by Col. J. D. Taylor. At the same time Russia and China increased their contribution to studies on UWB signals.

Then many academic programs started at LANL, LLNL and in a huge amount of U.S. universities with a goal to focus the attention on the physics of sub-nanosecond pulses. In 1994, T. E. McEwan created the Micropower Impulse Radar (MIR), which was the first UWB system able to work at a very low consumed power (\approx mW), being simultaneously compact and relatively inexpensive. The last important contributes came from Robert A. Scholtz and M. Z. Win who, respectively in (1993, 1998) and (1998), analyzed UWB applied to modern communications systems [46, 54–56].

1.5.2 Characteristics of UWB Signals

In 1989, the U.S. Department of Defense introduced the definition "ultra-wideband" to refer to a signal with at least a band of 1.5 GHz or a -20 dB fractional bandwidth exceeding 25% [49]. However, according to the Federal Communications Commission (FCC) [57] (Fig. 1.4), the UWB signal is characterized with a very short duration (on the order of the nanosecond), with a bandwidth larger than 500 MHz or a fractional bandwidth greater than 0.2, where the fractional bandwidth is defined as

$$B/f_c = 2 \cdot \frac{(f_H + f_L)}{(f_H - f_L)} \quad (1.6)$$

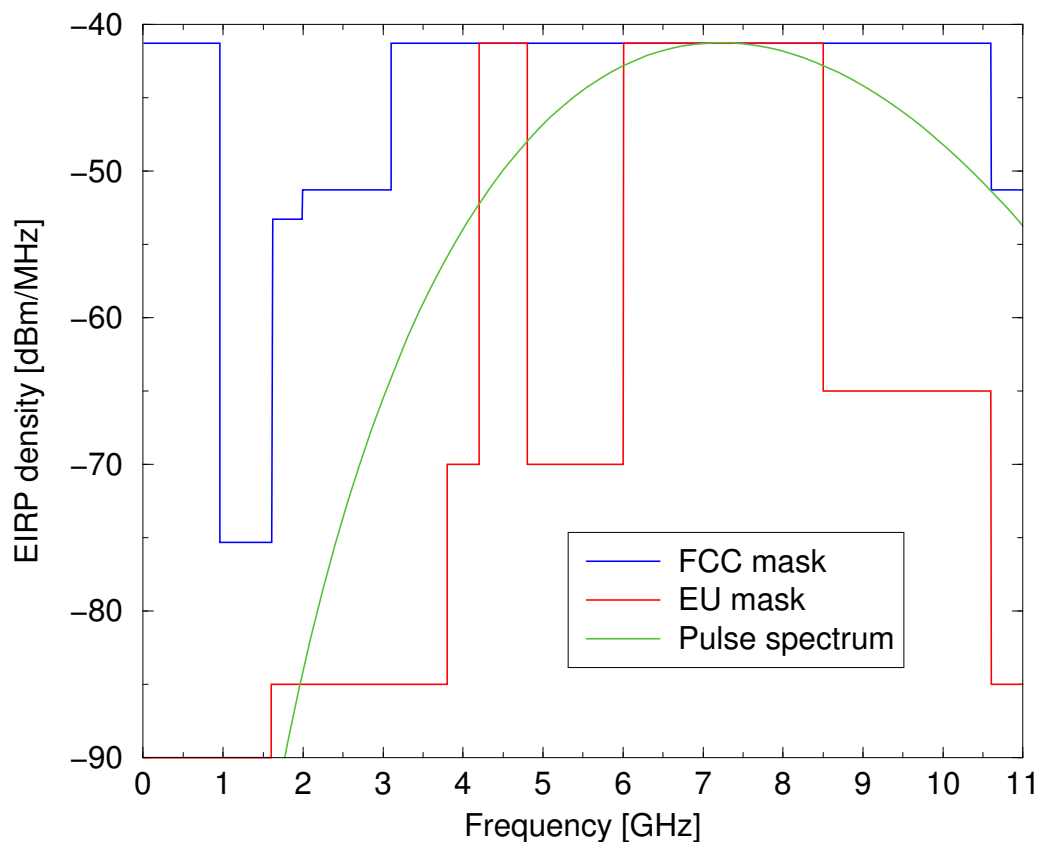


Figure 1.4: FCC and EU spectral masks, respectively, for indoor commercial systems in the absence of appropriate mitigation techniques. An example of 6th derivative of the Gaussian pulse spectrum is also reported [12].

with $f_c = (f_H + f_L)/2$, and $B = f_H - f_L$ being the band width of the signal, with f_H the upper frequency and f_L the lower frequency of the spectrum occupied by the signal and referred to -10 dB from the maximum radiated power spectral density.

In 2002 the FCC in USA regulated a "new bandwidth" (3.6 – 10.1 GHz), where UWB radios coexist with narrowband signals and the maximum of effective radiated isotropic power (EIRP) is also fixed to -41.3 dBm/MHz as shown in Fig. 1.4, which coincides with tolerated out of band emissions of radio devices.

UWB signals are promising for wireless communications as they present a great amount of valuable features. The most important properties that make UWB technology very promising are [46, 58–69]:

- accurate position location and ranging due to fine delay resolution;

- reduced fading due to finer multipath resolution.
- multiple access capability through spread spectrum (SS) techniques;
- underlay and covert communications due to low power spectral density (PSD).

The accurate position location derives from the very short duration of the pulses. In this way it is possible to distinguish near objects or to have more immunity with multipath. On the other side instead, the use of this sub-nanosecond pulse makes the synchronization more difficult, causing a degradation of the performance.

The use of SS techniques during the communication, such as frequency hopping, time hopping and direct sequence spread spectrum is a common practice, which provides a multiple access capability for the users.

Finally, it is anticipated that UWB devices will be simple to design and generally not very expensive. Furthermore, considering the Shannon theorem, we have for the capacity (in bits/s):

$$C = B \cdot \log_2 \left(1 + \frac{S}{B \cdot N_0} \right) \quad (1.7)$$

where B is the signal bandwidth, S and N_0 are respectively the signal power and the noise power spectral density, being $\text{SNR} = S/(BN_0)$. This very important formula means that the wider the band B , the higher data-rate at a given received power. Note that this does not always happen, but only when $\text{SNR} \gg 0$ the dependence between C and B is approximately linear. On the contrary, for small SNR, the channel capacity is approximately insensitive to the bandwidth, as a wider B implies also a higher noise power BN_0 .

In the last years, some commercial proprietary RTLSSs have been introduced, based on tags emitting UWB pulses with extremely low duty cycles to ensure high battery duration. Another example of low complexity tag architecture is given in [70], where the concept of a UWB-based pseudo-random active reflector, which does not require the presence in the tag of a modulator and demodulator, is introduced. This principle is largely at the basis of the current PhD work.

Among all the solutions, multi-carrier modulations such as orthogonal frequency division multiplexing (OFDM) may be also used to realize UWB systems, eventually combined with SS techniques, in order to counteract frequency selective channels [71]. A leading proposal for high-rate UWB is based on multiband (MB) OFDM, where frequency-hopping (FH) over a small number of carriers is used for interference mitigation (see the WiMedia

Alliance solution in [72]). Multi-band OFDM Physical Layer was initially proposed for IEEE 802.15 Task Group 3a [73] and then adopted in the ECMA 368 standard [74]. This technique, even if very promising and performing, was not deeply investigated due to its complexity, which makes this technology not suited for UWB backscatter communication, on the contrary of Impulse Radio systems [75].

1.5.3 Impulse Radio UWB

Since in the frequency domain the band occupied by the signal is very large (ultra wide bandwidth), the time duration of the pulse is on the order of nanoseconds or picoseconds. Typically in the literature the most common considered pulses are derived from the Gaussian pulse. This is related to the fact that the Gaussian pulse verifies the smallest possible time-bandwidth product, with a maximization of the range-rate resolution. [32, 76]. The Gaussian pulse is expressed as follows [77]

$$g(t) = \frac{V}{\sqrt{2\pi} \cdot \tau} \cdot e^{-t^2/2\tau^2} \quad (1.8)$$

where V is a parameter that influences the maximum of the power spectrum associated to the signal and τ is strictly related to the pulse width and thus to the width of the band in the frequency domain.

Usually fourth, fifth and sixth derivatives of the monocycle (first derivative Gaussian Pulse) are preferred, as the spectrum of monocycle starts from 0 Hz, also considering that a derivative in time implies a shaping of the spectral components towards higher frequencies. The generic expression of the n th derivative gaussian pulse is given by [77]

$$g_n(t) = -\frac{n-1}{\tau^2} g_{n-2}(t) - \frac{t}{\tau^2} g_{n-1}(t), \quad n \geq 1. \quad (1.9)$$

This pulse can be modulated either using pulse amplitude modulation (PAM) or pulse position modulation (PPM). An example of 6th derivative of the Gaussian pulse spectrum with $\tau = 0.192$ ns, compliant with FCC mask, is reported [12].

When applications have to follow european constraints, an example of possible pulse shape satisfying the European Union (EU) UWB regulation in the 3.1 – 4.8 GHz band is the RRC pulse, whose expression is given by

$$p(t) = \frac{4\beta}{\pi\sqrt{t_p}} \left(\cos[(1+\beta)\pi(t/t_p)] + \frac{1}{4\beta(t/t_p)} \sin[(1-\beta)\pi(t/t_p)] \right) \cdot \frac{1}{1 - (4\beta(t/t_p))^2} \cos(2\pi f_c t) \quad (1.10)$$

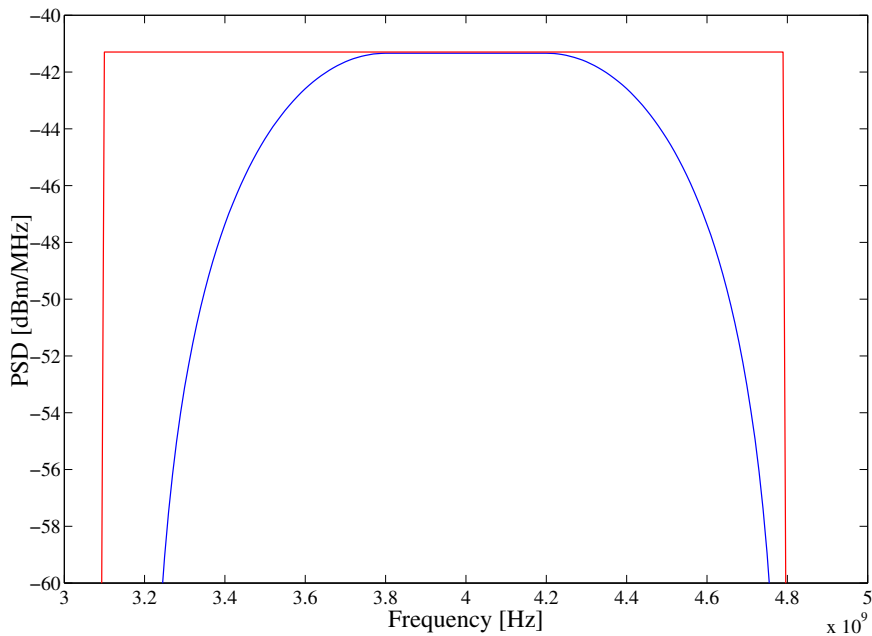


Figure 1.5: Example of a RRC PSD.

where β is the roll-off factor, f_c the center frequency, and t_p a parameter such that $W = (1 + \beta)/t_p$. An example of RRC PSD is reported in Fig. 1.5, where $\beta = 0.6$, $f_c = 3.95$ GHz and $t_p = 1$ ns are considered.

1.6 Passive and Semi-Passive UWB-RFID

When the main objective of an RFID system is to achieve a low cost, a small size and a very low power consumption, the best solution is to operate with passive or semi-passive tags. Even though active tags are better performing than passive ones, they still present inherent cost and power consumption problems.

A further step is to combine the benefits already mentioned for UWB technology and those of passive/semi-passive RFID in order to increase the performance of the system. Unfortunately the FCC regulatory constraints on the transmitted power by fixing the EIRP to be at most -41.3 dBm, which implies that a sufficient tag operation power cannot be extracted from the received UWB signal itself. Because of this problem, a promising solution could be the use of semi-passive tags, which harvest the energy from the surrounding environment in some manner in order to feed the control logic

(which needs more or less $1 \mu\text{W}$) [59]. In Sec. 1.6.1 a brief perspective about the combination of passive RFID and the UWB technology, highlighting the relative advantages and drawbacks is shown, with some applications examples.

1.6.1 UWB Antenna Backscattering

In order to design dedicated architectures for backscatter communications, it is fundamental to understand the basic EM mechanisms underlying the interaction between the reader's and tag's antennas. As previously mentioned, backscatter modulation consists of changing the antenna reflection properties according to information data [7]. In fact, when an EM wave encounters an antenna, it is partially reflected, but this phenomenon depends on the antenna configuration. Indeed, the antenna scattering mechanism is composed of a *structural* and of an *antenna mode* scattering [78, 79]. Although there is no unique definition of these contributions, let us intuitively highlight that the first primarily includes all backscattering effects not depending on the antenna loading (such as antenna support, connector...). The second, on the other hand, changes according to the variations of the electrical load that is connected to the tag, and thus data can be sent back to the reader through a proper variation of the antenna load characteristic without requiring a dedicated power source (backscatter modulation).¹ Thus the total scattering cross section at a given frequency can be expressed in the following expression

$$\sigma = |\sqrt{\sigma_s} + \sqrt{\sigma_a}e^{j\phi}|^2 \quad (1.11)$$

where σ_s and σ_a are respectively the radar cross section (RCS) of structural and antenna modes, while ϕ is the phase difference between the two modes [80].

When a UWB pulse is transmitted and UWB antennas are employed, the reflected signal takes the form shown in Fig. 1.6. In Fig. 1.7, the structural and antenna mode scattering components are plotted separately for convenience. The antenna mode scattered signal, reported in Fig. 1.8, can be varied according to the antenna load, Z_L , whereas the scattering of the structural mode remains the same. Among the various possibilities, three particular choices are of interest for passive UWB RFID: $Z_L = 0$ (short circuit), $Z_L = \infty$ (open circuit) and $Z_L = Z_A^*$ (matched load), where Z_A^* is the antenna impedance. Ideally, antenna mode scattered waveforms have a phase difference of 180° between the case of open and short circuit loads,

¹The structural mode scattered component is conventionally defined as the signal scattered when the antenna load is matched, or frequently, when it is short circuited [78].

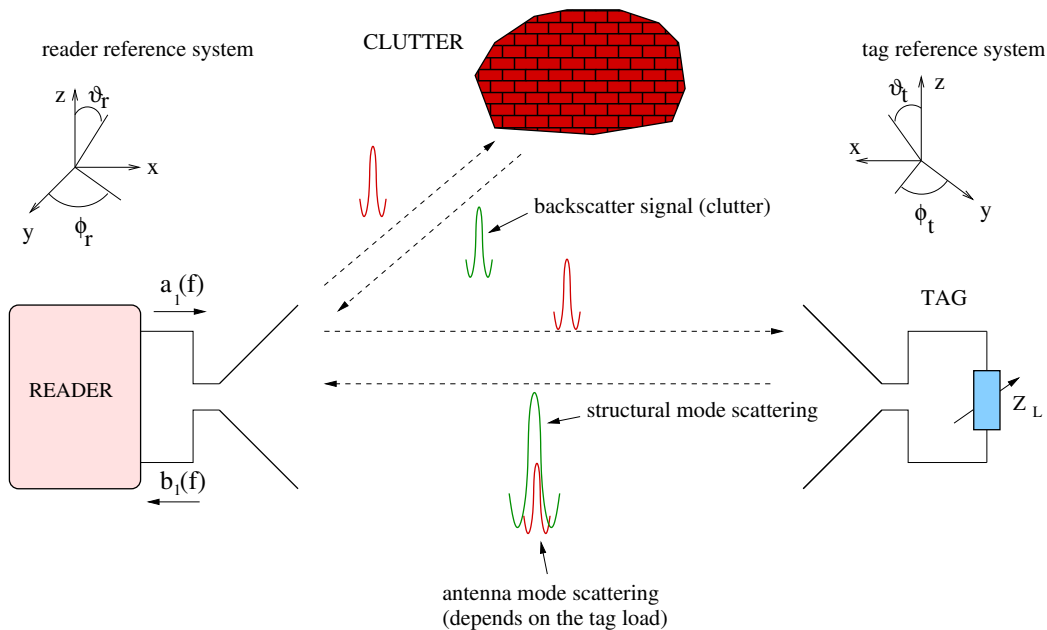


Figure 1.6: Multi-reader scenario with tags and scatterers placed in the environment.

whereas no antenna mode scattering exists in the case of a perfect matched load. In UWB antennas, the structural mode component takes a significant role in the total scattered signal; in fact, it is typically 1 or 2 orders of magnitude higher than that of the antenna mode [14, 81].

In addition, signals scattered by the surrounding environment (clutter) are unavoidably present and superimposed on the useful signal. In general, it is expected that the clutter and the antenna structural mode scattering have a significant impact at the reader's antenna, thus making the detection of the antenna mode backscattered signal (which carries data) a main issue in passive UWB RFID systems. This has not yet been widely addressed in the literature, and to this purpose ad hoc robust backscatter modulation schemes needs to be designed, as illustrated in the next chapters.

1.7 UWB RFID Backscattering: The State of The Art

The modulation of the backscattered signal is currently adopted in traditional passive UHF RFID tags based on CW signals to carry information from the tag to the reader.

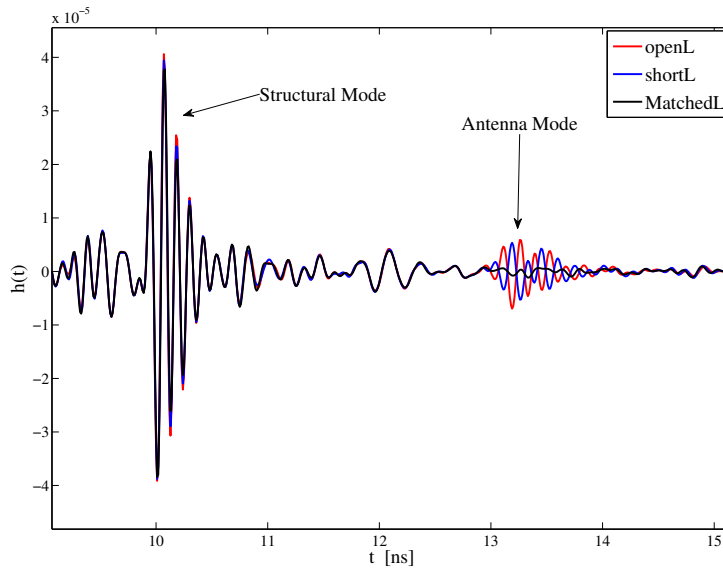


Figure 1.7: Structural and antenna modes measured in an anechoic chamber.

As compared to the extensive investigations of UHF RFIDs (see [7, 33, 34, 79, 82]), further investigation of backscatter properties when operating with UWB signals, especially in realistic environments, is needed [81, 83, 84]. In addition, apart from recent works (e.g. [13, 85–89]), there is no channel model for UWB backscattering available from the literature, to the best of the author’s knowledge.

Recently, some applications of UWB in tags based on backscatter modulation have been proposed. As stated in [12], one question is whether UWB RFID can be really seen as the next RFID generation and can replace current narrow band technologies. In [90], a hybrid UWB architecture is illustrated, where the reader broadcasts narrowband RF signals that carry command and clock signals and also provide energy to the tags, while conventional UWB transmission is applied to the reverse link. Unfortunately, those authors do not provide communication performance results. Hybrid architectures are also proposed in [13, 91].

The idea of passive tags based on UWB backscatter signaling is proposed in [92], in the case of an ideal scenario where neither clutter nor interference are present. Preliminary studies can be found in [14, 84, 93], where a flexible tag architecture as well as a backscatter signaling scheme robust to the presence of clutter are presented. However, UWB RFID solutions based on backscatter modulation have not been investigated in realistic scenarios in those papers. A few works emerged in the last years, such as in [94], where authors provide a time-of-arrival (TOA) estimate in realistic conditions, or

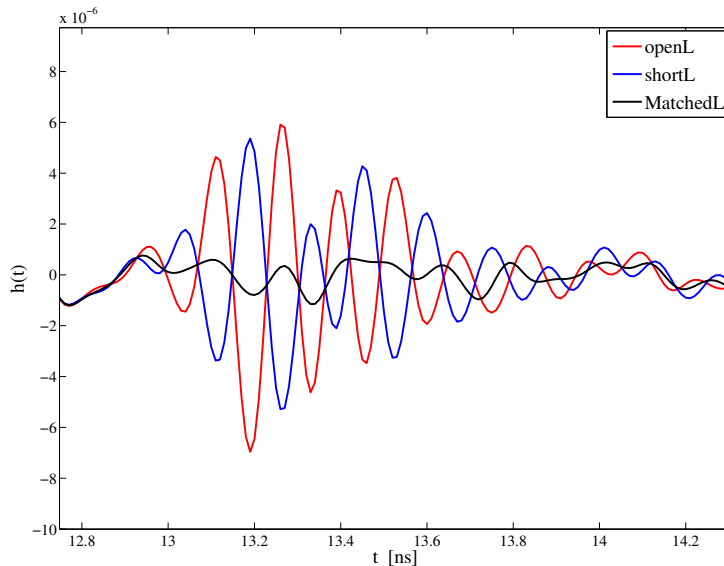


Figure 1.8: Antenna mode scattering contribution.

in [95, 96], where chipless UWB RFID tags solutions were analyzed.

In [97], a review of current RFID technology and its major shortcomings is given, proposing an UWB RFID system able to improve the performance through IR-UWB technology. [22] instead propose a new approach for secure passive RFIDs based on UWB communications adopting time-hopping (TH)-pulse position modulation (PPM)), where the hopping sequence is used as a secret parameter for the UWB communication link.

An energy detector (ED) structure for passive UWB-RFID positioning systems is reported in [98], where the ED receiver includes a 3.1 – 4.8 GHz analog front-end as well as high speed digital circuits and is implemented in 90 nm CMOS process, with a flexible back-end and a TOA estimator on FPGA. In [99], the architecture and performance of a non-coherent low complexity UWB impulse radio based transceiver designed for low data rate, low cost sensor network applications is presented, where the UWB-IR receiver utilizes a non-coherent, energy detection based approach.

1.8 General Motivations of the thesis work

According to the brief overview of the current passive UWB RFID technology reported in Sec. 1.7, many studies needed to be conducted on this appealing technology when the thesis began.

Being aware that before the design of proper system architectures for

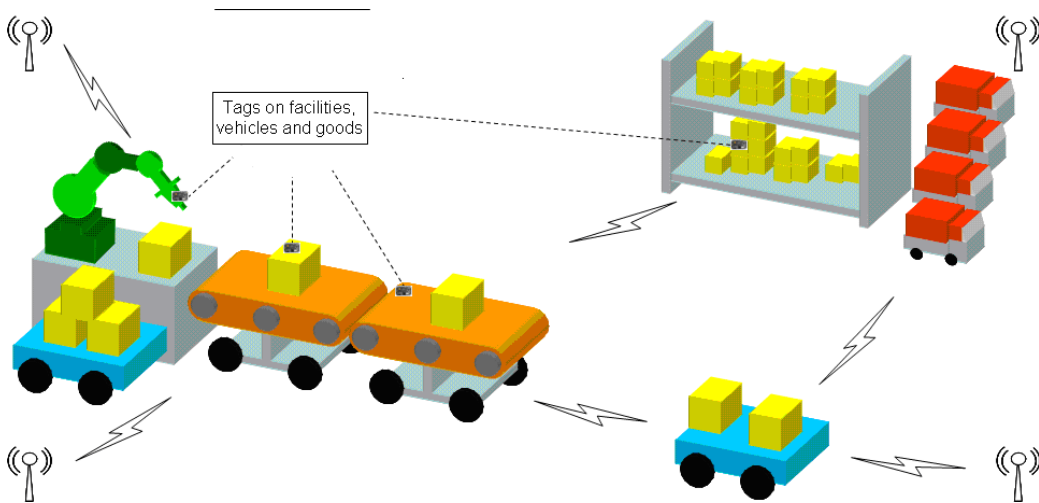


Figure 1.9: The internal logistics of a manufacturing plant [15].

backscatter communication it is fundamental to understand the basic EM mechanisms underlying the interaction between readers and tags, it has been considered more than relevant to join the expertise of two complementary laboratories, one associated with Ecole Polytechnique (ENSTA ParisTech) and the other from University of Bologna, in defining the thesis' objectives. For what the former is concerned, the competences on UWB antennas and EM aspects have been exploited to investigate the backscatter mechanism for antennas, both isolated and in presence of close disturbers. The collected measurements and analysis have been exploited through the know-how of the latter, in order to properly design a semi-passive UWB RFID system capable to achieve reliable performance in terms of tag detection and range trade-off.

This collaboration was enforced thanks to the European project SELECT, where, among all partners, the two cited institutions heavily contributed to the study of a new RFID UWB system. Here, SELECT is the acronym for "Smart and Efficient Location, identification, and Cooperation Techniques", and it focuses on studying innovative solutions enabling high-accuracy detection, identification, and location of objects/persons equipped with small ultra-low power tags, using a network of intelligent self-configuring radio devices [15]. One of the main final goals of the project is the built-in of a demonstrator that integrates, but is not limited to, RFID, UWB backscattering modulation and associated advanced algorithms.

In conclusion of this chapter, innovative and already known techniques are considered in this thesis in order to improve the detection and system coverage of RFID UWB tags, through the study of EM phenomena involved

in backscattered signals and through the design and optimization of communication schemes. Once signals have been studied and a system architecture has been proposed, signal detection reliability, range/data-rate trade off and service coverage analysis will be the major evaluation criteria of the study of the UWB RFID modulated backscattering based RFID systems, as explained further away in the manuscript.

Chapter 2

Electromagnetic Analysis of UWB RFID Tag Backscattering

2.1 Introduction

As stated in Chapter 1, an appropriate design of the reader-tag signaling architecture requires the knowledge of the phenomena that appear in the backscatter modulation mechanism. For this reason, this chapter is dedicated to the study of antenna backscattering, based on the superposition and the reciprocity principles. Starting from a simple and ideal scenario composed only of one reader and one tag, the analysis is then developed towards a more complex case that considers also environment reflections. In both cases, full EM simulation and measurement results are reported in order to assess the analysis previously conducted. An alternative methodology to link the tag transfer function with the backscattered response is furthermore described, which will be exploited in Sec. 3.3 for the evaluation of the detection and localization coverage, underlining the importance to conjugate the study of different system aspects.

2.2 Application of Superposition and Reciprocity Principles in Ideal Scenarios

Let us consider an ideal reader antenna with internal impedance (purely real) R_{ref} and unit gain (isotropic), nondephasing (see Fig. 2.1) [100]. The antenna of interest has internal impedance Z_a and complex gain G . The field radiated



Figure 2.1: Ideal reader (left) and tag (right) antennas in LOS.

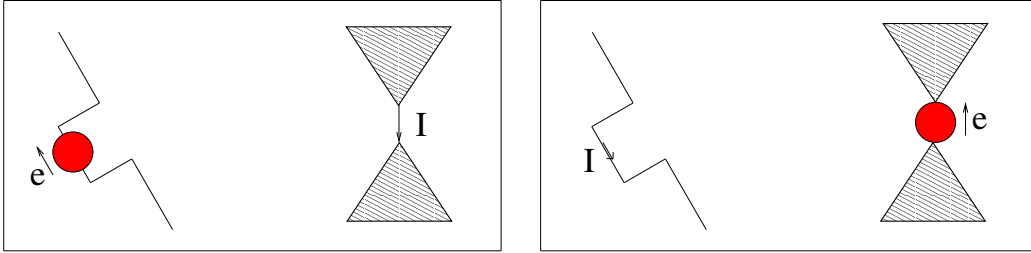


Figure 2.2: Left: Ideal reader antenna (transmitting) and tag antenna (receiving) in LOS. Right: Ideal reader antenna (receiving) and tag antenna (transmitting) in LOS.

at distance r by the ideal antenna is:

$$E = -j \frac{e^{-jkr}}{r} \frac{e\sqrt{\eta}}{\sqrt{4\pi R_{\text{ref}}}}. \quad (2.1)$$

where "e" is the reader excitation and η is the free space impedance. The antenna effective height (or length) h is defined by [101]

$$\mathcal{V}_{\text{emf}} = hE \quad (2.2)$$

where \mathcal{V}_{emf} is the antenna electromotive force. \mathcal{V}_{emf} is the open-circuit voltage at the tag terminals and is also given by the short-circuit current through

$$I = \frac{\mathcal{V}_{\text{emf}}}{Z_a} \quad (2.3)$$

having

$$h = IZ_a j \frac{r}{e^{-jkr}} \frac{\sqrt{4\pi R_{\text{ref}}}}{e\sqrt{\eta}}. \quad (2.4)$$

Here we used the total radiated power as (Poynting per surface sphere)

$$\frac{1}{2} \frac{|e|^2}{R_{\text{ref}}} = 4\pi r^2 \frac{1}{2} \frac{|E|^2}{\eta}. \quad (2.5)$$

From reciprocity, the configuration on the right of Fig. 2.2 gives the same current I as the picture on the left. When the antenna of interest is used as a radiator, let us call E_{ant} the field generated at the location of the ideal antenna. The ideal antenna effective area is

$$A_{\text{eff}} = \frac{\lambda^2}{4\pi} \quad (2.6)$$

and the power received into a matched load is given by

$$P_{\text{rML}} = A_{\text{eff}} \frac{|E_{\text{ant}}|^2}{2\eta} \quad (2.7)$$

which can be also expressed as

$$P_{\text{rML}} = \frac{1}{2} R_{\text{ref}} |I_{\text{ref}}|^2, \quad (2.8)$$

where I_{ref} is the current in the matched load. This current is a factor 2 less than the short-circuit current, giving thus $I_{\text{ref}} = I/2$. Then we have

$$\frac{1}{8} R_{\text{ref}} |I|^2 = \frac{|E_{\text{ant}}|^2}{2\eta} A_{\text{eff}}. \quad (2.9)$$

where I (non dephased with respect to the incoming field) equals to

$$I = E_{\text{ant}} \frac{\lambda}{\sqrt{\pi\eta R_{\text{ref}}}} \quad (2.10)$$

which gives the final expression of the tag effective height as

$$h = E_{\text{ant}} \frac{\lambda}{\sqrt{\pi\eta R_{\text{ref}}}} Z_{\text{a}} \frac{jr}{e^{-jkr}} \frac{\sqrt{4\pi R_{\text{ref}}}}{e\sqrt{\eta}} = \frac{\lambda Z_{\text{a}}}{60\pi} \frac{jr}{e^{-jkr}} \frac{E_{\text{ant}}}{e} \quad (2.11)$$

using $\eta = 120\pi$. This means that, using for instance a commercial electromagnetic software code under an excitation $e=1\text{V}$ that computes the normalized (dimensionless) quantity

$$\mathcal{E} = \frac{E_{\text{ant}}}{e} \frac{r}{e^{-jkr}} \quad (2.12)$$

the effective height of the antenna of interest is directly obtained from these computed fields. The expression is valid for whatever polarization and whatever antenna (complex) input impedance. Notably, \mathcal{E} can be seen as a transfer function relating the excitation voltage "e" to the voltage amplitude into the radiated spherical wave. For instance if the (real) antenna impedance is

R , the accepted power is $|e^2|/2R$ while for a lossless isotropic antenna the radiated power is

$$\frac{|E_{\text{ant}}^2|}{2\eta}4\pi r^2 = \frac{|e^2\mathcal{E}^2|}{60}. \quad (2.13)$$

Equating these powers brings

$$|\mathcal{E}^2| = \frac{30\Omega}{R} \quad (2.14)$$

which means that $|\mathcal{E}| = 1$ if $R = 30\Omega$.

2.3 Proposed Procedures for Tag Backscattering Reconstruction

Here different ways to reconstruct the antenna tag backscattering in an ideal environment are detailed. Note that the presence of an object behind the tag is here considered as an ideal condition, since the system tag-object can be characterized as the same entity. The main target of the proposed procedures is to validate the analysis conducted in Sec. 2.2, and to give some guidelines in order to improve the way to analyze and simulate the antenna backscattering, specially when huge databases of simulations have to be collected.

In the following, when the monostatic configuration is referred, transmitter and receiver are co-located. On the contrary, in bistatic configuration transmitter and receiver are located in different positions.

Direct injection of the load values in the electromagnetic simulator

The simplest procedure is to directly inject the load values into the designed antenna inside the simulator. Considering an electromagnetic tool such as Wipl-D[®] [102], a great advantage of RCS simulations is that only the antenna of interest needs to be included, as an ideal feeder is adopted by default. As no scatterers are here considered, a system composed of one antenna under test and an ideal radiator is exactly what occurs.

The main limitation of the procedure is that the load value has to be directly injected into the electromagnetic simulator. If a huge number of simulations has to be launched, many computational resources are required, which is highly time consuming. For this reason, it is convenient to move towards alternative solutions that provide the same results about the EM fields in shorter times and with a great reliability, as described in the following.

Use of the electromotive force Sec. 2.2 shows that it is possible to represent separately the short-circuit and the antenna mode scattering¹. Furthermore, we proposed a simple method to obtain the effect of any load connected to the tag. Here, we present two different approaches, based on the analytical evaluation of the \mathcal{V}_{emf} induced on the tag by an incident field radiated by the reader, which could be used instead of directly simulating the RFID tag connected to different loads.

Method 1 In this method we do not need the evaluation of the antenna effective height. Three simulations (or measurements) are required:

- 1a) In this configuration (which will provide the short-circuit scattering), the reader is excited by a voltage "e" and the tag is short-circuited (Fig. 2.2).
- 1b) This configuration is identical to 1a), except for the load seen by the tag, which is the impedance Z_L (e.g. $50\ \Omega$);
- 1c) Here the tag is excited by the voltage $V_{\text{excL}}=e$ and the reader is short-circuited.

By denoting E_b and E_a the backscattered fields of 1b) and 1a) respectively, we can say that $E_b - E_a$ is due to the antenna mode, since the short-circuit mode contribution is subtracted (as it does not depend on the load). Furthermore, with the knowledge of the antenna tag radiation in each direction known from 1c), it is possible to evaluate the complex voltage at tag terminals from

$$E_{\text{ant}} = E_b - E_a \quad (2.15)$$

and

$$u = \frac{E_{\text{ant}}}{E_{\text{radL}}} \cdot V_{\text{excL}} \quad (2.16)$$

where V_{excL} and E_{radL} are respectively the excitation voltage applied in 1c) and the radiated field with this excitation. Since the tag behaves as an electric generator when it operates in reception, we can obtain the tag electromotive force, as

$$\mathcal{V}_{\text{emf}} = u \cdot \frac{Z_L + Z_a}{Z_L} \quad (2.17)$$

where Z_L is the value of the impedance connected to the tag in simulation b) and Z_a is the tag antenna impedance (Fig. 2.3). From \mathcal{V}_{emf} , we can then

¹The backscattered signal from a short-circuited tag is arbitrarily chosen to be the structural mode scattering [78], coherently with the analysis in Sec. 2.2.

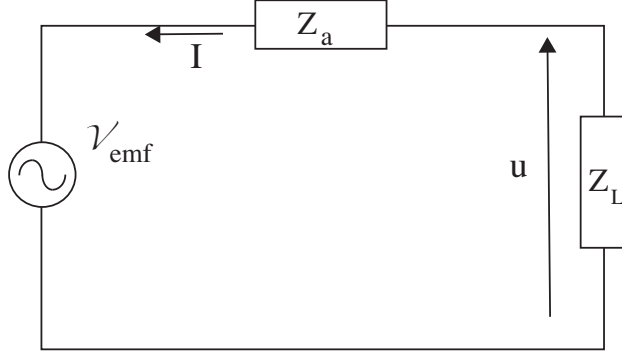


Figure 2.3: Tag electric scheme.

compute the voltage V_x over the load for any impedance, which subsequently allows to evaluate the radiated electric field E_x for the antenna mode in the following ways:

$$V_x = \mathcal{V}_{\text{emf}} \cdot \frac{Z_L}{Z_L + Z_a} \quad (2.18)$$

$$E_x = \frac{u}{V_{\text{excB}}} \cdot E_{\text{radB}}. \quad (2.19)$$

Finally, we can sum up the short-circuit scattering simulated in 1a) when the tag is connected to a short circuit load, with the fields E_x . In this way we obtain the complete response of the antenna when it is connected to any impedance, from a simple mathematical handling after 3 simulations. Moreover it is important to remark that we can now reproduce separately the two contributions.

Method 2 In this section we exploit the antenna effective height from (2.11). For this case, still three simulations or measurements are required:

- 2a) Simulation/measurement of the system shown in Fig. 2.2 in the left. This configuration will give the short-circuit scattering,
- 2b) Simulation/measurement of the electric field incident to the tag and which is radiated by the reader.
- 2c) Simulation/measurement of the tag impedance and of the radiated electric field, with the reader short-circuited, as 1c).

It is straightforward to compute \mathcal{V}_{emf} from the simulation/measurement results of 2c) applied to (2.11) and then of 2b) applied to (2.11). The expression is valid for whatever polarization and whatever antenna (complex) input impedance. As for method 1, we can now compute the voltage over

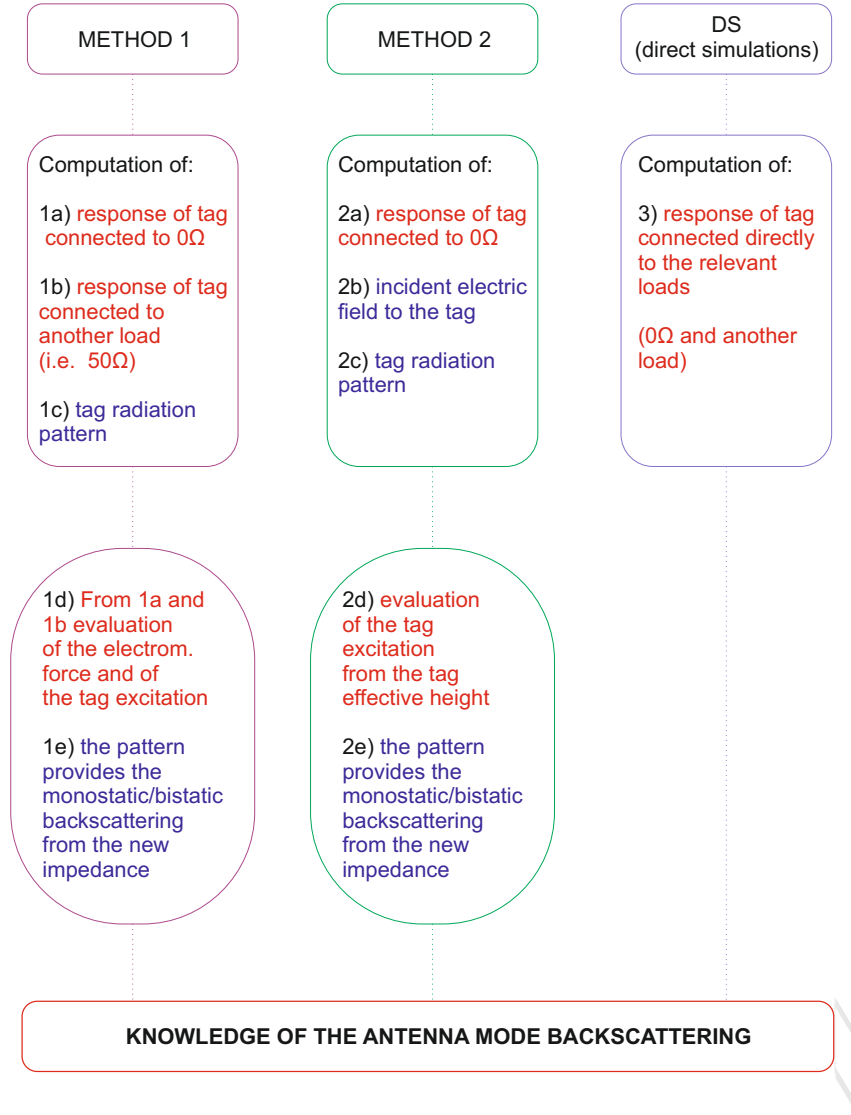


Figure 2.4: Summary scheme of the methodologies proposed.

Z_L and the electric field radiated in the antenna mode for any value of the impedance, according to (2.24) and (2.19) respectively, where V_{excL} and E_{excL} are respectively the excitation voltage applied in 2c) and the radiated field obtained in 2c). Finally, we have to sum up the antenna mode radiated field to the short-circuit mode radiation of 2a). In this way we have reconstructed

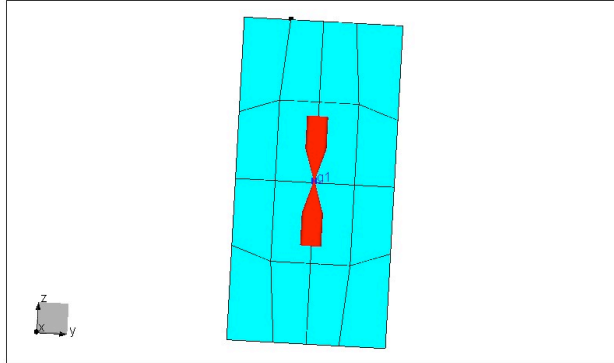


Figure 2.5: Dipole in proximity to a metal plate.

the complete response of the tag. Once more, it is important to remark that only two initial simulations are enough to evaluate the tag response for any impedance, since it is just a matter of applying the formulas reported in Sec. 2.2 once we have obtained the antenna effective height. In this way we do not need to re-simulate the RFID tag connected to another impedance.

Results The methods previously presented were tested with the WIPL-D[®] software, which is a method-of-moments based electromagnetic simulator [102]. In particular, the two approaches were compared with the direct simulations of the antenna response, following the procedures showed in Fig. 2.4. Finally the average powers obtained with each method were compared. For this purpose, a simple broadband dipole made of thick wires was used as the tag antenna. Each arm is 4 mm in diameter and 12 mm long, which results in an operational band width from 4 to 4.8 GHz. We simulated this antenna, first alone and secondly with a metal plate of size (30×60) mm² just behind it, as shown in Fig. 3.19. The distance between the tag and the plate have been varied from 0.5 cm up to 5 cm every 0.5 cm. For each distance, the dipole was successively connected to an open circuit (OC) and a short circuit (SC) load and the antenna backscattering response was simulated in monostatic mode under 1 V/m incident wave amplitude in vertical polarization, for 120 values of the azimuth angle over 360°. We take these simulations as a reference. In order to obtain the short-circuit scattering, we considered the monostatic simulation of the tag connected to 0Ω , which corresponds to case 1a) and 2a) of Sec. 2.3. In addition, we simulated the monostatic scattering with a load of 50Ω on tag terminals, corresponding to case 1b). Finally, we used the radiation mode of WIPL-D[®] under 1 V excitation of the tag, in order to evaluate its radiation pattern. This corresponds to both 1c) and 2b).

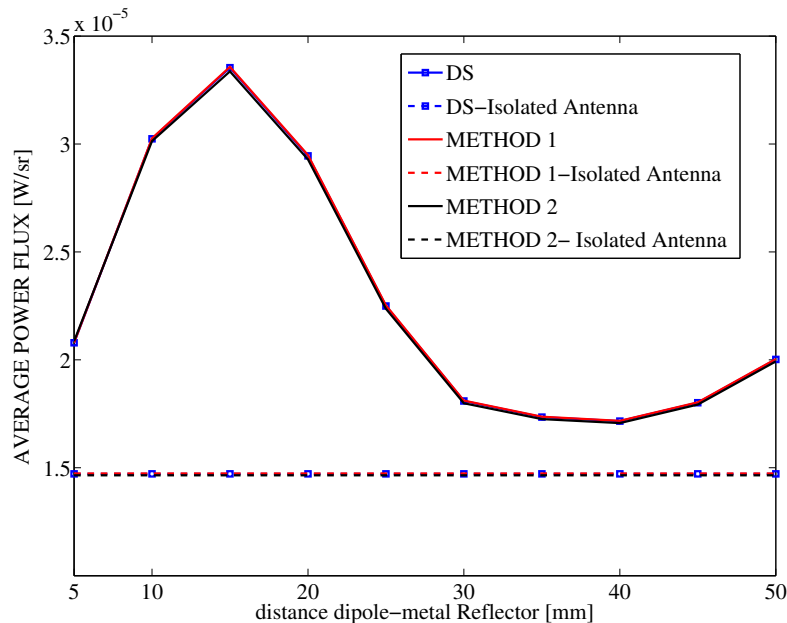


Figure 2.6: Average backscattered power flux vs. tag/metal plate distance. DS refers to the reference simulation.

In the results presented below we first give the average backscattered power flux in the antenna mode over the 120 azimuth angles, where for each value of the azimuth this flux is given by the Poynting vector as

$$P = \frac{|E_{\text{back}}|^2}{2\eta} \quad (2.20)$$

where E_{back} is the backscattered field at a given distance. The average backscattered power flux is reported in Fig. 2.6, as evaluated from the three different approaches presented in this paper. The mean errors achieved by both methods in comparison with the reference simulations are instead reported in Tab. 2.1. It appears that these errors are quite small and can be ascribed to numerical errors in the operation of the software, which does not exactly simulate the same configurations in the various cases. It is interesting to notice how the presence of the metal reflector affects the backscattering performance, since we collect much more power than for the isolated antenna.

We then performed in bistatic the same simulations previously done in the monostatic configuration. In particular, the antenna backscattering response was simulated for 120 values of the azimuth angle over 360° and 61 values of the elevation plane over 180° , under an excitation (1 V/m incident wave amplitude in vertical polarization) considered only on the direction $\vartheta = 90^\circ$,

Table 2.1: Average % error on the backscattered power for each method with respect to direct simulations.

Distance Dipole-metal	Method 1	Method 2
Isolated Antenna	0.02%	0.49%
d=0.5 cm	0.03%	0.35%
d=1 cm	0.08%	0.34%
d=2 cm	0.13%	0.57%
d=3 cm	0.10%	0.58%

$\varphi = 0^\circ$ (c.f. Fig. 2.6). Fig. 2.7 denotes the capability to plot separately the short-circuit and the antenna mode scattering and refers to a distance between the metal reflector and the tag of 3 cm. It shows the backscattered electric field amplitude, normalized to the maximum value of the short-circuit mode scattering, with curves plotted for a frequency of 4.4 GHz and for $\vartheta = 90^\circ$. As can be observed, we still have a full agreement between the two methods proposed in Sec. 2.3 since the plots are indistinguishable. Moreover, the antenna mode scattering along the direction of excitation $\varphi = 0$ is weak, since the distance between the antenna and the metal is close to $\lambda/2$, with a destructive superposition of the incident signal and the reflected one.

The total backscattered power in bistatic mode is reported in Fig. 3.28, as evaluated from the three approaches. We obtained these curves by integrating equation (3.7) over the sphere. From this plot we again confirm the good agreement between the two methods proposed here and the reference simulations (directly performed) of the antenna response. It is also interesting to notice how the dipole/metal reflector distance influences the performance. In particular, for $d = 34 \text{ mm} = \lambda/2$ and along the direction $\vartheta = 90^\circ$, $\varphi = 0^\circ$, the reflected signal is in phase opposition with the incident wave. Consequently, the tag receives a small amount of energy in its antenna mode and thus we obtain a minimum for the total backscattered power. On the contrary, for $d = 17 \text{ mm} = \lambda/4$, the two waves are in phase, thus the amplitude of the backscattered signal is summed up, giving a power gain factor of 4 as partly shown in Fig. 3.28. In fact, if we compare the curves in the presence of the metal reflector with the ones in its absence, we can notice a power gain factor smaller than 4 for $d = 17 \text{ mm}$ (or greater than 0 for $d = 34$). This effect can be related to the size of the metallic plate, which is far from being an approximation of the infinite size reflector.

Further simulations, measurements and deeper considerations concerning the tag-metal interaction follow in Chapter 3.

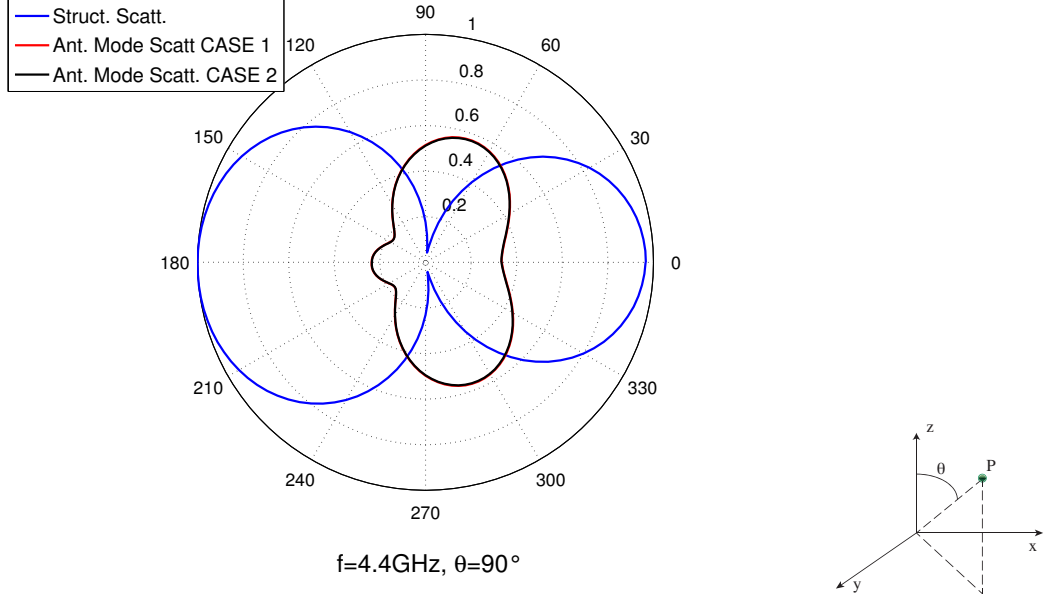


Figure 2.7: Simulated dipole in front of a metal plate.

2.4 Application of Superposition and Reciprocity Principles in Presence of Scatterers

Very generally speaking, irrespective of the nature of the (non magnetic) channel, the reciprocity principle allows to exchange the voltage source and the short-circuit as seen in the case of an ideal scenario. The backscattering antenna mode implies to compute the electromotive force in the reader, due to the voltage developed at the tag. We use the superposition principle, which allows to separate the electromagnetic state depicted in Fig. 2.9 in what can be called the structural mode (left-hand side of Fig. 2.10), where the reader transmits towards the short-circuited tag and the rest of the environment, and in the configuration reported on the right-hand side of Fig. 2.10, where the tag radiates towards the reader in what we can call the antenna mode.

In a multipath scenario described by a discrete channel model, \mathcal{V}_{emf} at the tag writes [103]:

$$\mathcal{V}_{\text{emf}} = \frac{\lambda Z_a}{60\pi} e \sum_i \mathcal{E}_i A_i \quad (2.21)$$

where

$$h_i = \frac{\lambda Z_a}{60\pi} \mathcal{E}_i \quad (2.22)$$

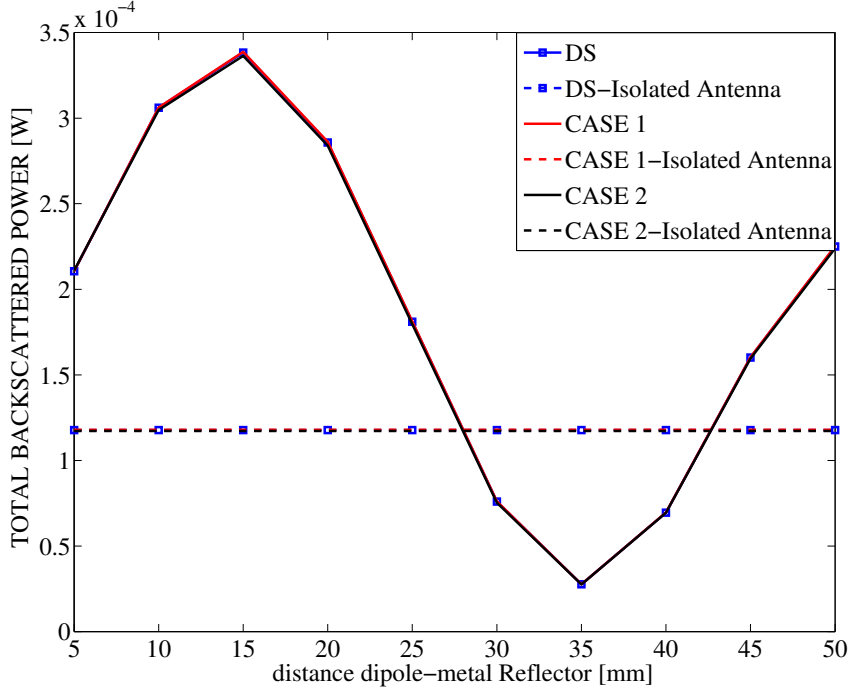


Figure 2.8: Total Backscattered power over the sphere vs tag/metal plate distance. DS refers to the reference simulation.

is the tag effective height ² in the direction of the incoming wave i of (complex) amplitude eA_i expressed in V/m. ³

Then, using Thevenin/Nortons theorems and referring to Fig. 2.11 on the right, we have:

$$I = \frac{\mathcal{V}_{\text{emf}}}{(Z_L + Z_a)} \quad (2.23)$$

and

$$u = \mathcal{V}_{\text{emf}} \frac{Z_L}{Z_L + Z_a} = \frac{\lambda}{60\pi} \frac{Z_a Z_L}{Z_L + Z_a} e \sum_i \mathcal{E}_i A_i. \quad (2.24)$$

When the tag is short-circuited, we have a short-circuit current I expressed as:

$$I = \frac{\mathcal{V}_{\text{emf}}}{Z_a} = \frac{\lambda}{60\pi} e \sum_i \mathcal{E}_i A_i. \quad (2.25)$$

²A term $-j$ must be added for completeness, but it is irrelevant here. See [104]

³ A_i can be seen as a transfer function relating the excitation voltage on the reader's antenna terminals to the field complex amplitude for path i . Of course this transfer function contains the reader's antenna complex gain in the path radiation direction and the specificities of the scattering events

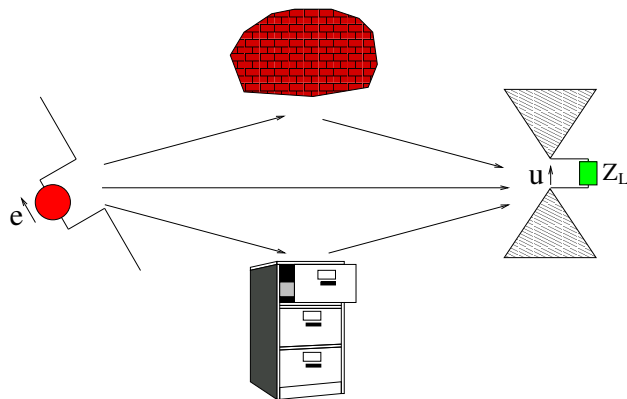


Figure 2.9: Ideal reader antenna (receiving) and tag antenna (transmitting) in LOS.

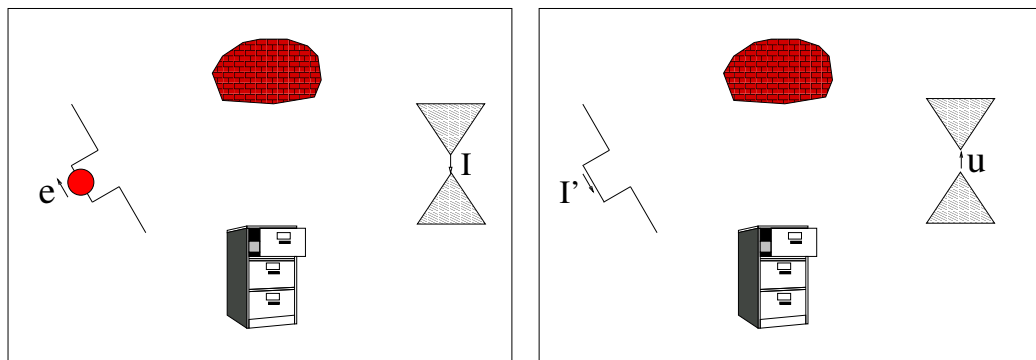


Figure 2.10: Left: Ideal reader antenna (transmitting) and tag antenna (receiving) in LOS and in presence of scatterers. Right: Ideal reader antenna (receiving) and tag antenna (transmitting) in LOS and in presence of scatterers.

In the structural scattering (left of Fig. 2.10), the current flowing in the reader's antenna is due to the voltage applied to this antenna and also to the backscattered signals from the short-circuited tag and the rest of the environment. In the antenna mode instead (right of Fig. 2.10), the tag radiation is received by the reader after going through the channel, which results in a short-circuit current I' in the reader.

According to the detection technique of RFID by modulated backscattering, the reader measures the difference between the signal it receives when the tag is connected to two different loads, the usual being SC and OC loads. Generally speaking, it measures the differences between the I' for the two loads.

Thus, as a consequence from eq. 2.24 and 2.25, and considering Fig. 2.11

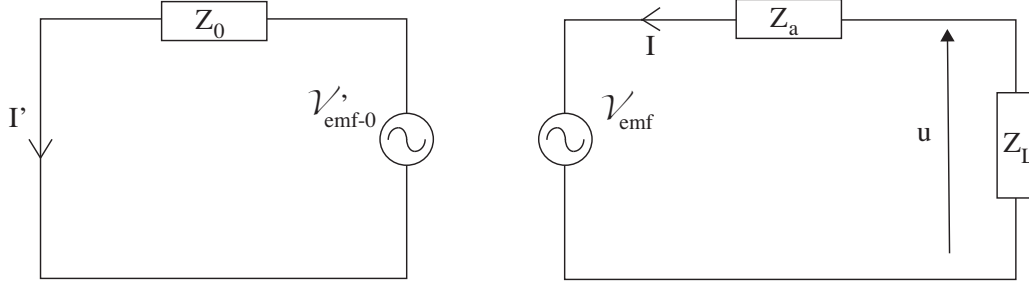


Figure 2.11: Left: Reader side for configuration of Fig. 2.10 on the right. Right: Tag side for configuration of Fig. 2.10 on the left.

we obtain

$$I' = \frac{\lambda}{60\pi} u \sum_i \mathcal{E}_i A_i = \left(\frac{\lambda}{60\pi} \right)^2 \frac{Z_a Z_L}{Z_a + Z_L} e \left(\sum_i \mathcal{E}_i A_i \right)^2. \quad (2.26)$$

In other words, we have the product (in the frequency domain) or the convolution (in the time domain) of the two channel responses. Since this SC currents flows in only the reader's impedance, using Thevenin/Nortons theorems and considering Fig. 2.11, the backscattered signal is due to an electromotive force expressed as:

$$\mathcal{V}'_{\text{emf-0}} = Z_0 \left(\frac{\lambda}{60\pi} \right)^2 \frac{Z_a Z_L}{Z_a + Z_L} e \left(\sum_i \mathcal{E}_i A_i \right)^2. \quad (2.27)$$

Now, if we take into account that in practice the received signal will be duplexed towards a matched load Z_0 , the current then truly flowing will be $I'/2$. For the short-circuited tag we have $\mathcal{V}'_{\text{emf-0}} = 0$ and for the open-circuited tag this yields

$$\mathcal{V}'_{\text{emf-0}} = Z_0 Z_a \left(\frac{\lambda}{60\pi} \right)^2 e \left(\sum_i \mathcal{E}_i A_i \right)^2. \quad (2.28)$$

The tag electromotive force finally yields:

$$\mathcal{V}'_{\text{emf-0}} = Z_0 \left(\frac{\lambda}{60\pi} \right)^2 \frac{Z_a Z_L}{Z_a + Z_L} e \left(\sum_{i,j} \mathcal{E}_i \mathcal{E}_j A_i A_j \right)^2 \quad (2.29)$$

which becomes

$$\mathcal{V}'_{\text{emf-0}} = Z_0 \left(\frac{\lambda}{60\pi} \right)^2 \frac{Z_a Z_L}{Z_a + Z_L} e \left(\sum_{i,j} \mathcal{E}_i \mathcal{E}_j |A_i| |A_j| e^{-j\omega(d_i+d_j)/c} \right)^2 \quad (2.30)$$

by expliciting the phase factor in the complex path amplitudes, neglecting any phase factor not related to the path propagation length d_i . From the Fourier transform of this equation, it will be immediate to observe that in the time domain all possible combinations of the path delays $\tau_i = d_i/c$ enter the electromotive force. This can be easily understood: in the antenna mode, each signal received along a certain path is retransmitted by the tag over all possible paths. The reciprocity principle is such that, although the tag radiates in all directions, only the waves following the same paths on the return as on the forward trip will arrive to the reader. Naturally, the signals experience the tag antenna gain both when entering the antenna and exiting it, which explains the formula above with great clarity.

2.5 Proposed Methodologies in Presence of Scatterers

Here we report simple procedures in order to extend the superposition principle above described in simulations and measurements to realistic scenarios. When scatterers are present in the environment, the previous proposed methodologies are indeed no more valid, since the multipath components of the backscattered signal also need to be accounted for.

Consider the sketch of Fig. 2.12, where an equivalent of the reader/tag system is reported in the form of a two port system between the source feeding the reader antenna and the load connected to the tag antenna. A representation with the S-matrix is very fruitful for the further analysis of simulations and experiments.

2.5.1 General Representation

Let us call respectively Γ_{IN_S} and Γ_{IN_O} the measured /simulated signals when the tag is connected alternatively to the SC load and the OC load. If this system is characterized by a vector network analyzer (VNA), Γ_{IN} can be seen as the effective S parameter seen by the instrument. It follows:

$$\begin{cases} \Gamma_{\text{IN}_S} = S_{11} + \frac{S_{12}S_{21}\Gamma_{\text{LS}}}{1-S_{22}\Gamma_{\text{LS}}} \\ \Gamma_{\text{IN}_O} = S_{11} + \frac{S_{12}S_{21}\Gamma_{\text{LO}}}{1-S_{22}\Gamma_{\text{LO}}} \end{cases} . \quad (2.31)$$

The difference $\Gamma_{\text{IN}_O} - \Gamma_{\text{IN}_S}$ gives the antenna mode scattering contribution antenna. The SC mode corresponds to $\Gamma_{\text{LS}} = -1$ while the OC to $\Gamma_{\text{LO}} = 1$.

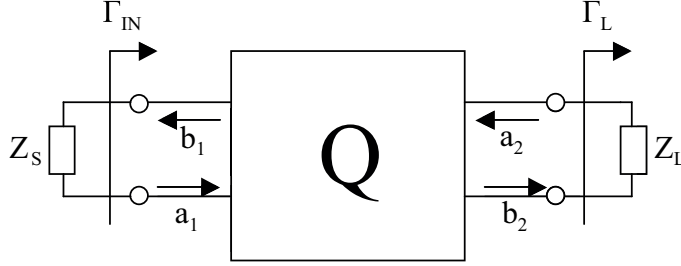


Figure 2.12: Sketch of the 2-ports system.

In these expressions, the reference tag impedance Z_0 used in the definition of the S parameters is arbitrary. However, we will use the conventional value of $50\ \Omega$. For the sake of clarity, let us stress that if the tag antenna happens to have an internal impedance of $50\ \Omega$, it corresponds to the minimum scattering condition in the antenna mode, i.e. matched load connected to the tag antenna. In fact, when the antenna is well-matched to the reference impedance Z_0 , i.e. $S_{22} = 0$, we can assume that the structural part corresponds to S_{11} . A common procedure for simulations and measurements is reported in this paragraph in order to use the superposition principle to reconstruct the antenna response, by simple manipulations of the S-matrix.

Method 1 Consider the RFID system associated to a two-port network, where the reader is connected to port 1 and the tag to port 2, as depicted in Fig. 2.12. The approach consists in performing two simulations/measurements with the tag connected to a short circuit and to another load (i.e. Z_L). In this way we have Γ_{IN_S} and $\Gamma_{IN_{50}}$. The difference between the 2 responses gives the signal part due to the antenna mode scattering. The electromotive force at tag terminals is evaluated considering the Z -matrix, where we have the following relations between currents and voltages, referring to scheme in Fig. 2.12:

$$\begin{cases} V_1 = Z_{11} \cdot i_1 + Z_{12} \cdot i_2 \\ V_2 = Z_{21} \cdot i_1 + Z_{22} \cdot i_2 \end{cases} \quad (2.32)$$

Multiplying the first equation by Z_{21} and the second one by Z_{11} we obtain

$$\begin{cases} Z_{21} \cdot V_1 = Z_{21} \cdot Z_{11} \cdot i_1 + Z_{21} \cdot Z_{12} \cdot i_2 \\ Z_{11} \cdot V_2 = Z_{21} \cdot Z_{11} \cdot i_1 + Z_{11} \cdot Z_{22} \cdot i_2 \end{cases} \quad (2.33)$$

and the difference between the 2 equations gives

$$Z_{11}V_2 - Z_{21} \cdot V_1 = (Z_{11}Z_{22} - Z_{12}Z_{21}) \cdot i_2 \quad (2.34)$$

which yields to

$$V_2 = \frac{(Z_{11}Z_{22} - Z_{12}Z_{21}) \cdot i_2 + Z_{21}V_1}{Z_{11}} \quad (2.35)$$

where the only unknown is i_2 since V_1 is the input voltage and thus usually an input parameter of our system. Now, considering the tag scheme reproduced in Fig. 2.3, it is possible to write

$$\mathcal{V}_{\text{emf-tag}} = \frac{(Z_{11} + Z_L + Z_{11}Z_{22} - Z_{21}Z_{12})}{(Z_{11} + Z_L + Z_{11}Z_{22} - Z_{21}Z_{12})} \cdot \frac{Z_{21}}{Z_{11}} V_1 = \frac{Z_{21}}{Z_{11}} V_1 \quad (2.36)$$

where V_1 is the excitation voltage at the reader port. In simulations performed with WIPL-D[®], V_1 can be manually set to any value, while in measurements it can be easily evaluated as

$$V_1 = (a_1 + b_1)\sqrt{Z_0}, \quad (2.37)$$

where a_1 and b_1 can be simply measured by the VNA and Z_0 is usually equal to 50Ω .

Then, from the typical two-port network relations concerning the S-matrix, we can write

$$b_{1L} = \left(S_{11} + \frac{\Gamma_L}{1 - \Gamma_L S_{22}} S_{12} S_{21} \right) a_1 \quad (2.38)$$

and

$$\begin{aligned} b_{1L} - b_{1S} &= S_{12} S_{21} \left(\frac{\Gamma_L}{1 - \Gamma_L S_{22}} + \frac{1}{1 + S_{22}} \right) a_1 \\ &= S_{12} S_{21} \frac{1 + \Gamma_L}{1 - \Gamma_L S_{22}} \cdot \frac{1}{1 + S_{22}} a_1 \end{aligned} \quad (2.39)$$

where b_{1L} and b_{1S} represent respectively the responses for a generic tag load Z_L and a SC tag. Then, the voltage V_{2L} at tag side, due to a generic load Z_L , is given by

$$V_{2L} = (a_{2L} + b_{2L})\sqrt{Z_0} = (\Gamma_L + 1)b_{2L}\sqrt{Z_0} \quad (2.40)$$

with

$$b_{2L} = S_{21}a_1 + S_{22}a_{2L} = S_{21}a_1 + S_{22}\Gamma_L b_{2L} \quad (2.41)$$

hence it yields:

$$V_{2L} = \sqrt{Z_0} \frac{1 + \Gamma_L}{1 - \Gamma_L S_{22}} S_{21} a_1. \quad (2.42)$$

Finally $b_{1L} - b_{1S}$ can be expressed as

$$b_{1L} - b_{1S} = \frac{S_{12}}{\sqrt{Z_0}(1 + S_{22})} V_{2L} = \frac{S_{12}}{\sqrt{Z_0}(1 + S_{22})} (V_{2L} - V_{2S}). \quad (2.43)$$

The effective reflection coefficient S_{11} seen by a VNA for a given load connected to the tag antenna, minus its value in the case of a SC is indeed proportional to the bias at the tag antenna ports. These relations facilitate the processing of data, as obviously the S and Z matrix are easily measured by the VNA or simulated by any electromagnetic tool, and thus from \mathcal{V}_{emf} of the tag evaluated with (2.36), it is possible to find any tag excitation.

Method 2 Consider that $\Gamma_{\text{IN}_L} - \Gamma_{\text{IN}_S}$ is directly proportional to the electric field radiated by the tag due to the antenna mode scattering (normalised with the incident one), as comes from the radar range equation. We refer again to V_x and V_L as the excitation voltage at tag ports when the tag radiates towards the reader in what we call the antenna mode scattering, in the case of loads Z_x and Z_L connected to the tag, respectively. Considering the following relations

$$\begin{cases} V_L : & \alpha_L = \Gamma_{\text{IN}_L} - \Gamma_{\text{IN}_S} \\ V_x : & \alpha_x = \Gamma_{\text{IN}_x} - \Gamma_{\text{IN}_S} \end{cases} \quad (2.44)$$

α_x can be obtained as

$$\alpha_x = \alpha_L \cdot \frac{V_x}{V_L}. \quad (2.45)$$

Note that this relation can be intuitively seen in (2.53), since Γ_{IN_L} and Γ_{IN_x} are directly proportional to the tag backscattered field, thus respectively with V_x and V_L . Operating in this way, we do not need anymore to evaluate $\mathcal{V}_{\text{emf-tag}}$ at the tag side, since

$$\frac{V_x}{V_L} = \frac{\mathcal{V}_{\text{emf}} \cdot \frac{Z_x}{Z_x + Z_a}}{\mathcal{V}_{\text{emf}} \cdot \frac{Z_L}{Z_L + Z_a}} = \frac{Z_x \cdot (Z_L + Z_a)}{Z_L \cdot (Z_x + Z_a)} \quad (2.46)$$

only depends on the ratio of the loads.

Results

The procedures presented above have been validated in simulations by considering a system composed of one reader antenna and one tag antenna placed at 1 m, where one metallic scatterer is present in the environment. Simulations were performed using the commercial tool WIPL-D over the bandwidth 7 – 12 GHz with a frequency step of 20 MHz, employing a simple thick dipole

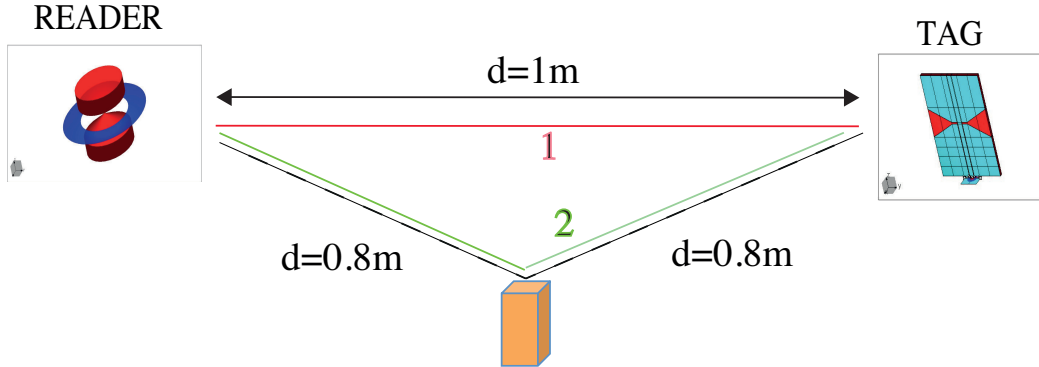


Figure 2.13: Simulated scenario.

as reader and a planar dipole as tag. The metallic object has dimensions $(4 \times 8 \times 8) \text{ cm}^3$ and it was placed in a lateral position at a distance of 0.8 m from both the reader and the tag. The RFID system was directly simulated connecting alternatively the tag to an OC and SC load, and also by applying the superposition principle as presented in Sec. 2.4, by simulating the S-Matrix of the system comprising the two antennas and the scatterer. Fig. 2.14 reports the obtained results for the antenna mode scattering, comparing the two methods. In particular, it shows not only an agreement between the methodologies (errors less than 1% for what concerns the mean energy of the channel response), but also a confirmation of all the comments that follow equation (2.26), regarding the convolution between the channel from reader to tag and the (identical) channel from tag to reader. In fact, it is possible to notice the convolution of the two channels looking at the 3 backscattered signals. The first one derives from the convolution of the 1st path with itself (marked as "A" in Fig. 2.14), the second signal "B" in Fig. 2.14 is twice the combination of the direct path with the path created by the scatterer. Finally, the last and smallest one indicated with "C", is the self-convolution of the path created by the scatterer.

Measurements were then performed in order to validate also experimentally the use of the superposition principle. We first measured the backscattering of a DFMS antenna [105–107] (playing the role of an RFID tag) positioned at a distance of 2.25 m from a Horn Lindgren 3117 employed as reference antenna (playing the role of reader), as shown in Fig. 2.15. We set the frequency bandwidth from 2 to 12 GHz with a step size of 5 MHz. The tag was connected alternatively to an OC and SC load through a delay line, and similarly to simulations the S-matrix of the system comprising the two antennas has been measured. A preliminary measurement setup resorting to only one reference antenna (reader, monostatic case) and a DFMS

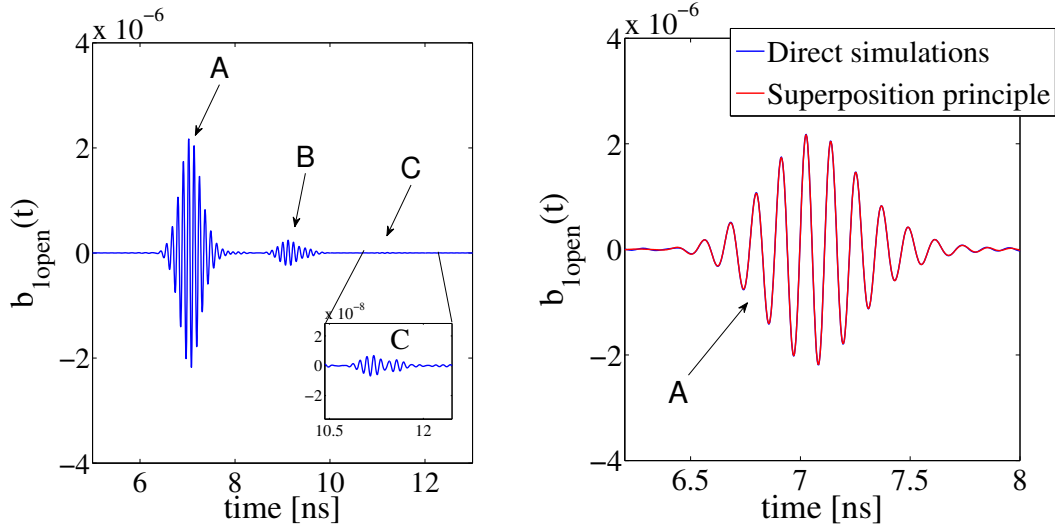


Figure 2.14: Left: complete received signal ($b_{1\text{Open}}$). Right: Comparison between direct simulations and use of the superposition principle adopting method 1.

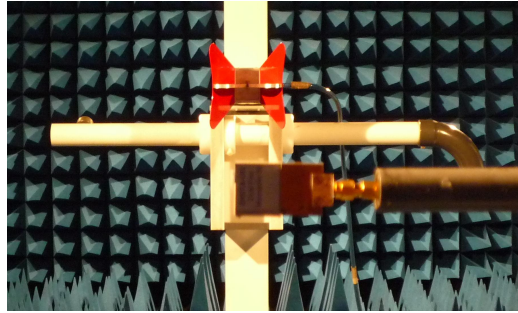


Figure 2.15: Measurement set-up inside the anechoic chamber.

antenna (tag) is first considered. Figure 2.16 shows the antenna mode scattering for the isolated RFID system (upper figure) and for the case when a metallic plate of dimensions $(20 \times 20) \text{ cm}^2$ is additionally placed between the 2 antennas at a distance of 1.10 m from the tag. The results confirm the similarity between the proposed methodology and the direct measurements of the backscattering response, although some differences in secondary lobes are visible, which can be ascribed to the manual changes of the load impedance and to some movement of cables. From this point of view, there is a clear practical advantage in resorting to a single two-port network measurement (one way channel) allowed by taking advantage of reciprocity, when we intend to measure (two way) backscattering channels. This is true when only the antenna mode backscattering is of interest, which is precisely the case

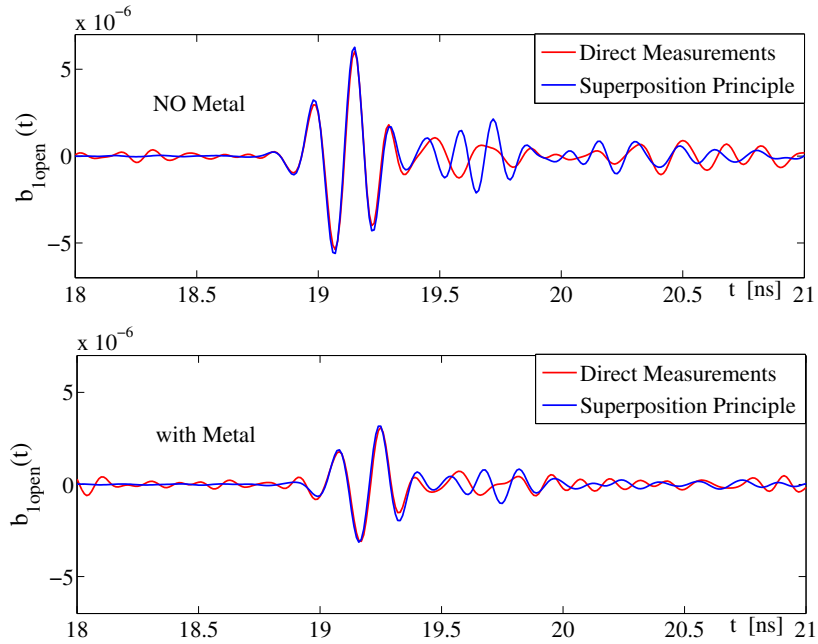


Figure 2.16: Measurement results. Method 1 is adopted for the superposition principle.

as regards load modulated backscattering for RFID. A single step procedure indeed provides a better reliability of the measurement, is less time consuming and easier to perform. Last but not least, a one way channel is obviously easier to measure than a two-way backscattering channel in terms of signal to noise ratio.

2.6 A Different Approach for Tag Backscattering Characterization

Here we formulate slightly differently the backscattering by the tag in the antenna mode [108]. Consider the one-port system with the port located at the reader side, the (loaded) tag being at distance r from the reader, as depicted in Fig. 2.17. The monostatic backscattering transfer function S_{11} , where a_1 and b_1 are respectively the transmitted and the received complex wave amplitudes by the reader antenna, is here defined for a given reference impedance. For an imperfectly matched reader antenna, this quantity includes the reflection coefficient of the antenna, to which is superimposed the signal backscattered by the antenna (and the clutter in the general case). Re-

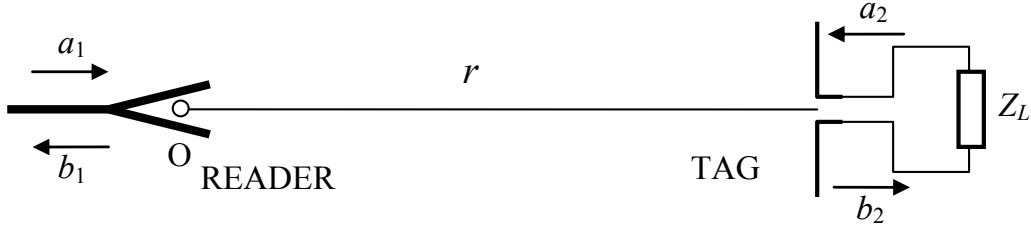


Figure 2.17: Reader tag configuration.

restricting to the signal backscattered by the tag antenna only in the following, S_{11} can be computed by analyzing in detail the various EM events.

In free space, the electric field incident in far field region on the tag can be expressed in the following way [109, 110]:

$$\mathbf{E}_{\text{inc}}^{\text{FF}}(\mathbf{r}) = \frac{e^{-jkr}}{r} \sqrt{\frac{\eta}{4\pi}} \cdot \mathbf{H}_{\text{read}}^{\text{T}}(\hat{\mathbf{r}}) \cdot a_1 \quad (2.47)$$

where $\mathbf{H}_{\text{read}}^{\text{T}}$ represents the transfer function of the reader in transmission, with $\hat{\mathbf{r}} = \mathbf{r}/\|\mathbf{r}\|$. The received signal b_1 is given by:

$$b_1 = \mathbf{H}_{\text{read}}^{\text{R}}(\hat{\mathbf{r}}) \cdot \sqrt{\frac{4\pi}{\eta}} \cdot \mathbf{E}_{\text{sc}}^{\text{FF}}(\mathbf{0}) \quad (2.48)$$

where $\mathbf{H}_{\text{read}}^{\text{R}}$ represents the reader antenna transfer function in reception, and the backscattered electric field in far field region $\mathbf{E}_{\text{sc}}^{\text{FF}}$ is taken at the origin, i.e. at distance r from the tag. If the polarization of each antenna is assumed to be perfectly linear and perfectly matched (polarization efficiency of 1), the fields can be considered scalars. The equations here reported can easily be generalized to any polarization. Under this assumption, we can define a transfer function for backscattering by the target in the following way:

$$H_{\text{tag}}^{\text{B}}(\hat{\mathbf{r}}) = \frac{4\pi r}{\lambda} \frac{E_{\text{sc}}^{\text{FF}}(\mathbf{r}) e^{jkr}}{E_{\text{inc}}^{\text{FF}}(\mathbf{r})} \quad (2.49)$$

which gives

$$|H_{\text{tag}}^{\text{B}}(\hat{\mathbf{r}})|^2 = \left(\frac{4\pi r}{\lambda}\right)^2 \frac{|E_{\text{sc}}^{\text{FF}}(\mathbf{r})|^2}{|E_{\text{inc}}^{\text{FF}}(\mathbf{r})|^2} = \frac{4\pi\sigma}{\lambda^2} \quad (2.50)$$

where σ is the antenna radar cross section of the tag antenna. Then it comes:

$$b_1 = H_{\text{read}}^{\text{R}}(\hat{\mathbf{r}}) \sqrt{\frac{4\pi}{\eta}} \left[\frac{\lambda e^{-jkr}}{4\pi r} H_{\text{tag}}^{\text{B}}(\hat{\mathbf{r}}) \right] H_{\text{read}}^{\text{T}}(\hat{\mathbf{r}}) \frac{e^{-jkr}}{r} \sqrt{\frac{\eta}{4\pi}} \cdot a_1 \quad (2.51)$$

and considering the reciprocity relation [111]

$$H_{\text{read}}^{\text{R}}(\hat{\mathbf{r}}) = -j \frac{\lambda}{4\pi} H_{\text{read}}^{\text{T}}(\hat{\mathbf{r}}) \quad (2.52)$$

the total round trip transfer function, i.e. S_{11} , is obtained as

$$S_{11} = \frac{b_1}{a_1} = H_{\text{read}}^{\text{T}}(\hat{\mathbf{r}}) \left[-j \left(\frac{\lambda}{4\pi r} \right)^2 e^{-j2kr} \right] \cdot H_{\text{tag}}^{\text{B}}(\hat{\mathbf{r}}). \quad (2.53)$$

(2.53) is very important as it links the tag transfer function and the complete backscatter response in a simple and immediate way. In fact, this expression will be used in Chapter 3 to simply reconstruct the antenna backscattering for different tag positions and orientations in space. It is now possible to give for H_{tag} an explicit form. Again by virtue of the superposition theorem, we can write:

$$H_{\text{tag}}^{\text{B}}(\hat{\mathbf{r}}) = H_{\text{tag-match}}^{\text{B}}(\hat{\mathbf{r}}) + H_{\text{tag-ant}}^{\text{B}}(\hat{\mathbf{r}}) \quad (2.54)$$

where $H_{\text{tag-match}}^{\text{B}}(\hat{\mathbf{r}})$ is the response for a load impedance equal to the reference impedance⁴, i.e. enforcing $a_2 = 0$, and $H_{\text{tag-ant}}^{\text{B}}(\hat{\mathbf{r}})$ is the additional backscattered signal when $a_2 \neq 0$. The latter is due to the tag antenna acting as a receiving antenna and subsequently as a transmitting antenna for the wave reflected by the load, which verifies $a_2 = \Gamma_{\text{L}} b_2$. By using for the tag the equations presented above for the reader, and considering now a two-port system with port 2 located at tag side, it comes:

$$b_2 = H_{\text{tag-ant}}^{\text{R}}(\hat{\mathbf{r}}) \sqrt{\frac{4\pi}{\eta}} \cdot E_{\text{inc}}^{\text{FF}}(\hat{\mathbf{r}}) + S_{22} \cdot a_2 \quad (2.55)$$

$$E_{\text{sc}}^{\text{FF}}(\mathbf{r}) = \frac{e^{-jkr}}{r} \sqrt{\frac{\eta}{4\pi}} \cdot H_{\text{tag-ant}}^{\text{T}}(\hat{\mathbf{r}}) \cdot a_2. \quad (2.56)$$

The combination of these equations with (2.49) yields:

$$\begin{aligned} H_{\text{tag-ant}}^{\text{B}}(\hat{\mathbf{r}}) &= \frac{4\pi}{\lambda} H_{\text{tag-ant}}^{\text{R}}(\hat{\mathbf{r}}) H_{\text{tag-ant}}^{\text{T}}(\hat{\mathbf{r}}) \cdot \frac{\Gamma_{\text{L}}}{1 - S_{22}\Gamma_{\text{L}}} \\ &= -j H_{\text{tag-ant}}^{\text{T}}(\hat{\mathbf{r}}) \cdot \frac{\Gamma_{\text{L}}}{1 - S_{22}\Gamma_{\text{L}}} \end{aligned} \quad (2.57)$$

In other words, in its antenna mode the tag antenna acts twice through its transfer function in transmission, as the result of reciprocity. The difference between the backscattered signals for open and short-circuit loads thus has a power proportional to $\frac{|H_{\text{tag-ant}}^{\text{T}}|^4}{|(1-S_{22}^2)|^2}$.

⁴which can also be called "structural mode" when the tag antenna is matched to this impedance ($S_{22}=0$)

2.7 Conclusions

In this chapter, the RFID tag backscattering has been analyzed in several ways, both in ideal and real conditions. Simple approaches for the tag antenna backscattering reconstruction have been shown and tested, with the final conclusion that the same results can be obtained by performing direct simulations/measurements or by means of the superposition and reciprocity principles. The proposed methodologies helped increase the comprehension of the phenomena that appear in the backscattering mechanism, with the opportunity to reduce the number of needed simulations or measurements, which are often very much time consuming for the creation of a database of tag backscattering properties.

The relation between the tag transfer function and the overall backscatter response will be exploited in Sec. 3.3, in order to evaluate the detection and localization coverage of tags in a monitored environment.

Chapter 3

Tag Backscattering Characterization in Presence of Nearby Objects

3.1 Introduction

In everyday life, RFID tag antennas are usually placed on objects that have to be detected, identified and possibly localized in a certain area. Given this reality, it is clear that investigating the impact of close objects on tag behavior is a necessity, since their presence may significantly affect the tag radiation characteristics, as partly seen in Sec. 2.3.

In order to obtain a characterization of the interaction between an UWB RFID antenna and a close disturber, assumed to modify the antenna radiation characteristics, we have measured the backscattered signals of different UWB antennas inside an anechoic chamber, in the presence of nearby objects, as deep studies on this topic have already been conducted only for current UHF RFID tags [112–119]. In the following, the measurement set-up and the obtained results are shown. Afterwards, measurements are post-processed in order to assess the detection coverage of tags and see how the presence of an object behind a tag affects the probability that the tag itself is seen by the reader, considering all possible tag positions and orientations.

Finally, a case study of particular interest is investigated, which is the interaction of an UWB antenna with a metallic reflector, whose effects greatly affect the antenna radiation characteristics as is well known from the literature. The analysis is conducted through simulations and measurements.

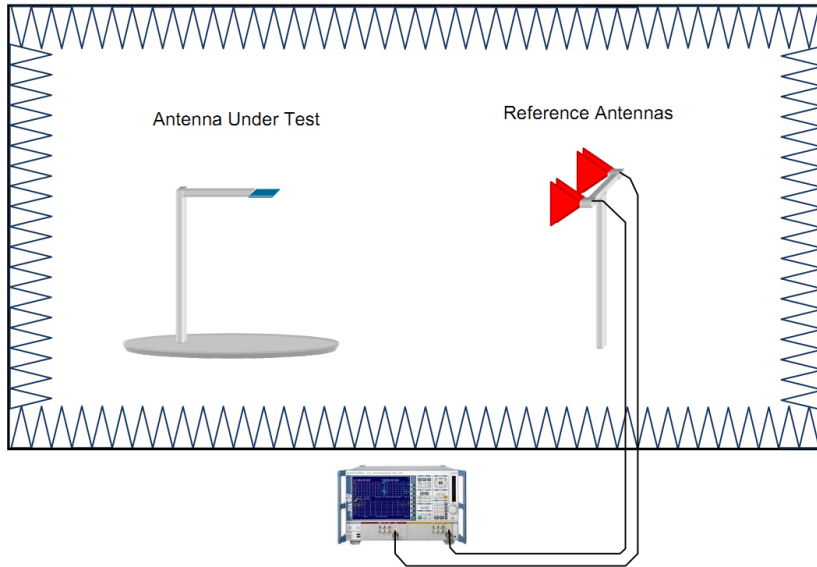


Figure 3.1: Measurement scenario

3.2 Tag Interaction with Objects

Here we report a description of the measurements carried out to characterize the signal backscattered by various UWB antennas in presence of different nearby objects, and for different orientations. The measurement campaign was conducted in collaboration with Valerio Casadei [120].

3.2.1 Measurement Set-Up

The data were collected in an anechoic chamber of Telecom ParisTech laboratories. The measurements were performed using a VNA, remotely controlled by a PC to initiate measurements and save data. The scenario is showed in Fig. 3.1, where an antenna under test (AUT) and two reference antennas, in quasi-monostatic configuration, are employed. The quasi-monostatic configuration was adopted since it guarantees a higher isolation between the transmit and the receive channels than the classical monostatic one. Different objects are positioned behind the antenna, to evaluate the AUT backscattering response in various conditions.

For this measurement campaign, two Horn Lindgren 3117 [121] were employed as reference antennas at a distance of 2.04 m from the tag (the AUT). Three different loads ($Z_L = 0$, $Z_L = 50\Omega$ and $Z_L = \infty$) were connected to the tag, via a delay line of length 54 cm intended to temporally discriminate the structural and the antenna modes, as shown in Fig. 3.2 on the left. Mea-

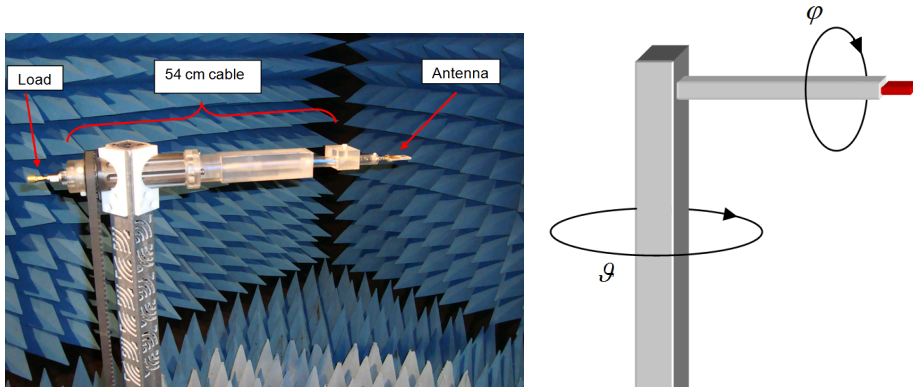


Figure 3.2: Left: Antenna connection and support configuration. Right: Measurement system rotations.

measurements were performed in the frequency domain by means of the VNA, in the band 2 – 12 GHz. The tag, mechanically supported over a vertical post specially designed by the manufacturer for a low electromagnetic signature, was rotated from $\varphi = 0^\circ$ to $\varphi = +360^\circ$ with a step size of 5° (see Fig. 3.2 on the right). In the following, the results refer to the measured bandwidth 3 – 5 GHz, unless otherwise indicated.

RFID Tag Antennas

The backscattering response was measured for both isolated antennas, and in the presence of objects in the immediate vicinity of the tag. The tag antennas that we employed during the measurement campaign are: a DFMM [105, 122–124], a DFMS [106, 107], a SLOT antenna and a PBD (see Table 3.1). These antennas were chosen for their moderate dimensions, which make them quite suitable for RFID applications.

In particular, the **PBD** has dimensions $(33 \times 20) \text{ mm}^2$, it is a planar and moderately directional dipole with a lateral feeding [125].

The **DFMS** $((40 \times 24) \text{ mm}^2)$, which is a vertically polarized planar monopole with a symmetry plane, has a radiation essentially omnidirectional, with gain variations in the azimuthal plane typically less than 5 dB [106].

The **DFMM** antenna $((33 \times 20) \text{ mm}^2)$ is quite similar to the DFMS, but the feeding is achieved through a microstrip waveguide instead of a stripline. Finally, the **SLOT** is linearly polarized along its two symmetry axis, and its radiation is mostly normal to the plane. Its dimensions $(60 \times 57) \text{ mm}^2$ are larger than the other antennas.

The **SLOT** $((60 \times 57) \text{ mm}^2)$ is linearly polarized along its two symmetry

axis, and its radiation is mostly normal to the plane. Its dimensions are significantly larger than the previously presented antennas.

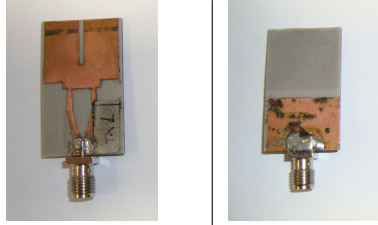
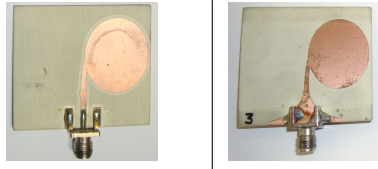
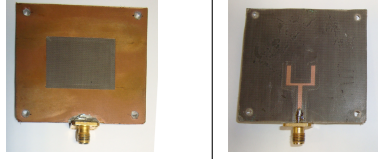
Antennas		Name and dimensions [mm]	-10 dB BW [GHz]
		DFMS 40 x 24	[2.4 - 7.3]
		DFMM 33 x 20	[4.8 - 11.4]
		PBD 45 x 40	[2.3 - 12]
		SLOT 60 x 57	[2.9 - 10.5]

Table 3.1: Antennas and descriptions

RFID Tag Antennas in Presence of Objects

Except for one, the chosen objects were all made of a flat plate of varying permittivity and thickness, as an attempt to represent in a simplified manner the wide range of materials and objects that might be placed near a tag. They were positioned at a distance of 1.2 cm from the antenna. Fig. 3.5 right shows an example of the DFMS-wood setup for $\varphi = 0$.

In particular, we considered the following objects depicted also in Fig. 3.3

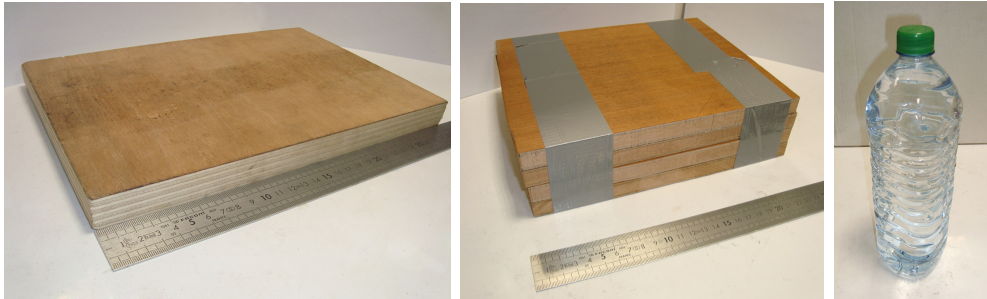


Figure 3.3: Left: 22 mm plywood block. Middle: 64 mm composite wood block. Right: plastic bottle full of tap water.

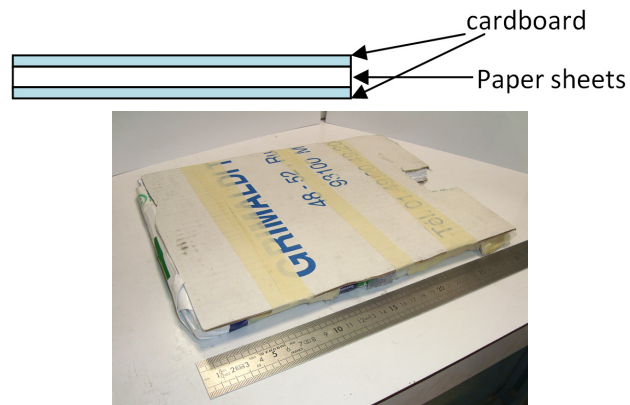


Figure 3.4: Paper block composition

and Fig. 3.4:

- Piece of plywood with size $(30 \times 20 \times 2.2) \text{ cm}^3$.
- 3 different layers of plywood put together, with an overall size $(24 \times 20 \times 6.5) \text{ cm}^3$.
- Block of standard printer paper of size $(32 \times 23 \times 2) \text{ cm}^3$, with additional cardboard pieces for the mechanical stability during measurements.
- Plastic bottle full of ordinary water, 1.5 l (diameter: 8 cm, height: 31 cm).

The case of metallic objects is partly addressed in Sec. 3.4, since it is more complicated and requires a specific study.

3.2.2 Results

From the measurements of the scattering matrix and from equation (2.53), it is possible to evaluate the tag transfer function, which comprises both

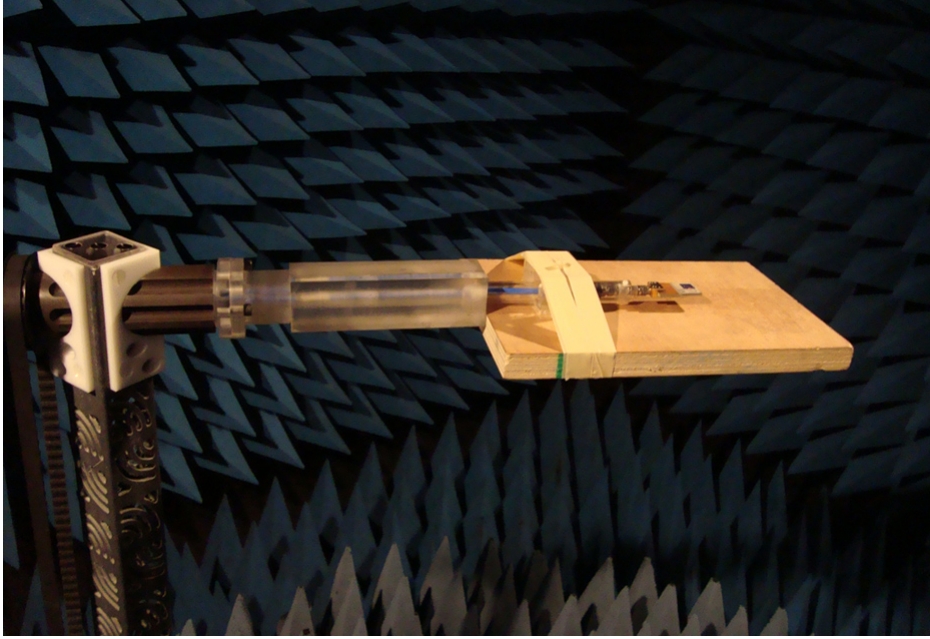


Figure 3.5: Wood panel in proximity of the tag antenna for $\varphi = 0$.

the structural and the antenna mode scattering. The collected data was first filtered in the frequency domain to avoid a ringing effect. After a first inverse Fourier transform, time gating was applied in order to isolate the complete antenna backscattering response from the mutual coupling between the reference antennas. After deconvoluting the impulse responses of the previously measured reference antennas and after removing the two ways channel path loss, measured data have been Fourier transformed back into the frequency domain.

In order to simply discriminate between the structural and the antenna mode scattering, the difference between the responses measured for an OC and a SC tag was computed. From (2.57) it comes that for a well matched antenna (i.e. $S_{22} \simeq 0$), it yields to

$$H_{\text{tag-ant}}^{\text{B}}(\hat{\mathbf{r}}) = -jH_{\text{tag-ant}}^{\text{T}^2}(\hat{\mathbf{r}}) \cdot \Gamma_{\text{L}} \quad (3.1)$$

where in case of perfect OC and SC it is

$$H_{\text{tag-ant}}^{\text{B-O}}(\hat{\mathbf{r}}) = -H_{\text{tag-ant}}^{\text{B-S}}(\hat{\mathbf{r}}) \quad (3.2)$$

with $H_{\text{tag}}^{\text{B,O}}(f, \varphi)$ and $H_{\text{tag}}^{\text{B,S}}(f, \varphi)$ referring respectively to an OC and a SC load. Thus, we consider here

$$H_{\text{tag-ant}}^{\text{B}} \approx \frac{H_{\text{tag}}^{\text{B,O}}(f, \varphi) - H_{\text{tag}}^{\text{B,S}}(f, \varphi)}{2} \quad (3.3)$$

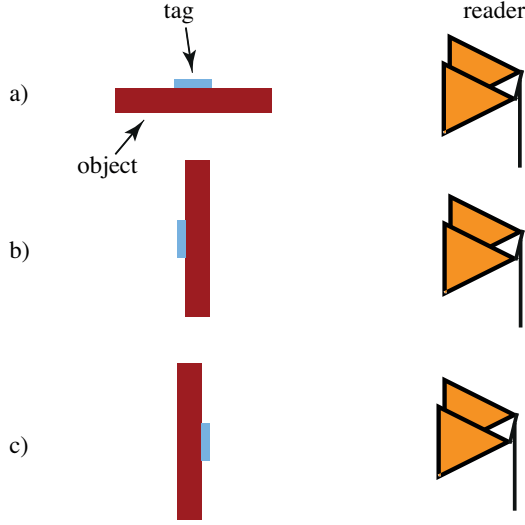


Figure 3.6: a) $\varphi = 0^\circ$. b) $\varphi = 90^\circ$ c) $\varphi = 270^\circ$.

being $H_{\text{tag}}^{\text{B,O}}$ and $H_{\text{tag}}^{\text{B,S}}$ the measured transfer function for an OC and a SC tag respectively. Figure 3.7 shows the tag mean backscattering gain, normalized with respect to the maximum isolated antenna mean backscattering gain, which is defined as follows:

$$G_{\text{tag-ant}}^{\text{Obj}}(\varphi) = \frac{\sum_{i=1}^{N_f} |H_{\text{tag-ant}}^{\text{B,Obj}}(f_i, \varphi)|^2}{\max_{\varphi} \left(\sum_{i=1}^{N_f} |H_{\text{tag-ant}}^{\text{B,Is}}(f_i, \varphi)|^2 \right)} \quad (3.4)$$

where N_f is the overall number of measured frequencies, and where we denoted as $H_{\text{tag-ant}}^{\text{B,Is}}$ and $H_{\text{tag-ant}}^{\text{B,Obj}}$ respectively the backscattered antenna modes related to the isolated antenna and to the tag-object configuration. For a specific configuration, the averaged gain over frequencies in (3.4) is normalized to the maximum gain related to the isolated tag antenna. Fig. 3.6 shows that $\varphi = 0$ corresponds to object plate parallel to the LOS between reader and tag, $\varphi = 90^\circ$ corresponds to when the object plate is perpendicular to the LOS between reader and tag and masks the tag from the reader, while $\varphi = 270^\circ$ refers to this same perpendicular configuration but with the tag directly visible from the reader.

Clearly, looking at Fig. 3.7, the effect of the object differs and depends on the antenna, which is a natural consequence of the difference in the radiation patterns of the isolated antennas. As an example, we consider the polar diagram concerning the DFMS antenna. If we look at the dashed line referring to the isolated antenna, a quite omnidirectional behavior is observable, while an increased directivity is noticed in the presence of the objects, especially with the bottle of water.

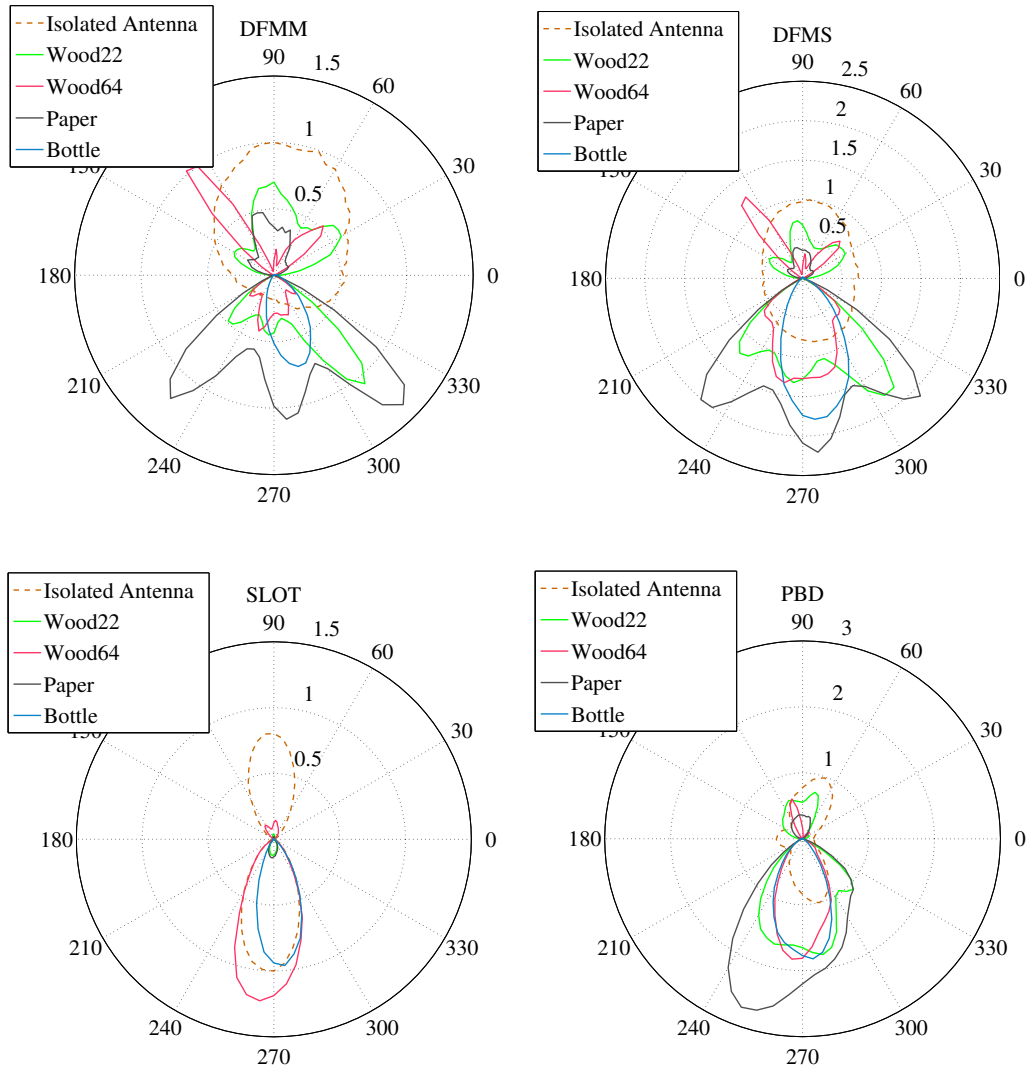


Figure 3.7: Linear normalized antenna mode tag backscattering gain for different antennas in the azimuth plane. The maximum measured isolated Antenna Mode tag backscattering values are in dB: DFMM=-0.94. DFMS=2.31. SLOT=7.99. PBD=5.32.

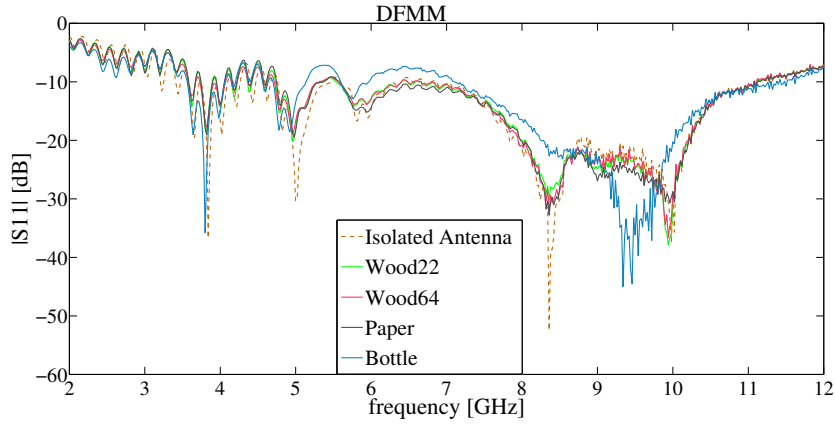


Figure 3.8: $|S_{11}|$ for the DFMM antenna.

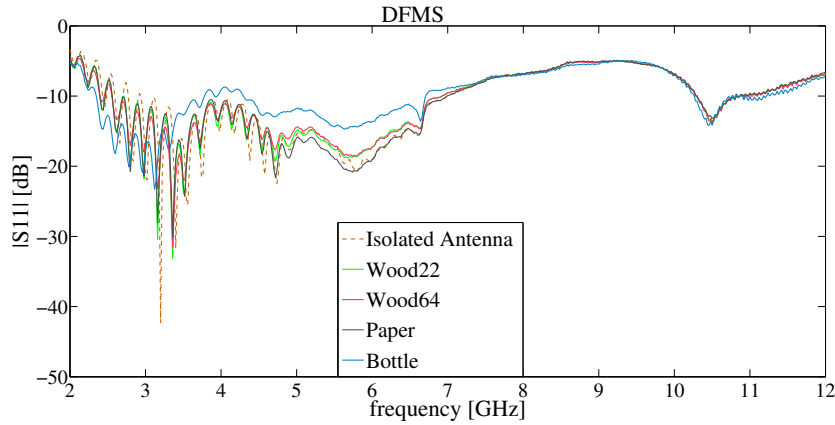


Figure 3.9: $|S_{11}|$ for the DFMS antenna.

The interaction between the antenna and the plate can be envisioned as follows:

- Partial reflection and multiple reflections of the radiated waves with the air-plate boundaries, at the two sides of the plate;
- Partial transmission of the waves.
- Dielectric material acting as a "lens", focusing the radiation in the material direction.
- Diffraction effects at the objects borders.

However these effects occur here in the near field of the antenna, since the distance is below $2D^2/\lambda \sim 96$ mm, where $D \sim 60$ mm) is the diameter of

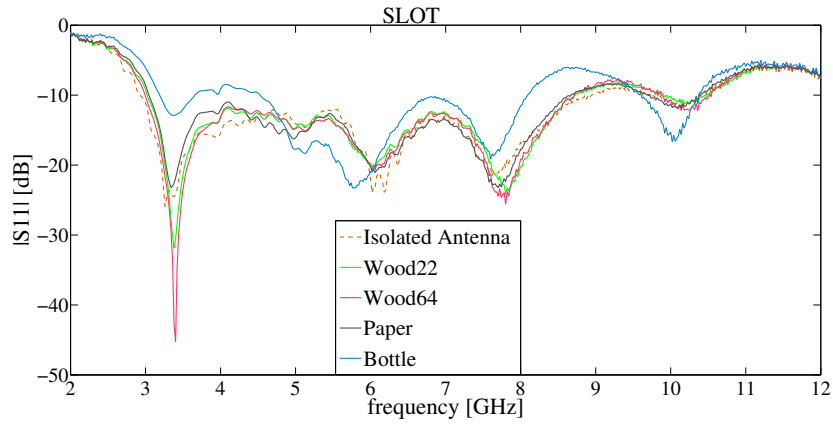


Figure 3.10: $|S_{11}|$ for the SLOT antenna.

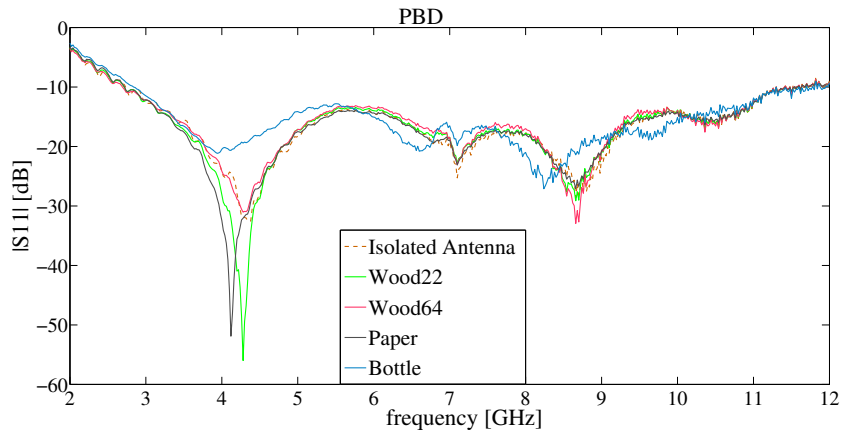


Figure 3.11: $|S_{11}|$ for the PBD antenna.

the smallest sphere containing the antenna and λ is the wavelength (75 mm on average). Due to its spatial extension, the antenna is not exactly a point source, as most of the currents tend to be localized near the feeding points or at borders of the metallic parts of the radiator. In addition, although the plate is fairly large with respect to the antenna size, it is not infinite (e.g. 32 cm of the paper vs a few cm of the antennas). It is, therefore, not possible to describe these effects as a point source radiator in interaction with an infinite plate with parallel boundaries, but we can expect that most of the effects will have somewhat the flavour of this simplistic description. The reflected angles depend on the direction of the incident radiation, and the interference effects will play a role, depending on the wave angles and polarization and on the plate thickness and permittivity.

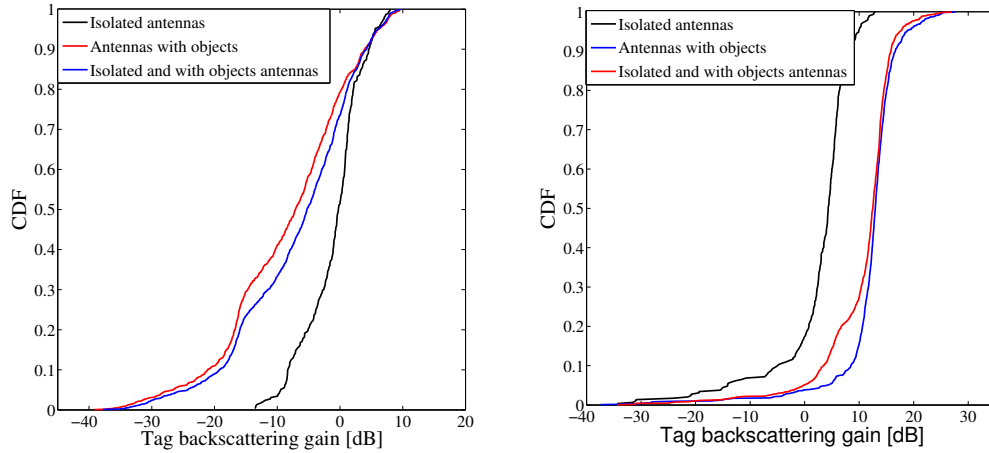


Figure 3.12: Left: Average tag backscattering gain CDFs concerning the antenna mode scattering. Right: Average tag backscattering gain CDFs concerning the structural mode scattering.

For what the bottle of water is concerned, we noticed that its presence greatly increases the antennas' directivity, as indeed liquid objects affect the antenna characteristics (see also Fig. 3.11 which shows the $|S_{11}|$ of the PBD antenna). Near water or other high-dielectric, high-loss material, antenna efficiency decreases because of dielectric loss [126]. Water loss is also exploited in some applications for liquid level detection as in [127], and it is characterized by a high permittivity (i.e. around 80). The reasons for the different EM behaviors are not easy to identify, as the different spatial distribution of the EM near-field can not be predicted easily in a sufficiently detailed way [128].

Figure 3.12 reports the CDFs of the average tag backscattering gain for what concerns the antenna (left) and the structural (right) mode scattering. These distributions highlight two competing effects regarding the backscattering gain in the azimuthal plane under the influence of objects: the structural mode gain is increased and the antenna mode gain is reduced. Overall, the structural mode backscattering is much larger than the antenna mode gain.

In the following section, we investigate to what extent these effects impact the tag detection coverage performance.

3.3 Impact of Tag Backscattering Characteristics on the Detection Coverage

Now that the antenna behavior has been characterized in the presence of a close disturber, it is important to evaluate how the performance is affected in terms of detection and localization coverage. This issue represents also an important link between the study of the signal involved in the backscatter mechanism, with the analysis of the system performance.

Starting from the analysis of Sec. 3.2, we now study how the presence of an object near an UWB tag antenna impacts the capability of a reader to detect this tag, depending on its position and orientation.

3.3.1 Case Study Scenario

The case study considers an RFID scenario in which 4 readers are placed at the corners of a (10×10) m² area. A regular square grid of tag positions every 20 cm (see Fig. 3.13) is used in order to compute the monostatic signal backscattered to each reader, for all orientation angles φ considered in the measurements described of Sec. 3.2. The reader antennas employed for this analysis are Tulip antennas¹, which are quite suitable for UWB RFID applications².

For this kind of analysis, the power backscattered by the tag for each position and orientation has to be determined. We therefore extrapolated H_{tag} for the specific reader-tag distance adopted during measurements (i.e. $d = 2.08$ m) using (2.53), obtaining 73 values of H_{tag} for the 73 measured tag orientations. These values were post-processed to reconstruct the round trip channel transfer function for different distances, again using (2.53). Finally, the received signal was simply expressed as the convolution in time between a transmitted RRC pulse compliant with the EU/FCC mask in the 3 – 5 GHz bandwidth as described in Sec. 1.5.3 and the channel impulse response described above.

We now give the definition used here of a covered point: a point is considered covered if the received SNR overcomes a certain threshold SNR_{th} , which guarantees a reliable tag detection for at least the 75% of orientations. As SNR_{th} we refer to the UWB-RFID system described and analyzed in Chapter 4 and 5, yielding the formula:

$$\text{SNR} = \frac{P_{\text{rx}} \cdot T_{\text{p}}}{K \cdot T_0 \cdot F} \quad (3.5)$$

¹Courtesy of R. D’Errico.

²These antennas were adopted in the European project SELECT [15]

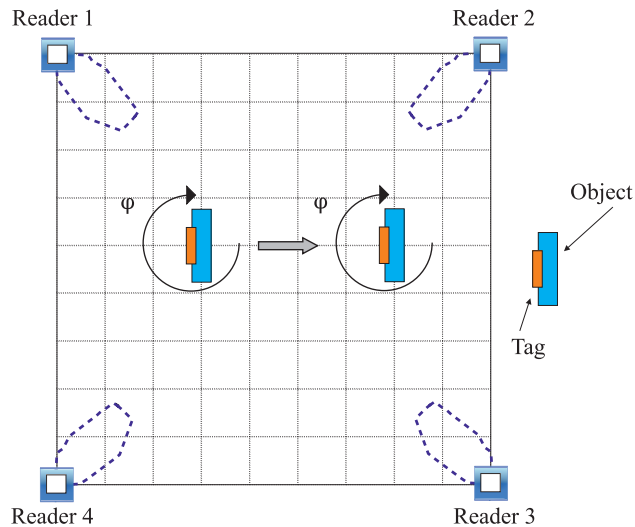


Figure 3.13: Ideal reader antenna (receiving) and tag antenna (transmitting) in LOS.

where T_p is the time frame, K the Boltzmann constant, T_0 the reference temperature and F the receiver noise figure.

We indicate with N_r the minimum number of readers that is required to "see" the tag. For a simple detection event, only one reader is enough, but in order to localize the tag we need at least $N_r = 2$ readers. Unfortunately this leaves some ambiguities³) and $N_r \geq 3$ is a more appropriate requirement.

3.3.2 Simulation Results

We set $T_p = 128 \text{ ns}^4$, $T_0 = 290^\circ\text{K}$ and $F = 5 \text{ dB}$, with $\text{SNR}_{\text{th}} = -25 \text{ dB}$. Note that this SNR_{th} value is directly taken from Ch. 5, where it is showed that it guarantees a good quality of detection. For each point of the grid and for the 73 considered tag orientations, the SNR derived in (3.5) has been evaluated and compared with the detection threshold at the readers. Blue and red points refer respectively to uncovered and covered positions in the map. Fig. 3.14 shows the coverage analysis for the DFMS antenna, for different values of N_r . As can be observed, if we increase (N_r), the coverage in the room becomes less favorable. One of the consequences is that obeying the EU/FCC mask makes the system too constrained to be directly useable, while with a power boost of 10 dB and $N_r \geq 3$, the area is almost entirely

³ $N_r = 2$, means that the tag might be in two points. If one of the points is outside the room, the ambiguity is solved.

⁴This parameter derives from the European project SELECT [15]

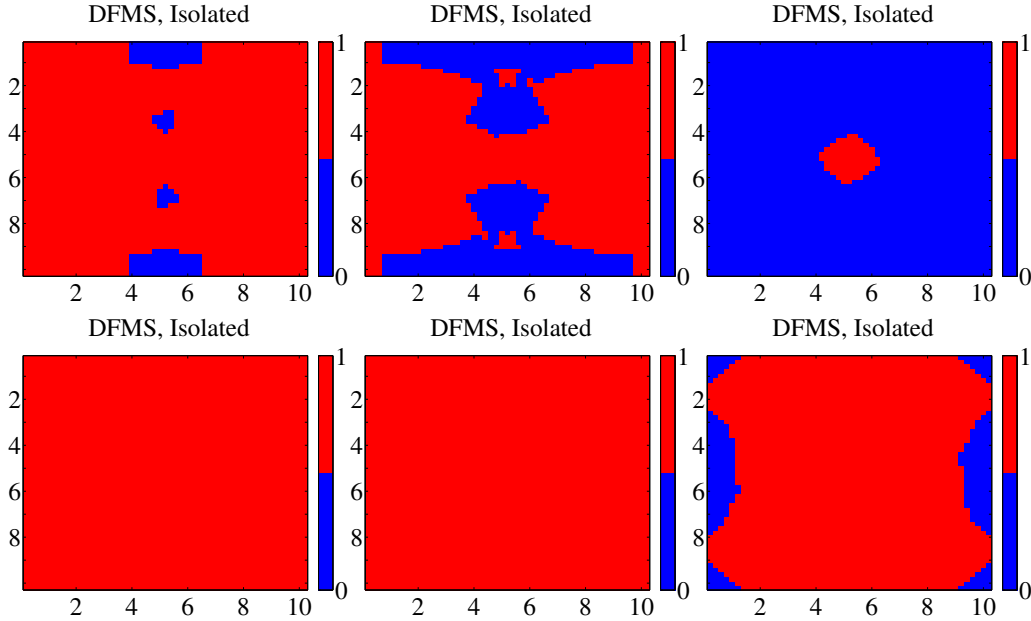


Figure 3.14: Top: Service coverage analysis for $N_r = 1$ (left), $N_r = 2$ (middle) and $N_r \geq 3$ (right). Bottom: same conditions of the top, with a boost of 10 dB in the transmitted power.

covered.

When objects are placed close to the tags, a good detection coverage with $N_r = 1$ is still quite accomplished, as depicted in Fig. 3.15. In general, the increase of directionality does not affect the capability of a tag to be detected by at least one reader. Things greatly change when at least two readers are required to see the tag. Figure 3.16 shows the service coverage analysis for $N_r = 2$, where it is evident how the presence of an object decreases the service coverage in the scenario. In fact, on one hand, the tag's directivity is increased, as shown in Fig. 3.7, with a consequent improvement of the SNR in a few directions, on the other hand, it is more difficult for the tag to be detected by two readers, since the backscattered power is concentrated only in certain directions.

A few solutions can be adopted to counteract this problem. The first is simply to increase the power transmitted by readers (here an increase of 10 dB was considered), which is not currently allowed by most regulations worldwide but might be in the future for certain use cases. The second is to use more than one tag on each object, i.e. to have a robust link budget in all directions. The last solution is to make use of relays, as investigated in [129], which seems to be a promising approach.

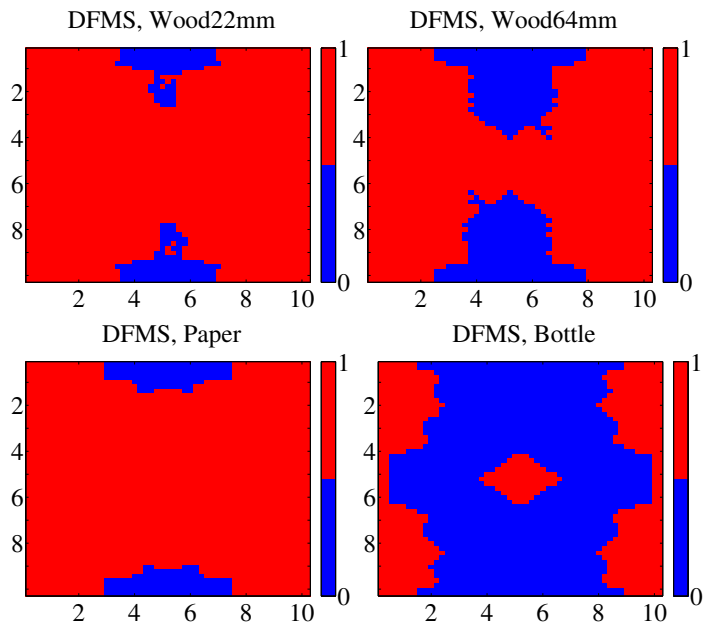


Figure 3.15: Service coverage analysis $N_r = 1$ and $\text{SNR}_{\text{th}} = -25$ dB. Top: DFMS with wood of thickness 22 mm (left) and wood of thickness 64 mm (right). Bottom: DFMS with paper and with bottle of water (right).

Finally, Fig. 3.17 reports the analysis for the other antennas, when $N_r = 2$ and a power boost of 10 dB is adopted. The results are consistent with the ones for the DFMS.

3.4 A Case Study: Tag Interaction with a Perfect Electric Conductor

It is well known that a close metallic reflector may detrimentally affect RFID tag detection, due to the interaction between the antenna and the metal [130–133]. However when a huge bandwidth is considered, such as UWB, the interaction effect is much less known as regards its impact on RFID detection. Given the importance of metal in everyday’s life and its presence in many objects, it is quite relevant to investigate this impact, which is the goal of the present section.

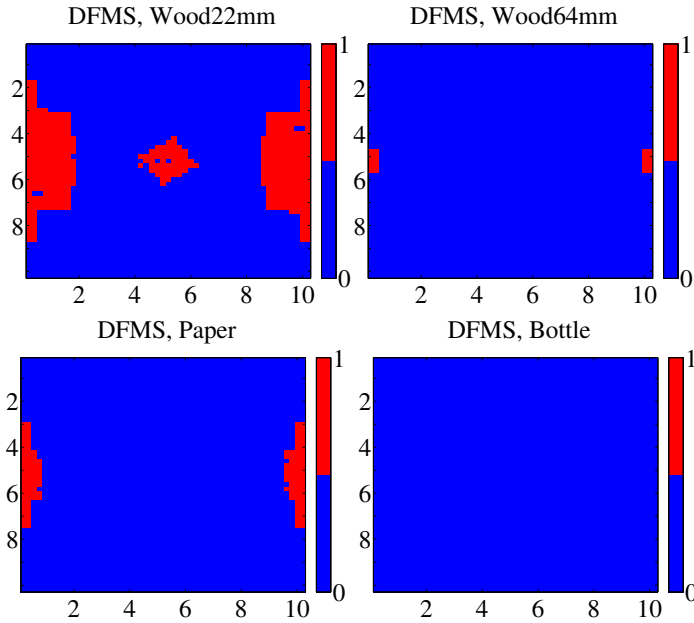


Figure 3.16: Service coverage analysis $N_r = 2$ and $\text{SNR}_{\text{th}} = -25$ dB. Top: DFMS with wood of thickness 22 mm (left) and wood of thickness 64 mm (right). Bottom: DFMS with paper and with bottle of water (right).

3.4.1 Antenna Backscattering Measurements in Presence of Metal

For an investigation of the interaction between an UWB RFID antenna and a close metallic reflector, the backscattered signals of three different UWB antennas, a DFMS, a DFMM and a thick UWB dipole (all fabricated at ENSTA-ParisTech and shown in Fig. 3.18), were measured inside an anechoic chamber in the presence of nearby metallic plates placed at different distances behind the tag.

Two Horn Lindgren 3117, placed in a quasi monostatic configuration and separated by 15 cm in order to guarantee a sufficient isolation between transmit and receive channels, were employed as reference antennas (reader) at a distance of 1.54 m from the tag. Three different loads ($Z_L = 0$, $Z_L = 50 \Omega$ and $Z_L = \infty$) were connected to the tag through a switch, via a delay line intended to temporally discriminate the structural and the antenna mode scattering. The measurements were performed in the frequency domain in the band 2 – 12 GHz, by means of a vector network analyzer. The tag, mechanically supported by a vertical post, was rotated from $\varphi = -180^\circ$ to $\varphi = +180^\circ$ with a step size of 5° . Two metal plates of dimensions $(5 \times 5) \text{ cm}^2$ and $(10 \times 10) \text{ cm}^2$ were alternatively positioned behind the antennas at a

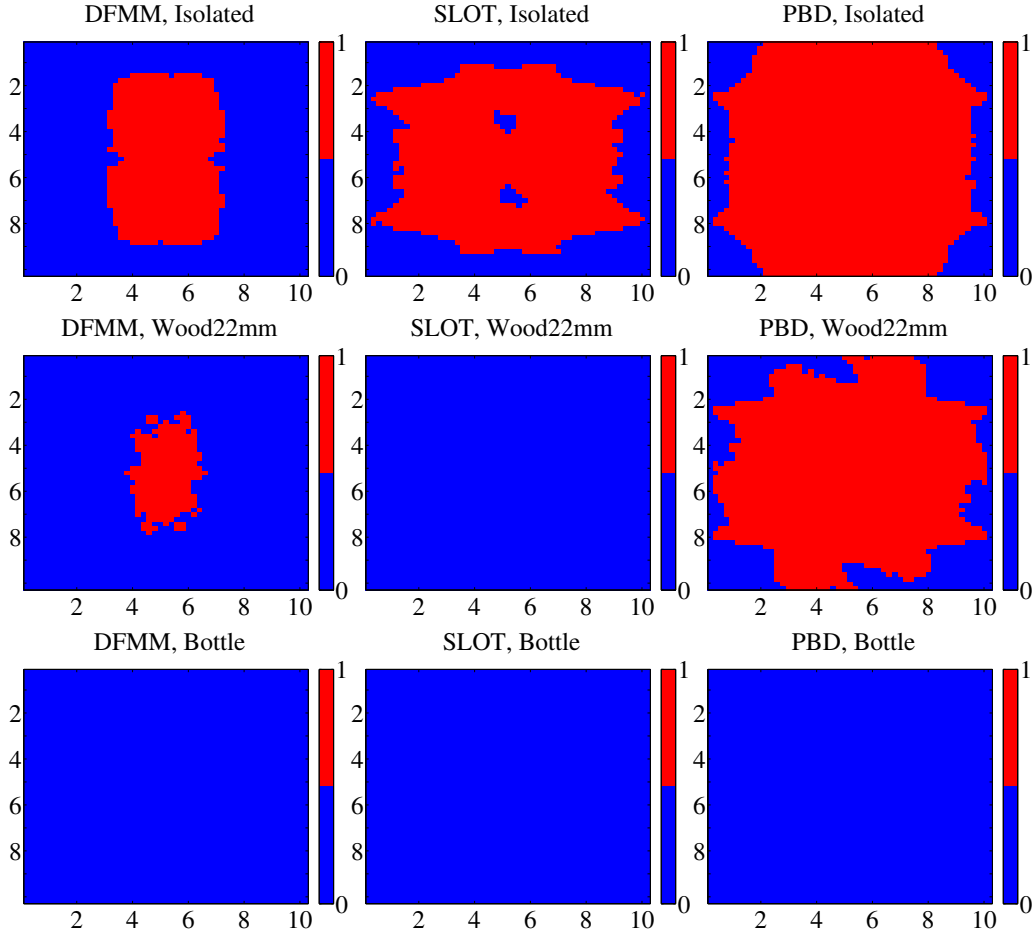


Figure 3.17: Service coverage analysis for $N_r = 2$ (middle) and power boost of 10 dB. Top: Isolated antennas. Middle: Antennas with wood of thickness 22 mm. Bottom: antennas with bottle. DFMM (left), SLOT (middle) and PBD (right).

distance of 1 cm. Figure 3.19 reports the measured UWB thick dipole with a metal plate of dimensions $(5 \times 5) \text{ cm}^2$.

In Fig. 3.20 the round trip channel transfer functions measured for the DFMS in presence or absence of a metal plate and connected to three different load conditions are shown. The results refer to the reader-tag orientation in the condition of maximum radiation, when the backscattered signal received from the tag is the strongest. In particular, a phase difference is clearly observed between the OC and SC load.

The signal peaks are higher for a metal plate placed 1 cm behind the tag (upper plot) than for an isolated antenna (lower plot). This is a somewhat surprising result, in that we commonly expect the metal to act as a short

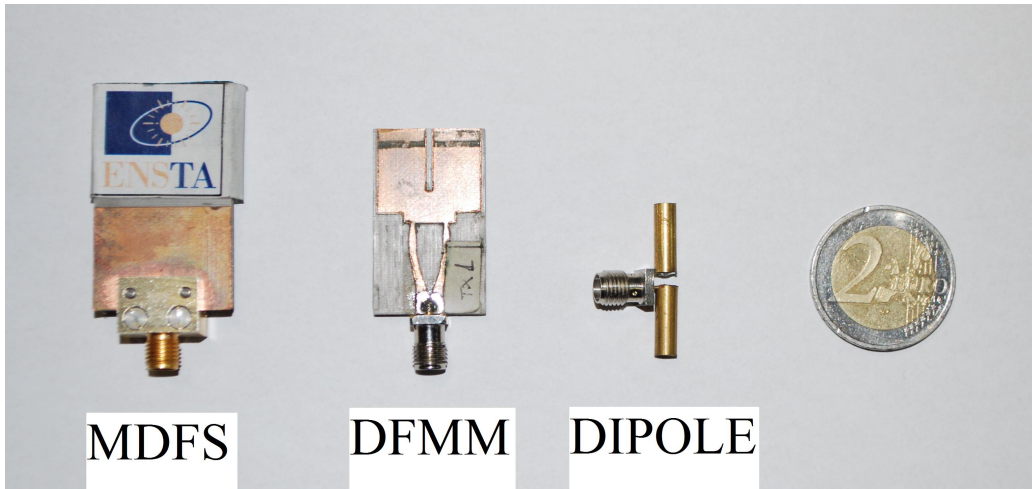


Figure 3.18: Measured antennas in presence of a metallic reflector.

circuit since the electric field vector is parallel to it. Actually, the situation is more complex than this simple view, due to the finite interaction distance and the finite antenna size, and also to the non unique wavelength in UWB signals. From the observed results, both the metal size and its distance to the antenna center are thus important parameters. We also expect ringing effects and metal plate diffraction to play a role in this phenomenon. This effect will be deeper investigated in the following section, showing simulation results.

3.4.2 Simulation of the Antenna Backscattering

Equation (2.53) expresses the round trip channel transfer function for passive UWB RFID, showing the contribution of the backscattered tag signal in $H_{\text{tag}}^{\text{B}}(\hat{\mathbf{r}})$. Furthermore, with this relation it is possible to link the simulated electric fields with the measured round trip channel transfer function. We simulated the DFMM and the thick dipole in the same frequency band as measurements, respectively 2 – 12 GHz and 4 – 4.8 GHz, every 5° over the azimuth. An absorber was similarly placed around the DFMM feeder to limit common mode currents, as shown in Fig. 3.21 in the left.⁵

Furthermore, also a planar UWB dipole between 3 and 13 GHz was simulated in order to analyze its backscattering response [134, 135].

With the tool Wipl-D, the backscattered signal of a planar dipole has been simulated with metallic objects of different shape and dimension positioned

⁵The antenna is a courtesy of R. D’Errico [134]

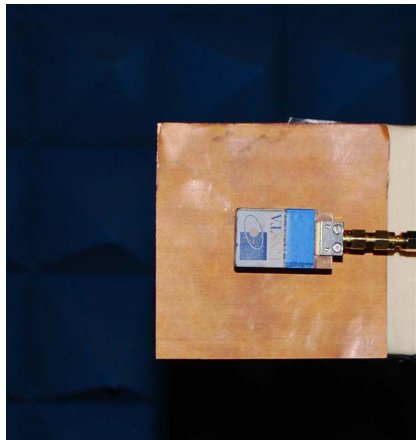


Figure 3.19: UWB thick dipole in the presence of a metal plate with dimensions $(5 \times 5) \text{ cm}^2$.

at 1 cm behind it. In particular, two metal plates of dimensions $(5 \times 5) \text{ cm}^2$ and $(10 \times 10) \text{ cm}^2$, identical to measured ones were adopted, together with a metal can as shown in Fig. 3.22. The system was tested in the frequency range 3 – 13 GHz. Figure 3.23 reports the simulated results. They still refer to the reader-tag orientation in the condition of maximum radiation when the backscattered signal received from the tag is the strongest, which corresponds to the normal to the metallic plane and antenna. Again, the antenna backscattering mode is obtained by connecting the tag alternatively to an OC and SC loads.

These results unambiguously confirm the increase of the received signal amplitude with respect to the isolated antenna, when a metallic object is placed behind it (Fig. 3.23). A planar reflector is, of course, more favourable to backscatter the incident field towards the same incident direction, and still for this situation a bigger plate seems to provide stronger signals. These unexpected results may lead to further studies on how the dimensions of the reflector may affect the backscattered signals.

Average Backscattered Energy Over the Azimuth Plane

Backscattering normally to the (planar) antenna and the planar metallic plate is obviously a highly particular case and it can be suspected that specific interference and directionality effects can explain the signal increase. Indeed, in the antenna mode the tag backscattered radiation is obviously affected by the metallic plate reflection towards the reader. For a more complete assessment, we show in Fig. 3.24 for the measured DFMS the monostatic backscattered pulse energy in the antenna mode, averaged over the

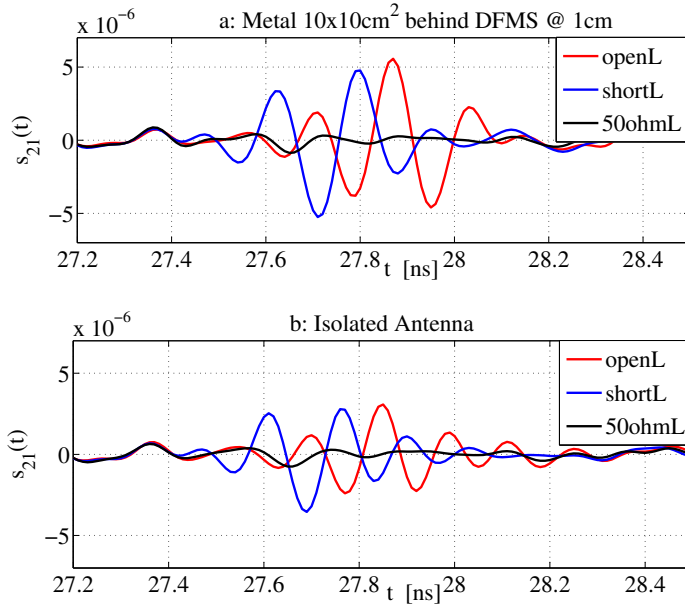


Figure 3.20: Top: Measured Antenna mode scattering with $10 \times 10 \text{ cm}^2$ metal placed 1 cm behind the DFMS. Bottom: isolated antenna case.

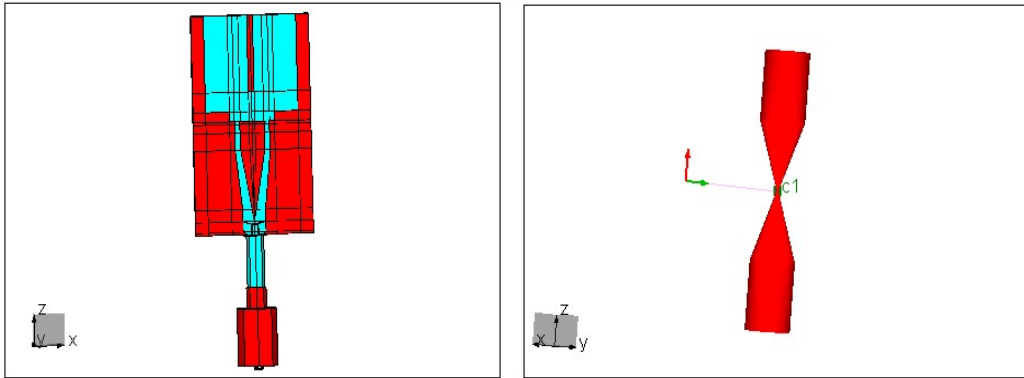


Figure 3.21: Left: simulated DFMM. Right: simulated thick broadband dipole.

whole azimuth plane (360°). This (normalized) energy is defined for each backscattering direction as the integrated squared impulse response over the pulse duration:

$$E = \int |S_{21}|^2 dt \quad (3.6)$$

In particular, Fig 3.24 for the measured DFMS antenna shows that even for the average energy, the metal reflector results in an increase with respect

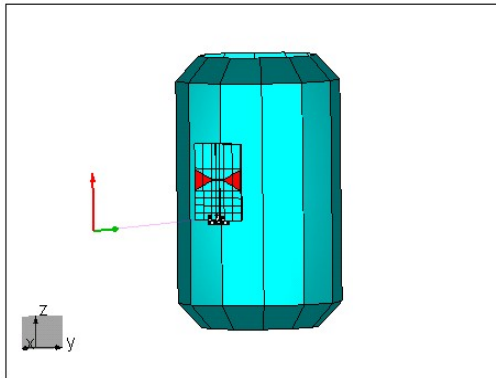


Figure 3.22: Metal can placed behind the planar UWB dipole.

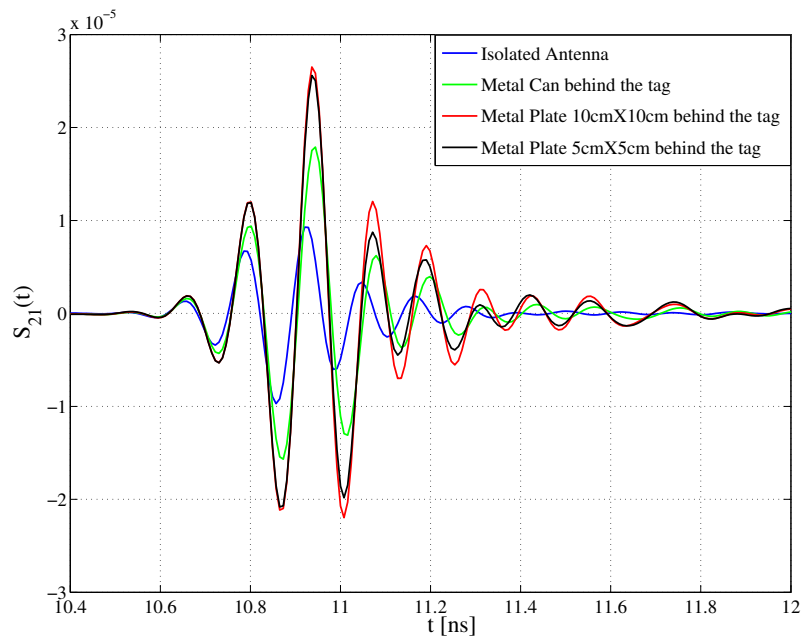


Figure 3.23: Simulated antenna mode scattering for the planar dipole.

to the isolated antenna. Not surprisingly, a bigger metal reflector is more favourable than a small one, especially for larger distances. It also appears that the distance between the metal reflector and the antenna center affects the average energy in a non monotonous way according to the distance, as shown in Fig 3.24. Given the wide band involved in this effect, too simple - wavelength based - considerations about the distance between the metal reflector and the tag antenna need be cautiously applied.

In Fig. 3.25 and 3.26 we report results obtained by simulations in com-

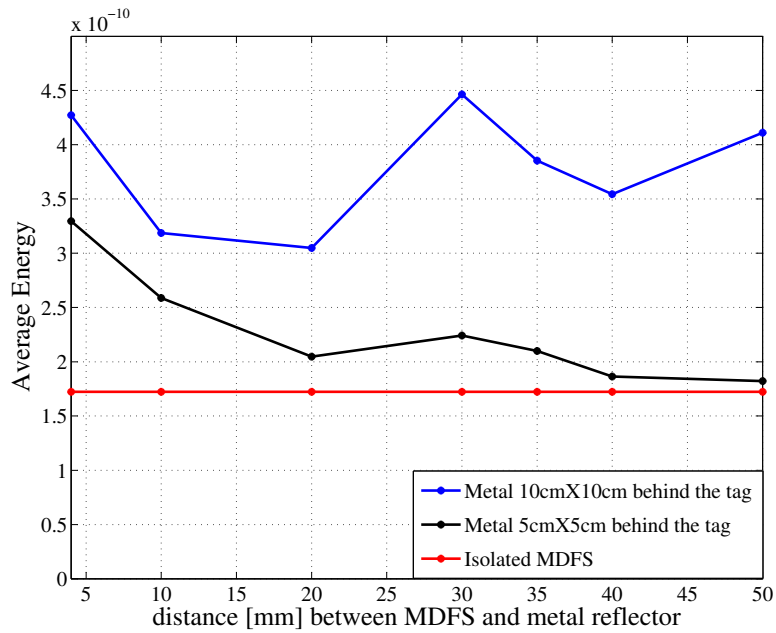


Figure 3.24: Average backscattered energy over the azimuth plane (measured DFMS).

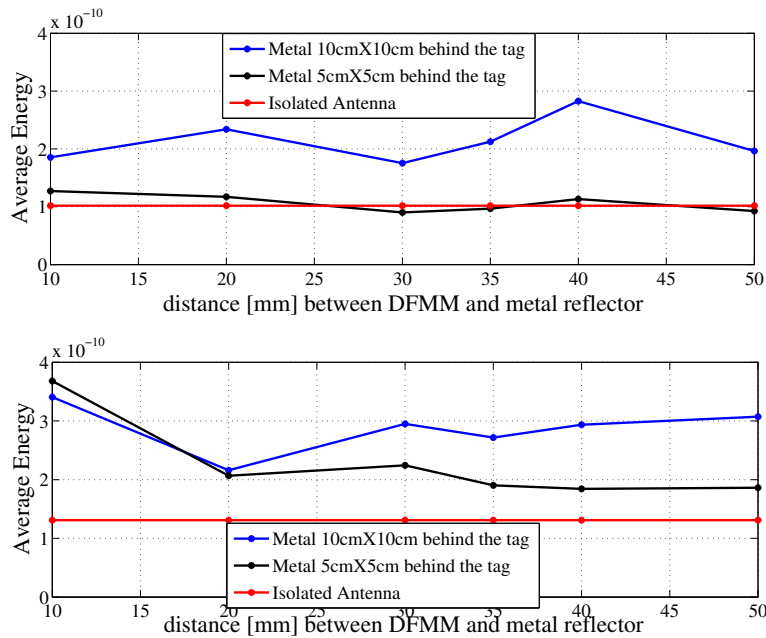


Figure 3.25: Top: Simulated average energy over the azimuth plane for the DFMM. Bottom: Measured average energy over the azimuth plane for the DFMM.

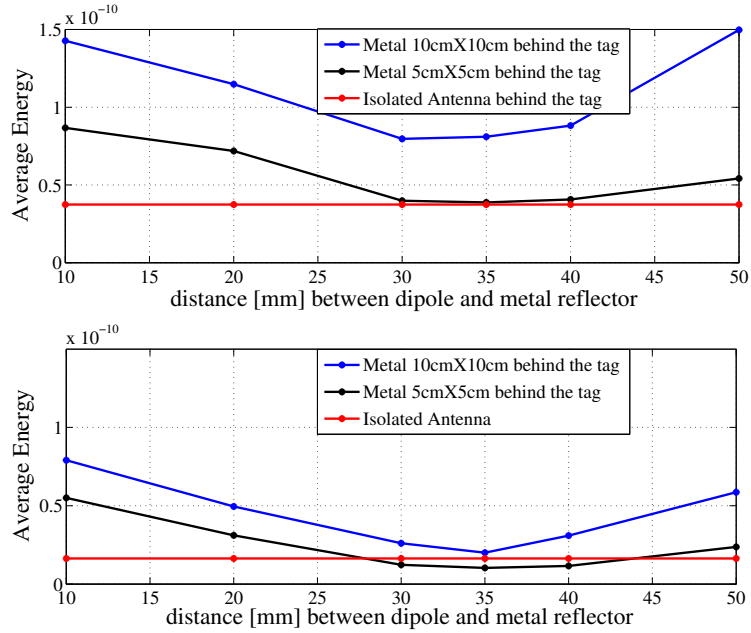


Figure 3.26: Top: Simulated average energy over the azimuth plane for the dipole. Bottom: Measured Average energy over the azimuth plane for the dipole.

parison with measurements (in relative units). In order to account for the true loads, which are neither pure SC nor pure OC due to the switch and the cables, the latter were calibrated and injected into the simulation by post-processing. Remaining errors may stem from the uncalibrated DFMM connector in the simulation. Anyway the main goal here is to show a qualitative agreement between measurements and simulations, as regards the increase of average backscattered energy by the presence of metal.

In Fig. 3.26, we note that the magnitude of results differs by almost a factor 2 between measurements and simulations. Various reasons may explain this discrepancy, such as a partial masking of the antenna by the mechanical support in some azimuth angles. However in all cases, the presence of the metal plane indeed increases the backscattered average energy. A fairly good agreement, at least qualitatively and in terms of distance dependences, is in particular seen for the dipole.

3.5 Total Backscattered Energy in Presence of Metal

We then performed in bistatic the simulation of the thick dipole backscattering response over 120 values of the azimuth angle over 360° and 61 values of the elevation plane over 180° , under an excitation (1 V/m incident wave amplitude in vertical polarization) considered only on the direction of the main lobe [100] (see Fig. 3.28 on the right). We simulated this antenna, both alone and with a metal plate of size $(3 \times 6) \text{ cm}^2$ (chosen for its dimensions comparable with the antenna size), $(10 \times 10) \text{ cm}^2$ and $(20 \times 20) \text{ cm}^2$ behind it at different distances, as shown in Fig. 3.21 on the right. The distance between the tag and the plates have been varied from 0.5 cm up to 5 cm every 0.5 cm. For each distance, the dipole was successively connected to an OC and a SC load and the antenna backscattering response was simulated.

The total backscattered normalized power flux (NPF) in bistatic mode is reported in Fig. 3.28. It is evaluated by integrating the Poynting vector

$$P = \frac{|E_{\text{back}}|^2}{2\eta} \quad (3.7)$$

over the sphere, where E_{back} is the backscattered field at a given distance, and then normalizing it with respect to the total backscattered power flux of the isolated antenna.

From this plot we again confirm the increase of the backscattered power flux, which is strictly related to the dipole/metal reflector distance. Consider the two distances $d = 34 \text{ mm} = \lambda/2$ and $d = 17 \text{ mm} = \lambda/4$ in the direction of the excitation wave. For what the former is concerned, in this case the reflected signal is in phase opposition with the incident wave. Consequently, the tag receives a small amount of energy in its antenna mode and thus we obtain a minimum for the total backscattered power. On the contrary, considering the latter, for $d = 17 \text{ mm} = \lambda/4$, the two waves are in phase, thus the amplitude of the backscattered signal is summed up, giving a power gain factor of even more than 4 as it is partly shown in Fig. 3.28.

From the previous results, it seems that the presence of a metallic plate is a favorable factor which increases the backscattered energy. But it is far from being like this. In fact, looking at the 2-D and 3-D patterns averaged over frequencies shown in Fig. 3.27, it comes out that the antenna directivity is increased since the metal is acting as a reflector, and for many directions the backscattered power is far from being the same as for the isolated antenna. This effect is better analyzed in the next section, where the detection and localization coverage are evaluated in 2-D, in order to assess how the metal plate impacts the reader-tag link.

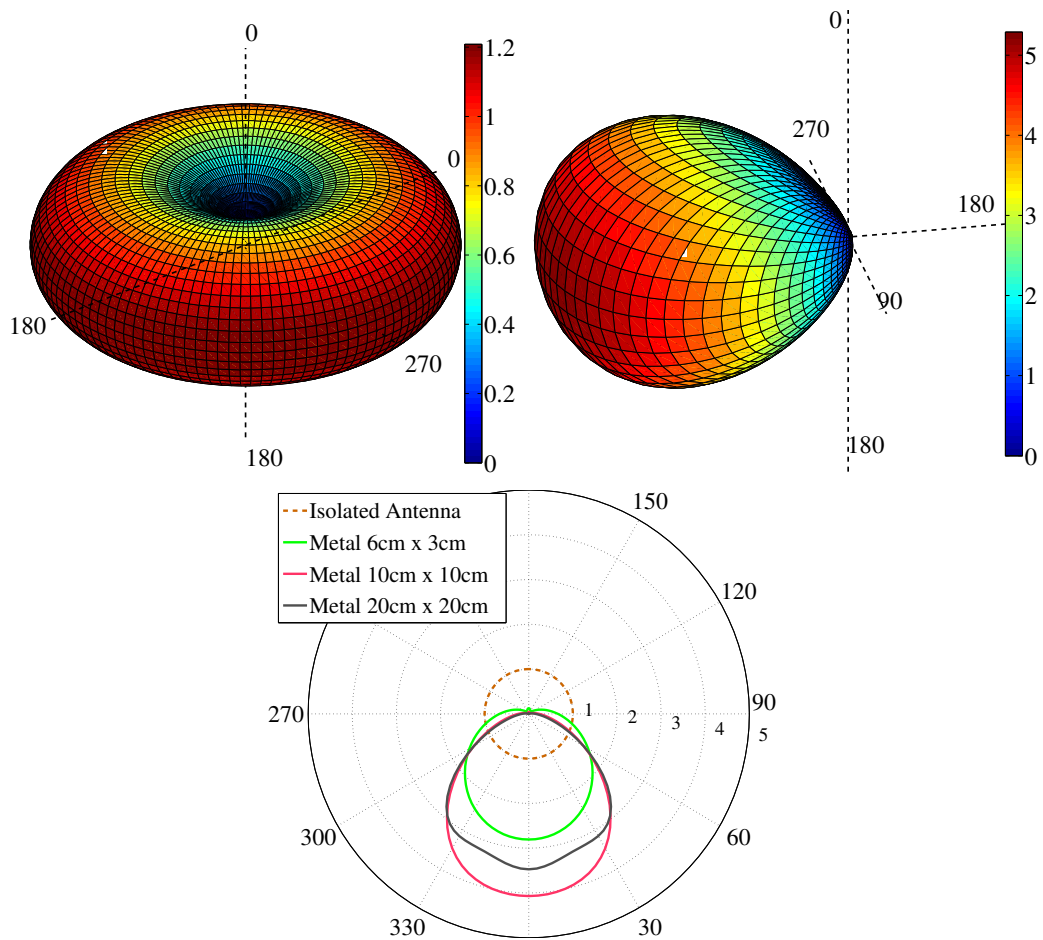


Figure 3.27: Top: 3-D mean realized gain for isolated dipole (left) and with a plate ($10 \times 10 \text{ cm}^2$) behind (right). Bottom: mean realized gain over the azimuth plane for isolated dipole and in presence of metals.

To confirm the negative effect of the metal, we finally excited our system dipole-metal in all the 3-D directions previously considered, evaluating for each excitation the backscattered power flux. We then averaged these powers, obtaining the results reported in Fig. 3.28 on the right, which clearly shows how much the presence of the metal affect the backscattered power flux. Note that after 2 cm, there is a moderate dependency between the distance.

3.6 Conclusions

The interaction between passive UWB RFID antennas with close disturbers has been addressed in this chapter, basing the analysis on measurements. In

particular, it has been shown how the radiation characteristics are greatly affected by the presence of the object, and the measured data has been exploited to validate the detection and localization coverage using parameters and data of Chapter 4 and 5.

Then, the particular case study of the interaction between a tag and a close metallic reflector has been investigated. It has been shown that the average backscattered energy in the monostatic antenna mode, and the total backscattered power (in bistatic mode, when the system is excited in the direction of maximum radiation) are increased in the presence of a metallic object placed at close distances. This effect counters simple intuition and combats the well known belief for UHF-RFID that metals are detrimental to the RFID detection range. It likely results from a combination of very wide band effects. On the contrary, when the bistatic power flux is averaged over the sphere, the detrimental effects of the metal plate have been clearly demonstrated. Further studies need be carried out, for example, by analyzing the respective roles of the tag antenna and the reflector.

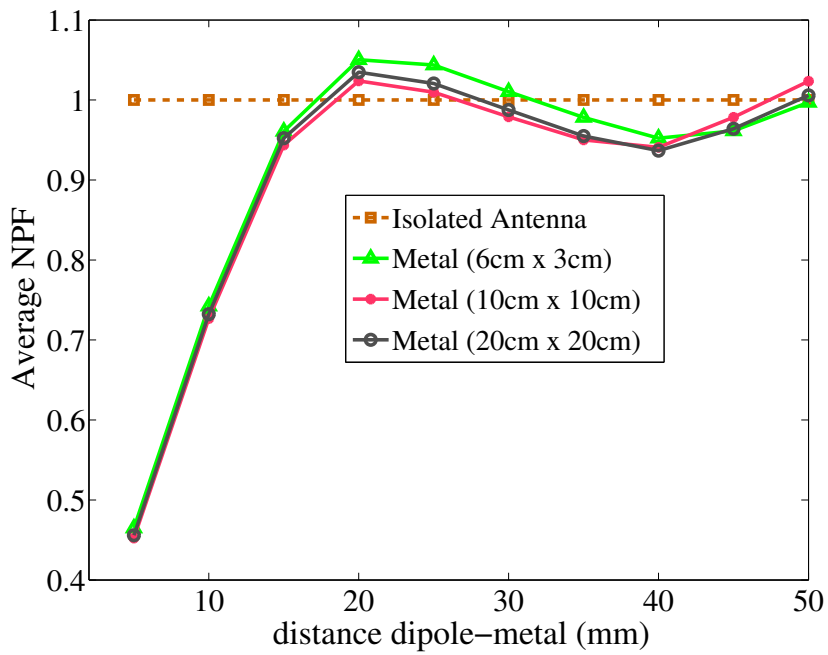
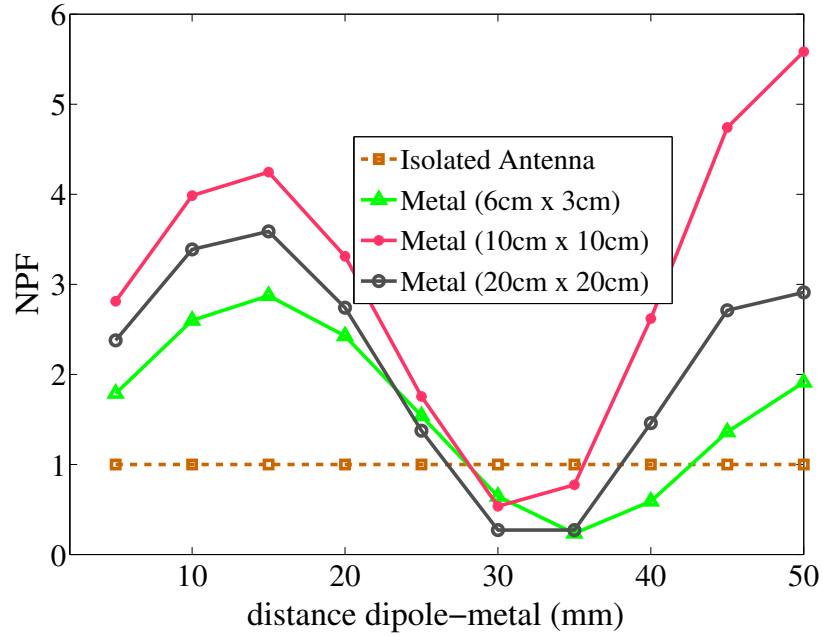


Figure 3.28: Left: total backscattered power over the sphere vs tag/metal plate distance. Right: Average 3D power flux.

Chapter 4

UWB RFID System Architecture and Implementation Issues

4.1 Introduction

In the previous chapters, the tag antenna backscattering has been analyzed in different configurations, both in ideal and realistic conditions. Then, the interaction of a UWB antenna with a close disturber has been characterized, as it usually happens in RFID working conditions. The obtained results were adopted in order to evaluate the detection and localization coverage in a $(10 \times 10) \text{ m}^2$ cell. As anticipated, a proper design of a reader-tag signaling scheme based on the modulation of the backscattered signal requires the knowledge of the backscatter mechanism. In addition, measured data can be included in simulations to test the system performance. Now the study moves to the analysis of a UWB RFID robust architecture based on the modulation of the backscattering signal, which is able to guarantee a reliable reader-tag communication and a proper tag detection.

We investigate here some of the issues that arise when such a system has to be designed under real HW constraints according to the objectives of the european project SELECT. In this chapter, the reader-tag signaling structure is described, the clock drift problem and the quantization issue are presented, and a system architecture for mitigating the presence of multi-tag interference and of strong clock drift is addressed, jointly with the investigation of different spreading code design strategies. Processing schemes and performance of such a system are then detailed in Chapter 5 and 6.

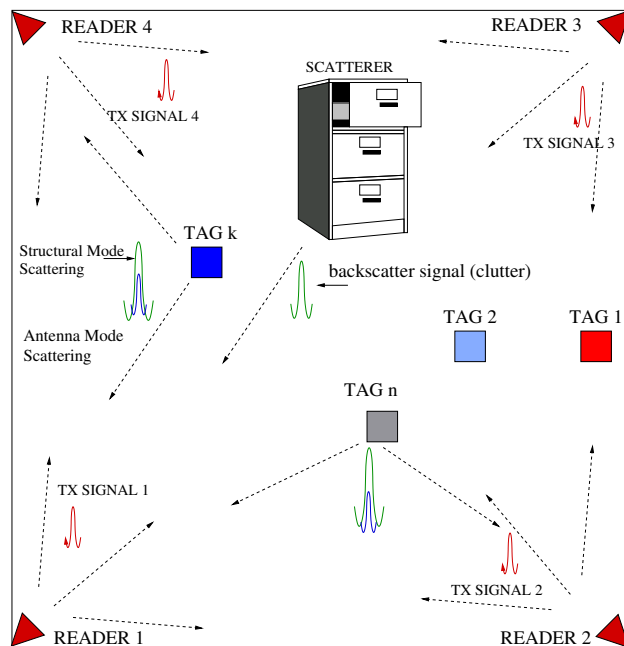


Figure 4.1: Multi-reader scenario with N_{tag} tags.

4.2 System Design

When extremely low-power consumption tags are required semi-passive tags represent one of the most promising solution. In semi-passive tags using backscatter modulation, the energy available from harvesting or batteries is used only for memory access or modulation operation without powering an active transmitter. The high accuracy estimation of the TOA from the backscatter signals enables accurate localization of tags in addition to their detection [11, 12, 136]. Figure 4.1 shows an example of a scenario (cell) composed of 4 readers monitoring a square room, where each reader interrogates N_{tag} tags located in the same area through the emission of an UWB interrogation signal specific of each reader. To save energy, tags are normally in sleep state and are woken up through the transmission of a wake-up signal (e.g., an unmodulated UHF carrier). Then all tags reflect the incoming UWB signals by means of backscatter modulation according to their own code and their internal information bit. As will be detailed in the next section, signals backscattered by different tags and originated by different readers can be distinguished through spreading codes applied to the transmitted and reflected signals at the reader and tag, respectively. Several issues arise due to the presence of clutter (the signal backscattered by the environment), multi-tag interference, tag clock drift, and the poor link budget for to the two-hop

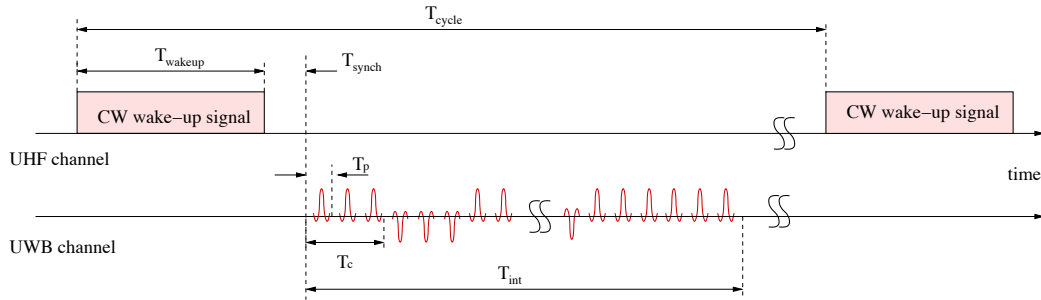


Figure 4.2: Reader UHF and UWB transmitted signals.

link. These issues have been partially and separately investigated in the literature [14, 94, 137, 138].

4.3 Reader Transmitted Signal Format

In a semi-passive UWB-RFID system based on backscatter modulation, the reader is the only active device capable of transmitting and receiving signals, since tags act as reflectors, as will be detailed in Sec. 4.4. After the transmission of the wake-up signal (e.g., in the UHF band), the reader starts sending the UWB interrogation signal, as reported in Fig. 4.2

In Fig. 4.3 the symbol structure, related to the reader's transmitted interrogation signal, is reported. Specifically, a symbol time T_s is composed of N_c chips, of duration T_c , each carrying N_{pc} pulses.

According to a direct-sequence multiple access scheme, we consider these chips modulated by an antipodal binary spreading sequence $\{d_n\}$ of length N_c chips specific for the reader (reader's code). In particular the transmitted interrogation signal is given by

$$s_{\text{reader}}(t) = \sum_{m=0}^{N_r-1} s(t - mN_cT_c) \quad (4.1)$$

where N_r is the number of symbols, of duration $T_s = N_cT_c$, composing an interrogation cycle, and with

$$s(t) = \sum_{n=0}^{N_c-1} d_n g(t - nT_c) \quad (4.2)$$

and

$$g(t) = \sum_{i=0}^{N_{pc}-1} v(t - iT_p) \quad (4.3)$$

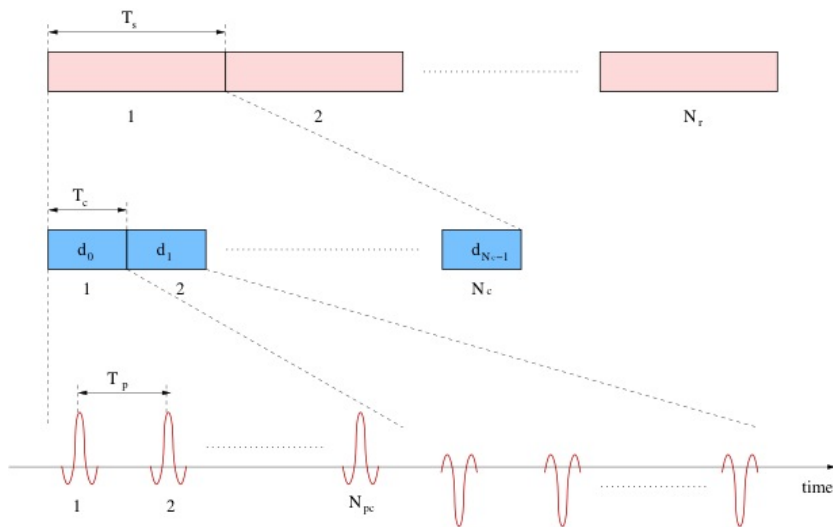


Figure 4.3: The UWB interrogation signal structure.

indicating the waveform associated to each chip. This waveform is composed of N_{pc} elementary UWB pulses, centered at frequency f_c and with bandwidth W , each of energy $E_p = \int_0^{T_p} v^2(t) dt$. The pulse repetition period (PRP) T_p is chosen so that all backscattered signals are received by the reader before the transmission of the successive pulses thus avoiding inter-frame interference. Moreover, the pulse energy E_p and the PRP T_p are chosen to guarantee a radiated spectrum emission compliant with the regulation mask in terms of EIRP [57].

After the transmission of each pulse, the reader's receiving section (see Fig. 4.4 for an example of a complete reader receiver structure) collects the backscatter response from the tags located in the environment, as well as the environment response (i.e., the clutter) in order to detect the intended tag as will be detailed in the next section.

4.4 Tag Backscatter Modulation

As reported in Sec. 4.3, when adopting backscatter modulation, the reader interrogates a tag through the wireless channel in order to obtain data stored on it. The tag sends its information back to the reader by a simple modulation of the backscatter signal through proper variations of the load connected to the tag antenna [12, 14]. As described in the previous chapters, the tag's response is composed of the structural mode scattering and the antenna mode scattering. Figure 4.5 shows the structure of the tag where antenna

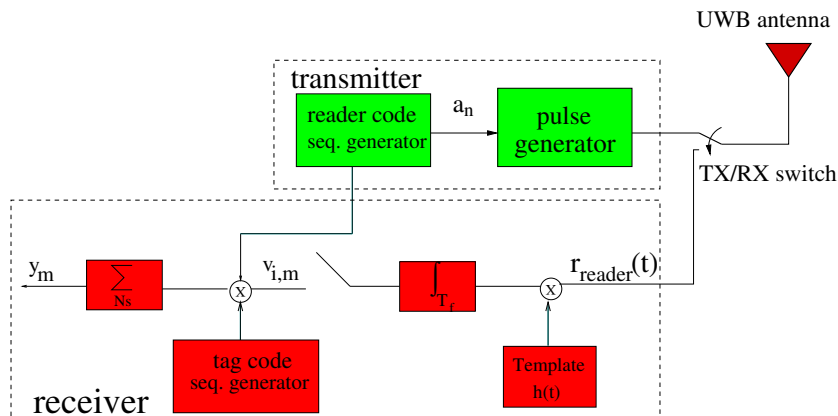


Figure 4.4: Example of reader internal structure.

backscattering properties are changed by varying the antenna load using an UWB switch. Specifically, the switch connects the antenna to two different loads, according to a modulating signal $m(t)$. When an OC and SC are adopted as antenna loads, the resulting modulation corresponds to a phase inversion of 180° of the backscattered pulse polarity (i.e., a binary phase shift keying (BPSK) modulation).¹ To make the uplink communication between the k th tag and the reader robust to the presence of clutter and interference as well as to allow multiple access, each tag is designed to change its status (short or open circuit) at each chip time $T_c = N_{\text{pc}} T_p$, according to an antipodal tag's code $\{c_n^{(k)}\}$, for $n = 0, \dots, N_c - 1$, and to the information bit $\{b_m^{(k)}\}$, for $m = 0, \dots, N_r - 1$.² More precisely, $b_m^{(k)}$ is the antipodal data value of user k related to its m th symbol, associated to N_s pulses, with symbol time T_s , as will be detailed in Sec. 4.6. Thus, the modulation due to the data symbol is constant over N_s pulses.

Note that, in this semi-passive tag design, the battery embedded in the tag is not used to power-up the tag for signal transmission, but only to feed other circuitry related to control logic and memory, and to change the backscatter switch status, as depicted in Fig. 4.5. Different embodiments can be foreseen to get sufficient energy. Thanks to the extremely low-power consumption of this architecture, energy harvesting techniques can be adopted instead of batteries.

¹However, non-idealities related to the adopted switch may affect the pulse polarity, reducing the cross-correlation between the received waveforms for the two different loads.

²Provided that the total number of pulses per symbol $N_s = N_c N_{\text{pc}}$ is the same at reader and tag side, we assume for convenience of notation the same values N_{pc} and N_c for both tags and reader's code.

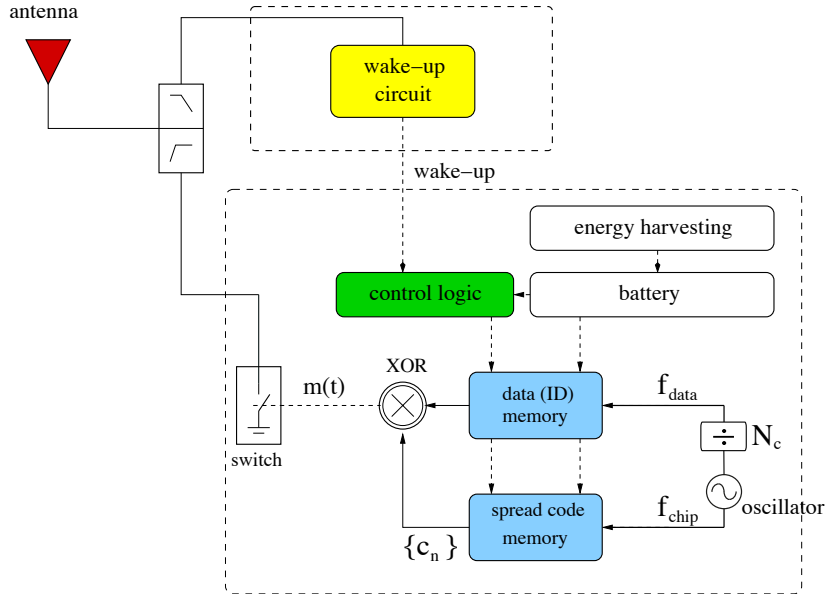


Figure 4.5: Tag internal structure.

In order to save energy, tags are usually maintained in sleeping mode, and they are woken up once the reader starts its interrogation phase. The wake-up signal emitted by the reader enables powering up the wake-up circuit in the tag which itself powers up a control circuit that, once the transmission of the CW signal has ended, activates the switching procedure controlled by the digital logic. The tag clock is generated by means of an oscillator at frequency $f_{\text{chip}} = 1/T_c$, that has to cope with the stringent frequency (both accuracy and drift) requirements. For this purpose, a quartz crystal-based oscillator represents an appropriate solution to overcome such limitations.

Note that the frequency f_{chip} is necessary to produce the timing for the spreading memory, while for the data memory a frequency $f_{\text{data}} = 1/T_s$ is required.

4.5 Design Issues

In this section, some of the issues that have to be faced for a proper system design are detailed. In particular, as several readers and tags have to access the channel at the same time, it is important that a robust synchronization

procedure among all the devices is guaranteed. Once the synchronization has ended, residual offsets and the presence of strong tag clock drift have to be counteracted, as they could be detrimental for a proper reader-tag communication. In addition, if not accounted, the multi-reader interference might represent a serious problem for the analog-to-digital converter (ADC), as it is many dBs higher than other signals, and for the general degradation of the performance.

4.5.1 Synchronization Procedure

There are two synchronization procedures that have to be accomplished: the inter-reader synchronization, and the tags wake-up procedure, as usually they are in sleeping state in order to save energy.

For what the former is concerned, it can be achieved through the combination of Ethernet message exchanges (coarse synchronization), and TOA estimate of UWB signals transmitted by each reader. Since the direct link between readers is much more favorable than the reader-tag signaling (see Sec. 4.5.2), the accumulation of N_s pulses guarantees that synchronization among readers can be kept in the order of a few ns, using conventional TOA estimation techniques [11].

Once readers synchronization has been performed, tags wake-up procedure can start. In order to save energy, tags are usually maintained in sleeping mode, and they are woken up once the reader starts its interrogation phase. The wake-up can be obtained by the adoption of a UHF CW signal emitted by the reader as reported in Fig. 4.2, which enables powering up a UHF circuit in the tag (see Fig. 4.5) by charging a capacitor via antenna and a rectifier circuit. The resulting voltage is used to power up a control circuit that, once the transmission of the CW signal has ended as shown in Fig. 4.6, activates the switching procedure controlled by the digital logic that is powered by the battery embedded in the tag. The backscatter modulation is then enabled and the antenna load alternates according to the sequence $\{c_n\}$ and optional information symbol $\{b_k\}$. Thus, the propagation-loss dependent charging time³ of the capacitor does not induce a jitter for the starting time of the modulation, since the discharge is not affected by the pathloss and its start does not depend on the positions and orientations of the tags.

In addition, the wake-up procedure keeps the system complexity affordable, as the system becomes quasi-synchronous once the wake-up process has ended. Operating in this way, code generators at tags and reader side are

³This is due to the narrowband UHF signals that may experience selectively channels, and to different reader-tag distances.

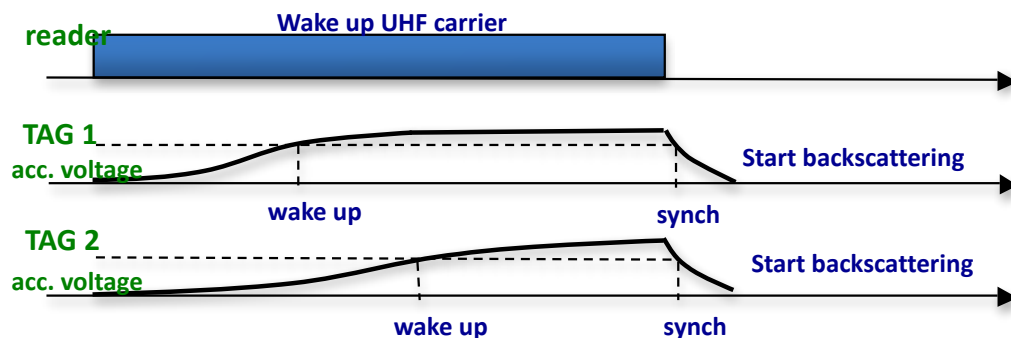


Figure 4.6: Wake-up synchronization procedure.

synchronized at about chip level, avoiding thus exhaustive code acquisition search for synchronization during the tag detection process, as detailed in the following section.⁴

4.5.2 ADC design analysis

When clutter removal is not possible using analog circuits due to hardware constraints and it has to be performed in digital domain, as in the SELECT project, it becomes important to well dimension the ADC at the receiver section, estimating the correct number m of bits required to achieve a correct analog to digital conversion of the received signal, without an overestimation of the resources. The following analysis is carried out with a particular emphasis on the dynamic range characterization (i.e., maximum clutter versus useful backscattered signal, amplitudes) and the SQNR before and after the de-spreading phase.

Analysis of the Dynamic Range at the ADC Input

The main issue to be addressed for the design of the ADC is the dynamic range at the receiver input, as it determines the number of bits required given a requirement in terms of tolerable SQNR. In fact, assuming that the full ADC dynamic is exploited, it is important to determine which contributions affect the dynamic range at the ADC input.

For the analysis, a L -levels mid-riser quantizer (L even) is adopted, with quantization levels associated to the central value of the quantization intervals, with $L = 2^m$, where m is the number of adopted quantization bits, M

⁴This process can be very complex due to the high number of pulses per symbol N_s necessary to overcome link-budget constraints.

denotes the maximum dynamic (i.e., a dynamic range $[-M; M]$) with uniform quantization. Now let us analyze the overall signal present at the input of a specific reader. It is composed of different components: backscattered signals by the tags related to the specific reader or to other readers, interference coming from other readers and clutter response. These components have to be separately analyzed, in order to estimate the dynamic range and, more precisely, to understand if the useful signal plus noise is quantized with sufficient accuracy. In particular, the tag backscatter signal path loss of a tag at distance d_{r-t} from the reader in free space condition can be expressed as

$$PL_{r-t} = \frac{P_t}{P_r} = \left[G_R^2 G_{\text{tag}} \left(\frac{\lambda}{4\pi d_{r-t}} \right)^4 \right]^{-1} \quad (4.4)$$

where G_R , G_{tag} , λ and d_{r-t} are, respectively, the reader antenna gain, tag overall gain (including twice the antenna gain and the lines/switch losses), the wave length and the distance. The reader interference path loss, corresponding to an interfering reader at distance d_{r-r} from the receiving reader, can be expressed as

$$PL_{r-r} = \frac{P_t}{P_r} = \left[G_R^2 \left(\frac{\lambda}{4\pi d_{r-r}} \right)^2 \right]^{-1}. \quad (4.5)$$

The path loss experienced by the reflections related to the same reader interrogation signal from an object of RCS σ at distance d_{r-obj} , is expressed as

$$PL_{r-obj} = \frac{P_t}{P_r} = \left[\sigma G_R^2 \frac{\lambda^2}{(4\pi)^3} \left(\frac{1}{d_{r-obj}} \right)^4 \right]^{-1}. \quad (4.6)$$

For the clutter here we consider a worst-case (but realistic for many industrial applications) model for the reflector as a square metallic plate of area $A = (50 \times 50)\text{cm}^2$ in front of the transmitting/receiving reader at distance d_{r-obj} (here assumed to be the same as d_{r-t} , while echoes coming from the environment are assumed to be lower than this structural scatter. Figure 4.7 reports the peak of the received signal amplitudes in [V] as a function of the reader-tag (object) distance, considering the previous path loss evaluated in free space propagation condition. A reader with 5 dBi antenna gain, a tag considered in the maximum reader's antenna direction equipped with an 1 dBi antenna and 2 dB switch losses have been considered. A transmitted signal compliant with the IEEE 802.15.4a emission mask in the 3–5 GHz is considered. In the analyzed scenario, as shown in Fig. 4.7, the interfering reader signal is in general the highest component present at the input of the

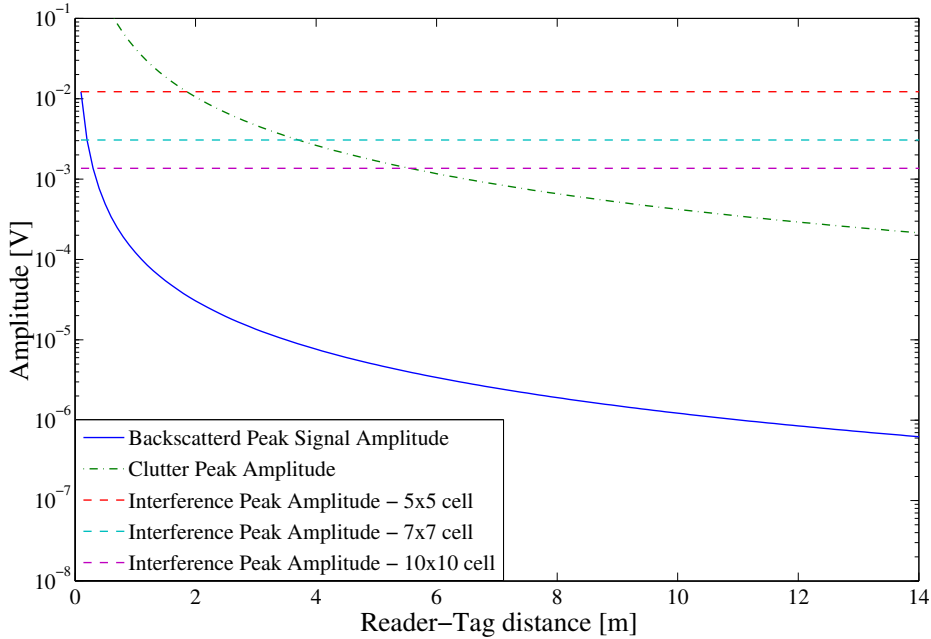


Figure 4.7: Received signal amplitude [V]. Concerning interference from other readers, different cell sizes are considered.

ADC. This signal is independent on the reader-tag distance and its value is fixed once defined the geometry of the environment. Thus, a LNA with a finite set of possible amplification values is sufficient to lock the system at the required dynamic once the clutter/interference level has been estimated (it is only function of the geometry, antennas radiation patterns and propagation environment).

Analysis on the Number of Bits Required

Once defined the minimum interfering reader distance, we analyze in the following the requirement on the amplitude of the quantization step with respect to the amplitude of the signal (interference/clutter and useful backscattering component).

Figure 4.8 shows the peaks of received signals amplitudes in [V], obtained with the same simulation parameter as for Fig. 4.8. Quantization steps amplitudes are associated to different m . Interfering reader amplitude and quantization levels are related to a $(10 \times 10) \text{ m}^2$ square cell, and a noise standard deviation of $22 \mu\text{V}$ is considered (the value is measured from real HW). As the quantization step must be smaller than the lower signal plus noise component, i.e., the useful backscatter signal plus the noise, from

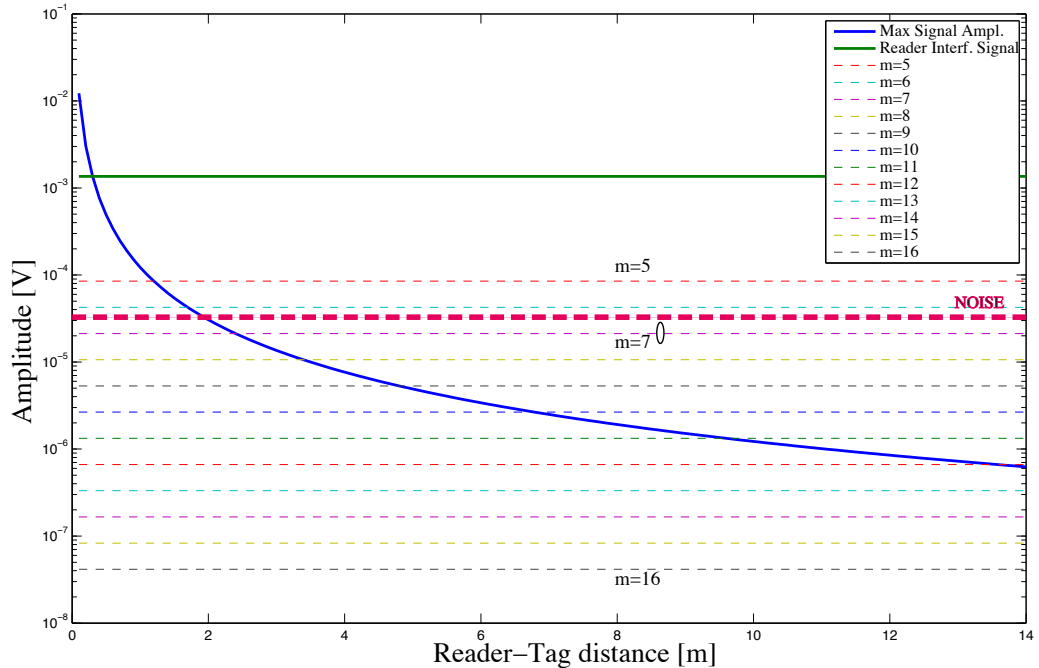


Figure 4.8: Received signal amplitude [V], where quantization steps amplitudes are associated to different m . Interfering reader amplitude and quantization levels related to a $(10 \times 10) \text{ m}^2$ square cell.

fig. 4.8 7 bits, i.e. $m = 7$, seem a minimum requirement inside the ADC, considering that the quantization step amplitude is at the noise level.

Then the minimum number of bits required in the ADC is analyzed as a function of SQNR at the ADC output. Here we consider that the digital conversion of the received signal is performed before the de-spreading operation, and we indicate with SQNR_{in} and SQNR_{out} the SQNR before and after de-spreading respectively. In Appendix A, the relation between the SQNR_{in} and SQNR_{out} is derived with the conclusion that different results can be obtained according to SNR regime (low or high) at the receiver section. In particular, for low SNR, the accumulation of N_s pulses at the receiver section implies not only a processing gain of N_s in terms of SNR, but also for what the SQNR is concerned. In the following the low SNR regime is assumed, as it is the case for UWB RFID based on backscatter modulated signal. Considering X as the input of the quantizer, the output \hat{X} can be described as X plus a (quantization) noise term, i.e.

$$\hat{X} = X + \epsilon_x. \quad (4.7)$$

Under the hypothesis of fine quantization (uniform distribution of the error

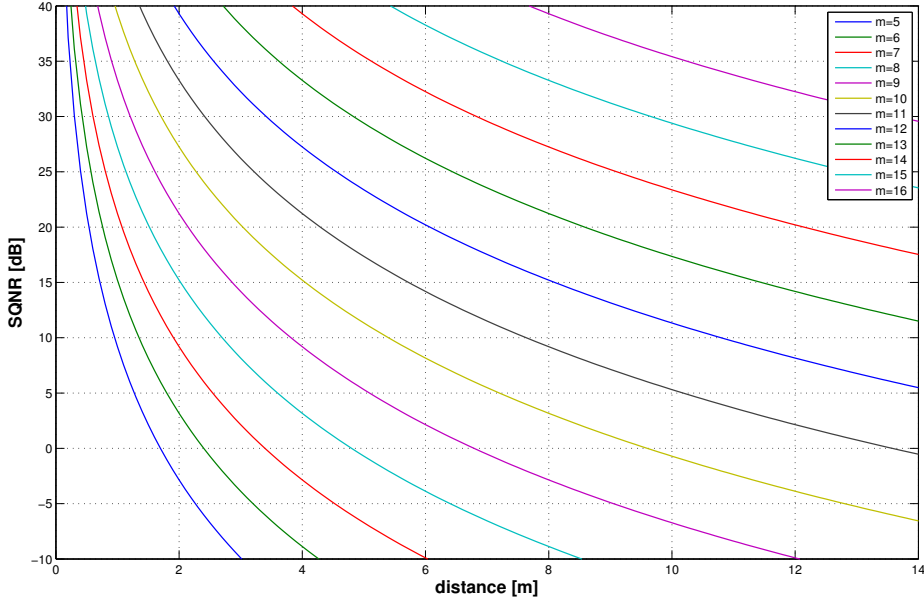


Figure 4.9: SQNR_{in} at the de-spreader input for a $10 \times 10 \text{ m}^2$ square cell, as a function of useful tag distance, reported for different m .

in q), we have:

$$\mathbb{E} [\epsilon_x^2] = \mathbb{E} \left[\left(\hat{X} - X \right)^2 \right] = \frac{M_c^2}{3L^2} \quad (4.8)$$

where M_c is the clutter/interference amplitude (maximum ADC dynamic range). Considering, for each distance, the useful backscattering signal as a uniform random variable distributed in $[-M_s, M_s]$ we obtain for the SQNR, defined as the ratio between the useful backscatter signal power and the quantization noise power, the following relationship

$$\text{SQNR} = \frac{3M_s^2 L^2}{M_c^2}. \quad (4.9)$$

This relation is used to obtain results reported in Fig. 4.9, where the SQNR_{in} at the de-spreader input is reported for different m and for a $(10 \times 10) \text{ m}^2$ square cell, as a function of useful tag distance.

Generally speaking, a high SQNR allows considering the additional noise source due to the analog to digital conversion as negligible with respect to the thermal noise and the quantized signal. Here we have to account the processing gain due to the de-spreading operation. As shown in Appendix A, a low SNR regime implies that additional 39 dB have to be accounted for the SQNR_{out} , due to (an ideal) processing gain of $N_s = 8192$ pulses per bit.

Thus, if a $SQNR_{in}$ of -10 dB is considered, a $SQNR_{out}$ of about 30 dB is obtained adopting at least 9 – 10 bits, which let to quantize signals deriving from tags at 12 m from the reader adding a negligible quantization noise (yellow curve) (note that 12 m is the maximum reader-tag distance in the scenario, as usually a blind meter is considered around each reader).

4.5.3 Tag Clock Drift Model

Among all the requirements to be accomplished, tags have to be low cost with small size. For this reason, low cost tag oscillators are usually adopted, which may significantly affect the overall system performance due to the effects of strong non-idealities of the generated clock. For a comprehension of how much the clock drift and the residual of the synchronization procedure impact the performance, we define here a simplified model with a common glossary. In particular, we indicate:

- synchronization offset: an initial uncertainty on the time scale due to the initial synchronization algorithm
- clock skew (CS) the difference between tag and reader time perception
- clock drift: positive or negative deviation in the timing of a circuit due to a different clock frequency with respect to the source (i.e., the main effect of the clock accuracy).

We then consider here the following linear model for the CS:

$$CS(t) = S_{\text{offset}} + D \cdot t \quad (4.10)$$

where D is the tags clock accuracy (e.g., 100 ppm, 0.01%).

S_{offset} represents the clock offset which it is assumed to be the residual clock mismatch after the synchronization procedure, due to non idealities in the system, the propagation delay of the wake-up signal (depends on tags position and orientation) (< 100 ns) and the readers synchronization residual offset (values are expected to be lower than 20 ns).

The representation of the model is depicted in Fig. 4.10. Note that the reader clock drift is considered negligible with respect to the tag clock drift.

4.6 Tag-to-Reader Communication

Tag to reader communication is now considered, accounting for all the non-idealities previously presented. After the transmission of the wake-up signal

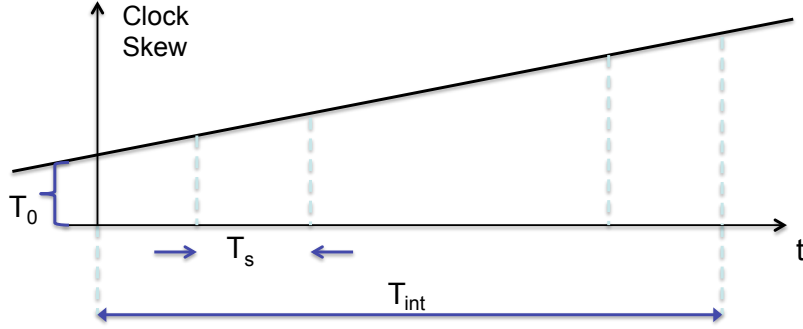


Figure 4.10: The considered clock skew model.

(e.g., in the UHF band), the reader starts sending the UWB interrogation signal described in Sec. 4.3, as reported in Fig. 4.2.

When tags are woken up thanks to the wake-up signal, they activate their backscatter modulator that starts switching the antenna load according to the tags' codes $\{c_n^{(k)}\}$. The reader and the tags have independent clock sources, thus they have to be considered asynchronous. However, the wake-up signal can also be exploited to reset the tag spreading code generator as shown in Fig. 4.5. This allows considering the system as quasi-synchronous, thus drastically reducing the code acquisition time as will be clarified afterward.

The presence of a low cost oscillator in the tag and the typical long duration of the symbol⁵ make clock drift effects not negligible after the reception of a few symbols. We consider here the simplified model in (4.10) where the clock drift mainly derives from the presence of a tag oscillator with frequency slightly different from the nominal one.⁶ According to this assumption, the clock skew between the k th tag and the reader can be modeled as $\delta^{(k)}(t) = T_o^{(k)} + D^{(k)}t$, where $T_o^{(k)}$ is the residual initial offset after the wake-up, and $D^{(k)}$ is the clock drift. Therefore, the backscatter modulator signal commanding the switch of the k th tag can be written as

$$m^{(k)}(t) = \sum_{m=0}^{N_r-1} \sum_{n=0}^{N_c-1} b_m^{(k)} c_n^{(k)} \cdot \Pi\left(\frac{1}{\tilde{T}_c} \left[t - mN_c\tilde{T}_c^{(k)} - n\tilde{T}_c^{(k)} - T_o^{(k)} \right]\right) \quad (4.11)$$

with $\tilde{T}_c^{(k)} = T_c (1 + D^{(k)})$ and $\Pi(t)$ denoting the rectangular function of unitary duration for $t \in [0, 1]$. In this way the polarity of the reflected signal changes

⁵The duration is higher with respect to conventional active UWB transmission schemes due to the need to counteract the poor link budget typical of two-hop links through the collection of a higher number of UWB pulses per symbol [85].

⁶This is equivalent to consider, as first approximation, the effects of the phase noise constant on a symbol time T_s , (i.e., neglecting the presence of a fast jitter).

each chip time (i.e., every N_{pc} pulses) according to the k th tag's code value $c_n^{(k)}$.

Due to the reciprocity principle, the signal backscattered by the tag propagates to the reader antenna on the same wireless channel related to the reader-tag transmission [85]. The received signal at reader side can be written as⁷

$$r_{\text{reader}}(t) = \sum_{k=1}^{N_{\text{tag}}} [(s_{\text{reader}}(t) \otimes h^{(k)}(t)) \cdot m^{(k)}(t)] \otimes h^{(k)}(t) + s_{\text{reader}}(t) \otimes h^{(C)}(t) + n(t) = w(t) + n(t) \quad (4.12)$$

where $h^{(k)}(t)$ is the one-way channel impulse response (CIR) related to the reader- k th tag link, $h^{(C)}(t)$ is the CIR of the environment comprehensive of tags' structural scatterings (that is, the unmodulated response), and $n(t)$ is additive white Gaussian noise (AWGN) with two-sided power spectral density $N_0/2$. We consider the CIRs $h^{(k)}(t)$ and $h^{(C)}(t)$ static over the N_r interrogation symbols.⁸ The tag antenna structural mode is treated as part of clutter since it is not affected by data modulation. Note that the received signals are obtained through the double convolution of the transmitted signal with the one-way CIR [85, 103].

It is interesting to remark that the clock drift in conventional active UWB communication systems affects the instant in which UWB pulses are transmitted by tags: thus the TOA and the PRP, as seen at the receiver, result different from that expected, and proper synchronization schemes have to be implemented if T_s is not small. Contrary, the TOA (hence the PRP) of the backscattered pulses in backscattering communication are not affected by the clock drift (because generated by the reader itself), since clock drift modifies only how signals are modulated at the tag side, as depicted in Fig. 4.11. As direct consequence tag's code as seen by the reader (which is tuned on the expected symbol duration T_s) starts exhibiting an increasing offset after the transmission of a certain number of data symbols, in addition to the initial residual offset of the wake-up phase.

4.7 Signal De-Spreading

As a result of the spreading process at the transmitter, and the backscatter modulation in the tag, the signal backscattered by the generic intended tag

⁷Operator \otimes denotes the convolution.

⁸For the validity of the following discussions and schemes it is sufficient the CIRs static on the symbol time T_s .

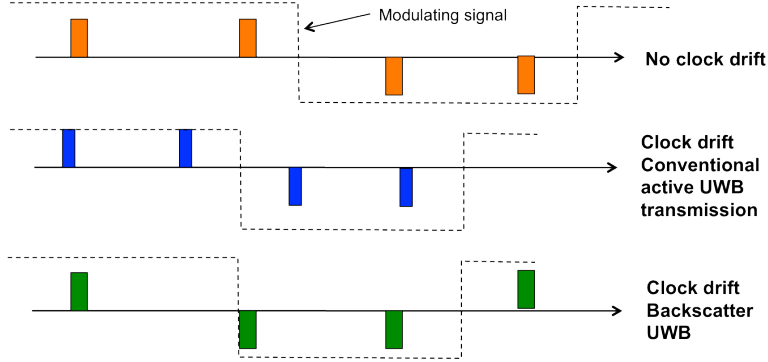


Figure 4.11: Clock drift effects on passive and active communication.

\hat{k} results to be spread by the composed code $\{d_n \cdot c_n^{(\hat{k})}\}$, whereas the clutter results to be spread by the reader code $\{d_n\}$ only. Therefore, through the de-spreading process shown in Fig. 4.4 it is possible to discriminate an intended tag signal from the other tags' signals (that act as interference) and from the clutter and the noise. Specifically, the tag backscattered signal de-spreading is operated coherently accumulating the N_s channel responses (CRs) composing a symbol, using the combined code $\{d_n \cdot c_n^{(\hat{k})}\}$ related to the intended useful tag of index \hat{k} .⁹ This allows discriminating the backscatter signal associated to a specific reader-tag couple. We define the periodically repeated sequences (with period N_s) $\{\tilde{c}_l^{(k)}\} \triangleq \{c_{\lfloor l/N_{pc} \rfloor}^{(k)}\}$ and $\{\tilde{d}_l\} \triangleq \{d_{\lfloor l/N_{pc} \rfloor}\}$, for $l = 0, 1, \dots, N_s - 1$, with $\tilde{c}_{l+N_s}^{(k)} = \tilde{c}_l^{(k)}$ and $\tilde{d}_{l+N_s} = \tilde{d}_l$.

The wake-up offset $T_o^{(k)}$ and the clock drift $D^{(k)}$ generate an uncertainty on the offset (phase) of the tag spreading code with respect to the reader's local clock. To overcome tag clock drift effects, the simplest solution is to adopt codes with $N_{pc} \gg 1$ (i.e., with higher chip time T_c), more robust to the presence of drift, as will be detailed in Sec. 4.8. In alternative, tag detection can be performed jointly with code acquisition, requiring the availability of de-spreading outputs for different code shifts within the expected maximum acquisition range. This is achieved by correlating the backscatter response with differently shifted versions of $\{\tilde{c}_l^{(\hat{k})}\}$ and in-phase version of $\{\tilde{d}_l\}$. We consider N_{span} shifts with span step Δ for code acquisition, determining an overall acquisition range of $\Delta(N_{span} - 1)$. Figure 4.12 shows the battery of parallel de-spreading blocks which lets to avoid a serial search of the code shift, which would cause a long acquisition time.

⁹This is equivalent to a process gain, (i.e., an enhancement of the SNR), of a factor N_s .

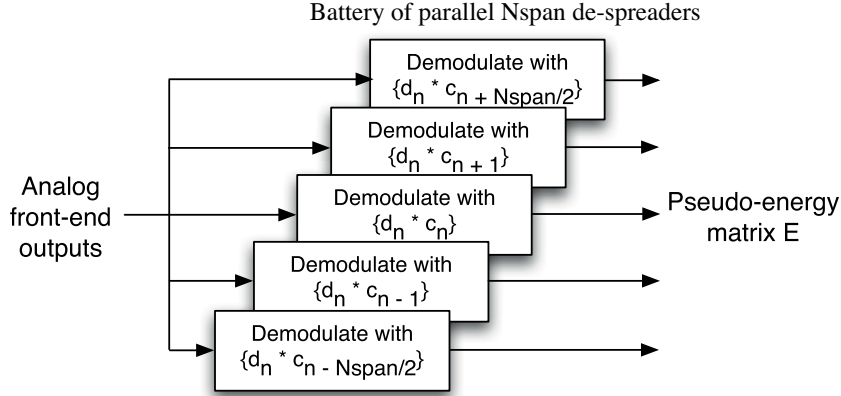


Figure 4.12: Parallel de-spreading blocks.

The values of N_{span} and Δ have to be determined according to the robustness of codes to shifts and to the expected clock drift and initial offset due to the non ideal wake-up procedure. In addition N_{span} should be chosen not too large in order to keep the system complexity affordable. The trade-off between N_{span} and Δ is investigated in Chapter 5, while different code strategies are studied in the following.

4.8 Tags Code Assignment Strategies

The backscatter communication scheme hides several potential issues that have to be addressed during the design of spreading codes used by the N_{tag} tags in the monitored area. In fact, it is necessary to fulfill various requirements, such as

- suppression or mitigation of the multi-tag interference
- provide a sufficient available number of codewords for a specific code length N_c
- counteract other effects such as clutter and clock drift.

Here below we detail these aspects, and their impact on code design.

Number of Available Codewords A system with N_{tag} tags in the same environment requires the adoption of N_{tag} different codewords, apart from

Table 4.1: Clutter rejection and process gain properties of odd codes.

Code type $N_{\text{pc}} \times N_c$	N_s	Clutter residual	Clutter rejection [dB]
1×8191	8191	1:8191	78
2×4095	8190	2:8190	72
4×2047	8188	4:8188	66
8×1023	8184	8:8184	60
16×511	8176	16:8176	54
32×255	8160	32:8160	48
64×127	8128	64:8128	42
128×63	8064	128:8064	36

special cases where the same codeword is assigned to different users.¹⁰ Considering that longer codewords imply higher complexity and a longer symbol time, it is necessary to adopt the shortest code length available which lets to fulfill the other requirements here reported.

Link-Budget Improvement The de-spreading process at receiver side must guarantee an accumulation of a sufficient number \hat{N}_s of pulses per symbol to reach the target SNR after the de-spreading corresponding to a reliable communication between reader and tags, as described in Sec. 5.4.2. There are several ways to fulfill such a requirement. The simplest option is to assign codes of length $N_c = N_s \geq \hat{N}_s$ (i.e., with $N_{\text{pc}} = 1$). An alternative solution is represented by the use of a shorter code of length $N_c < N_s$ with $N_{\text{pc}} > 1$ pulses per chip, and $N_s = N_c N_{\text{pc}} \geq \hat{N}_s$. The first option lets to manage a greater number of users in the environment, as the number of available codewords is greater than adopting $N_c < N_s$. On the contrary, the second solution reduces the tag complexity and power consumption since the UWB switch works at lower frequency, but at the expense of less codewords available given a specific N_s .

Clutter Removal For what clutter removal is concerned, we show in Sec. 5.2 that if the tag code is exactly balanced, the clutter is completely removed at the output of the de-spreading process, regardless the reader's

¹⁰This is possible adopting proper code families and assigning the some sequence with a different initial phase (shift) to different users. Here we consider each tag with a unique sequence.

code $\{d_n\}$. Differently, if the code is not exactly balanced a clutter residual might be present. Specifically, according to (5.6), if the number of $' + 1'$ and $' - 1'$ differs for one chip, as happen for example for m -sequences (odd codes), we have N_{pc} clutter responses $\tilde{r}_c(t)$ summed up to the useful de-spreaded signal in (5.2). Table 4.1 summarizes this effect considering odd codes starting from a code with $N_{\text{pc}} = 1$ and increasing N_{pc} till 128, under the constraints $N_s > \hat{N}_s = 8000$.¹¹ In particular, the second column shows the reduction of the process gain N_s while increasing N_{pc} since original code-words are odd. The third and fourth columns put in evidence the decreasing in clutter rejection capability, which decreases as N_{pc} increases.

When strong clutter is present in the environment the adoption of an odd code with $N_{\text{pc}} > 1$ may compromise the functionality of the system. Coherently with [139], the adoption of an exactly balanced even code, able to cancel out the clutter component, is mandatory to avoid clutter effects in harsh environments.

Interference Mitigation The tag code must guarantee a reliable reader-tag communication depending on the scenario considered in terms of reader-tag synchronization capability and multi-tag interference. Specifically, the code behavior in the presence of these effects (lack of synchronization and presence of interference) must be separately analyzed for $N_{\text{pc}} = 1$ and $N_{\text{pc}} > 1$.

In case we considered an ideal synchronous scenario, with all tags' codes synchronous at PRP level, orthogonal codes would result the best option, since the interference would be always canceled out and clutter perfectly removed as they are perfectly balanced [138]. In this ideal case, there is no difference between the two approaches in terms of interference rejection. Unfortunately a perfect synchronization for all the tags is difficult to achieve as well as to maintain due to the clock drift effect $D^{(k)}$ and the residual wake-up offset $T_o^{(k)}$ described in Sec. 4.6.

Considering, instead, a completely asynchronous scenario where tags' codes are not kept synchronized and each backscatter modulator is completely free-running, it is well known that pseudo-noise (PN) codes represent, in general, a good solution which allows to control the interference [140]. As PN codes are composed of odd sequences, extended PN codes are a potential solution to completely remove clutter without a significant performance loss, as proposed in [138]. On the contrary, orthogonal codes offer in this scenario poor performance due to the not optimal cross-correlation properties when not aligned. In case (extended) PN codes are adopted, the two considered

¹¹This value is taken from the link budget analysis carried out in Sec. 5.4.2.

Table 4.2: Interference mitigation properties of PN codes.

Code type $N_{\text{pc}} \times N_{\text{c}}$	N_{s}	$\theta^{(\text{peak})}$	$\hat{\theta}^{(\text{peak})}$	Min. interf. residual	Min. interf. mitigation [dB]
1×8191	8191	129	129	129:8191	36
2×4095	8190	129	258	258:8190	30
4×2047	8188	65	260	260:8188	30
8×1023	8184	65	520	520:8184	24
16×511	8176	33	528	528:8176	24
32×255	8160	33	1056	1056:8160	18
64×127	8128	17	1088	1088:8128	17
128×63	8064	17	2176	2176:8064	11

approaches, that is, $N_{\text{pc}} = 1$ and $N_{\text{pc}} > 1$, are not equivalent. In fact, suppose of having a set of codewords of length N_{c} . Define the periodic cross correlation function (CCF) between a pair of different code sequences x and y of length N_{c} as $\theta_{x,y}(m)$, for $m = 0, 1, \dots, N_{\text{c}} - 1$, where $\theta_{x,y}(m) = \langle x, T^m y \rangle$, with $\langle a, b \rangle$ denoting the inner product between sequences a and b , and T^m denoting the operator which shifts vectors cyclically to the left by m places.¹² The behavior of the CCF determines the interference level at the output of the de-spreading process [138]. Let us now indicate with \hat{x} and \hat{y} the code sequences obtained as chip repetition of a factor N_{pc} of x and y . We have that $\hat{\theta}_{\hat{x},\hat{y}}(l)$, for $l = 0, 1, \dots, N_{\text{s}} - 1$, is the CCF between the pair of code sequences \hat{x} and \hat{y} of length N_{s} . When $N_{\text{pc}} = 1$, $N_{\text{s}} = N_{\text{c}}$ and obviously $\hat{\theta}_{\hat{x},\hat{y}}(l) = \theta_{x,y}(m)$, since $\hat{x} = x$ and $\hat{y} = y$. Differently, if $N_{\text{pc}} > 1$ is adopted, the resulting code of length N_{s} exhibits a CCF $\hat{\theta}_{\hat{x},\hat{y}}(l)$ which can be expressed as a function of the original $\theta_{x,y}(m)$ as¹³

$$\hat{\theta}_{\hat{x},\hat{y}}(l) = N_{\text{pc}} \theta_{x,y}(\lfloor l/N_{\text{pc}} \rfloor) + (l \bmod N_{\text{pc}}) [\theta_{x,y}(\lfloor l/N_{\text{pc}} \rfloor + 1) - \theta_{x,y}(\lfloor l/N_{\text{pc}} \rfloor)]. \quad (4.13)$$

As it is possible to observe from (4.13), when adopting $N_{\text{pc}} > 1$, the CCF peak $\hat{\theta}^{(\text{peak})} = \max_l \{|\hat{\theta}_{\hat{x},\hat{y}}(l)|\}$, given by $\hat{\theta}^{(\text{peak})} = N_{\text{pc}} \max_l \{|\theta_{x,y}(\lfloor l/N_{\text{pc}} \rfloor)|\}$, is worsened of a factor N_{pc} with respect to the original code, that is $\hat{\theta}^{(\text{peak})} =$

¹²Sequences x and y denote, respectively, the intended useful tag code $\{c_i^{(\hat{k})}\}$ and the k -th tag code $\{c_i^{(k)}\}$ assigned to another user, with $k \neq \hat{k}$.

¹³The expression is derived from [140, eq. 1.11].

$N_{\text{pc}} \max_m \{|\theta_{x,y}(m)|\} = N_{\text{pc}} \theta^{(\text{peak})}$. Thus, the adoption of a code with $N_{\text{pc}} > 1$ results in an increasing of the peak (and average) value of the CCF $\hat{\theta}(l)$, that is a decreasing of the code interference mitigation capability. However, it is well known that a shorter sequence presents a lower peak for its CCF $\theta_{x,y}(m)$, which is directly related to the sequence length [140]. Thus, we have two conflicting factors: on one side, the interference level is increased by the fact that $N_{\text{pc}} > 1$, but on the other side it is decreased thanks to the adoption of a shorter code $N_c < N_s$.

Table 4.2 shows the values of the peak CCFs $\theta^{(\text{peak})}$ and $\hat{\theta}^{(\text{peak})}$ for different N_{pc} , as well as the resulting minimum interference mitigation level for classical PN codes, in particular codes derived from maximal connected sets of m -sequences presenting the optimal three-valued cross correlation spectrum¹⁴ $\{-1, -\theta^{(\text{peak})}, \theta^{(\text{peak})} - 2\}$ (e.g., Gold sequences [141, 142]) [140].¹⁵ Looking at the last column on the right of Table 4.2 it is evident how the gain in interference mitigation capability presented by the adoption of a code with shorter N_c is not sufficient to counteract the decreasing in interference mitigation capability due to the increased N_{pc} necessary for guarantee the target \hat{N}_s . Due to this effect, considering an asynchronous scenario, we have that the best performance in terms of interference mitigation is achieved by adopting the strategy with $N_{\text{pc}} = 1$.

Wake-up Offset and Clock Drift constraints Due to the non-idealities of the wake-up process described in Sec. 4.6, small residual offsets with respect to the reader timing of tag codes are present (quasi-synchronous scenario). In this case it is important to exploit this peculiarity, by assigning (to tags) codes able to guarantee the orthogonality (or very small cross-correlation values) even in the presence of these small offsets [143]. In the presence of significant clock drift, the scenario from quasi-synchronous can become asynchronous, so that codes are also required to preserve good correlation properties also in asynchronous conditions.

Moreover a code presenting $N_{\text{pc}} > 1$ is intrinsically more robust to synchronization errors and the presence of clock drift. As an example, consider the useful tag code is shifted of q PRPs with respect to the code generator at reader side due to the presence of offsets. Thus, the process gain, instead of being N_s , as expected, is equal to the code autocorrelation function (ACF) evaluated in q , that is $\hat{\theta}_{\hat{x},\hat{x}}(q)$, where \hat{x} is the tag code $\{\tilde{c}_i^{(k)}\}$ [138]. According

¹⁴For $N_c = 4095$ and $N_c = 255$ there are no preferred pairs of m -sequences so the corresponding CCFs do not exhibit the optimal three-valued spectrum.

¹⁵Similar considerations can be formulated for extended PN codes considering a less favorable interference mitigation capability.

to (4.13), as N_{pc} increases, the ACF function presents smoother transitions making the de-spreading more robust to synchronization errors.

To counteract the effects of the wake-up offset and of clock drift we may operate in two directions. The first and simplest solution is to adopt $N_{\text{pc}} \gg 1$, which guarantees a lower receiver complexity at the expense of a reduced number of available codewords and lower interference mitigation. This corresponds to set $n = N_{\text{span}} = 1$ and thus $(n+\nu)\Delta = 0$ in (5.2). The second and more complex approach, which uses smaller values of N_{pc} (ideally $N_{\text{pc}} = 1$ for the best interference mitigation), requires the adoption of tag code acquisition schemes at the receiver to deal with the non ideal wake-up offset, as well as code tracking schemes to compensate the clock drift during the demodulation of the successive bits. In this case the adoption of a code with good ACF (ideally, m -sequence) is beneficial for acquisition and tracking. It has to be remarked that with small N_{pc} it becomes important to adopt a small span step Δ (e.g., $\Delta = 1$ if $N_{\text{pc}} = 1$) to have a refined code acquisition search which can increase the complexity in case of high wake-up offset $T_o^{(k)}$. As will be investigated in the numerical results in Chapter 5, a trade-off between N_{pc} , hence the required Δ , and the corresponding system complexity has to be found.

4.9 Inter-Reader Interference

From the analysis of Sec. 4.5.2, it has emerged that inter-reader interference suppression or mitigation is one of the main issues for what the dynamic range is concerned. In addition, the suppression of such a signal is important for the avoidance of false alarms in tag detection.

A typical cell scenario reported in Fig. 4.13, foresees 4 readers placed at the corners of the area. In this analysis, the presence of obstacles is neglected, assuming that the highest interference contribution comes from the opposite reader in case of free-space propagation as also confirmed by simulations reported in Sec. 4.5.2 and measurements described in [15]. In general we can assume a lower level for the interference coming from the two neighbor readers in the case of partial directive antennas at transmitting and/or receiving stage. A higher level is expected in case of adoption of omnidirectional antennas. We can thus foresee three different situations for the signal transmitted by reader #2 (opposite reader) and received by reader #3, as depicted in Fig. 4.13:

- Case 1: reader #2 signal is reflected (backscattered) by the useful tag;

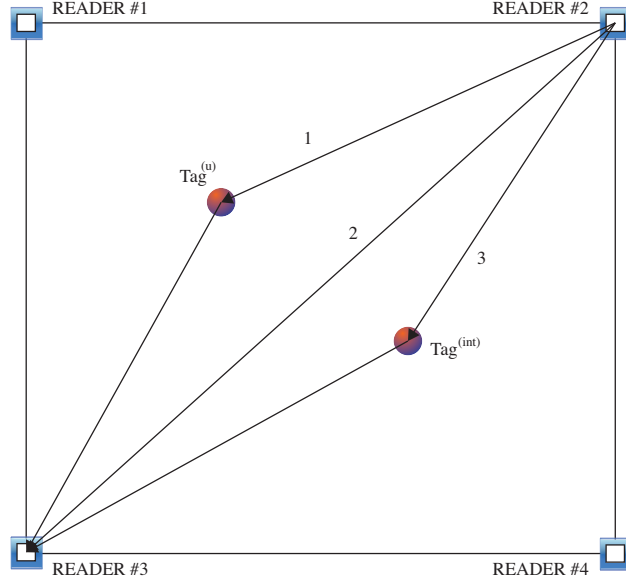


Figure 4.13: Interference scenario.

- Case 2: direct link (or through multipath) exists between readers #2 and #3 (strongest interfering signal);
- Case 3: reader #2 signal is reflected by a tag different from the useful one.

It is assumed that the interrogation signals transmitted by readers #2 and #3 are generated using, respectively, the spreading codes $\{d_i^{(2)}\}$ and $\{d_i^{(3)}\}$, and that the intended useful and the interfering tags have codes $\{c_i^{(u)}\}$ and $\{c_i^{(int)}\}$, respectively. To detect the presence of the useful tag, reader #3 performs a de-spreading operation using the composed code $\{c_i^{(u)}d_i^{(3)}\}$, according to the procedure described in Sec. 4.7. The level of interference suppression strongly depends on the cross and double cross correlation properties of the code sequences involved, as explained in the following.

For the previous described three cases relating to reader #2-reader #3 interference, we have different situations after the de-spreading at reader #3 side. In particular, for case 1, where reader #2 signal is reflected by the useful tag, the signal component related to the received signal transmitted by reader #2, is proportional to

$$\sum_{i=1}^{N_s} d_i^{(2)} c_i^{(u)} d_i^{(3)} c_i^{(u)} = \sum_{i=1}^{N_s} d_i^{(2)} d_i^{(3)} \left(c_i^{(u)}\right)^2 = \sum_{i=1}^{N_s} d_i^{(2)} d_i^{(3)} \quad (4.14)$$

which is 0 in case reader #2 and #3 codes are orthogonal, and readers are synchronized at PRP level. Thus, the interferer signal passing through the useful tag is completely suppressed. In case of less stringent synchronization at reader level a residual interference is expected: unfortunately, as demonstrated in Sec. 4.5.2, this signal is many dBs higher than the useful backscattered signal, and even a residual can be comparable or even higher than the intended useful one. This does not represent a problem for tag detection (the useful tag is present as hypothesis), but could create ambiguities during the localization procedure.

Concerning instead case 2 (direct reader-reader link), the signal component present at the output of reader #3 de-spreader, related to the received signal transmitted by reader #2, is proportional to

$$\sum_{i=1}^{N_s} d_i^{(2)} c_i^{(u)} d_i^{(3)} \quad (4.15)$$

while in case 3 it becomes

$$\sum_{i=1}^{N_s} d_i^{(2)} c_i^{(u)} d_i^{(3)} c_i^{(\text{int})} . \quad (4.16)$$

The situation is more complicated, as it is required to have three or four codewords orthogonal to each other, which is very difficult, or even impossible, to be achieved if at least one device is not perfectly synchronized (at PRP level) with respect to the others. If this condition is not satisfied, we may have an interferer component, which is many times higher than the useful one, and neither detection nor data demodulation would be possible. In Appendix B, a few more considerations are conducted, and the combination of more partial solutions is proposed.

So far, the more reliable solution is represented by the time division multiple access (TDMA), where different time slots are assigned to different readers for transmission. In this way the inter reader interference is avoided, and the dynamic range is reduced, with the advantage of an ADC with a reduced number of quantization bits. TDMA can be performed at different rate considering the alternation of the transmitting reader at each PRP, each chip, each symbol or each transmitted packet. The main disadvantage of TDMA is that there is a reduction of the system update rate and constraints on the maximum tags allowed speed, if object tracking is performed.

Finally, note that TDMA at reader level does not prevent that code division multiple access (CDMA) techniques are adopted for tags medium access control (MAC).

4.10 Conclusions

In this chapter, an UWB RFID system based on the modulation of the backscattered signal has been addressed. Implementation issues that can arise during system design are described, and correspondent solutions have been proposed in order to counteract the problems. The joint adoption of code acquisition schemes with codes properly designed in order to combat all the system non-idealities, is proposed to guarantee reliable performance. In Chapter 5, different codes performance will be studied, and the trade-off between N_{span} and Δ will be investigated.

Chapter 5

Robust Tag Detection Scheme to the Presence of Interference and Drift

5.1 Introduction

As detailed in Chapter 4 for UWB RFID based on the modulation of the backscattered signal, several issues arise due to the presence of clutter (the signal backscattered by the environment), multi-tag interference, tag clock drift (due to typical poor local oscillator performance), and the poor link budget intrinsic of the backscattering mechanism [85, 138, 139]. These issues have been only partially and separately investigated in the literature [14, 94, 137–139, 144].

In this chapter, the design of a system architecture capable of tag detection even in presence of multi-tag interference and strong clock drift is addressed, starting from the general system analysis conducted in Chapter 4. A low complexity non-coherent detection scheme is proposed and analyzed and the different spreading code design strategies described in Sec. 4.8 are investigated in terms of detection performance. Specifically, the near-far interference problem, which derives from the semi-passive nature of the system and the joint adoption of UWB signals [145–147], is addressed, and a solution to counteract this issue is proposed in order to guarantee robust tag detection. Finally, simulative results assess the performance in terms of tags detection capability, which provide an insight on how system parameters such as code length, interference level, and clock drift affect the system performance and hence system design guidelines.

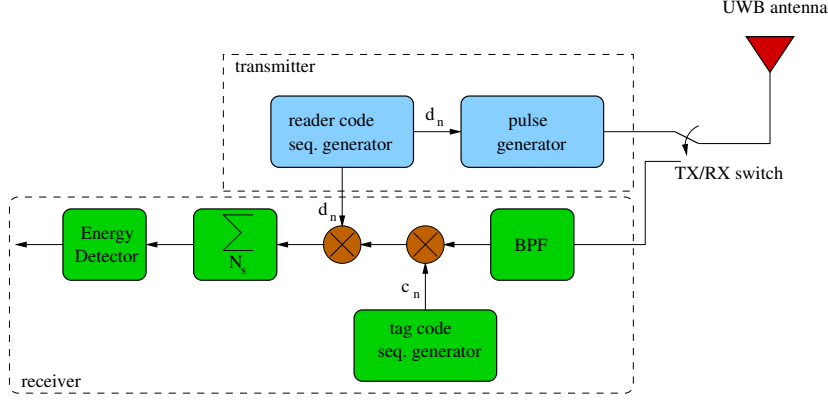


Figure 5.1: Reader internal structure.

5.2 Signal De-Spreading

Consider the code acquisition scheme described in Sec. 4.7, and the reader architecture depicted in Fig. 5.1, while refer to Fig. 4.5 for the tag structure. We assume here that $\{b_m\}$ is a sequence of $+1$, as it usually happens for tag detection. Again, the tag backscattered signal de-spreading is operated coherently accumulating the N_s CRs composing a symbol, adopting the periodically repeated sequences (with period N_s) $\{\tilde{c}_l^{(k)}\} \triangleq \{c_{\lfloor l/N_{pc} \rfloor}^{(k)}\}$ and $\{\tilde{d}_l\} \triangleq \{d_{\lfloor l/N_{pc} \rfloor}\}$, for $l = 0, 1, \dots, N_s - 1$, with $\tilde{c}_{l+N_s}^{(k)} = \tilde{c}_l^{(k)}$ and $\tilde{d}_{l+N_s} = \tilde{d}_l$. Without loss of generality, we consider the detection of tag $\hat{k} = 1$ by observing the first symbol (i.e., acquiring N_s pulses). The received signal $r_{\text{reader}}(t)$ is first passed through an ideal bandpass filter of bandwidth W with center frequency f_c to eliminate out-of-band noise.¹ The filtered signal is denoted by

$$\tilde{r}(t) = \tilde{w}_u(t) + \tilde{n}(t) \quad (5.1)$$

where $\tilde{w}_u(t) = w(t) \otimes h_F(t)$, $h_F(t)$ is the impulse response of the filter, and the term $\tilde{n}(t) = n(t) \otimes h_F(t)$ is a zero-mean Gaussian random process with autocorrelation function $R_{\tilde{n}}(\tau) = WN_0 \text{sinc}(W\tau) \cos(2\pi f_c \tau)$. De-spreading is operated by coherently accumulating N_s CRs. Specifically we have

$$y_n(t) = \sum_{l=0}^{N_s-1} \tilde{d}_l \tilde{c}_{l+(n+\nu)\Delta}^{(1)} \tilde{r}(t-lT_p) \quad (5.2)$$

with $\nu = -(N_{\text{span}}+1)/2$, $n = 1, 2, \dots, N_{\text{span}}$. In case a code acquisition scheme is not adopted, because the code is sufficiently robust to the expected offset

¹This operation is necessary since the considered receiver is energy-based.

(i.e., if $N_{\text{pc}} \gg 1$ as discussed in Sec. 4.8), we have $N_{\text{span}} = 1$ and thus $(n + \nu)\Delta = 0$.

In particular it is possible to decompose (5.2) as $y_n(t) = x_n(t) + z_n(t)$, with the noise term $z_n(t)$ given by

$$z_n(t) = \sum_{l=0}^{N_s-1} \tilde{d}_l \tilde{c}_{l+(n+\nu)\Delta}^{(1)} \tilde{n}(t-lT_p) \quad (5.3)$$

which is a zero-mean, Gaussian random process with autocorrelation function $N_s R_{\tilde{n}}(\tau)$. The term $x_n(t)$ can be instead expressed as

$$x_n(t) = \sum_{l=0}^{N_s-1} \tilde{d}_l \tilde{c}_{l+(n+\nu)\Delta}^{(1)} \tilde{r}_u(t-lT_p) + \sum_{l=0}^{N_s-1} \tilde{d}_l \tilde{c}_{l+(n+\nu)\Delta}^{(1)} \tilde{r}_c(t-lT_p) \quad (5.4)$$

where the received useful signal component $\tilde{r}_u(t)$ is given by

$$\tilde{r}_u(t) = \sum_{k=1}^{N_{\text{tag}}} [(s_{\text{reader}}(t) \otimes h^{(k)}(t)) \cdot m^{(k)}(t)] \otimes h^{(k)}(t) \otimes h_F(t). \quad (5.5)$$

Note that here we comprise in $\tilde{r}_u(t)$ both the useful and the interferer tags' responses. Signal $\tilde{r}_c(t)$ denotes the clutter component $\tilde{r}_c(t) = s_{\text{reader}}(t) \otimes h^{(C)}(t) \otimes h_F(t)$. With the assumption on the clutter CIR $h^{(C)}(t)$ stationary over a symbol time T_s , we have that the clutter channel response is given by $\tilde{r}_c(t-lT_p) = \tilde{d}_l \zeta(t)$, for $t \in [0, T_p]$, $\forall l$, with $\zeta(t) = v(t) \otimes h^{(C)}(t) \otimes h_F(t)^2$. In this manner, the clutter component at the output of the de-spreading process results

$$\sum_{l=0}^{N_s-1} \tilde{d}_l \tilde{c}_{l+(n+\nu)\Delta}^{(1)} \tilde{r}_c(t-lT_p) = \zeta(t) \sum_{l=0}^{N_s-1} \tilde{c}_{l+(n+\nu)\Delta}^{(1)}, \quad t \in [0, T_p]. \quad (5.6)$$

Equation (5.6) shows that the clutter component at the output of the de-spreading process is canceled provided that the tag code $\{\tilde{c}_l^{(1)}\}$ (i.e., $\{c_l^{(1)}\}$) is exactly balanced (i.e., with the same number of $' + 1'$ and $' - 1'$). This and other properties that tags' codes have to fulfill have been described in Sec. 4.8.

5.3 Tag Detection

The first task to be accomplished by the reader is the tag detection, that is the process to detect the presence of a specific tag in the monitored area.

² $v(t)$ was defined in (4.3)

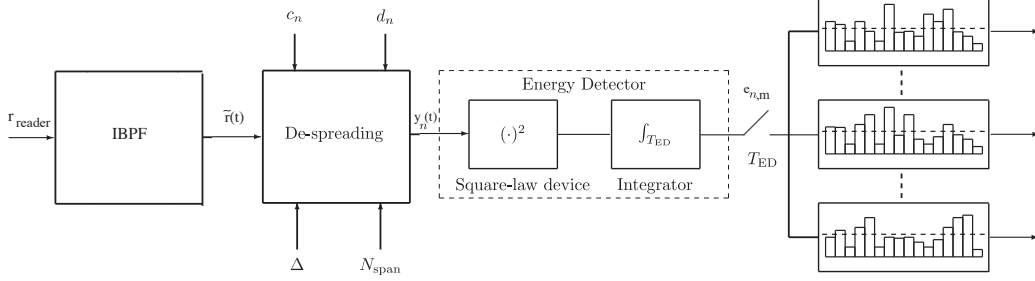


Figure 5.2: Tag detection scheme.

The detection in parallel of N tags requires that N detection circuits are employed at receiver section, with a consequent increase of complexity. For this reason, the tag detection scheme we propose, reported in Fig. 5.2, is a partially non-coherent approach based on energy detection, which helps to keep the system complexity affordable, thanks to the possibility of adopting sub-Nyquist sampling rates [148–150]. According to the considerations made in Sec. 5.2, we assume to adopt balanced codes, so that (5.4) reduces to

$$x_n(t) = \sum_{l=0}^{N_s-1} \tilde{d}_l \tilde{c}_{l+(n+\nu)\Delta}^{(1)} \tilde{r}_u(t-lT_p). \quad (5.7)$$

The term $x_n(t)$ can be further detailed considering that $\tilde{r}_u(t)$ is the combination of N_{tag} tags CRs (backscatter), that is

$$x_n(t) = \sum_{l=0}^{N_s-1} \tilde{d}_l \tilde{c}_{l+(n+\nu)\Delta}^{(1)} \sum_{k=1}^{N_{\text{tag}}} \omega^{(k)}(t-lT_p) \quad (5.8)$$

where the single-tag channel response is

$$\omega^{(k)}(t) = [(s_{\text{reader}}(t) \otimes h^{(k)}(t)) \cdot m^{(k)}(t)] \otimes h^{(k)}(t) \otimes h_F(t). \quad (5.9)$$

The de-spreading process is then followed by energy evaluations performed over the PRP T_p , that is

$$e_{n,m} = \int_{(m-1)T_{\text{ED}}}^{mT_{\text{ED}}} y_n^2(t) dt \quad n = 1, 2, \dots, N_{\text{span}}, \quad m = 1, 2, \dots, N_{\text{bin}} \quad (5.10)$$

with $N_{\text{bin}} = \lfloor T_p/T_{\text{ED}} \rfloor$ representing the number of integration bins each PRP is divided into, and with T_{ED} the integration time. The detection strategy consists in comparing each element $e_{n,m}$ with a threshold $\xi_{n,m}$. If the energy

value of at least one bin is above the threshold, then the tag is considered detected. Obviously, the challenging issues is the evaluation of the threshold $\xi_{n,m}$.

To this purpose, we define the global probability of false alarm (PFA) as the probability of deciding that the tag is present when it is not present in the considered environment, and the global probability of detection (PD) the probability of taking the correct decision when the tag is present. We then define \mathcal{H}_1 and \mathcal{H}_0 the hypotheses related to the presence and absence of the tag, respectively. The choice of the threshold affects the performance of the detection scheme in terms of PD and PFA. Low values for the threshold lead to higher PFA and higher PD. The vice versa holds for high values of $\xi_{n,m}$. For further convenience we define the single-bin PFA as the probability that the single bin energy exceeds the threshold when the tag is not present, and the single-bin PD as the probability that the single bin exceeds the threshold when the tag is effectively present. Global PFA and PD are indicated in the following with capital letters, specifically P_{FA} and P_D , respectively, whereas the single-bin PFA and PD, for the bin of coordinate (n, m) , are indicated with lower cases, specifically $p_{FA}^{(n,m)}$ and $p_D^{(n,m)}$, respectively. If the threshold is exceeded, the coordinates (\hat{n}, \hat{m}) associated to the maximum provide an estimate of the tag clock offset and a coarse estimate of the signal TOA, respectively, thanks to the adoption of UWB signals. The maximum resolution in TOA estimation (and hence ranging) is determined by T_{ED} [11]. TOA estimates can be further improved by adopting ranging strategies as described in [11].

5.3.1 Threshold Evaluation Criteria

The usual strategy for signal detection is defining a fixed threshold, that is a threshold $\xi_{n,m} = \xi$ [151]. However, this approach is not suitable in UWB-RFID systems based on backscatter modulation in presence of multi-tag interference. In fact, the useful tag can be hidden by interference peaks coming from tags closer to the reader than the intended useful one (i.e., a near-far effect). This fact is clearly depicted in Fig. 5.3, which shows an example of energy matrix $\mathbf{E} = \{e_{n,m}\}$ where the near-far effect is evident. If a constant threshold over all bins were adopted, the PFA would increase significantly due to the presence of interferers close to the reader. The effect is very pronounced in this kind of system due to the two-hop propagation channel, as the received power, in free-space propagation, is proportional to d^{-4} , where d is the reader-tag distance [12, 85]. Assuming a useful and an interferer tag at distance, respectively, d_U and d_I from the reader, the difference in dB of the receiving power at reader side from the two tags is $40[\log_{10}(d_U) - \log_{10}(d_I)]$ dB.

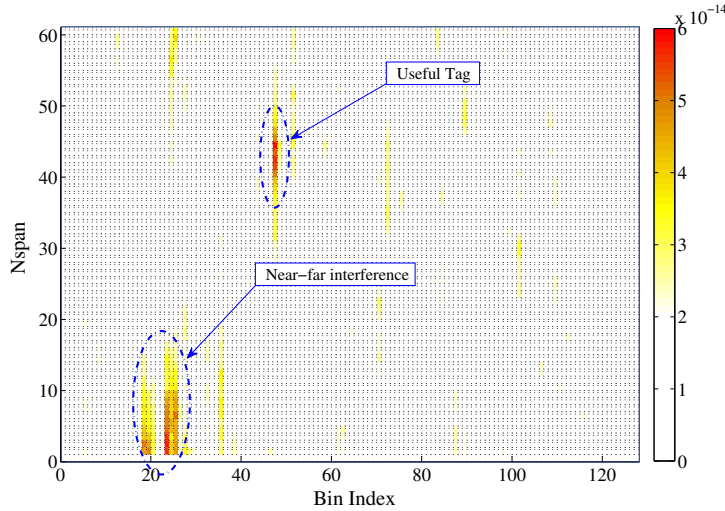


Figure 5.3: Example of energy matrix \mathbf{E} in presence of wake-up offset, clock drift and near-far interference effect.

For example, considering a useful and an interferer tag placed, respectively, at $d_U = 10$ m and $d_I = 2$ m from the reader, we find a difference of approximately 27 dB in the signals amplitude. If this difference is not properly managed by the interference mitigation capability provided by the tag codes, a high PFA due to near-far effects is expected.³ Unfortunately classical power control approaches, as usually adopted in CDMA systems, cannot be used due to the passive nature of the communication here considered. Therefore we propose a bin-dependent threshold strategy able to counteract near-far effects. In the following the threshold will be analytical computed considering a constant target PFA P_{FA}^* , under the hypothesis of absence and presence of multi-tag interference.

Consider now the elements $e_{n,m}$ of the energy matrix. The presented decision rule consist in

$$\text{Decide : } \begin{cases} \hat{\mathcal{H}}_0, & \text{if } e_{n,m} < \xi_{n,m} \forall n, m, \\ \hat{\mathcal{H}}_1, & \text{if } \exists \{n, m\} \text{ s.t. } e_{n,m} \geq \xi_{n,m}. \end{cases} \quad (5.11)$$

Define now the normalized test

$$\Lambda^{(n,m)} = \frac{2}{N_s N_0} e_{n,m} \underset{\hat{\mathcal{H}}_0}{\overset{\hat{\mathcal{H}}_1}{\gtrless}} \tilde{\xi}_{n,m} \quad (5.12)$$

³The effects are obviously even more pronounced in presence of multiple interfering tags and multipath propagation.

where $\tilde{\xi}_{n,m} = \frac{2}{N_s N_0} \xi_{n,m}$. According to the approach proposed in [152] we have

$$\Lambda^{(n,m)} = \frac{2}{N_s N_0} \int_{(m-1)T_{\text{ED}}}^{mT_{\text{ED}}} y_n^2(t) dt \simeq \frac{1}{\sigma^2} \sum_{i=(m-1)N}^{mN} y_{n,i}^2(t) \quad (5.13)$$

where $N = 2WT_{\text{ED}}$, $\sigma^2 = N_s N_0 W$ is the noise variance, and $y_{n,i}$ are for odd i (even i) the samples of the real (imaginary) part of the equivalent low-pass (ELP) $\hat{y}_n(t)$ of $y_n(t)$, with $y_n(t) = \Re \{ \hat{y}_n(t) e^{j2\pi f_c t} \}$, taken at Nyquist rate $W/2$ in each interval T_{ED} .⁵

It is well known that the output of the energy detector is distributed according to a central Chi-square distribution, with probability distribution function (p.d.f.) $f_C(y, \nu)$, under \mathcal{H}_0 , and according to a non-central Chi-square distribution, with p.d.f. $f_{\text{NC}}(y, \lambda, \nu)$, under \mathcal{H}_1 [152]. For further convenience we report the p.d.f.s of these random variables (r.v.s), having indicated with $\tilde{\nu}$ the number of degrees of freedom, and with λ the non-centrality parameter, that is

$$f_{\text{NC}}(y, \lambda, \tilde{\nu}) = \frac{1}{2} e^{-\frac{y+\lambda}{2}} \left(\frac{y}{\lambda} \right)^{\frac{\tilde{\nu}-2}{4}} I_{\frac{\tilde{\nu}-1}{2}}(\sqrt{y\lambda}), \quad y \geq 0, \quad (5.14)$$

$$f_C(y, \tilde{\nu}) = \frac{y^{\frac{(\tilde{\nu}-1)}{2}}}{2^{\frac{\tilde{\nu}}{2}} \Gamma\left(\frac{\tilde{\nu}}{2}\right)} e^{-\frac{y}{2}}, \quad y \geq 0 \quad (5.15)$$

where $I_\kappa(\cdot)$ denotes the κ th order modified Bessel function of the first kind [154, p. 374] and $\Gamma(\cdot)$ is the gamma function [154, p. 255].

In the following we propose two different threshold criteria according to the presence or not of multiple tags in the environment.

Single-Tag Scenario

In the absence of interference (i.e., $N_{\text{tag}} = 1$) the only component at the de-spreader output under hypothesis \mathcal{H}_0 is the noise $z_n(t)$ (i.e., $x_n(t) = 0$). A threshold-crossing event in absence of the useful tag, causing a false alarm, happens when the r.v. $\Lambda^{(n,m)}|_{\mathcal{H}_0}$ is above the threshold $\tilde{\xi}_{n,m}$, where we have indicated with $\Lambda^{(n,m)}|_{\mathcal{H}_0}$ the test (5.12) under the hypothesis \mathcal{H}_0 , that is

$$\Lambda^{(n,m)}|_{\mathcal{H}_0} = \frac{2}{N_s N_0} \int_{(m-1)T_{\text{ED}}}^{mT_{\text{ED}}} z_n^2(t) dt \simeq \frac{1}{\sigma^2} \sum_{i=(m-1)N}^{mN} z_{n,i}^2 \quad (5.16)$$

⁴The approximation is valid for high values of N . See also [153]

⁵We consider $WT_{\text{ED}} \in \mathbb{N}$.

where $z_{n,i}$ are the sampling expansion coefficients of the ELP $\hat{z}_n(t)$ of $z_n(t)$. Since $z_{n,i}$ are statistically independent Gaussian r.v.s with zero mean and unit variance, the r.v. $\Lambda^{(n,m)}|_{\mathcal{H}_0}$ is central Chi-square distributed, with N degrees of freedom. This results in a single-bin PFA $p_{FA}^{(n,m)}$ given by

$$p_{FA}^{(n,m)} = \int_{\tilde{\xi}_{n,m}}^{\infty} f_C(y, N) dy = \frac{\Gamma\left(\frac{N}{2}, \frac{\tilde{\xi}_{n,m}}{2}\right)}{\Gamma\left(\frac{N}{2}\right)} = \tilde{\Gamma}\left(\frac{N}{2}, \frac{\tilde{\xi}_{n,m}}{2}\right) \quad (5.17)$$

where we used [151,155,156] to solve the integral, with $\Gamma(a, x) = \int_x^{\infty} t^{a-1} e^{-t} dt$ the upper incomplete gamma function and $\tilde{\Gamma}(\cdot, \cdot)$ the gamma regularized function. Since the only component at the de-spreader output is the noise $z_n(t)$, the single-bin PFA results to be the same in each bin, that is $p_{FA}^{(n,m)} = p_{FA}$, $\forall n, m$. This leads to a constant threshold $\tilde{\xi}_{n,m} = \tilde{\xi}$, $\forall n, m$. Under the assumption of independent energy bins in n and m we have that the global PFA is⁶

$$P_{FA} = 1 - (1 - p_{FA})^M \simeq Mp_{FA} \quad (5.18)$$

where $M = N_{\text{bin}} \times N_{\text{span}}$. The threshold ξ , corresponding to the global PFA P_{FA}^* , can be then calculated by inverting (5.18) and (5.17) obtaining

$$\xi = \frac{N_s N_0}{2} \cdot 2 \tilde{\Gamma}^{-1}\left(\frac{P_{FA}^*}{M}, \frac{N}{2}\right) \quad (5.19)$$

which now depends on the target PFA P_{FA}^* .

Once the threshold is set to guarantee a certain PFA, we can determine the correspondent single-bin PD. Under the hypothesis \mathcal{H}_1 , the ED statistics $\Lambda^{(n,m)}|_{\mathcal{H}_1}$ is given by

$$\Lambda^{(n,m)}|_{\mathcal{H}_1} = \frac{2}{N_s N_0} \int_{(m-1)T_{\text{ED}}}^{mT_{\text{ED}}} (x_n(t) + z_n(t))^2 dt \simeq \frac{1}{\sigma^2} \sum_{i=(m-1)N}^{mN} (x_{n,i} + z_{n,i})^2 \quad (5.20)$$

where $x_{n,i}$ are the sampling expansion coefficients of the ELP $\hat{x}_n(t)$ of $x(t)$. Since $z_{n,i}$ are statistically independent Gaussian r.v.s with zero mean and unit variance, the r.v. $\Lambda^{(n,m)}|_{\mathcal{H}_1}$ is non-central Chi-square distributed, with N degrees of freedom, and non-centrality parameter $\lambda_{n,m} = 2\gamma_{n,m}$, where the

⁶This assumption is exact in case of $N_{\text{span}} = 1$, since the energy bins are independent, while results an approximation when $N_{\text{span}} > 1$ as the energy matrix elements are correlated for different code shifts. Consequently, (5.19) leads to a threshold more conservative than the necessary and, consequently, a PD lower than expected.

SNR per bin is denoted by

$$\gamma_{n,m} = \frac{1}{N_s N_0} \int_{(m-1)T_{\text{ED}}}^{mT_{\text{ED}}} x_n(t)^2 dt \simeq \frac{1}{2\sigma^2} \sum_{i=(m-1)N}^{mN} x_{n,i}^2. \quad (5.21)$$

The single-bin PD $p_D^{(n,m)}$ is then given by [151, 155, 156]

$$p_D^{(n,m)} = Q_k \left(\sqrt{\lambda_{n,m}}, \sqrt{\tilde{\xi}} \right) \quad (5.22)$$

where $k = N/2$ and $Q_k(\alpha, \beta) = \int_{\beta}^{\infty} x \left(\frac{x}{\alpha}\right)^{k-1} \exp\left\{-\frac{x^2 + \alpha^2}{2}\right\} I_{k-1}(\alpha x) dx$ is the generalized Marcum's Q function of order k . The global PD P_D can be finally computed as

$$P_D = 1 - \prod_{n=1}^{N_{\text{span}}} \prod_{m=1}^{N_{\text{bin}}} \left(1 - p_D^{(n,m)}\right) \quad (5.23)$$

under the approximation of having independent energy bins.

Multi-Tags Scenario

We now extend the derivation 5.3.1 to include the multi-tag interference effect in the threshold evaluation process. As previously discussed, a proper threshold design is fundamental to avoid the detrimental effects of near-far interference.

We consider now N_{tag} tags placed in the environment. Without loss of generality we consider tag $\hat{k} = 1$ as the intended one to be detected, while tags for $k = 2, 3, \dots, N_{\text{tag}}$ are considered as interferers. In this case, also in absence of the useful tag, $x_n(t) \neq 0$ due to the presence of the residual interference term after the de-spreading [138]. For further convenience, we distinguish the case whether the desired tag is present or absent, by defining

$$\begin{cases} x_n^{(\mathcal{H}_0)}(t) = \sum_{l=0}^{N_s-1} \tilde{d}_l \tilde{c}_{l+(n+\nu)\Delta}^{(1)} \sum_{k=2}^{N_{\text{tag}}} \omega_k(t), \\ x_n^{(\mathcal{H}_1)}(t) = \sum_{l=0}^{N_s-1} \tilde{d}_l \tilde{c}_{l+(n+\nu)\Delta}^{(1)} \sum_{k=1}^{N_{\text{tag}}} \omega_k(t). \end{cases} \quad (5.24)$$

Since $z_{n,i}$ are statistically independent Gaussian r.v.s with zero mean and unit variance, under both hypotheses \mathcal{H}_0 and \mathcal{H}_1 the r.v. $\Lambda^{(n,m)}$, that is, the ED output, is non-central Chi-square distributed with N degrees of freedom, and with a non-centrality parameter depending on \mathcal{H}_0 and \mathcal{H}_1 . Under the hypothesis \mathcal{H}_0 (no useful tag), the ED output results in

$$\Lambda^{(n,m)}|_{\mathcal{H}_0} = \frac{2}{N_s N_0} \int_{(m-1)T_{\text{ED}}}^{mT_{\text{ED}}} \left(x_n^{(\mathcal{H}_0)}(t) + z_n(t)\right)^2 dt \simeq \frac{1}{\sigma^2} \sum_{i=(m-1)N}^{mN} \left(x_{n,i}^{(\mathcal{H}_0)} + z_{n,i}\right)^2 \quad (5.25)$$

where $x_{n,i}^{(\mathcal{H}_0)}$ are the sampling expansion coefficients of the ELP $\hat{x}_n^{(\mathcal{H}_0)}(t)$ of $x_n^{(\mathcal{H}_0)}(t)$, leading to the non-centrality parameter $\lambda_{n,m}^{(\mathcal{H}_0)} = 2\gamma_{n,m}^{(\mathcal{H}_0)}$ where the interference-to-noise ratio (INR) per bin is defined as

$$\gamma_{n,m}^{(\mathcal{H}_0)} = \frac{1}{N_s N_0} \int_{(m-1)T_{\text{ED}}}^{mT_{\text{ED}}} x_n^{(\mathcal{H}_0)}(t)^2 dt \simeq \frac{1}{2\sigma^2} \sum_{i=(m-1)N}^{mN} \left(x_{n,i}^{(\mathcal{H}_0)}\right)^2. \quad (5.26)$$

A threshold-crossing event in absence of the useful tag, causing the false alarm event, happens when the r.v. $\Lambda^{(n,m)}|_{\mathcal{H}_0}$ is above the threshold $\tilde{\xi}_{n,m}$. This results in a single-bin PFA $p_{FA}^{(n,m)}$ given by

$$p_{FA}^{(n,m)} = \int_{\tilde{\xi}_{n,m}}^{\infty} f_{\text{NC}}(y, \lambda_{n,m}^{(\mathcal{H}_0)}, N) dy = Q_k \left(\sqrt{\lambda_{n,m}^{(\mathcal{H}_0)}}, \sqrt{\tilde{\xi}_{n,m}} \right) \quad (5.27)$$

where we used [151, 155, 156] to solve the integral. The non-centrality parameters are strictly related to the interference level at each bin $e_{n,m}$, then a constant PFA in each bin, that is $p_{FA}^{(n,m)} = p_{FA}$, $\forall n, m$, is obtained if a bin-dependent threshold $\xi_{n,m}$ is adopted according to (5.27). In particular, under the assumption of independent energy bins in n and m as in (5.18), the threshold $\xi_{n,m}$ can be calculated from (5.18) and (5.27) as

$$\xi_{n,m} = \frac{N_s N_0}{2} \cdot \left[Q_k^{-1} \left(\sqrt{\lambda(\mathcal{H}_0)_{n,m}}, \frac{P_{FA}^*}{M} \right) \right]^2 \quad (5.28)$$

with $Q_k^{-1}(\cdot, \cdot)$ denoting the inverse generalized Marcum Q function. Again, once the bin-dependent threshold is set to guarantee a certain PFA, we can determine the correspondent single-bin PD. Under the hypothesis \mathcal{H}_1 , the ED output is described by

$$\Lambda^{(n,m)}|_{\mathcal{H}_1} = \frac{2}{N_s N_0} \int_{(m-1)T_{\text{ED}}}^{mT_{\text{ED}}} \left(x_n^{(\mathcal{H}_1)}(t) + z_n(t)\right)^2 dt \simeq \frac{1}{\sigma^2} \sum_{i=(m-1)N}^{mN} \left(x_{n,i}^{(\mathcal{H}_1)} + z_{n,i}\right)^2 \quad (5.29)$$

where $x_{n,i}^{(\mathcal{H}_1)}$ are the sampling expansion coefficients of the ELP $\hat{x}_n^{(\mathcal{H}_1)}(t)$ of $x_n^{(\mathcal{H}_1)}(t)$, leading to the non-centrality parameter $\lambda_{n,m}^{(\mathcal{H}_1)} = 2\gamma_{n,m}^{(\mathcal{H}_1)}$, where the interference-plus-signal-to-noise-ratio (ISNR) per bin is defined as

$$\gamma_{n,m}^{(\mathcal{H}_1)} = \frac{1}{N_s N_0} \int_{(m-1)T_{\text{ED}}}^{mT_{\text{ED}}} x_n^{(\mathcal{H}_1)}(t)^2 dt \simeq \frac{1}{2\sigma^2} \sum_{i=(m-1)N}^{mN} \left(x_{n,i}^{(\mathcal{H}_1)}\right)^2. \quad (5.30)$$

The single-bin PD $p_D^{(n,m)}$ is then given by [151, 155, 156]

$$p_D^{(n,m)} = Q_k \left(\sqrt{\lambda_{n,m}^{(\mathcal{H}_1)}}, \sqrt{\tilde{\xi}_{n,m}} \right) \quad (5.31)$$

and the global PD P_D can be computed according to (5.23).

The presented tag detection scheme in the presence of interference requires the knowledge of the INR per bin in order to define the proper bin-dependent threshold $\xi_{n,m}$ according to (5.28) necessary to keep $P_{FA} < P_{FA}^*$. In Sec. 5.4 practical approaches for defining the threshold without exact a-priori knowledge of the interference level will be detailed.

Note that the detection performance in terms of PD in (5.22) and (5.31) is related to N_s . Since the transmitting power of the UWB transmitter is constrained by maximum spectrum emission masks, N_s results the design parameter to be determined to guarantee a target PD P_D^* given a certain reader-tag distance. Numerical results in Sec. 5.4 will provide an example of system design.

5.4 Numerical Results

In this section we present an example of system design, and performance evaluated in realistic conditions. Specifically we analyze the ROC, that is we simulate the tag detection rate as a function of the false alarm rate considering the low complexity non-coherent scheme based on energy detection proposed in Sec. 5.3.

5.4.1 Simulation Parameters

We adopt $T_p = 128$ ns.⁷ A reader with $G_r = 5$ dBi antenna gain, tags equipped with a $G_t = 1$ dBi antenna and $L_t = 2$ dB switch losses have been considered. Results have been obtained starting from dense multipath channel responses with exponential power delay profile and Nakagami- m fading (severity factor $m = 3$), a root-mean-square channel delay-spread of 20 ns⁸ and paths separated of 2 ns apart [65, 157]. A transmitted signal compliant with the IEEE 802.15.4a emission mask in the 3.2–4.7 GHz is considered, adopting root-raised cosine pulses with pulse width parameter $T_w = 1$ ns, roll-off factor $\beta = 0.6$ and center frequency $f_c = 4$ GHz. A receiver noise figure $F = 4$ dB is considered and an ideal bandpass filter with bandwidth $W = 2$ GHz and center frequency f_c . Energy evaluations are performed in a bin of width $T_{ED} = 1$ ns.

⁷This and the next system specifications are driven by the outcome of the European project SELECT, <http://www.selectwireless.eu>

⁸This value is comprehensive of the two-way link of the backscatter signal [85].

5.4.2 System Design

Link Budget Analysis

An appropriate design of the number of pulses per symbol is crucial to guarantee a target PD P_D^* also for tags placed at a certain distance from the reader. Thus we derive, under some approximations, a proper value of N_s greater than the minimum required \hat{N}_s which preserves a certain P_D^* . In particular we assume i) AWGN conditions, ii) received pulse energy always entirely included in one bin, iii) absence of interference and ideal tag code phase retrieving with $N_{\text{span}} = 1$. Operating in this way, from (5.23) we have $P_D = p_D^{(n,m)}$, which is imposed to be equal to the target P_D^* . According to (5.22), we can thus relate P_D^* to $\lambda(d)$, where $\lambda(d) = 2 \text{SNR}_p(d)$, having indicated with $\text{SNR}_p(d)$ the SNR obtained after the de-spreading process for a reader-tag distance d , that is⁹

$$\text{SNR}_p(d) = \frac{N_s}{N_0} \frac{E_p}{P_L(d)}. \quad (5.32)$$

The factor $P_L(d)$ indicates the free-space path-loss, that is¹⁰

$$P_L(d) = \left(\frac{4\pi d f_c}{c} \right)^4 \frac{L_t}{G_r^2 G_t^2} \quad (5.33)$$

with c denoting the speed of light. Noticing that the threshold

$$\tilde{\xi} = 2 \tilde{\Gamma}^{-1} \left(\frac{P_{FA}^*}{N_{\text{bin}}}, WT_{\text{ED}} \right) \quad (5.34)$$

does not depend on N_s , it is possible to obtain the number of pulses per symbol inverting (5.22) combined with (5.32) as

$$N_s \geq \hat{N}_s = \left\lceil \frac{N_0 P_L(d)}{2E_p} \left[Q_K^{-1} \left(P_D^*, \sqrt{\tilde{\xi}} \right) \right]^2 \right\rceil \quad (5.35)$$

with $N_0 = k_B F T_o$, $T_o = 290 \text{ K}$ the reference temperature, and k_B the Boltzmann constant. Substituting the simulation parameters indicated in Sec. 5.4.1, and considering $P_{FA}^* = 10^{-3}$ and $P_D^* = 0.9$, we obtain the curve providing N_s as function of the distance depicted in Fig. 5.4. It is worthwhile to notice that $N_s = 8192$ guarantees a reading range of about 6.5 m when the

⁹Note that under our approximations, the SNR per bin is coincident with the overall SNR.

¹⁰Here we adopt a central-frequency approximation.

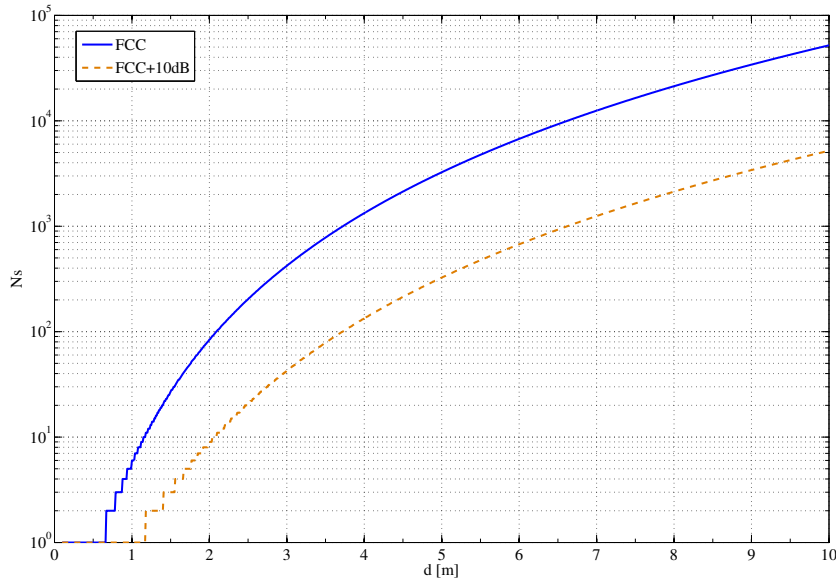


Figure 5.4: Minimum number of pulses per symbol as function of the reader-tag distance.

FCC mask is respected, while the same reading range can be achieved with about $N_s = 1024$ when a power boost of 10 dB is adopted in transmission. For specific scenarios, the power boost of 10 dB could be ad hoc solution to overcome the link budget limitation without increasing the system complexity. Note also that tag detection performance in line-of-sight (LOS) conditions is mainly due to the direct-path.

Tags Code Assignment

For what concerns the code family choice, an interesting possibility for the UWB-RFID system is to adopt *Orthogonal Gold codes* [158]. These codes are exactly orthogonal in the synchronous scenario ($l = 0$), and maintain the properties of extended Gold Codes (low cross-correlation) in the asynchronous scenario. They are constructed by lengthening of one chip the *Preferentially-Phased* Gold codes [159], that present the optimum value -1 of cross-correlation between all the pairs of codewords when aligned. In this manner a balanced code is obtained enabling the complete clutter cancellation. By using these codewords, the detection procedure is performed in a quasi-orthogonal environment without suffering strong interference. The possibility of adopting such a family of codes is very interesting in the presence of wake-up offset without code acquisition by increasing N_{pc} (i.e. increasing the effective chip time). Since the codes present an orthogonal behavior when

aligned, increasing N_{pc} does not causes excessive interference degradation during the detection phase.

5.4.3 Results

In the following results, the intended useful tag is considered placed at 7 m from the reader, while the interferers placement in the scenarios varies according to the specific conditions considered.

Performance in Synchronous and Asynchronous Scenarios

Figure 5.5 shows the ROC corresponding to perfectly synchronous and asynchronous scenarios with ideal code phase retrieving. We consider 59 interfering tags uniformly distributed from 5 to 9 m, to reproduce interference effects. We adopt three codes families, orthogonal Walsh codes, orthogonal Gold codes and extended quasi-balanced Gold codes, to assess the analysis conducted in Sec. 4.8. For what extended Gold codes are concerned, they are obtained by lengthening of one chip quasi-balanced Gold codes without any kind of phase optimization when aligned. Specifically, the sequences constructed in [160] are adopted. We consider $N_c = 128$ and $N_c = 1024$ in order to evaluate the impact of the different code length on the interference mitigation capability.

It is notable that in Fig. 5.5 codes with $N_c = 1024$ are more performing than codes with $N_c = 128$, thanks to their better interference mitigation properties, in agreement with Sec. 4.8. In particular, orthogonal Walsh codes in synchronous scenario represent the benchmark, since the interference is completely removed. On the contrary, their performance drastically degrades when the scenario becomes asynchronous. For what extended Gold codes are concerned, they evidence a loss while the scenario is synchronous, but they allow satisfactory detection capabilities also in asynchronous conditions. Orthogonal Gold codes represent instead the best trade-off for both scenarios since they achieve a detection rate higher than 0.9 with a false alarm of 10^{-3} also in the asynchronous scenario, while maintaining the optimal behavior of Walsh codes in perfectly synchronous scenario.

Performance in Presence of Tag Clock Drift and Wake-Up Offset

Once we have seen that orthogonal Gold codes are the best compromise to work in both synchronous and asynchronous conditions, we then tested this code family in quasi-synchronous scenario, that is in presence of a residual

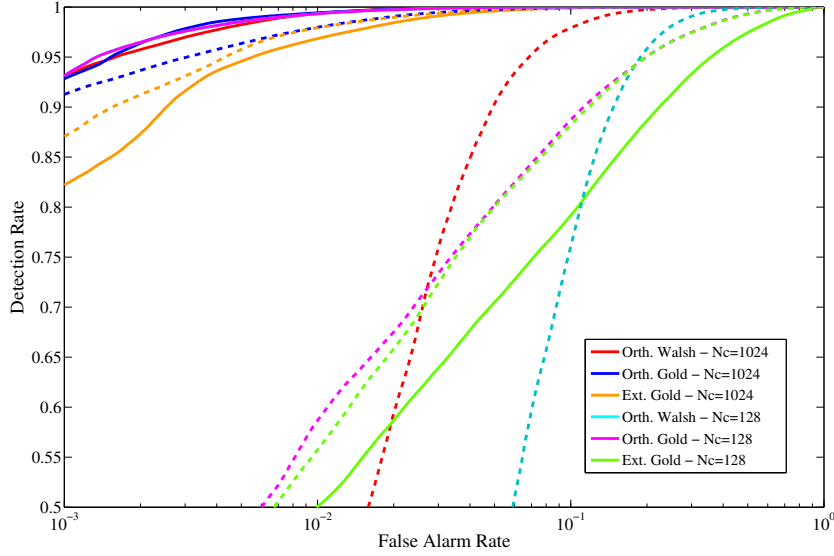


Figure 5.5: ROC for tag detection in UWB backscatter system. Continuous lines (—) refer to the perfectly synchronous scenario, dashed lines (---) refer to the asynchronous scenario, with ideal code phase retrieving.

synchronization offset and strong tag clock drift, as happens when considering the described wake-up process.

Figure 5.6 shows the ROC when an offset of 500 ns, and a drift of 100 ppm are considered. The 10th bit of the transmitted preamble is analyzed for detection purposes, and an acquisition window $(N_{\text{span}} - 1)\Delta = 40$, with different values of N_{span} and Δ , is considered to counteract the drift effects. Performance is evaluated considering both $N_c = 1024$ and $N_c = 128$. We consider again 59 interfering tags uniformly distributed from 5 to 9 m, to reproduce interference effects.

In contrast with Fig. 5.5, now codes with $N_c = 128$ are more performing. This can be explained by two effects. The first is that codes with $N_c = 128$ have an autocorrelation function more robust to the presence of code shifts due to drift and wake-up offset than codes with $N_c = 1024$, as explained in Sec. 4.8. Then, from the analysis in Sec. 4.8 it has emerged that large N_c leads to better interference mitigation in fully asynchronous scenario, where all code shifts are possible. On the other hand, in the quasi-synchronous scenario here considered, cross-correlations with $N_c = 128$ perform better, as the number of possible shifts $(N_{\text{span}} - 1)\Delta = 40$ is lower than the equivalent number of pulses per chip N_{pc} ($N_{\text{pc}} = 64$ when $N_c = 128$), while it is not the case for $N_c = 1024$ with $N_{\text{pc}} = 8$.

Figure 5.6 shows also that for $N_c = 128$ code acquisition schemes with

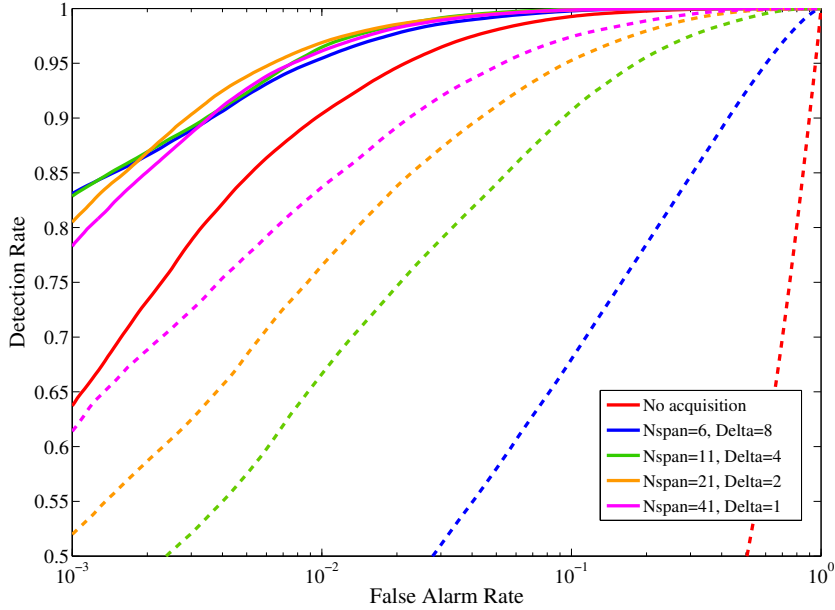


Figure 5.6: ROC for tag detection in UWB backscatter system, when orthogonal Gold codes are adopted in presence of tag clock drift and code acquisition schemes in a quasi-synchronous scenario. Continuous lines (–) refer to $N_c = 128$, dashed lines (--) refer to $N_c = 1024$.

small N_{span} (i.e. $N_{\text{span}} = 6$ and $N_{\text{span}} = 11$) let to achieve detection rate higher than 80% for false alarms in the order of 10^{-3} , preventing the system complexity to not become too much high. Performance for $N_c = 1024$ is instead quite poor even when code acquisition schemes are adopted, and this can be ascribed to the increase in the false alarm events when code phase search is performed, jointly with a less robust autocorrelation function to the presence of drift.

Performance in Presence of Near-Far Effects

It should be remarked that in the previous simulations near-far effects are negligible, as all the users were approximately placed around the useful intended tag. In a real scenario, it may happen to have some interfering tags significantly closer than the useful one to the reader, with the consequence of potential near-far effects. In this case classical power control approaches of CDMA systems cannot be adopted due to the passive communication nature of the system.

If a constant threshold over all the bins were adopted, the probability of false alarm due to an interferer very close to the reader would increase

significantly. This effect is particularly emphasized since in UWB backscattering systems the path loss difference for tags at different distances from the reader (i.e., the dynamic range at the receiver excluding the clutter effect) could be significant due to the two-hop link. To understand this problem, Fig. 5.7 shows the ROC when 19 interfering tags are uniformly distributed between 2.8 m and 3.2 m, while now the useful tag is placed at 6 m in order to guarantee a reliable detection also for codes with $N_c = 1024$. In fact, orthogonal Gold codes, with $N_c = 1024$, are adopted, a synchronization offset of 500 ns, and a drift of 100 ppm are considered. The 16th bit of the transmitted preamble (a sequence of all '1') is analyzed for detection purposes and the acquisition window is fixed to $40T_p$ when performing synchronization. As clearly depicted in Fig. 5.7, the system suffers of near-far effects when a constant threshold over all the bins is considered (dashed lines). Thus a possible solution is represented by the adoption of a threshold which accounts for the interference effects, that is, a bin-dependent variable threshold ξ_m , $m = 1, 2, \dots, N_{\text{bin}}$, computed such that, in the presence of interference, the PFA is constant for each bin. An empirical approach adopted for simulations considers a threshold reflecting the tag path-loss behavior until the tag energy, integrated in T_{ED} , falls below the noise floor N_0WT_{ED} , then adopting the constant threshold for the last bins following this point. Figure 5.7 shows that, when the bin-dependent threshold is adopted (continuous lines), near-far effects are significantly mitigated and a detection rate higher than 0.8 with a false alarm of 10^{-3} can be achieved when N_{span} is set to 41. In fact, with this solution, all the possible useful tag code shifts are considered inside the acquisition window to counteract clock drift, obtaining particular benefits in terms of codes autocorrelation properties and thus in the performance.

The design and adoption of the threshold described in (5.28) is currently under investigation, and it is expected that it can guarantee reliable tag detection performance even when strong near-far interference effects are present, as it was here the case.

5.4.4 Considerations on Threshold SNR for Detection Coverage in Sec. 3.3

The direct-path signal-to-noise ratio, related to a single received waveform, is defined as $\text{SNR}_{\text{sp}} = E_p/N_0$, where the received energy of the direct path E_p is evaluated by integrating the first-path as

$$E_p = \frac{1}{R} \int_{T_{oA}-T_w/2}^{T_{oA}+T_w/2} r^2(t) dt \quad (5.36)$$

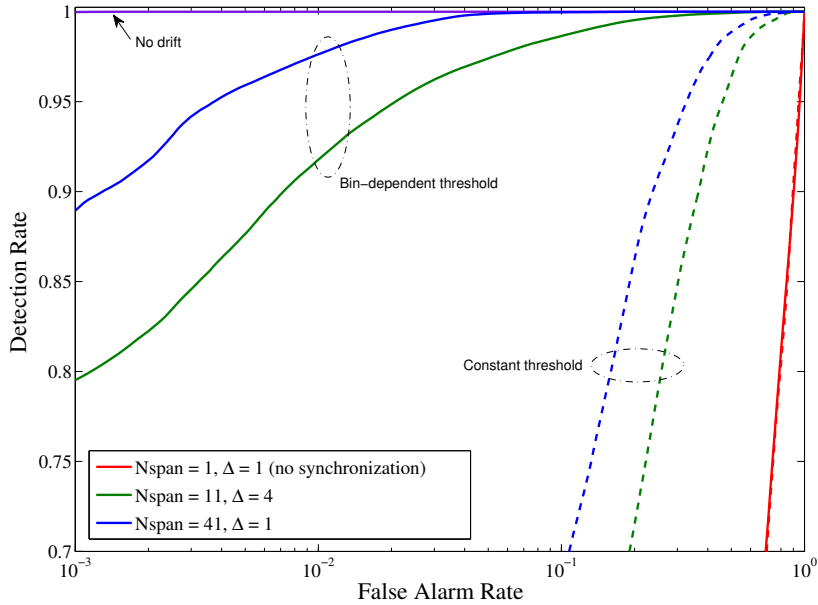


Figure 5.7: ROC for tag detection in presence of synchronization offset, clock drift and near-far interference effects. Continuous lines (—) refer to the bin-dependent threshold, dashed lines (---) refer to the constant threshold.

being " ToA " the time of arrival of the maximum peak of the received waveform and $r(t)$ the received pulse and $R = 50 \Omega$. As already stated, tag detection performance in LOS conditions is mainly due to the direct-path.

In particular, we define, according to the different operative conditions, the threshold SNR SNR_{th} , necessary to fulfill the requirements of having a tag detection of 90% with a false alarm rate $< 10^{-3}$. From simulations results, it can be derived that $SNR_{th} = -27.6$ dB, when the useful tag is positioned at 7 m in the proposed scenario and in ideal conditions (that is, in perfectly synchronous scenarios with the adoption of orthogonal Walsh codes, where non idealities, such as clock drift, are not present). Then, SNR_{th} is set to -25 dB to account for further system non-idealities, such as signal quantization and so on, which were neglected during simulations. This value is exploited in detection and localization coverage performance evaluation in Sec. 3.3

5.5 Conclusions

In this chapter it has been shown that the joint use of orthogonal Gold codes with proper low-complexity detection and synchronization schemes involving

bin-dependent thresholding is a promising solution to overcome implementation impairments and near-far effects. After the description of the proposed tag detection scheme, tag detection performance has been evaluated in terms of detection and false alarm rate, to analyze the robustness of different code families in different scenarios.

Chapter 6

Processing Scheme for Data Demodulation

6.1 Introduction

In Chapter 5, a robust tag detection scheme has been described in order to guarantee reliable detection even when strong non idealities are present. Once the intended useful tag is considered detected, the reader interrogates the tag in order to obtain data stored on it.

In this chapter, signal processing schemes are proposed starting from considerations reported in Chapter 4 and 5 with the purpose to demodulate the payload $\{b_m\}$ contained in the tag memory even in the presence of multiple tags. No extensive literature is present concerning the evaluation of communication performance for UWB RFID based on the modulation of the backscatter signal, and it is mainly related to different architectures or only AWGN channels [161]. Starting from experimental data collected both in ideal and real environment, the performance of the proposed architecture is assessed in terms of range/data rate trade-off, clutter suppression and multiple access capability.

6.2 System Model

Consider a scenario where a reader interrogates N_{tag} tags located in the same area as considered in the previous chapters.

Consider the transmitted interrogation signal given in (4.1), (4.2) and

(4.3). The signal received by the k th tag is given by:

$$r_{\text{tag}}^{(k)}(t) = \sum_{n=-\infty}^{\infty} d_n \cdot p^{(k)}(t - nT_p) \quad (6.1)$$

where $p^{(k)}(t)$ is the downlink (reader-tag) channel response to a transmitted pulse which includes also the propagation delay.

The reader and the tags have their own clock sources and hence they have to be treated as asynchronous. We denote with $\Delta^{(k)} = \delta^{(k)} + T_c u^{(k)}$, with u_k integer and $0 \leq \delta^{(k)} < T_c$, the clock offset of the k th tag with respect to the reader clock. We neglect here the clock drift so that the backscatter modulator signal in (4.11) commanding the tag's switch, can be expressed as

$$\begin{aligned} m^{(k)}(t) &= \sum_{n=0}^{N_r-1} \sum_{i=0}^{N_s-1} c_i^{(k)} b_n^{(k)} \Pi \left(\frac{1}{T_c} [t - nT_s - iT_c - \Delta^{(k)}] \right) \\ &= \sum_{n=0}^{M-1} c_n^{(k)} b_{f(n)}^{(k)} \Pi \left(\frac{1}{T_c} [t - (n + u^{(k)})T_c - \delta^{(k)}] \right) \end{aligned} \quad (6.2)$$

with $M = N_r N_c$, and having defined $f(n) \triangleq \lceil n/N_s \rceil$ and $\Pi(t) \triangleq 1$ for $t \in [0, 1]$ and zero otherwise.¹

Specifically, each tag information symbol $b_n^{(k)} \in \{-1, +1\}$ is associated to N_s pulses, thus the symbol duration equals $T_s = T_p N_s$. In this way the polarity of the reflected signal changes according to the tag's code sequence during a symbol time, whereas the information symbol affects the entire sequence pulse's polarity at each symbol.

According to (6.1) and (4.11), and considering perfect pulse symmetry in the two antenna load conditions, the signal scattered by the k th tag can be written as (see also the example in Fig. 6.1 where $N_{\text{pc}} = 1$ is considered for simplicity)

$$\begin{aligned} s_{\text{tag}}^{(k)}(t) &= r_{\text{tag}}^{(k)}(t) \cdot m^{(k)}(t) \\ &= \sum_{n=0}^{M-1} d_n \left[c_{n-u^{(k)}}^{(k)} b_{f(n-u^{(k)})}^{(k)} p_{\text{I}}^{(k)}(t - nT_c) + c_{n-u^{(k)}-1}^{(k)} b_{f(n-u^{(k)}-1)}^{(k)} p_{\text{II}}^{(k)}(t - nT_c) \right], \end{aligned} \quad (6.3)$$

¹Operator $\lceil x \rceil$ denotes the smallest integer larger than or equal to x .

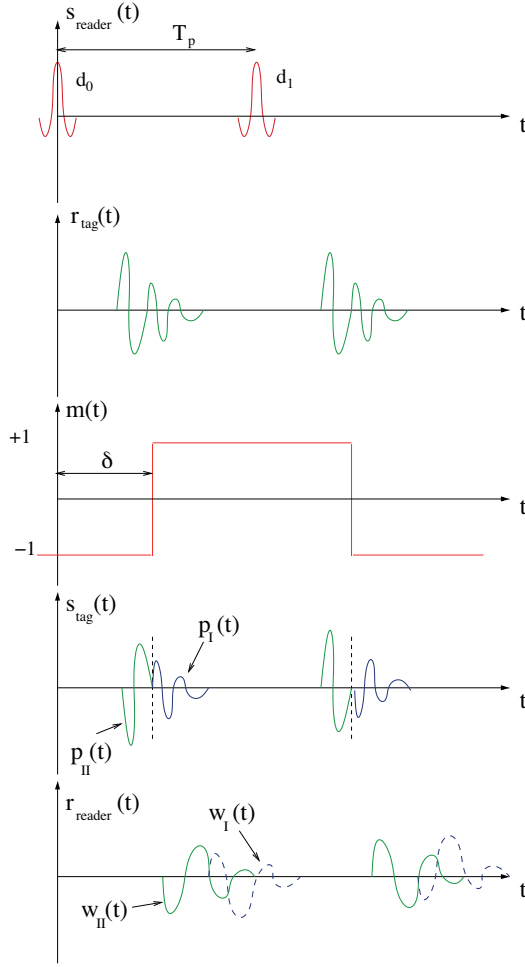


Figure 6.1: The behavior of the signals described in Sec. 6.2.

where we defined

$$p_{\text{I}}^{(k)}(t) \triangleq p^{(k)}(t) \cdot \Pi\left(\frac{t - \delta^{(k)}}{T_c - \delta^{(k)}}\right), \quad (6.4)$$

$$p_{\text{II}}^{(k)}(t) \triangleq p^{(k)}(t) \cdot \Pi\left(\frac{t}{\delta^{(k)}}\right). \quad (6.5)$$

The main task of the receiver section of the reader is to correctly detect the useful backscattered signal component (i.e., the antenna mode scattering dependent on antenna load changes due to the tag code and its information data) from those backscattered by the antenna structural mode and other scatterers (clutter) which are, in general, dominant [14]. The received signal

at the reader is

$$r_{\text{reader}}(t) = \sum_{k=1}^{N_{\text{tag}}} r_{\text{reader}}^{(k)}(t) + \sum_{n=0}^{M-1} d_n w^{(C)}(t - nT_c) + n(t), \quad (6.6)$$

where $n(t)$ is the AWGN with two-sided power spectral density $N_0/2$ and $w^{(C)}(t)$ is the backscattered version of the waveform $g(t)$ due to the clutter component which also accounts for pulse distortion, multipath propagation, and tag's antenna structural mode. The signal $r_{\text{reader}}^{(k)}(t)$ represents the received useful component due to the k th tag, i.e.,

$$r_{\text{reader}}^{(k)}(t) = \sum_{n=-\infty}^{\infty} d_n \left[c_{n-u^{(k)}}^{(k)} b_{f(n-u^{(k)})}^{(k)} w_{\text{I}}^{(k)}(t - nT_c) + c_{n-u^{(k)}-1}^{(k)} b_{f(n-u^{(k)}-1)}^{(k)} w_{\text{II}}^{(k)}(t - nT_c) \right], \quad (6.7)$$

having denoted $w_{\text{I}}^{(k)}(t)$ and $w_{\text{II}}^{(k)}(t)$, respectively, the uplink channel response to $p_{\text{I}}^{(k)}(t)$ and $p_{\text{II}}^{(k)}(t)$ (see Fig. 6.1). Note that $w^{(k)}(t) = w_{\text{I}}^{(k)}(t) + w_{\text{II}}^{(k)}(t)$ is the round-trip response to $g(t)$ of the backscatter link. More details can be found in [12].

Consider now the reader's receiver scheme reported in Fig. 4.4, where the received signal is correlated with a local waveform template $h(t)$ with unitary energy. The output is then sampled at intervals $t_{i,m} = iT_p + mT_s + \tau_0$, with $i = 0, 1, \dots, N_s - 1$, thus obtaining the following samples:

$$v_{i,m} = \int_0^{T_p} h(t) r_{\text{reader}}(t - t_{i,m}) dt = r_{\text{reader}}(t_{i,m}) \otimes h(-t_{i,m}) \quad (6.8)$$

$$= \sum_{k=1}^{N_{\text{tag}}} v_{i,m}^{(k)} + v_{i,m}^{(C)} + z_{i,m},$$

where^d

$$v_{i,m}^{(k)} = \sum_{n=0}^{M-1} d_n \left[c_{n-u^{(k)}}^{(k)} b_{f(n-u^{(k)})}^{(k)} \gamma_{\text{I}}^{(k)}(iT_p + mT_s + \tau_0 - nT_p) + c_{n-u^{(k)}-1}^{(k)} b_{f(n-u^{(k)}-1)}^{(k)} \gamma_{\text{II}}^{(k)}(iT_p + mT_s + \tau_0 - nT_p) \right],$$

$$v_{i,m}^{(C)} = \sum_{n=0}^{M-1} d_n \gamma^{(C)}(iT_p + mT_s + \tau_0 - nT_p). \quad (6.9)$$

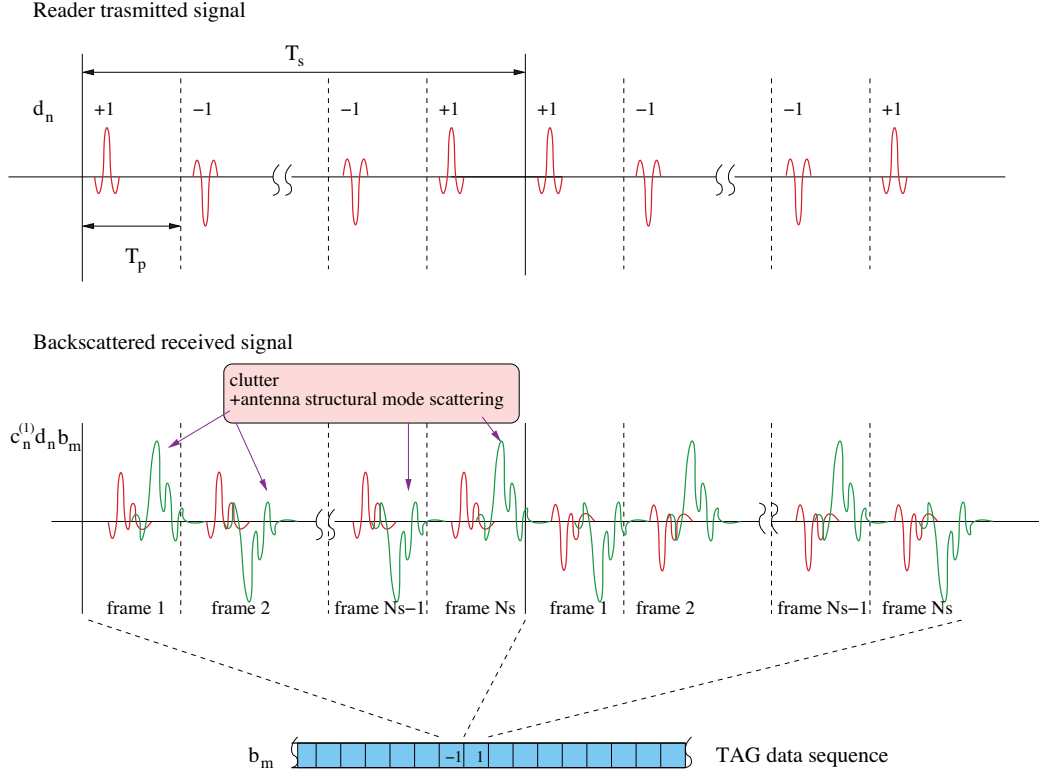


Figure 6.2: Clutter removal after signal de-spreading.

In (6.8) and (6.9), we have defined $\gamma_I^{(k)}(t) \triangleq w_I^{(k)}(t) \otimes h(-t)$, $\gamma_{II}^{(k)}(t) \triangleq w_{II}^{(k)}(t) \otimes h(-t)$, $\gamma^{(C)}(t) \triangleq w^{(C)}(t) \otimes h(-t)$, $z(t) \triangleq n(t) \otimes h(-t)$, and $z_{i,m} \triangleq z(iT_p + mT_s + \tau_0)$.^e

Without loss of generality, we consider the problem of detecting the data bit $b_m^{(1)}$ of tag #1 (useful tag). As shown in Fig. 4.4, to remove the clutter component at the receiver, the sampled signal $v_{i,m}$ is multiplied by the composite sequence $\{c_n^{(1)} \cdot d_n\}$, which identifies both the reader and the desired tag #1, as depicted in Fig. 6.2. Note that code acquisition schemes described in Sec 4.7 are here neglected, that is we assume here $\Delta = 0$ and $N_{\text{span}} = 1$.

In particular, all the resulting N_s samples at the output of the correlator composing a data symbol are summed up to form the m th decision variable at the detector input. Considering that $c_{i+mN_s}^{(k)} = c_i^{(k)}$, and $d_{i+mN_s} = d_i \forall i$, the decision variable for the m th symbol $b_m^{(1)}$ becomes

$$\begin{aligned}
y_m &= \sum_{i=0}^{N_s-1} c_i^{(1)} d_i v_{i,m} \\
&= \gamma_{\text{I}}^{(1)}(\tau_0) \sum_{i=0}^{N_s-1} \left[d_i^2 c_i^{(1)} c_{i-u^{(1)}}^{(1)} b_{f(mN_s-u^{(1)})}^{(1)} \right] + \gamma_{\text{II}}^{(1)}(\tau_0) d_0^2 c_0^{(1)} c_{-u^{(1)}-1}^{(1)} b_{f(mN_s-u^{(1)}-1)}^{(1)} \\
&\quad + \gamma_{\text{II}}^{(1)}(\tau_0) \sum_{i=1}^{N_s-1} \left[d_i^2 c_i^{(1)} c_{i-u^{(1)}-1}^{(1)} b_{f(mN_s-u^{(1)}-1)}^{(1)} \right] + \Psi_m + y_m^{(C)} + z_m,
\end{aligned} \tag{6.10}$$

where it is

$$y_m^{(C)} = \sum_{i=0}^{N_s-1} c_i^{(1)} d_i \sum_{n=-\infty}^{\infty} d_n \gamma^{(C)}(iT_p + mT_s + \tau_0 - nT_p) = \gamma^{(C)}(\tau_0) \sum_{i=0}^{N_s-1} c_i^{(1)} \tag{6.11}$$

and $z_m \triangleq \sum_{i=0}^{N_s-1} d_i c_i z_{i,m}$ is a Gaussian distributed r.v. with zero mean and variance $\sigma_z^2 = N_s N_0/2$.

The component Ψ_m accounts for the multi-user interference (MUI) and can be expressed as follows:

$$\begin{aligned}
\Psi_m &= \sum_{k=2}^{N_{\text{tag}}} \sum_{i=0}^{N_c-1} c_i^{(1)} d_i v_{i,m}^{(k)} \\
&= \sum_{k=2}^{N_{\text{tag}}} \left\{ \gamma_{\text{I}}^{(k)}(\tau_0) \sum_{i=0}^{N_c-1} \left[d_i^2 c_i^{(1)} c_{i-u^{(k)}}^{(k)} b_{f(m-u^{(k)})}^{(k)} \right] \right. \\
&\quad + \gamma_{\text{II}}^{(k)}(\tau_0) d_0^2 c_0^{(1)} c_{-u^{(k)}-1}^{(k)} b_{f(m-u^{(k)}-1)}^{(k)} \\
&\quad \left. + \gamma_{\text{II}}^{(k)}(\tau_0) \sum_{i=1}^{N_c-1} \left[d_i^2 c_i^{(1)} c_{i-u^{(k)}-1}^{(k)} b_{f(m-u^{(k)}-1)}^{(k)} \right] \right\} \tag{6.12}
\end{aligned}$$

whose effect on the decision variable strictly depends on the cross-correlation property between codes $\{c_i^{(1)}\}$ and $\{c_i^{(k)}\}$.

In the following, we assume that code synchronization is achieved after an initial acquisition phase, i.e., $u^{(1)} = 0$. To this purpose, powerful acquisition techniques (e.g., [63]) can be adopted. From (6.10), we have

$$\begin{aligned}
y_m &= b_m^{(1)} \left[\gamma_{\text{I}}^{(1)}(\tau_0) N_s + \gamma_{\text{II}}^{(1)}(\tau_0) \sum_{i=1}^{N_s-1} c_{i-1}^{(1)} c_i^{(1)} \right] \\
&\quad + \gamma_{\text{II}}^{(1)}(\tau_0) c_{-1}^{(1)} c_0^{(1)} b_{m-1}^{(1)} + \Psi_m + y_m^{(C)} + z_m.
\end{aligned} \tag{6.13}$$

Looking at (6.13), it can be noted that the useful term depends on the partial autocorrelation properties of code $\{c_i^{(1)}\}$.

As a further hypothesis, we assume that a perfect TOA estimate is available. The TOA estimator robust to clutter proposed in [94] can be adopted to this purpose. Once the TOA is known, the reader can adjust its internal clock so that it becomes synchronous to that of the intended tag, i.e., $\delta^{(1)} = 0$, and the optimal choice for τ_0 can be derived. In such a case^g

$$\gamma_I^{(1)}(\tau_0) = E_w = \int_{-\infty}^{\infty} (w^{(1)}(t))^2 dt \quad (6.14)$$

and (6.13) can be further simplified leading to

$$y_m = b_m^{(1)} N_s E_w + \Psi_m + y_m^{(C)} + z_m = b_m^{(1)} \rho E_s + y_m^{(C)} + \Psi_m + z_m, \quad (6.15)$$

where $E_s = N_s E_w$, and ρ is the normalized cross-correlation between pulses $w_I^{(1)}(t)$ and $h(t)$, which accounts for the mismatch due to pulse distortion. Parameters E_w and E_s represent the average received energy per pulse and symbol, respectively. For further convenience, we define the signal-to-clutter ratio (SCR) as

$$\text{SCR} = \frac{E_s}{N_s E_c} \quad (6.16)$$

where $E_c = \int_0^{T_p} (w^{(C)}(t))^2 dt$ is the energy per pulse of the clutter component.

Note that the accurate estimation of τ_0 , which is a peculiarity of UWB signals, allows for high accuracy ranging, and hence high accuracy localization of the tag when at least three readers access the tag [11, 12, 30].

6.3 Laboratory Measurements

Experimental data were collected in two different scenarios in ENSTA - Paris-Tech laboratory. The first scenario is in a controlled environment consisting of an anechoic chamber. Data collected can be successfully utilized to characterize the UWB antenna backscatter properties and to assess the system performance in ideal conditions. The second scenario (shown in Fig. 6.4) is a realistic indoor environment consisting of a laboratory with furniture and having dimensions $5.13 \times 4.49 \text{ m}^2$. In this case, the data collected enable the performance characterization in close-to-reality conditions.

In both scenarios, the backscattering signals from an UWB antenna were measured in the frequency domain by means of a vector network analyzer

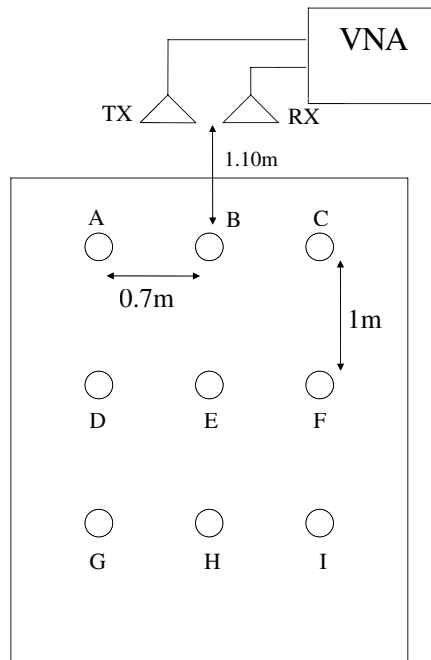


Figure 6.3: Grid considered for the measurement campaign at ENSTA-ParisTech. The distances between each point and the antennas connected to the vector network analyzer are also reported.

in the 2 – 12 GHz band with steps of 5 MHz. Two Horn Lindgren 3117 antennas were employed as reference antennas. They were placed in a quasi-monostatic configuration, separated by 18 cm, guaranteeing a high isolation between the transmit and receive channels as shown in Fig. 6.4. The UWB scattering of a DFMS antenna was tested. In particular, the DFMS is a small planar antenna of dimensions $(40 \times 24 \times 3) \text{ mm}^3$ characterized by moderately directional and non-dispersive properties, which make it quite suitable for RFID tags [162]. Three different load conditions (open-circuit, short-circuit, and matched) and several antenna orientations were considered. Inside the anechoic chamber, the antenna under test was placed on a 3D positioner at distance $d_{\text{ref}} = 1.46 \text{ m}$ (DFMS) from the reference antennas dressed with absorbers to create a quasi-free-space condition. The laboratory environment consisted of a room of dimension $(5.13 \times 4.49) \text{ m}^2$, where a rectangular grid of nine points as shown in Fig. 6.3, spaced out of about 1 m in depth and 70 cm in width, was defined. The tag DFMS antenna was positioned alternatively in each point on a vertical support still dressed with absorbers. For both cases, a simple data post-processing was performed to obtain the antenna backscattering response from the measured parameter $S_{21} = H(f; d_{\text{ref}}, X, \Theta)$,



Figure 6.4: Indoor scenario considered for the measurement campaign at ENSTA-ParisTech.

where H denotes the round trip channel transfer function in the frequency domain measured for a tag placed at distance d_{ref} from the reader, X refers to different tag load configurations (i.e. $X = 0$ and $X = 1$ means respectively short and open circuit tag), and Θ indicates the reader-tag orientation in the 3D space. The collected data were first windowed in the frequency domain to avoid ringing effect. Then, applying the inverse Fourier transform, the signal in the time domain was derived. In the post-processing phase, the transmitted pulse has been chosen to obtain a transmitted signal compliant with the 3.1 – 10.6 GHz FCC mask. Specifically, the 6th derivative Gaussian monocycle has been considered, as described in Sec. 1.5.3 [11]. Figure 6.5 a shows the backscattered signal in the anechoic chamber for OC and SC conditions. In order to easily discriminate in the time domain the structural mode from the antenna mode, a $50\ \Omega$ coaxial cable (delay line) of electric length 40 cm was inserted between the tag antenna and the load.

The structural and antenna modes can be clearly distinguished, where only the latter depends on the antenna load. In particular, the difference of 180° for the antenna mode scattering between the two load conditions is clearly evidenced. It has to be remarked that the delay line used for measurements is not required in a real system implementation as the communication scheme proposed in this article is able to discriminate between the antenna and structural mode components, even if they are time overlapped, as will be illustrated in the next section.

In Fig. 6.5b, an example of backscattered signal received in the laboratory scenario from the tag placed at location H (distance 3.10 m) is reported. As

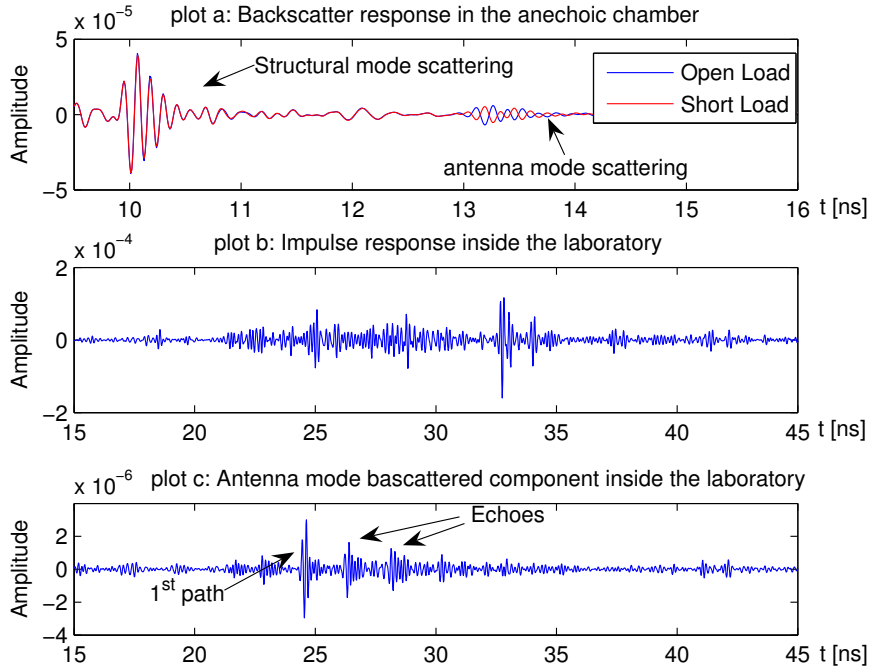


Figure 6.5: Example of backscatter responses collected inside in the anechoic chamber (plot a) at distance $d_{\text{ref}} = 1.46$ m, in the laboratory (plot b) grid location H at distance of 3.10 m, and of the only antenna mode contribution after clutter removal (plot c) in the same location H.

can be noted, several clutter components (including the antenna structural mode) are present. Figure 6.5c shows the antenna mode backscattered signal (of interest) after clutter removal. Owing to its small amplitude, it turns out to be completely buried within the clutter component. The presence of some echoes received after the first direct path is also clearly seen and can be ascribed to indirect paths between the tag and the reader. In most of the considered configurations, the normalized cross-correlation ρ between the backscattered signals in the case of open- and short-circuit loads is close to -1 , as expected for antenna mode signals. This good symmetry property is useful in case of signaling schemes employing antipodal pulses and justifies, in the following analysis, the approximation of perfect pulse symmetry, i.e., $w(t) = w(t; d, 0, \Theta) = -w(t; d, 1, \Theta)$, where for notation compactness, we have hidden in $w(t)$ the explicit dependence on d and Θ .

6.4 Numerical Results

In order to evaluate the performance of the proposed passive UWB RFID communication system, the following parameter values have been considered, if otherwise indicated: $T_p = 100$ ns, $F = 4$ dB (receiver noise figure), and EIRP = -6.7 dBm.

6.4.1 System Performance in a Single-Tag Scenario

We now investigate the performance in a single-tag scenario to gain some insights about the attainable ultimate performance using the backscatter communication mechanism. The complete multi-tag scenario will be investigated in the numerical results using experimental data. In the absence of other tags in the environment, from (6.12) we have $\Psi_m = 0$, whereas clutter contribution is completely suppressed thanks to the adoption of zero mean codes.

The simplest UWB receiver is the single-path matched filter (SPMF) [62] where, in the absence of other information, $h(t)$ can be chosen to be proportional to $w(t; d_{\text{ref}}, 0, \Theta_{\text{max}})$, i.e., the received pulse at the reference distance d_{ref} in free-space propagation at the orientation Θ_{max} of maximum tag's antenna radiation. This receiver is optimal in AWGN at Θ_{max} , but it is in general sub-optimal in a multipath scenario. In such a case, the receiver in Fig. 4.4 can easily be extended to obtain a Rake structure composed of a number L_p of fingers, each of them synchronized to a different path [48, 163]. The performance of the SPMF, or any other receiver solutions such as those based on Rake structures, are bounded by the ideal matched filter (IMF) receiver. The IMF receiver is equivalent to a Rake receiver with unlimited correlators (*all Rake Receiver*) and a perfect estimate of the received waveform to be used as local template $h(t)$ [62, 164]. This means that $h(t)$ is proportional to the effective received waveform $w(t)$ and, consequently, the performance of the IMF can be obtained by setting $\rho = 1$ in (6.15). In general, from (6.15), it is easy to show that the bit error probability (BEP) is given simply by [12, 14]

$$P_b = \frac{1}{2} \operatorname{erfc} \left(\sqrt{\frac{E_s \rho^2}{N_0}} \right), \quad (6.17)$$

where $\operatorname{erfc}(\cdot)$ is the complementary error function.

For further convenience, we define $G_{\text{ref}} = E_{\text{ref}}/E_t$, i.e., the round-trip channel power gain at the reference distance d_{ref} and at the maximum direction of radiation Θ_{max} in AWGN scenario, where E_{ref} is the received energy

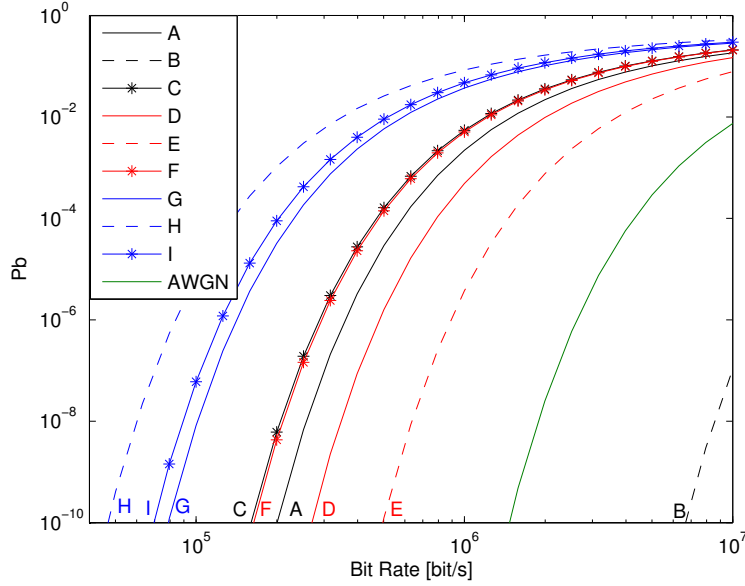


Figure 6.6: BEP as a function of the bit rate R_b in different tag locations (Laboratory scenario). The SPMF receiver is considered.

per pulse at the reference distance d_{ref} and E_t is the energy associated to the transmitted pulse. In addition, we assume a typical exponential path loss law where the power path loss exponent β usually ranges between ≈ 1.8 and ≈ 4 [165]. The BEP can be rewritten as

$$P_b = \frac{1}{2} \operatorname{erfc} \left(\sqrt{\frac{P_t G_{\text{ref}} \rho^2 \left(\frac{d_{\text{ref}}}{d}\right)^{2\beta}}{N_0 R_b}} \right), \quad (6.18)$$

where $R_b = 1/(N_c T_c)$ is the data rate (symbol rate), and $P_t = E_t/T_p$. It is interesting to note that the exponent 2β is present in (6.18) instead of β to account for the two-way link.

BEP–Data Rate in Single-Tag Laboratory Scenario

Results related to the SPMF and IMF receivers in every location in the grid inside the laboratory are shown in Figs. 6.6 and 6.7, respectively, in terms of BEP calculated using (6.18) and deriving ρ from measurements. For the sake of comparison, the performance in AWGN is also reported for $d = 1.46$ m. As expected, the performance of the IMF receiver is significantly better than that obtained using the simple SPMF receiver because all the useful energy coming from multipath is captured and the performance depends only on

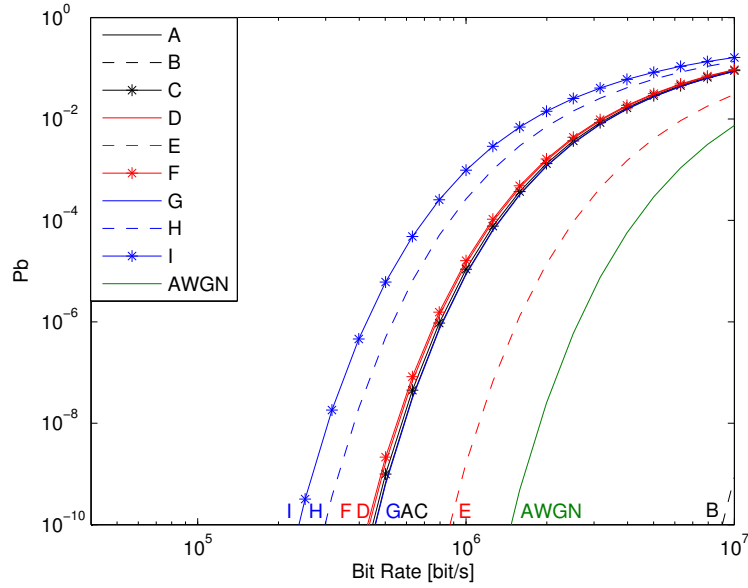


Figure 6.7: BEP as a function of the bit rate R_b in different tag locations (Laboratory scenario). The IMF receiver is considered.

the received power. In fact, the SPMF receiver is not able to collect the energy from multipath and suffers from pulse distortion due to propagation as well as antenna effects. This problem can be mitigated by considering more complex receiver structures such as those based on Rake solutions performance of which is bounded by the one provided by the IMF receiver. The performance obtained with the tag located at location B is better than that in AWGN condition because of the shorter distance (1.10 vs. 1.46 m). Note that in some cases tags placed at larger distances provide a better performance. This depends on the higher amount of energy that can be collected in some locations because of the presence of richer multipath components in the received signal.

As a numerical example, with a target BEP $P_b = 10^{-3}$, data rates up to 200 kbit/s at a distance of 3.10 m with a transmitted power lower than 1 mW are feasible in a realistic environment.

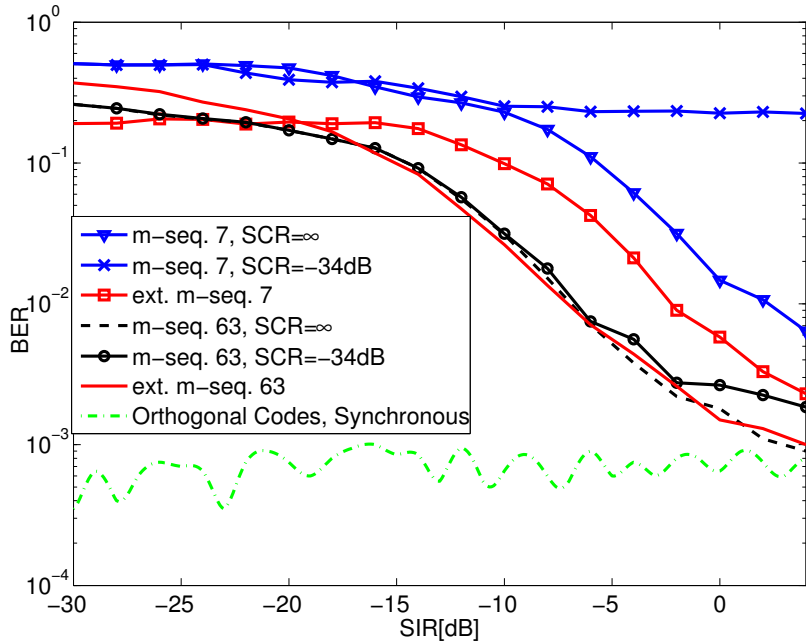


Figure 6.8: BER as a function of the SIR in the anechoic chamber scenario where clutter is summed up artificially. DFMS antenna considered.

6.5 System performance in a Multi-Tags Scenario

6.5.1 BER–SIR in Multi-Tags Anechoic Chamber Scenario with Artificial Clutter

We evaluate the BER in the presence of an interfering tag as a function of the signal-to-interference ratio (SIR). The SNR has been fixed to 7 dB, corresponding to an error floor of about 10^{-3} in the absence of interference. Results have been obtained by Monte Carlo simulations starting from antenna backscatter measurements in anechoic chamber. The interfering tag, the clutter and the thermal noise signal components have been added artificially according to the set SNR, SIR, and SCR values.

The clutter waveform has been taken from measurements in the laboratory environment. The worst-case scenario with the interfering signal completely overlapped to the useful one is considered.

In Fig. 6.8, results associated to different spreading codes are compared. In the quasi-synchronous scenario, orthogonal Hadamard codes are used. As expected, the performance is not sensitive to the presence of both the inter-

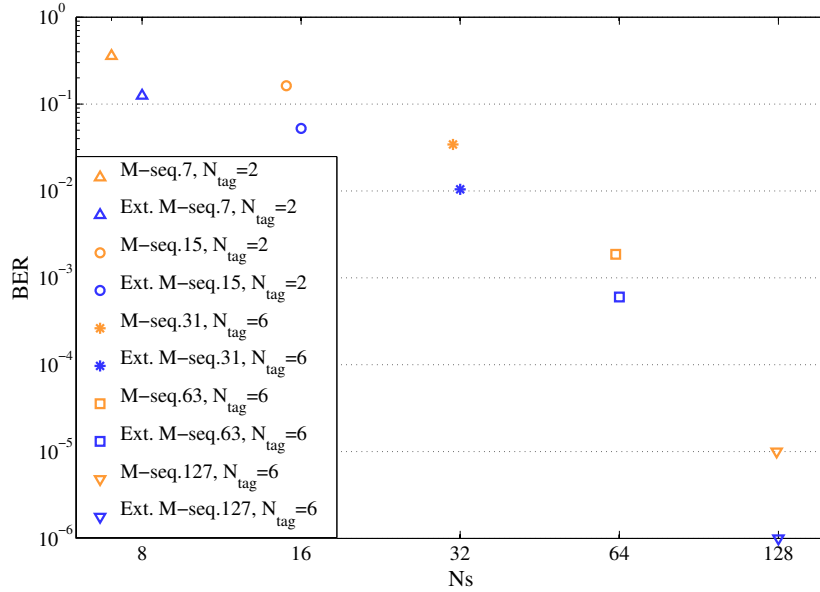


Figure 6.9: BER vs N_s in multi-tag laboratory environment and asynchronous scenario.

ference and the clutter (because of the zero-mean code used). In the asynchronous scenario, m -sequences spreading codes of length 7 and 63 have been considered. From the curve corresponding to m -seq. 7, it can be observed that when the clutter is present and it is significant ($SCR = -34$ dB), even for large SIR values, the performance is limited by the clutter. A remarkable improvement can be obtained by extending the length of the code by one (zero-mean code). When longer codes are used (e.g., m -seq. 63), the impact of clutter becomes less significant and good performance can be achieved even using quasi zero-mean codes. These considerations suggest that the adoption of extended m -sequences is the appropriate choice, especially when working with short codes.

6.5.2 BER- N_s in Multi-Tag Laboratory Scenario

In Fig. 6.9 the bit error rate (BER) as a function of the number of pulses per symbol N_s , when $N_{tag} = 6$ tags are present, is reported. Curves are obtained for $T_p = 64$ ns. A RRC, compliant to the EU-UWB mask in the bandwidth 3.1 – 4.8 GHz is used as transmitted signal. At the receiver side, a SPMF is considered which is adapted to the received pulse at the reference distance in free-space propagation in the direction of tag's maximum radiation.

The signal measured from the location D of the grid is considered as that backscattered by the useful tag, and the backscattered signals coming from

locations A, B, C, E, F constitute the MUI. In the asynchronous scenario, where reader and tags are not synchronized, it is possible to observe the beneficial impact of extended m -sequences with lengths 31, 63, 127 on the BER. In the same plot we also report the performance obtained when only one interfering tag located in F is present. Again, the use of an extended m -sequence leads to an improved performance. This confirms that extended m -sequences are a good solution for clutter and MUI mitigation in asynchronous scenarios, in total agreement with considerations on Chapter 4 for what a fully asynchronous scenario is concerned,

6.5.3 BER- N_s in Multi-Tags Multipath Scenario with Artificial Clutter

We analyze now the BER in a more complex scenario in which 59 interfering tags are present, as a function of the total number of pulses per symbol N_s , with $T_p = 128$ ns, $N_{pc} = 1$ and $N_c = 1024$. Results have been obtained by Monte Carlo simulations, starting from channel responses drawn from the 802.15.4a CM1 channel model [165]: a double convolution of the transmitting RRC pulse with the channel impulse response has been performed in order to take into account the two-way link of the backscattered signal. The useful tag have been placed at 7 m distance from the reader, which is characterized by an antenna gain of 5 dBi, while the interfering tags have been considered uniformly distributed in one meter around the useful tag. For what the clutter is concerned, a uniform power delay profile in the overall interval T_p has been taken into account, with paths spaced apart of 0.95 ns, each path's amplitude characterized by Nakagami- m fading, with $m = 3$, and a root-mean-squared value of 0.5 mV at the receiver. In Fig 6.10 results related to different spreading codes are compared. In a quasi-synchronous scenario, where tags' and reader's code generators are synchronized, and the time-of-arrival of the interference components depends only on tags' position, the performance of zero-mean orthogonal Hadamard codes results to be not affected by MUI and clutter. On the contrary, when reader and tags are asynchronous, the performance of the system when using orthogonal codes drastically degrades due to the joint effect of multipath and poor cross-correlation properties of the codes (MUI). For what the m -sequences are concerned, as can be noticed in Fig. 6.10, significant performance degradation is obtained in the presence of strong clutter since sequences are not balanced. On the other hand, the choice of zero mean codes (extended m -sequences) still confirms to be a good solution to avoid clutter effects at the expense of a slight performance loss due to degraded cross-correlation properties.

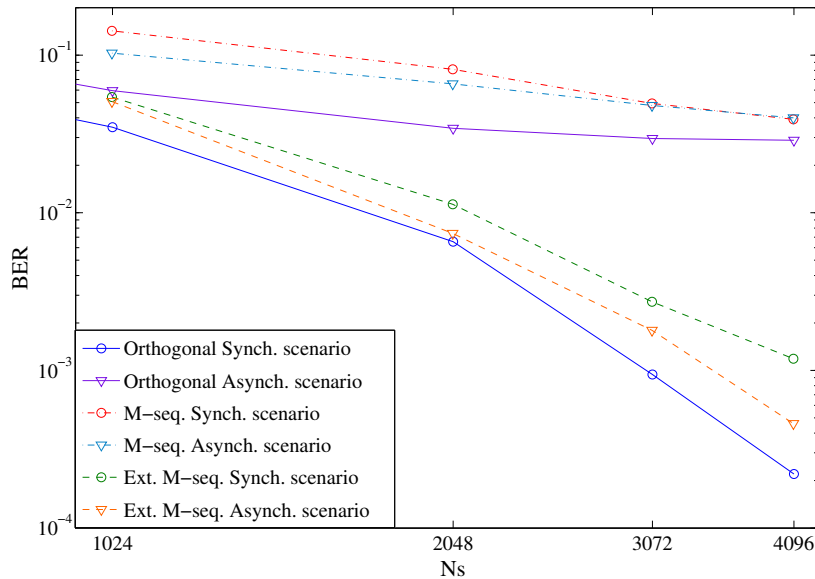


Figure 6.10: BER vs N_s in multipath 802.15.4a CM1 channel.

6.6 Conclusions

In this Chapter we have addressed UWB RFID systems adopting backscatter modulation by proposing a reader and tag architecture for data communication able to work in the presence of strong clutter and interference. The achievable range and performance has been investigated using measured data collected in controlled and realistic environments. It has been shown that clutter is one of the main limiting factor and that it can be mitigated or suppressed through the architecture proposed and the adoption of zero mean spreading codes without compromising the performance in multi-tag scenario. Numerical results show that operating ranges of several meters are feasible in realistic scenarios with a transmitted power less than 1 mW.

Conclusions and Perspectives

This work was developed with the intent to study UWB RFID systems based on the modulation of the backscattered signal considering different related issues. The European Project SELECT gave the motivation and the opportunity to investigate the combination of UWB and RFID technologies which are expected together to overcome many limitations of current narrowband RFID devices. The consciousness that before the design of proper system architectures for backscatter communication it was fundamental to understand the basic EM mechanisms underlying the interaction between readers and tags, was reflected in a wide investigation ranging from EM characterization of backscatter links to the definition and design of signal structures and transmission schemes. The validation was performed through both analytical and experimental results. Specifically, Chapter 1 showed a general overview about current UWB RFID technologies, discussing their main limitation when adopted in RTLS in industrial environments.

In Chapter 2 the tag backscattering properties were analyzed in several ways, both in ideal and real conditions. Simple approaches for the tag antenna backscattering component reconstruction were shown and tested, with the final conclusion that the same results can be obtained by performing direct simulations/measurements or by means of the superposition and reciprocity principles. The proposed methodologies helped to increase the comprehension of the phenomena which appear in the backscattering mechanism, with the opportunity to avoid the adoption of simulations and measurements which are often very time demanding. In addition, the relation between the tag transfer function and the overall backscatter response was exploited in Sec. 3.3 to evaluate the detection and localization coverage in a monitored environment, by underlying the link between the analysis concerning the EM signals and the system architecture.

The interaction between passive UWB RFID antennas with close disturbers was addressed in Chapter 3, and the study was based on measurements in an anechoic chamber. In particular, it was shown how the tag radiation characteristics are greatly affected by the presence of the object,

and the measured data were exploited to validate the detection and localization coverage using the system set-up described in Chapter 4 and the SNR threshold derived in Chapter 5. The interaction between a tag and a close metallic reflector was also investigated. It was shown that the average backscattered energy in the monostatic antenna mode is increased in the presence of a metallic object placed at close distances. This effect counters simple intuition and combats the well known belief for UHF-RFID that metals are detrimental to the RFID detection range. Further studies need be carried out, for example, by averaging the energy over the whole sphere or by analyzing the respective role of the tag antenna and the reflector.

In Chapter 4, an UWB RFID system based on the modulation of the backscattered signal was addressed. Implementation issues that can arise during system design are described, and corresponding solutions were proposed in order to counteract the main issues. The joint adoption of code acquisition schemes with codes properly designed to combat all the system non-idealities, was proposed to guarantee reliable performance. It was actually shown in Chapter 5 that the joint use of orthogonal Gold codes with proper low-complexity detection and synchronization schemes involving bin-dependent thresholding is a promising solution to overcome implementation impairments, such as tag clock drift and near-far effects. The tag detection performance was evaluated in different scenarios in terms of detection and false alarm rates, so to analyze the robustness of the proposed schemes with different code families.

In Chapter 6, a UWB RFID reader and tag architecture for data communication based on backscatter modulation was proposed, which is able to work in the presence of strong clutter and interference. The achievable range and performance were investigated, showing that clutter is the main limiting factor and that it can be mitigated or suppressed through the architecture proposed and the adoption of zero mean spreading codes.

The obtained results showed that the UWB RFID based on the modulation of the backscatter signal represents a promising candidate for the next RFID generation, due to the evaluable performance achieved with a low cost reader-tag architecture.

However, further work still need to be carried out in order to completely validate the proposed UWB RFID system.

For what concerns the analysis of the signals involved in the backscatter mechanism, the results reported in Chapter 2 and 3 can stimulate a deeper research on this topic, especially about the interaction between a UWB antenna and a metallic reflector. Some of the first results combat the well known belief that metallic plates close to the tag are detrimental for reader-tag communication, and thus further analysis is required. For example, the

respective roles of the tag antenna and the reflector could be separately investigated.

Furthermore, the proposed system architecture can be exploited also for TOA estimate and positioning. Due to the adoption of the UWB technology, it is expected that a localization performance in the order of the sub-meter level can be guaranteed. This is also currently investigated within the SELECT consortium in order to achieve the demonstration of the UWB backscattering based RFID system targeted in the project.

Other future works can investigate different readers configurations in the scenario, in order to optimize the detection and localization coverage. Among all the solutions, readers working in bistatic configuration could be matter of study, as it might be a promising approach to improve the tag localization. In this sense, the RFID technology could be jointly adopted with radar sensor networks (RSNs) [166–169] to enhance the localization of passive tags (without active transmitters) as well as of moving passive objects which are not equipped with tags.

Appendix A

Theoretical Analysis on the SQNR Before and After De-spreading

The purpose of this analysis is to derive the relationship between the SQNR at the ADC output and the output of the despreader as a function of the number of pulses N_s . In the figure below we report the analyzed ADC-Despreader section where the ADC output is multiplied by the tag code $\{c_i\}$, and then it is accumulated for N_s times. With the purpose of clutter removal, the code $\{c_i\}$ is designed to be balanced, i.e., with an equal number $N_s/2$ of "+1s" and "-1s".

In particular, we can express the input signal X_i , corresponding to the i -th sample taken within the generic symbol time, as:

$$X_i = x_u + x_c + n_i \quad (\text{A.1})$$

for $i = 1, \dots, N_s$, where x_u is the useful signal component, x_c is the clutter component (which mainly affects the upper bound of the dynamic range at the ADC input), and n_i is the additive Gaussian noise. The useful signal component and the clutter component are modeled as random variables both constant within a symbol time, whereas the thermal noise samples $\{n_i\}$ are independent Gaussian random variables.

We can express the output \hat{X}_i of the ADC as

$$\hat{X}_i = x_u + x_c + n_i + \epsilon_x \quad (\text{A.2})$$

where ϵ_{x_i} is the quantization noise. Under quite general conditions on the statistics and dynamic of x_u and x_c , it turns out that the quantization noise is a uniformly distributed random variable in $[-\delta/2, \delta/2]$, where δ corresponds

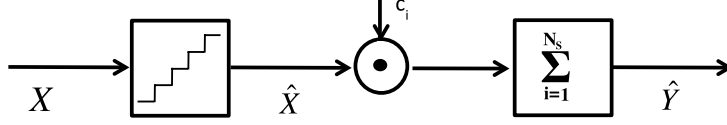


Figure A.1: The considered scheme for the ADC and despreader.

to the quantization step amplitude¹.

Now, looking at the output of the accumulator, we can express \hat{Y} (under the hypothesis of zero mean code) as

$$\hat{Y} = N_s \cdot x_u + n_{out} + \epsilon_y \quad (\text{A.3})$$

where n_{out} is given by

$$n_{out} = \sum_{i=1}^{N_s} c_i \cdot n_i \quad (\text{A.4})$$

and

$$\epsilon_y = \sum_{i=1}^{N_s} c_i \epsilon_{x_i} \quad (\text{A.5})$$

The SQNR_{in} and SQNR_{out} , respectively, at the output of the ADC and of the accumulator are:

$$\text{SQNR}_{in} = \frac{\mathbb{E}\{x_u^2\}}{\mathbb{E}\{\epsilon_x^2\}} \quad (\text{A.6})$$

and

$$\text{SQNR}_{out} = \frac{N_s^2 \cdot \mathbb{E}\{x_u^2\}}{\mathbb{E}\{\epsilon_y^2\}} \quad (\text{A.7})$$

In the following, we find the relationship between $\mathbb{E}\{\epsilon_y^2\}$ and $\mathbb{E}\{\epsilon_x^2\}$. In particular, we can write the second-order moment of ϵ_y as

$$\mathbb{E}\{\epsilon_y^2\} = \mathbb{E}\left\{\left(\sum_{i=1}^{N_s} c_i \cdot \epsilon_{x_i}\right)^2\right\} = \mathbb{E}\left\{\sum_{i=1}^{N_s} c_i^2 \cdot \epsilon_{x_i}^2 + 2 \cdot \sum_{i=1}^{N_s-1} \sum_{j=i+1}^{N_s} c_i \cdot \epsilon_{x_i} \cdot c_j \cdot \epsilon_{x_j}\right\} \quad (\text{A.8})$$

We derive now (A.8) between the input and output stages for two extreme cases: low SNR (where the thermal noise amplitude is larger than the quantization step), and high SNR (thermal noise negligible with respect to the quantization step).

¹This assumption is in general a good approximation if the dynamic of the signals is sufficiently larger than δ and for a wide range of signal statistics.

A.1 Analysis at Low SNR

In this case, we can assume that ϵ_{x_i} and ϵ_{x_j} are independent (due to the Gaussian thermal noise), obtaining:

$$\mathbb{E} \left\{ 2 \cdot \sum_{i=1}^{N_s-1} \sum_{j=i+1}^{N_s} c_i \cdot \epsilon_{x_i} \cdot c_j \cdot \epsilon_{x_j} \right\} = 0 \quad (\text{A.9})$$

and thus we can write

$$\mathbb{E} \{ \epsilon_y^2 \} = \mathbb{E} \left\{ \sum_{i=1}^{N_s} c_i^2 \cdot \epsilon_{x_i}^2 \right\} = \sum_{i=1}^{N_s} c_i^2 \cdot \mathbb{E} \{ \epsilon_{x_i}^2 \} = N_s \cdot \mathbb{E} \{ \epsilon_x^2 \}. \quad (\text{A.10})$$

Finally we have the expression:

$$\text{SQNR}_{\text{out}} = \frac{N_s^2 \cdot \mathbb{E} \{ x_u^2 \}}{N_s \cdot \mathbb{E} \{ \epsilon_x^2 \}} = N_s \cdot \text{SQNR}_{\text{in}} \quad (\text{A.11})$$

where it is evident the processing gain of N_s not only in the SNR but also in the SQNR. Thanks to the process gain N_s a lower SQNR can be tolerated at the input port of the de-spreading (i.e., a very raw useful signal amplitude digital conversion) since the useful signal will be correctly retrieved anyway (i.e., detected with good resolution in the digital domain) thanks to processing gain due to de-spreading plus accumulation.

Figure A.2 shows simulation results of the proposed system obtained in Matlab, where a receiver noise figure of 4 dB has been considered to dimension the thermal noise, and different numbers of quantization bits have been adopted inside the ADC, whose range is determined by fixing a maximum clutter value of 14 mV. Results are in agreement with the previous mathematical relations, apart from the case of 5 bits, for which the assumptions behind the model are no more fully verified.

A.2 Analysis at High SNR

At high SNR, the quantization noise does not depend on the thermal noise but only on the useful signal and clutter components. Specifically, within one observed bit, the clutter is constant and the useful signal assumes only two values through the code symbols $\{c_i\}$. Consequently, ϵ_{x_i} and ϵ_{x_j} are not statistically independent and previous equations are no more valid since the terms cannot be neglected. In fact, conditioned on the code, ϵ_{x_i} can take only

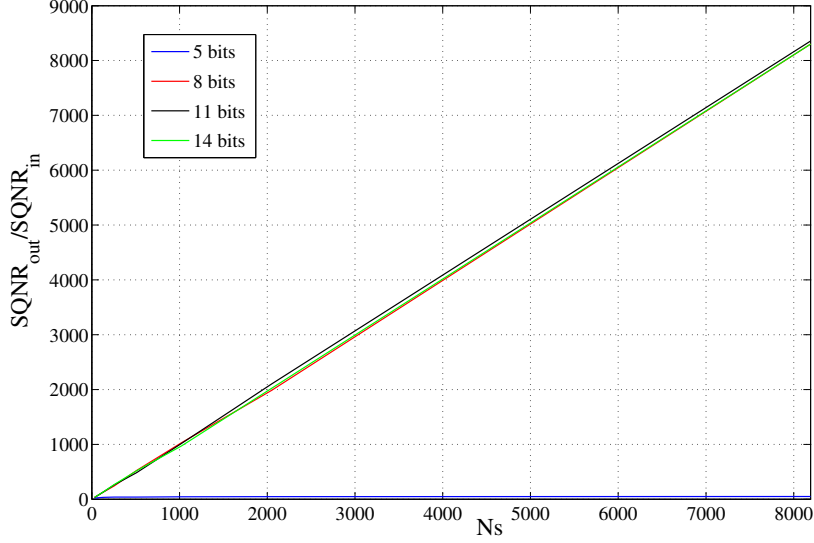


Figure A.2: SQNR at the output of the de-spreader-accumulator, for low SNR.

two different values leading to $\epsilon_{x_i|+1} = \epsilon_{x|+1}$ and $\epsilon_{x_i|-1} = \epsilon_{x|-1}$ depending on the value of the i th symbol c_i . We can write $\mathbb{E}\{\epsilon_y^2\}$ as:

$$\begin{aligned}
\mathbb{E}\{\epsilon_y^2\} &= \mathbb{E} \left\{ \sum_{i=1}^{\frac{N_s}{2}} c_i^2 \cdot \epsilon_{x_i|+1}^2 + \sum_{i=\frac{N_s}{2}+1}^{N_s} c_i^2 \cdot \epsilon_{x_i|-1}^2 + 2 \cdot \sum_{i=1}^{\frac{N_s}{2}-1} \sum_{j=i+1}^{\frac{N_s}{2}} c_i \cdot \epsilon_{x_i|+1} \cdot c_j \cdot \epsilon_{x_j|+1} \right. \\
&\quad \left. + 2 \cdot \sum_{i=\frac{N_s}{2}+1}^{N_s-1} \sum_{j=i+1}^{N_s} c_i \cdot \epsilon_{x_i|-1} \cdot c_j \cdot \epsilon_{x_j|-1} \right\} \\
&= \mathbb{E} \left\{ \epsilon_{x|+1}^2 \cdot \left(\sum_{i=1}^{\frac{N_s}{2}} c_i \right)^2 + \epsilon_{x|-1}^2 \cdot \left(\sum_{i=\frac{N_s}{2}+1}^{N_s} c_i \right)^2 \right\}
\end{aligned} \tag{A.12}$$

where we assumed, without loss of generality, that the first $N_s/2$ symbols of code $\{c_i\}$ are "+1" and the rest are "-1". Then we have

$$\begin{aligned}
\mathbb{E}\{\epsilon_y^2\} &= \mathbb{E} \left\{ \left(\frac{N_s}{2} \cdot \epsilon_{x|+1} \right)^2 \right\} + \mathbb{E} \left\{ \left(-\frac{N_s}{2} \cdot \epsilon_{x|-1} \right)^2 \right\} \\
&= \frac{N_s^2}{4} \cdot \mathbb{E}\{\epsilon_{x|+1}^2\} + \frac{N_s^2}{4} \cdot \mathbb{E}\{\epsilon_{x|-1}^2\} = \frac{N_s^2}{2} \cdot \mathbb{E}\{\epsilon_x^2\}
\end{aligned} \tag{A.13}$$

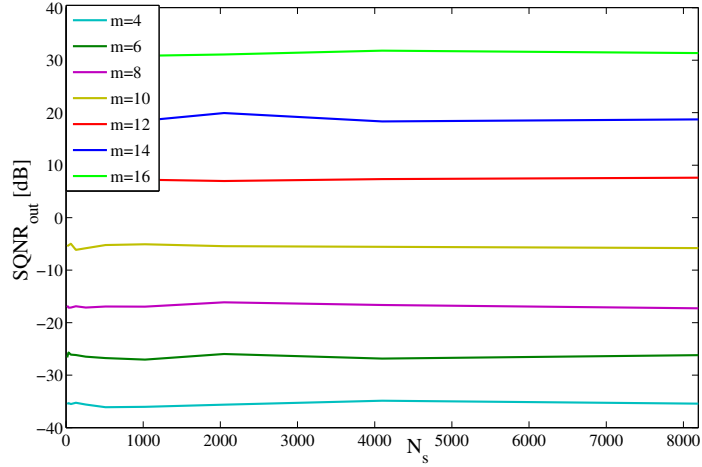


Figure A.3: SQNR_{out} as a function of N_s , for high SNR.

where

$$\mathbb{E} \{ \epsilon_x^2 \} = \frac{1}{2} \mathbb{E} \{ \epsilon_{x|+1}^2 \} + \frac{1}{2} \mathbb{E} \{ \epsilon_{x|-1}^2 \}. \quad (\text{A.14})$$

We finally obtain the SQNR_{out} expression as

$$\text{SQNR}_{\text{out}} = \frac{N_s^2 \cdot \mathbb{E} \{ x_u^2 \}}{\frac{N_s^2}{2} \cdot \mathbb{E} \{ \epsilon_x^2 \}} = 2 \cdot \text{SQNR}_{\text{in}} \quad (\text{A.15})$$

where no dependence on N_s is present, and the processing gain is only 3 dB. The SQNR at the de-spreader output section does not depend on N_s , as previously demonstrated and also reported in Fig. A.3 (note also the expected gap of 6 dB/bit).

In Fig. A.4, it is evident that with a higher number of bits in the ADC, $\text{SQNR}_{\text{out}}/\text{SQNR}_{\text{in}}$ tends to be 3 dB, in according to what previously stated. For lower values of m , differences come from the quantization since, again, the model proposed in the hypothesis is not valid.

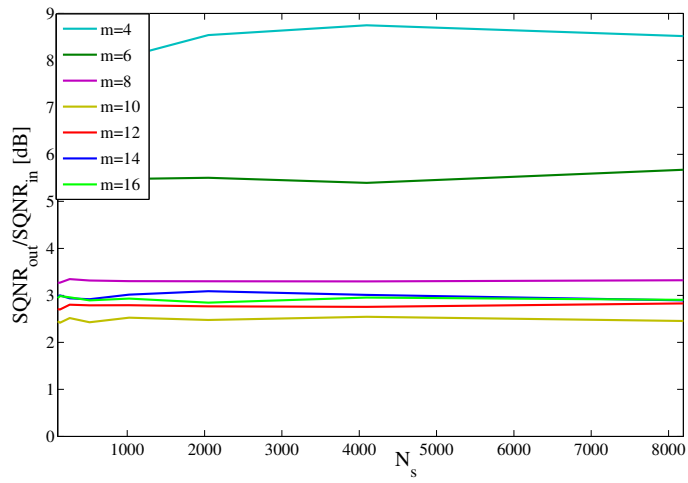


Figure A.4: Relation between $SQNR_{out}$ and $SQNR_{in}$, for high SNR.

Appendix B

General Solutions for Readers Medium Access Control

B.1 Codewords Assignment

B.1.1 Same Codewords Assigned to all the Readers

It has been mentioned that the effect of inter-reader interference strongly depends on crossed characteristics of the spreading codes involved. A first simple option is the assignment of the same codewords to all the readers. All readers transmitted signals reflected by the useful tag (case 1 of Sec. 4.9) can now be considered as useful components, as it is

$$\sum_{i=1}^{N_s} d_i^{(2)} d_i^{(3)} = \sum_{i=1}^{N_s} \left(d_i^{(3)}\right)^2 = N_s \quad (\text{B.1})$$

that is, this contribution is no more interference, but it contributes in enhancing the processing gain (actually this is true if we suppose all readers perfectly synchronized at PRP level and we neglect the possibility of destructive interference due to the path composition at different time-of-arrival (TOA) for both direct paths and multipath components). For case 2, relating to Sec. 4.9, the strongest interferer component is suppressed if the tag codes have zero mean value (this requirement must be also satisfied to remove the clutter), as we have

$$\sum_{i=1}^{N_s} d_i^{(2)} d_i^{(3)} c_i^{(u)} = \sum_{i=1}^{N_s} \left(d_i^{(3)}\right)^2 c_i^{(u)} = \sum_{i=1}^{N_s} c_i^{(u)} = 0 \quad (\text{B.2})$$

In the third case, the interfering component is suppressed or reduced depending to the cross-correlations among tags, since the residual component after

de-spreading is proportional to

$$\sum_{i=1}^{N_s} d_i^{(2)} d_i^{(3)} c_i^{(u)} c_i^{(\text{int})} = \sum_{i=1}^{N_s} \left(d_i^{(3)} \right)^2 c_i^{(u)} c_i^{(\text{int})} = \sum_{i=1}^{N_s} c_i^{(u)} c_i^{(\text{int})}. \quad (\text{B.3})$$

However, it has to be remarked that in this configuration it is expected that the interfering level is negligible because of the poor path-loss (double hop). The advantages of this first solution are:

- The strongest interferer component is suppressed if the tags codes have zero mean value (as it should be for the clutter issue);
- the processing gain is increased, since signals transmitted by other readers can be considered as the useful one, so generally speaking the detection capability is enhanced;
- It is easy to perform.

The main, and not negligible, drawback is that with this configuration it is not possible to estimate the TOA of a tag, thus losing the capability to localize the tags, as only their detection is possible, which is quite limiting in many industrial applications.

B.1.2 Adoption of Performing Codes

A smarter code design and assignment than Sec. B.1.1 is necessary to provide significant inter-reader interference mitigation. Situation in case 2 is the most critical one, therefore we concentrate the attention to this configuration.

For what tags and readers codes are concerned, we have to analyze double and triple cross-correlations. In fact, generalizing the previous analysis, we can call

- Signal component received from the interfering reader is spread using code $d_i^{(\text{int})}$
- Signal component received from the intended tag is spread using the combined code $d_i^{(u)} c_i^{(u)}$
- The useful reader performs the de-spreading with the combined code using different shifts for tag code in order to synchronize, i.e. $d_i^{(u)} c_{i-k}^{(u)}$.

The impact of the interference depends on the double cross-correlation between these three codes, where one out of three could not be aligned as $\sum_i^{N_s} d_i^{(\text{int})} d_i^{(u)} c_{i-k}^{(u)}$.

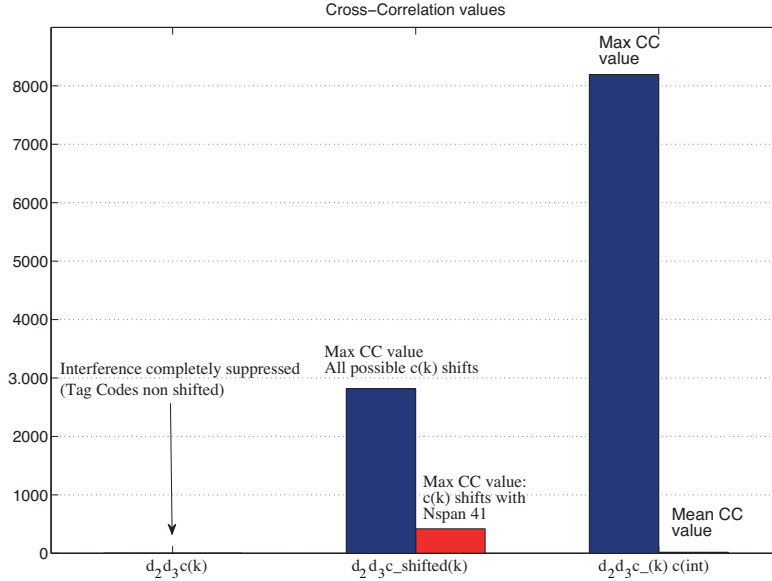


Figure B.1: Double/triple cross-correlations when orthogonal Gold Codes ($N_c = 128$) are assigned to the readers and to the tags.

Based on the analysis presented in Sec. 4.8 it was concluded that for the multi-tag single reader scenario orthogonal Gold codes offer a good trade-off in terms of robustness to clutter, multi-tag interference, and clock drift. In the complete scenario employing multiple readers, the idea is to reuse the same orthogonal Gold codewords for the readers. In fact, we discovered that the correlation between two codewords gives a new codeword that does not belong to the orthogonal Gold family, but it is still orthogonal (when aligned) to other orthogonal Gold codewords. This means that the product $\{d_i^{(\text{int})} d_i^{(\text{u})}\}$ does not belong to the orthogonal Gold codes family, and that $\sum_i^{N_s} d_i^{(\text{int})} d_i^{(\text{u})} c_{i-k}^{(\text{u})}$ has still a low double cross-correlation, even for small misalignments of the tag code. In Fig B.1 we report an example of double and triple cross-correlations when orthogonal Gold codes with $N_c = 128$ are assigned to the readers and to the tags. We can notice that:

- When codes are aligned, the double cross-correlation is 0 (see Fig. B.1 on the left);
- When the useful tag code is not aligned to the readers' codes, due to acquisition schemes, a residual is present (see Fig. B.1 in the middle); note that a generic example, $N_{\text{span}} = 41$, is considered;
- Triple cross-correlation is instead maximum, since the combination of

3 codewords can give another codeword of the same family. On the other side, its mean value is very low (see Fig. B.1 on the right).

This solution allows for a significant reduction of inter-reader interference at the same time giving the flexibility to assign a different code to each reader thus preserving the possibility to overcome the disadvantages of the first solution.

B.1.3 Alternative Solutions

An alternative solution is represented by multi user detection for interference cancellation. This technique presupposes the estimation of all the interference present in the scenario, the detection of all the readers signals, and the digital cancellation in a recursive way (Multi User Detection with successive interference cancellation techniques) at the expense of a high receiver complexity.

Another alternative is to adopt, as reader multiple access technique, the TH, where different codes are assigned to the readers that vary their PRPs, according to a statistical procedure: as general example, the 128 ns PRP would represent an average value during the symbol time. This approach can mitigate the interference without assuring a complete cancellation requiring some hardware flexibility at the both transmitting and receiving side a. A possible solution is represented by the removal of the multi-reader interference directly in the analog domain (before the ADC).

Finally, in order to mitigate this strong interference problem, one solution would be to block somewhat the LOS path using alternately polarized readers [170]. In fact, the readers at opposite corners (in the reference scenario) are shadowed by using orthogonal polarizations. In addition, adjacent antennas (we have 4 readers and only 2 polarization degrees of freedom), can be 45 degrees polarization rotated versus the interfered antenna. This procedure can only mitigate the interference deriving from other readers, but it has been shown in [15] that the reduction can be in the order of 20 dBs.

Bibliography

- [1] C. Floerkemeier, M. Langheinrich, E. Fleisch, F. Mattern, and S. E. Sarma, Eds., *The Internet of Things. First International Conference, IOT 2008, Zurich, Switzerland, March 26-28, 2008, Proceedings*, ser. LNCS, vol. 4952. Berlin Heidelberg New York: Springer, Mar. 2008, available in print and online.
- [2] R. H. Weber, “Internet of things new security and privacy challenges,” *Computer Law amp; Security Review*, vol. 26, no. 1, pp. 23 – 30, 2010.
- [3] A. Iera, C. Floerkemeier, J. Mitsugi, and G. Morabito, “The internet of things,” *IEEE Wireless Communications*, vol. 17, no. 6, pp. 8 –9, december 2010.
- [4] J. Zheng, D. Simplot-Ryl, C. Bisdikian, and H. Mouftah, “The internet of things,” *IEEE Communications Magazine*, vol. 49, no. 11, pp. 30 – 31, november 2011.
- [5] L. Atzori, A. Iera, and G. Morabito, “The internet of things: A survey,” *Computer Networks*, vol. 54, no. 15, pp. 2787 – 2805, 2010.
- [6] J. Mentzer, W. DeWitt, J. Keebler, S. Min, N. Nix, C. Smith, and Z. Zacharia, “Defining supply chain management,” *Journal of Business logistics*, vol. 22, no. 2, pp. 1–25, 2001.
- [7] V. Chawla and D. S. Ha, “An overview of passive RFID,” *IEEE Applications & Practice*, pp. 11–17, Sep 2007.
- [8] R. Fontana, E. Richley, and J. Barney, “Commercialization of an ultra wideband precision asset location system,” in *IEEE Conference on Ultra Wideband Systems and Technologies*, nov. 2003, pp. 369 – 373.
- [9] S. Gezici, Z. Tian, G. Giannakis, H. Kobayashi, A. Molisch, H. Poor, and Z. Sahinoglu, “Localization via ultra-wideband radios: a look at positioning aspects for future sensor networks,” *IEEE Signal Processing Magazine*, vol. 22, no. 4, pp. 70 – 84, july 2005.

- [10] J.-Y. Lee and R. A. Scholtz, "Ranging in a dense multipath environment using an UWB radio link," *IEEE J. Select. Areas Commun.*, vol. 20, no. 9, pp. 1677–1683, Dec. 2002.
- [11] D. Dardari, A. Conti, U. Ferner, A. Giorgetti, and M. Z. Win, "Ranging with ultrawide bandwidth signals in multipath environments," *Proc. of IEEE, Special Issue on UWB Technology & Emerging Applications*, vol. 97, no. 2, pp. 404–426, Feb 2009.
- [12] D. Dardari, R. D'Errico, C. Roblin, A. Sibille, and M. Z. Win, "Ultrawide bandwidth RFID: The next generation?" *Proceedings of the IEEE, Special Issue on RFID - A Unique Radio Innovation for the 21st Century.*, vol. 98, no. 9, pp. 1570 –1582, Sep 2010.
- [13] D. Arnitz, U. Muehlmann, and K. Witrisal, "UWB ranging in passive UHF RFID: proof of concept," *Electronics Letters*, vol. 46, no. 20, pp. 1401 –1402, 30 2010.
- [14] D. Dardari and R. D'Errico, "Passive ultrawide bandwidth RFID," in *IEEE Global Communications Conference (GLOBECOM 2008)*, New Orelans, LA, USA, Nov. 2008.
- [15] <http://www.selectwireless.eu/>.
- [16] P. Withington, H. Fluhler, and S. Nag, "Enhancing homeland security with advanced UWB sensors," *IEEE Microwave Magazine*, Sep. 2003.
- [17] "To strengthen european technology: The support of RFID within FP7," *European Commission DG Information Society and Media / Unit G2 "Microsystems"*, Sep. 2007.
- [18] C. Mutti and C. Floerkemeier, "CDMA-based RFID systems in dense scenarios: Concepts and challenges," Las Vegas, USA, apr 2008, pp. 215–222.
- [19] A. Muchkaev, "Carrierless RFID system," U.S. Patent 7,385,511 B2, Jun. 10, 2008.
- [20] D. Kim, M. Ingram, and J. Smith, W.W., "Measurements of small-scale fading and path loss for long range RF tags," *IEEE Transactions on Antennas and Propagation*, vol. 51, no. 8, pp. 1740–1749, Aug. 2003.
- [21] ISO 18000 Part 6, "Information technology automatic identification and data capture - radio frequency identification for item management air interface," 2003.

- [22] D. Ha and P. Schaumont, “Replacing cryptography with ultra wide-band (UWB) modulation in secure RFID,” in *IEEE International Conference on RFID*, Grapevine, TX, USA, Mar. 2007.
- [23] J. Griffin and G. Durgin, “Reduced fading for RFID tags with multiple antennas,” *IEEE International Symposium on Antennas and Propagation*, pp. 1201–1204, June 2007.
- [24] EPCGlobal, “Class 1 generation 2 UHF air interface protocol standard v.1.0.9,” 2005.
- [25] R. Das and P. Harrop, “RFID forecast, players and opportunities 2007-2017,” available online at <http://www.idtechex.com>, 2007.
- [26] M. Baghaei-Nejad, Z. Zou, H. Tenhunen, and L.-R. Zheng, “A novel passive tag with asymmetric wireless link for RFID and WSN applications,” *IEEE International Symposium on Circuits and Systems (IS-CAS)*, pp. 1593–1596, May 2007.
- [27] K. Finkenzeller and R. Waddington, *RFID handbook: radio-frequency identification fundamentals and applications*. John Wiley, 1999.
- [28] K. Finkenzeller, *RFID Handbook: Fundamentals and Applications in Contactless Smart Cards and Identification. Second Edition*. Wiley, 2004.
- [29] M. Meyers, *Comptia:RFID+certification Passport*. McGraw-Hill, 2007.
- [30] D. Dardari, E. Falletti, and M. Luise, in *Satellite and Terrestrial Radio Positioning Techniques - A signal processing perspective*. Elsevier Ltd, London, 2011.
- [31] M. Win, A. Conti, S. Mazuelas, Y. Shen, W. Gifford, D. Dardari, and M. Chiani, “Network localization and navigation via cooperation,” *IEEE Communications Magazine*, vol. 49, no. 5, pp. 56–62, may 2011.
- [32] R. Verdone, D. Dardari, G. Mazzini, and A. Conti, *Wireless Sensor and Actuator Networks: Technologies, Analysis and Design*. Elsevier, 2008.
- [33] D. Kim, M. Ingram, and W. Smith, “Small-scale fading for an indoor wireless channel with modulated backscatter,” *IEEE 54th Vehicular Technology Conference*, vol. 3, pp. 1616–1620 vol.3, 2001.

- [34] J. Griffin and G. Durgin, “Link envelope correlation in the backscatter channel,” *IEEE Communications Letters*, vol. 11, no. 9, pp. 735–737, September 2007.
- [35] V. Viikari, P. Pursula, and K. Jaakkola, “Ranging of UHF RFID tag using stepped frequency read-out,” *IEEE Sensors Journal*, vol. 10, no. 9, pp. 1535–1539, Sept. 2010.
- [36] G. Li, D. Arnitz, R. Ebel, U. Muehlmann, K. Witrisal, and M. Vossiek, “Bandwidth dependence of cw ranging to UHF RFID tags in severe multipath environments,” in *IEEE International Conference on RFID*, April 2011, pp. 19–25.
- [37] D. Arnitz, U. Muehlmann, and K. Witrisal, “Characterization and modeling of UHF RFID channels for ranging and localization,” *IEEE Transactions on Antennas and Propagation*, vol. 60, no. 5, May 2012.
- [38] D. Dobkin, *The RF in RFID, Passive UHF RFID in Practice*. Newnes, 2008.
- [39] G. R. Paolo Talone, *RFID Tecnologia e applicazioni: Fondamenti delle tecniche e cenni sulle applicazioni di una tecnologia silenziosamente pervasiva*. Fondazione Ugo Bordoni, 2008.
- [40] H. Kuchling, *Taschenbuch der Physik*. Verlag Hari Deutsch, Thun und Frankfurt/Main, ISBN 3-87144-097-3, 2008.
- [41] C. Hartmann, “A global SAW ID tag with large data capacity,” in *IEEE Proceedings on Ultrasonics Symposium*, vol. 1, oct. 2002, pp. 65 – 69 vol.1.
- [42] C. Hartmann, P. Hartmann, P. Brown, J. Bellamy, L. Claiborne, and W. Bonner, “Anti-collision methods for global SAW RFID tag systems,” in *IEEE Ultrasonics Symposium*, vol. 2, aug. 2004, pp. 805 – 808 Vol.2.
- [43] *The State of Radio Frequency Identification (RFID) Implementation and Its Policy Implications*. IEEE USA Books and eBooks, 2005.
- [44] G. De Vita and G. Iannaccone, “Ultra-low-power flash memory in standard 0.35 μm CMOS for passive microwave RFID transponders,” in *Proceedings of IEEE International Symposium on Circuits and Systems (ISCAS)*, May 2006, pp. 4 pp.–3921.

- [45] R. J. Fontana and S. J. Gunderson, "Ultra-wideband precision asset location system," *Proc. of IEEE Conf. on Ultra Wideband Systems and Technologies (UWBST)*, vol. 21, no. 1, pp. 147–150, May 2002.
- [46] M. Z. Win and R. A. Scholtz, "Impulse radio: How it works," *IEEE Commun. Lett.*, vol. 2, no. 2, pp. 36–38, Feb. 1998.
- [47] *Proc. of IEEE, Special Issue on UWB Technology & Emerging Applications*, Feb 2009.
- [48] A. Giorgetti, M. Chiani, and M. Z. Win, "The effect of narrowband interference on wideband wireless communication systems," *IEEE Trans. Commun.*, vol. 53, no. 12, pp. 2139–2149, Dec. 2005.
- [49] L. Yang and G. B. Giannakis, "Ultra-wideband communications: an idea whose time has come," *IEEE Signal Processing Mag.*, vol. 21, no. 6, pp. 26–54, Nov. 2004.
- [50] T. Barrett, "History of ultra wideband (uwb) radar and communications: Pioneers and innovators," in *Proc. Progress in Electromagnetics Symposium*, 2000.
- [51] H. Harmuth, "Applications of walsh functions in communications," *IEEE Spectrum*, vol. 6, no. 11, pp. 82–91, Nov. 1969.
- [52] R. Fontana, "A brief history of UWB communications," in *White Paper, Multispectral Solutions*.
- [53] G. Ross and K. Robbins, "Base-band radiation and reception system," U.S. Patent Application 3,739,392, 12, 1973.
- [54] R. A. Scholtz, "Multiple access with time-hopping impulse modulation," in *Proc. Military Commun. Conf.*, Boston, MA, Oct. 1993.
- [55] M. Z. Win and R. A. Scholtz, "On the robustness of ultra-wide bandwidth signals in dense multipath environments," *IEEE Commun. Lett.*, vol. 2, no. 2, pp. 51–53, Feb. 1998.
- [56] ———, "On the energy capture of ultra-wide bandwidth signals in dense multipath environments," *IEEE Commun. Lett.*, vol. 2, no. 9, pp. 245–247, Sep. 1998.
- [57] Federal Communications Commission, "Revision of part 15 of the commission's rules regarding ultra-wideband transmission systems, first report and order (ET Docket 98-153)," Adopted Feb. 14, 2002, Released Apr. 22, 2002.

- [58] L. Zhao, A. M. Haimovich, and H. Grebel, “Performance of ultra-wideband communications in the presence of interference,” in *Proc. IEEE Int. Conf. on Commun.*, vol. 10, Helsinki, FINLAND, Jun. 2001, pp. 2948–2952.
- [59] J. A. Paradiso and T. Starner, “Energy scavenging for mobile and wireless electronics,” *IEEE Pervasive Computing*, pp. 18–26, Jan-Mar 2005.
- [60] M. Z. Win, “A unified spectral analysis of generalized time-hopping spread-spectrum signals in the presence of timing jitter,” *IEEE J. Select. Areas Commun.*, vol. 20, no. 9, pp. 1664–1676, Dec. 2002, .
- [61] M. Z. Win and R. A. Scholtz, “Ultra-wide bandwidth time-hopping spread-spectrum impulse radio for wireless multiple-access communications,” *IEEE Trans. Commun.*, vol. 48, no. 4, pp. 679–691, Apr. 2000.
- [62] ———, “Characterization of ultra-wide bandwidth wireless indoor communications channel: A communication theoretic view,” *IEEE J. Select. Areas Commun.*, vol. 20, no. 9, pp. 1613–1627, Dec. 2002, .
- [63] W. Suwansantisuk and M. Z. Win, “Multipath aided rapid acquisition: Optimal search strategies,” *IEEE Trans. Inform. Theory*, vol. 52, no. 1, pp. 174–193, Jan. 2007.
- [64] M.-S. Alouini, A. Scaglione, and G. B. Giannakis, “PCC: Principal components combining for dense correlated multipath fading environments,” in *Proc. IEEE Semiannual Veh. Technol. Conf.*, vol. 5, Boston, MA, Sep. 2000, pp. 2510–2517.
- [65] D. Cassioli, M. Z. Win, and A. F. Molisch, “The ultra-wide bandwidth indoor channel: from statistical model to simulations,” *IEEE J. Select. Areas Commun.*, vol. 20, no. 6, pp. 1247–1257, Aug. 2002.
- [66] Y.-L. Chao and R. A. Scholtz, “Ultra-wideband transmitted reference systems,” *IEEE Trans. Veh. Technol.*, vol. 54, no. 5, pp. 1556–1569, Sep. 2005.
- [67] J. D. Choi and W. E. Stark, “Performance analysis of ultra-wideband spread-spectrum communications in narrowband interference,” in *Proc. Military Commun. Conf.*, vol. 21, no. 1, Anaheim, CALIFORNIA, Oct. 2002, pp. 1075–1080.

- [68] J. Conroy, J. L. LoCicero, and D. R. Ucci, "Communication techniques using monopulse waveforms," in *Proc. Military Commun. Conf.*, vol. 2, Atlantic City, NJ, Oct. 1999, pp. 1181–1185.
- [69] J. R. Foerster, "The performance of a Direct Sequence spread ultra-wideband system in the presence of multipath, narrowband interference and multi-user interference," in *Proc. of IEEE Conf. on Ultra Wideband Systems and Technologies (UWBST)*, Baltimore, MD, May 2002, pp. 87–91.
- [70] D. Dardari, "Pseudo-random active UWB reflectors for accurate ranging," *IEEE Commun. Lett.*, vol. 8, no. 10, pp. 608–610, Oct 2004.
- [71] M. Chiani and A. Giorgetti, "Coexistence between UWB and narrowband wireless communication systems," *Proceedings of the IEEE*, vol. 97, no. 2, pp. 231–254, Feb. 2008.
- [72] WiMedia Alliance, "Wimedia," 2005. [Online]. Available: <http://www.wimedia.org>
- [73] *Expected performance and attribute criteria approved for P802.15.3a Alt PHY Selection Criteria, IEEE 802.15.3a official website.* [Online]. Available: <http://www.ieee802.org/15/pub/TG3a.html>.
- [74] ECMA368 ecma-international, "High rate ultra wideband PHY and MAC standard," 2006. [Online]. Available: <http://www.ecma-international.org/publications/files/ECMA-ST/ECMA-368.pdf>
- [75] J. Fernandes and D. Wentzloff, "Recent advances in IR-UWB transceivers: An overview," in *Proceedings of IEEE International Symposium on Circuits and Systems (ISCAS)*, 30 2010-June 2, pp. 3284–3287.
- [76] X. Luo, L. Yang, and G. B. Giannakis, "Designing optimal pulse-shapers for ultra-wideband radios," *Journal of Communications and Networks*, vol. 5, no. 4, pp. 344–353, Dec. 2003.
- [77] H. Sheng, P. Orlik, A. Haimovich, L. Cimini, and J. Zhang, "On the spectral and power requirements for ultra-wideband transmission," in *IEEE International Conference on Communications (ICC)*, vol. 1, May, pp. 738–742 vol.1.
- [78] R. C. Hansen, "Relationship between antennas as scatters and as radiators," *Proceedings of the IEEE*, vol. 77, no. 5, 1989.

- [79] K. Penttila, M. Keskilammi, L. Sydanheimo, and M. Kivikoski, "Radar cross-section analysis for passive RFID systems," *IEE Proc. on Microwave and Antennas Propagation*, vol. 153, no. 1, pp. 103–109, Feb. 2006.
- [80] S. Hu, H. Chen, C. Law, Z. Shen, L. Zhu, W. Zhang, and W. Dou, "Backscattering cross section of ultrawideband antennas," *IEEE Antennas and Wireless Propagation Letters*, vol. 6, pp. 70–73, 2007.
- [81] S. Hu, C. L. Law, Z. Shen, L. Zhu, W. Zhang, and W. Dou, "Backscattering cross section of ultrawideband antennas," *IEEE Antennas Wireless Propagat. Lett.*, vol. 6, pp. 70–72, 2007.
- [82] D. Arnitz, K. Witrissal, and U. Muehlmann, "Multifrequency continuous-wave radar approach to ranging in passive UHF RFID," *IEEE Transactions on Microwave Theory and Techniques*, vol. 57, no. 5, pp. 1398–1405, May 2009.
- [83] S. Hu, Y. Zhou, C. L. Law, and W. Dou, "Study of a uniplanar monopole antenna for passive chipless UWB-RFID localization system," *IEEE Trans. Antennas Propagat.*, vol. 58, no. 2, pp. 271–278, 2010.
- [84] F. Guidi, D. Dardari, C. Roblin, and A. Sibille, "Backscatter communication using ultrawide bandwidth signals for RFID applications," in *D. Giusto et al. (eds.), The Internet of Things: 20th Tyrrhenian Workshop on Digital Communications, SpringerScience+BusinessMedia, Pula, Sardinia, ITALY, Sep. 2009*, pp. 251–262.
- [85] R. D'Errico, "An indoor backscattering channel characterization for UWB passive RFID applications," in *6th European Conference on Antennas and Propagation (EUCAP)*, march 2012, pp. 1169–1173.
- [86] Z. Mhanna, A. Sibille, M. Yousuf, and C. Roblin, "Parametric statistical modeling of power gain patterns for RFID backscattering channels," in *6th European Conference on Antennas and Propagation (EUCAP)*, March 2012, pp. 1041–1045.
- [87] D. Arnitz, U. Muehlmann, and K. Witrissal, "Wideband characterization of backscatter channels: Derivations and theoretical background," *IEEE Transactions on Antennas and Propagation*, vol. 60, no. 1, pp. 257–266, Jan. 2012.

- [88] ———, “Wideband characterization of backscatter channels,” in *11th European Wireless Conference- Sustainable Wireless Technologies (European Wireless)*, April 2011, pp. 1–7.
- [89] Z. Mhanna and A. Sibille, “A statistical UWB-RFID backscattering channel model incorporating propagation and tag variability,” in *IC1004 TD(12) 04012*, 2-4 May, 2012.
- [90] Z. Zou, M. Baghaei-Nejad, H. Tenhunen, and L.-R. Zheng, “An efficient passive RFID system for ubiquitous identification and sensing using impulse UWB radio,” *e & i Elektrotechnik und Informationstechnik, Springer Wien*, vol. 124, no. 11, pp. 397–403, Nov. 2007.
- [91] M. Baghaei-Nejad, D. Mendoza, Z. Zou, S. Radiom, G. Gielen, L.-R. Zheng, and H. Tenhunen, “A remote-powered RFID tag with 10mb/s UWB uplink and -18.5dbm sensitivity UHF downlink in 0.18um CMOS,” in *IEEE International on Solid-State Circuits Conference - Digest of Technical Papers (ISSCC)*, Feb. 2009, pp. 198–199, 199a.
- [92] J. Reunamaki, “Ultra wideband radio frequency identification techniques,” U.S. Patent 7,154,396, Dec. 26, 2006.
- [93] D. Dardari, “Method and apparatus for communication in ultra-wide bandwidth RFID systems,” International Patent Application PC-T/IB2009/000 360, Feb. 25, 2009.
- [94] C. Xu and C. Law, “TOA estimator for UWB backscattering RFID system with clutter suppression capability,” *EURASIP Journal on Wireless Communications and Networking*, vol. 2010, p. 46, 2010.
- [95] Y. Shen and C. L. Law, “A low-cost UWB-RFID system utilizing compact circularly polarized chipless tags,” *IEEE Antennas and Wireless Propagation Letters*, vol. 11, pp. 1382–1385, 2012.
- [96] A. Lazaro, A. Ramos, D. Girbau, and R. Villarino, “Chipless UWB RFID tag detection using continuous wavelet transform,” *IEEE Antennas and Wireless Propagation Letters*, vol. 10, pp. 520–523, 2011.
- [97] K. K. Lee, H. Hjortland, and T. Lande, “Ir-ubw technology on next generation rfid systems,” in *NORCHIP, 2011*, nov. 2011, pp. 1–4.
- [98] Z. Zou, T. Deng, Q. Zou, M. Sarmiento, F. Jonsson, and L.-R. Zheng, “Energy detection receiver with TOA estimation enabling positioning in passive UWB-RFID system,” in *IEEE International Conference on Ultra-Wideband (ICUWB)*, vol. 2, sept. 2010, pp. 1–4.

- [99] L. Stoica, A. Rabbachin, H. O. Repo, T. S. Tiuraniemi, and I. Oppermann, “An ultrawideband system architecture for tag based wireless sensor networks,” *IEEE Trans. Veh. Technol.*, vol. 54, no. 5, pp. 1632–1645, Sep. 2005.
- [100] F. Guidi, M. Sacko, A. Sibille, and C. Roblin, “Electromagnetic analysis of RFID tag backscattering,” in *JNCW, 2011*, Paris, France, 2011.
- [101] C. Balanis, *Antenna Theory*, 3rd ed. Wiley, 2005.
- [102] <http://www.wipl-d.com/>.
- [103] F. Guidi, M. Sacko, A. Sibille, and C. Roblin, “Analysis of uwb rfid tag backscattering in the presence of scatterers,” in *General Assembly and Scientific Symposium, 2011 XXXth URSI*, aug. 2011, pp. 1–4.
- [104] Y. Lo and S. W. Lee, *Antenna Handbook: Theory, Applications and Design*. New York, NY: Van Nostrand Reinhold, 1988.
- [105] H. Ghannoum, S. Bories, and R. D’Errico, “Small-size UWB planar antenna and its behaviour in WBAN/WPAN applications,” in *The Institution of Engineering and Technology Seminar on Ultra Wideband Systems, Technologies and Applications*, april 2006, pp. 221–225.
- [106] S. Bories, H. Ghannoum, and C. Roblin, “Robust planar stripline monopole for UWB terminal applications,” in *IEEE International Conference on Ultra-Wideband, ICU*, sept. 2005, pp. 80–84.
- [107] H. Ghannoum, C. Roblin, and S. Bories, “UWB antennas in body area networks,” in *IEEE International Workshop on Antenna Technology Small Antennas and Novel Metamaterials*, 2006, pp. 136–139.
- [108] D. Dardari, F. Guidi, C. Roblin, and A. Sibille, “Ultra-wide bandwidth backscatter modulation: Processing schemes and performance,” *EURASIP Journal on Wireless Communications and Networking*, vol. 2011:47, no. 1, 2011.
- [109] C. Roblin, S. Bories, and A. Sibille, “Characterization tools of antennas in the time domain,” in *Int. Workshop on Ultra Wideband Systems IWUBS*, June 2-5 2003.
- [110] A. Sibille, S. Bories, R. D’Errico, and C. Roblin, “UWB antenna performance evaluation from the communication system point of view,” in *3rd International Symposium on Wireless Communication Systems, 2006 (ISWCS)*, Sept., pp. 417–422.

- [111] X. Begaud, *UWB Antennas*. Wiley, 2011.
- [112] J. Griffin, G. Durgin, A. Haldi, and B. Kippelen, “RF tag antenna performance on various materials using radio link budgets,” *IEEE Antennas and Wireless Propagation Letters*, vol. 5, no. 1, pp. 247–250, Dec. 2006.
- [113] D. Dobkin and S. Weigand, “Environmental effects on RFID tag antennas,” in *IEEE MTT-S International Microwave Symposium Digest*, June 2005, pp. 4 pp.–.
- [114] L. Ukkonen, M. Schaffrath, J. Kataja, L. Sydanheimo, and M. K. , “Evolutionary RFID tag antenna design for paper industry applications,” *International Journal of Radio Frequency Identification Technology and Applications*, vol. 1, no. 1, pp. 107–122, January 2006. [Online]. Available: <http://inderscience.metapress.com/content/B66RKU2L45AJKPUP>
- [115] G. Marrocco, “The art of UHF RFID antenna design: impedance-matching and size-reduction techniques,” *IEEE Antennas and Propagation Magazine*, vol. 50, no. 1, pp. 66–79, feb. 2008.
- [116] ———, “RFID antennas for the UHF remote monitoring of human subjects,” *IEEE Transactions on Antennas and Propagation*, vol. 55, no. 6, pp. 1862–1870, June 2007.
- [117] G. Marrocco, L. Mattioni, and C. Calabrese, “Multiport sensor RFIDs for wireless passive sensing of objects - basic theory and early results,” *IEEE Transactions on Antennas and Propagation*, vol. 56, no. 8, pp. 2691–2702, Aug. 2008.
- [118] E. Koski, K. Koski, L. Ukkonen, L. Sydanheimo, J. Virtanen, T. Bjorninen, and A. Elsherbeni, “Performance of inkjet-printed narrow-line passive UHF RFID tags on different objects,” in *IEEE International Symposium on Antennas and Propagation (APSURSI)*, July 2011, pp. 537–540.
- [119] K. V. S. Rao, P. Nikitin, and S. Lam, “Antenna design for UHF RFID tags: a review and a practical application,” *IEEE Transactions on Antennas and Propagation*, vol. 53, no. 12, pp. 3870–3876, Dec. 2005.
- [120] V. Casadei, “Experimental characterization of backscattering properties of uwb antennas in the presence of close objects,” Master’s thesis, University of Bologna, 2012. [Online]. Available: <http://amslaurea.unibo.it/4073/>

- [121] <http://www.ets-lindgren.com/3117/>.
- [122] R. D’Errico and A. Sibille, “Interaction between close radiators in UWB arrays,” in *International Conference on Electromagnetics in Advanced Applications*, Sept. 2007, pp. 5–8.
- [123] R. D’Errico, A. Sibille, A. Giorgetti, and M. Chiani, “Antenna diversity in uwb indoor channel,” in *IEEE International Conference on Ultra-Wideband (ICUWB)*, vol. 2, Sept. 2008, pp. 13–16.
- [124] R. D’Errico, H. Ghannoum, C. Roblin, and A. Sibille, “Small semi directional antenna for uwb terminal applications,” in *EuCAP First European Conference on Antennas and Propagation*, Nov. 2006, pp. 1–6.
- [125] C. Roblin and A. Sibille, “Modeling of the influence of body-worn antennas upon the path loss variability in uwb wban scenarios,” in *XXXth URSI General Assembly and Scientific Symposium*, Aug. 2011, pp. 1–4.
- [126] S. Aroor and D. Deavours, “Evaluation of the state of passive UHF RFID: An experimental approach,” *IEEE Systems Journal*, vol. 1, no. 2, pp. 168–176, Dec. 2007.
- [127] A. Guillet, A. Vena, E. Perret, and S. Tedjini, “Design of a chipless RFID sensor for water level detection,” in *15th International Symposium on Antenna Technology and Applied Electromagnetics (ANTEM)*, June 2012, pp. 1–4.
- [128] F. Fuschini, C. Piersanti, L. Sydanheimo, L. Ukkonen, and G. Falciasecca, “Electromagnetic analyses of near field UHF RFID systems,” *IEEE Transactions on Antennas and Propagation*, vol. 58, no. 5, pp. 1759–1770, may 2010.
- [129] D. Dardari, N. Decarli, A. Guerra, and A. Conti, “Enhanced localization coverage with non-regenerative UWB relays,” in *20th European Signal Processing Conference (EUSIPCO)*, Bucharest, Romania, Aug. 2012.
- [130] L. Sydnheimo, L. Ukkonen, and M. Kivikoski, “Effects of size and shape of metallic objects on performance of passive radio frequency identification,” *The International Journal of Advanced Manufacturing Technology*, vol. 30, pp. 897–905, 2006. [Online]. Available: <http://dx.doi.org/10.1007/s00170-005-0133-7>

- [131] L. Ukkonen, L. Sydanheimo, and M. Kivikoski, “Effects of metallic plate size on the performance of microstrip patch-type tag antennas for passive RFID,” *IEEE Antennas and Wireless Propagation Letters*, vol. 4, pp. 410 – 413, 2005.
- [132] H. Kwon and B. Lee, “Compact slotted planar inverted-F RFID tag mountable on metallic objects,” *Electronics Letters*, vol. 41, no. 24, pp. 1308–1310, Nov. 2005.
- [133] C. Cho, H. Choo, and I. Park, “Design of novel rfid tag antennas for metallic objects,” in *IEEE Antennas and Propagation Society International Symposium*, July 2006, pp. 3245–3248.
- [134] R. D’Errico, C. Roblin, and A. Sibille, “A statistical analysis of antenna scattering in uwb arrays,” in *3rd European Conference on Antennas and Propagation*, march 2009, pp. 2562–2566.
- [135] Y. Kim and D. H. Kwon, “CPW-fed planar ultra wideband antenna having a frequency band notch function,” *Electronics Letters*, vol. 40, pp. 403–405(2), April 2004.
- [136] Y. Shen and M. Win, “Fundamental limits of wideband localization; part I: A general framework,” *IEEE Transactions on Information Theory*, vol. 56, no. 10, pp. 4956 –4980, oct. 2010.
- [137] V. Heiries, K. Belmkaddem, F. Dehmas, B. Denis, L. Ouvry, and R. D’Errico, “UWB backscattering system for passive RFID tag ranging and tracking,” in *IEEE International Conference on Ultra-Wideband (ICUWB)*, sept. 2011, pp. 489 –493.
- [138] D. Dardari, F. Guidi, C. Roblin, and A. Sibille, “Ultra-wide bandwidth backscatter modulation: Processing schemes and performance,” *EURASIP Journal on Wireless Communications and Networking*, vol. 2011:47, no. 1, 2011.
- [139] F. Guidi, N. Decarli, D. Dardari, C. Roblin, and A. Sibille, “Performance of UWB backscatter modulation in multi-tag RFID scenario using experimental data,” in *IEEE International Conference on Ultra-Wideband, ICUWB 2011*, Bologna, Italy, sep 2011, pp. 1–5.
- [140] D. Sarwate and M. Pursley, “Crosscorrelation properties of pseudorandom and related sequences,” *Proceedings of the IEEE*, vol. 68, no. 5, pp. 593 – 619, may 1980.

- [141] R. Gold, "Optimal binary sequences for spread spectrum multiplexing (corresp.)," *IEEE Transactions on Information Theory*, vol. 13, no. 4, pp. 619–621, October 1967.
- [142] O. Rothaus, "Modified gold codes," *IEEE Transactions on Information Theory*, vol. 39, no. 2, pp. 654–656, Mar 1993.
- [143] P. Fan, "Spreading sequence design and theoretical limits for quasisynchronous cdma systems," *EURASIP Journal on Wireless Communications and Networking*, vol. 2004, no. 1, p. 724989, 2004.
- [144] N. Decarli, F. Guidi, A. Conti, and D. Dardari, "Interference and clock drift effects in UWB RFID systems using backscatter modulation," in *IEEE International Conference on Ultra-Wideband, ICUWB 2012*, Syracuse, USA, sep 2012, pp. 1–5.
- [145] M. Flury, R. Merz, and J.-Y. Le Boudec, "Robust non-coherent timing acquisition in IEEE 802.15.4a IR-UWB networks," in *IEEE 20th International Symposium on Personal, Indoor and Mobile Radio Communications*, Sept. 2009, pp. 1642–1646.
- [146] W. Lovelace and J. Townsend, "Threshold discrimination and blanking for large near-far power ratios in UWB networks," *IEEE Transactions on Communications*, vol. 53, no. 9, pp. 1447–1450, Sept. 2005.
- [147] ———, "Chip discrimination for large near far power ratios in UWB networks," in *IEEE Military Communications Conference (MILCOM)*, vol. 2, Oct. 2003, pp. 868–873 Vol.2.
- [148] K. Witrisal, G. Leus, G. Janssen, M. Pausini, F. Troesch, T. Zasowski, and J. Romme, "Noncoherent ultra-wideband systems," *IEEE Signal Processing Magazine*, vol. 26, no. 4, pp. 48 –66, july 2009.
- [149] K. Witrisal, "A tutorial on noncoherent UWB systems." [Online]. Available: <http://www.spsc.tugraz.at/people/klaus/WitrisalTutorial08.pdf>
- [150] T. Gigl, F. Troesch, J. Preishuber-Pfluegl, and K. Witrisal, "An analysis of coherent and non-coherent receivers for ranging in IEEE 802.15.4a," *Journal of Electrical and Computer Engineering; Special Issue on Ultra-Wideband Circuits, Systems, and Applications*, p. 9 pp., 2012.

- [151] A. Mariani, A. Giorgetti, and M. Chiani, “Effects of noise power estimation on energy detection for cognitive radio applications,” *IEEE Transactions on Communications*, vol. 59, no. 12, pp. 3410–3420, december 2011.
- [152] H. Urkowitz, “Energy detection of unknown deterministic signals,” *Proceedings of the IEEE*, vol. 55, no. 4, pp. 523–531, april 1967.
- [153] D. Slepian and E. Sonnenblick, “Eigenvalues associated with prolate spheroidal wave functions of zero order,” *Bell System Technical Journal*, vol. 44, pp. 1745–1759, Oct. 1965.
- [154] M. Abramowitz and I. A. Stegun, *Handbook of Mathematical Functions with Formulas, Graphs, and Mathematical Tables*. Washington, D.C.: United States Department of Commerce, 1970.
- [155] F. Digham, M.-S. Alouini, and M. Simon, “On the energy detection of unknown signals over fading channels,” in *IEEE International Conference on Communications (ICC)*, vol. 5, may 2003, pp. 3575–3579 vol.5.
- [156] D. Torrieri, *Principles of Spread-Spectrum Communication Systems*. Springer, 2005.
- [157] T. Quek and M. Win, “Analysis of UWB transmitted-reference communication systems in dense multipath channels,” *IEEE Journal on Selected Areas in Communications*, vol. 23, no. 9, pp. 1863–1874, Sept. 2005.
- [158] H. Donelan and T. O’Farrell, “Method for generating sets of orthogonal sequences,” *Electronics Letters*, vol. 35, no. 18, pp. 1537–1538, sep 1999.
- [159] R. De Gaudenzi, C. Elia, and R. Viola, “Bandlimited quasi-synchronous cdma: a novel satellite access technique for mobile and personal communication systems,” *IEEE Journal on Selected Areas in Communications*, vol. 10, no. 2, pp. 328–343, feb 1992.
- [160] K. Karkkainen and P. Leppanen, “The importance of initial-phase selection agreement of PN sequences from the standpoint of numerical analysis and simulation of a DS-CDMA system,” in *IEEE Global Telecommunications Conference (GLOBECOM)*, vol. 6, 1998, pp. 3295–3301.

- [161] P. Wu and R. Minghao, "Link performance analysis for ultrawide bandwidth RFID," in *Second International Conference on Digital Manufacturing and Automation (ICDMA)*, Aug. 2011, pp. 689–692.
- [162] J. Langley, P. Hall, and P. Newham, "Balanced antipodal Vivaldi antenna for wide bandwidth phased arrays," *IEE Proc. on Microwave and Antennas Propagation*, vol. 143, no. 2, Apr. 1996.
- [163] A. Giorgetti, M. Chiani, and M. Win, "Ultrawide bandwidth RAKE reception in the presence of narrowband interference," in *IEEE 59th Vehicular Technology Conference, VTC*, vol. 3, may 2004, pp. 1659–1663 Vol.3.
- [164] R. Mallik and M. Win, "Analysis of hybrid selection/maximal-ratio combining in correlated Nakagami fading," *IEEE Transactions on Communications*, vol. 50, no. 8, pp. 1372 – 1383, aug 2002.
- [165] A. Molisch, K. Balakrishnan, D. Cassioli, C.-C. Chong, S. Emami, A. Fort, J. Karedal, J. Kunisch, H. Schantz, U. Schuster, and K. Siwiak, "IEEE 802.15.4a channel model - final report," 2005.
- [166] J. Liang and Q. Liang, "Design and analysis of distributed radar sensor networks," *IEEE Transactions on Parallel and Distributed Systems*, vol. 22, no. 11, pp. 1926–1933, 2011.
- [167] S. Bartoletti, A. Giorgetti, and A. Conti, "UWB sensor radar networks for indoor passive navigation," in *IEEE Tyrrhenian Workshop on Advances in Radar and Remote Sensing*, 2012, pp. 140–145.
- [168] E. Paolini, A. Giorgetti, M. Chiani, R. Minutolo, and M. Montanari, "Localization capability of cooperative anti-intruder radar systems," *EURASIP Journal on Advances in Signal Processing, Special Issue on Cooperative Localization in Wireless Ad Hoc and Sensor Networks*, 2008.
- [169] M. Chiani, A. Giorgetti, M. Mazzotti, R. Minutolo, and E. Paolini, "Target detection metrics and tracking for UWB radar sensor networks," in *Proc. IEEE Int. Conf. on Ultra-Wideband (ICUWB)*, 2009, pp. 469–474.
- [170] SELECT deliverable D2.1.2 Backscatter propagation model: Final report, 31/07/2012.